



ARISTOTLE UNIVERSITY OF
THESSALONIKI
FACULTY OF SCIENCES
SCHOOL OF GEOLOGY
DEPARTMENT OF
METEOROLOGY AND CLIMATOLOGY



Study of Atmosphere-Wildland Fires Interactions, using Numerical Models, in Greece

Stergios Kartsios

PhD Thesis

Thessaloniki

2020





ΑΡΙΣΤΟΤΕΛΕΙΟ ΠΑΝΕΠΙΣΤΗΜΙΟ ΘΕΣΣΑΛΟΝΙΚΗΣ
ΣΧΟΛΗ ΘΕΤΙΚΩΝ ΕΠΙΣΤΗΜΩΝ
ΤΜΗΜΑ ΓΕΩΛΟΓΙΑΣ
ΤΟΜΕΑΣ ΜΕΤΕΩΡΟΛΟΓΙΑΣ ΚΑΙ ΚΛΙΜΑΤΟΛΟΓΙΑΣ



ΣΤΕΡΓΙΟΣ Β. ΚΑΡΤΣΙΟΣ

Πτυχιούχος Φυσικός

MSc Μετεωρολογίας Κλιματολογίας και Ατμοσφαιρικού Περιβάλλοντος

ΜΕΛΕΤΗ ΤΗΣ ΑΛΛΗΛΕΠΙΔΡΑΣΗΣ ΑΤΜΟΣΦΑΙΡΑΣ – ΔΑΣΙΚΩΝ ΠΥΡΚΑΓΙΩΝ ΜΕ ΤΗ
ΒΟΗΘΕΙΑ ΑΡΙΘΜΗΤΙΚΩΝ ΜΟΝΤΕΛΩΝ ΣΤΟΝ ΕΛΛΑΔΙΚΟ ΧΩΡΟ

ΔΙΔΑΚΤΟΡΙΚΗ ΔΙΑΤΡΙΒΗ

ΘΕΣΣΑΛΟΝΙΚΗ

2020





ΣΤΕΡΓΙΟΣ Β. ΚΑΡΤΣΙΟΣ

ΜΕΛΕΤΗ ΤΗΣ ΑΛΛΗΛΕΠΙΔΡΑΣΗΣ ΑΤΜΟΣΦΑΙΡΑΣ – ΔΑΣΙΚΩΝ ΠΥΡΚΑΓΙΩΝ ΜΕ ΤΗ ΒΟΗΘΕΙΑ ΑΡΙΘΜΗΤΙΚΩΝ ΜΟΝΤΕΛΩΝ ΣΤΟΝ ΕΛΛΑΔΙΚΟ ΧΩΡΟ

Υποβλήθηκε στο Τμήμα Γεωλογίας Α.Π.Θ.

Τομέας Μετεωρολογίας και Κλιματολογίας

Ημερομηνία Προφορικής Εξέτασης: 20 Μαρτίου 2020

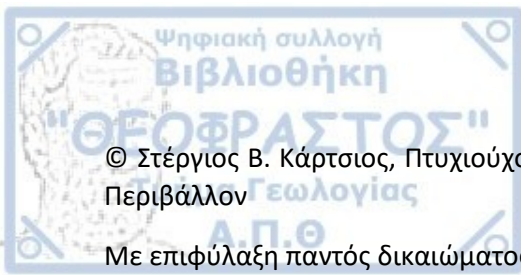
Αριθμός Παραρτήματος Επιστημονικής Επετηρίδας Τμήματος Γεωλογίας Ν° 197

Τριμελής Συμβουλευτική Επιτροπή

1. Ομότιμος Καθηγητής Καρακώστας Θεόδωρος, Επιβλέπων
2. Αναπληρωτής Καθηγητής Πυθαρούλης Ιωάννης, Μέλος Τριμελούς Συμβουλευτικής Επιτροπής
3. Καθηγητής Δημητρακόπουλος Π. Αλέξανδρος, Μέλος Τριμελούς Συμβουλευτικής Επιτροπής

Εξεταστική Επιτροπή

1. Ομότιμος Καθηγητής Καρακώστας Θεόδωρος
2. Αναπληρωτής Καθηγητής Πυθαρούλης Ιωάννης
3. Καθηγητής Δημητρακόπουλος Π. Αλέξανδρος
4. Καθηγητής Φείδας Χαράλαμπος
5. Καθηγητής Ζάνης Πρόδρομος
6. Διευθυντής Ερευνών Αμοιρίδης Βασίλης
7. Αναπληρωτής Καθηγητής Κατσαφάδος Πέτρος



© Στέργιος Β. Κάρτσιος, Πτυχιούχος Φυσικός, MSc Μετεωρολογία, Κλιματολογία και Ατμοσφαιρικό Περιβάλλον

Με επιφύλαξη παντός δικαιώματος

ΜΕΛΕΤΗ ΤΗΣ ΑΛΛΗΛΕΠΙΔΡΑΣΗΣ ΑΤΜΟΣΦΑΙΡΑΣ – ΔΑΣΙΚΩΝ ΠΥΡΚΑΓΙΩΝ ΜΕ ΤΗ ΒΟΗΘΕΙΑ ΑΡΙΘΜΗΤΙΚΩΝ ΜΟΝΤΕΛΩΝ ΣΤΟΝ ΕΛΛΑΔΙΚΟ ΧΩΡΟ – Διδακτορική Διατριβή

© Stergios B. Kartsios, BSc Physicist, MSc Meteorology, Climatology and Atmospheric Environment

All rights reserved

STUDY OF ATMOSPHERE – WILDLAND FIRES INTERACTIONS, USING NUMERICAL MODELS, IN GREECE – Ph.D. Thesis

Citation

Κάρτσιος Σ. Β., 2020. – Μελέτη της αλληλεπίδρασης Ατμόσφαιρας – Δασικών Πυρκαγιών με τη βοήθεια Αριθμητικών Μοντέλων στον Ελλαδικό χώρο. Διδακτορική Διατριβή, Τμήμα Γεωλογίας Α.Π.Θ., Αριθμός Παραρτήματος Επιστημονικής Επετηρίδας Τμ. Γεωλογίας Ν° 197, 229 σελ.

Kartsios S. B., 2020. - Study of Atmosphere-Wildland Fires Interactions, using Numerical Models, in Greece. Ph.D. Thesis, School of Geology, Aristotle University of Thessaloniki, Annex Number of Scientific Annals of the School of Geology N° 197, 229 pp.

Απαγορεύεται η αντιγραφή, αποθήκευση και διανομή της παρούσας εργασίας, εξ ολοκλήρου ή τμήματος αυτής, για εμπορικό σκοπό. Επιτρέπεται η ανατύπωση, αποθήκευση και διανομή για σκοπό μη κερδοσκοπικό, εκπαιδευτικής ή ερευνητικής φύσης, υπό την προϋπόθεση να αναφέρεται η πηγή προέλευσης και να διατηρείται το παρόν μήνυμα. Ερωτήματα που αφορούν τη χρήση της εργασίας για κερδοσκοπικό σκοπό πρέπει να απευθύνονται προς το συγγραφέα.

Οι απόψεις και τα συμπεράσματα που περιέχονται σε αυτό το έγγραφο εκφράζουν το συγγραφέα και δεν πρέπει να ερμηνευτεί ότι εκφράζουν τις επίσημες θέσεις του Α.Π.Θ.



Στην οικογένειά μου



Αντί προλόγου

Οι δασικές πυρκαγιές αποτελούν το σημαντικότερο πρόβλημα του χερσαίου φυσικού περιβάλλοντος, με μεγάλες κοινωνικοοικονομικές επιπτώσεις. Ο τουρισμός, η μελισσοκομία, η υλοτομία κ.α., έχουν ως κινητήρια δύναμη τα δάση και τα οικοσυστήματά τους. Πολλά από αυτά γειννιάζουν με αστικές ή και τουριστικές περιοχές και δέχονται ολοένα και περισσότερη πίεση από τη μεταβολή των χρήσεων γης.

Οι δασικές πυρκαγιές είναι μία σύνθετη διαδικασία φυσικών φαινομένων, διαφορετικών χώρο-χρονικών κλιμάκων και διεργασιών. Η παρούσα Διδακτορική Διατριβή συμβάλει στη μελέτη των διεργασιών αυτών, με τη βοήθεια αριθμητικών μεθόδων. Η άμεση σύζευξη του αριθμητικού μοντέλου πρόγνωσης καιρού WRF με το μοντέλο συμπεριφοράς πυρός SFIRE εξασφαλίζει τη βέλτιστη ανάδραση μεταξύ φωτιάς και ατμοσφαιρικής ροής, καθώς η *φωτιά δημιουργεί τον δικό της καιρό*. Η μελέτη της ανάδρασης ατμόσφαιρας-πυρός πραγματοποιείται σε επίπεδο μικρο-κλίμακας (μικρο-β, μικρο-γ) αλλά και στη μέσο-κλίμακα (μέσο-α, μέσο-β), με σκοπό την αξιολόγηση του αριθμητικού συνδυασμού και την ανάδειξη των διεργασιών που συνεισφέρουν θετικά σε περιπτώσεις ακραίας συμπεριφοράς μιας πυρκαγιάς.

Η παρούσα Διδακτορική Διατριβή αποτελείται από πέντε κεφάλαια. Στο πρώτο κεφάλαιο αναφέρονται οι κυριότερες αλληλεπιδράσεις μεταξύ ατμόσφαιρας - πυρός, παρουσιάζονται εν συντομία διαχρονικά στοιχεία για τις δασικές πυρκαγιές στην Ελλάδα, παρατίθενται οι βασικότεροι δείκτες και τα συστήματα κινδύνου έναρξης δασικών πυρκαγιών, καταγράφεται η εξέλιξη των μοντέλων συμπεριφοράς πυρός, ενώ παρουσιάζονται τα «2^{ης} γενιάς» αριθμητικά μοντέλα ατμόσφαιρας-πυρός. Το δεύτερο κεφάλαιο παρουσιάζει τον αριθμητικό συνδυασμό WRF-SFIRE, μαζί με τα παρατηρησιακά δεδομένα που χρησιμοποιήθηκαν για την αξιολόγησή του. Το τρίτο κεφάλαιο εξετάζει στη μικρο-κλίμακα, την ευαισθησία του συνδυασμού ως προς το βάθος απόσβεσης των εκλυόμενων ροών θερμότητας από τη φωτιά προς τα κατώτερα τμήματα της τροπόσφαιρας καθώς και την επίδραση αυτής στη συμπεριφορά του πυρός, στα δυναμικά χαρακτηριστικά της ροής και στις ιδιότητες της επαγωγικής στήλης θερμότητας. Στο τέταρτο κεφάλαιο πραγματοποιείται η εφαρμογή του συνδυασμού με σκοπό τη μελέτη δυο ακραίων επεισοδίων, α) της φονικής πυρκαγιάς στην Ανατολική Αττική και β) της πυρκαγιάς στα Γεράνια Όρη (περιοχή Κινέτα, Δυτική Αττική), στις 23^{ης} Ιουλίου 2018, αναλύονται οι επικρατούσες ατμοσφαιρικές συνθήκες και εξετάζεται ο ρόλος της τοπογραφίας στην εξέλιξη τους. Το πέμπτο κεφάλαιο αποτελεί την ανασκόπηση των αποτελεσμάτων του τρίτου και τέταρτου κεφαλαίου.

Καινοτομία της Διδακτορικής Διατριβής αποτελεί το γεγονός ότι για πρώτη φορά ελέγχεται ο μηχανισμός αναπαράστασης της κατακόρυφης κατανομής των ροών θερμότητας από το πυρικό προς το ατμοσφαιρικό μοντέλο και επισημαίνεται ο ρόλος του βάθους απόσβεσης (*heat extinction depth*) στα αποτελέσματα της βραχυπρόθεσμης πρόγνωσης της εξέλιξης του πυρός. Επίσης, δημιουργείται βάση καύσιμης ύλης για την Ελλάδα ως προς την κατηγοριοποίηση του Northern Forest Fire Laboratory (NFFL), με βάση τις κατηγορίες χρήσεων γης από τη βάση CORINE και αξιολογείται ως προς την εγκυρότητά της. Τέλος, η εφαρμογή του συνδυασμού WRF-SFIRE κατά τη διάρκεια ακραίων δασικών πυρκαγιών στον Ελλαδικό χώρο βρίσκεται ανάμεσα στις πρώτες προσπάθειες για τη δυναμική εφαρμογή ενός συστήματος έγκαιρης πρόγνωσης της εξέλιξης του πυρός σε επιχειρησιακό επίπεδο.





Η ενασχόλησή μου με το αντικείμενο της *Πύρο-Μετεωρολογίας* στη παρούσα Διδακτορική Διατριβή, αποτελεί συνέχεια της τριβής μου κατά τη διάρκεια του Μεταπτυχιακού Προγράμματος Σπουδών, στον Τομέα Μετεωρολογίας και Κλιματολογίας, Α.Π.Θ. Για πάνω από εννέα χρόνια, ο Τομέας αποτέλεσε το δεύτερο σπίτι μου, με έπλασε ως επιστήμονα και με εφοδίασε για τη συνέχεια.

Πρωτίστως, θα ήθελα να ευχαριστήσω θερμά τον επιβλέποντα της Διδακτορικής Διατριβής, Ομότιμο Καθηγητή Α.Π.Θ. Καρακώστα Θεόδωρο, για την αμέριστη εμπιστοσύνη προς το πρόσωπό μου, την καθοδήγησή του, τις προτροπές του αλλά και την πολύτιμη βοήθειά του σε μια περίοδο δύσκολη βιοποριστικά. Τον ευχαριστώ για την ανθρώπινη πλευρά του και τις φιλικές συζητήσεις που είχαμε.

Επίσης θα ήθελα να ευχαριστήσω τον Αναπληρωτή Καθηγητή Α.Π.Θ. Πυθαρούλη Ιωάννη, ο οποίος μου σύστησε την αριθμητική πρόγνωση καιρού και αφιέρωσε χρόνο μαζί μου, γύρω από θέματα του μοντέλου και όχι μόνο. Οι επισημάνσεις του υπήρξαν εφαλτήριο για ποιοτικότερη έρευνα. Τον θεωρώ συνεργάτη μου και γνωρίζω πως και εκείνος το ίδιο.

Ευχαριστώ τον Καθηγητή Α.Π.Θ. Δημητρακόπουλο Π. Αλέξανδρο για τις συζητήσεις που είχαμε, τα σχόλιά του και το χρόνο που διέθεσε για να γίνει η συγκεκριμένη έρευνα καλύτερη. Η συμβολή του ήταν καθοριστική.

Ευχαριστώ τα υπόλοιπα μέλη της επταμελούς εξεταστικής επιτροπής, Καθηγητή Α.Π.Θ. Φείδα Χαράλαμπο, Καθηγητή Α.Π.Θ. Ζάνη Πρόδρομο, Διευθυντή Ερευνών ΕΑΑ Αμοιρίδη Βασίλη και Αναπληρωτή Καθηγητή Χ.Π. Κατσαφάδο Πέτρο, για τα πολύτιμα σχόλιά τους πάνω στο παρών σύγγραμμα.

Στο σημείο αυτό θα ήθελα να ευχαριστήσω την Αναπληρώτρια Καθηγήτρια Α.Π.Θ. Κατράγκου Ελένη, για την ευκαιρία που μου προσέφερε ώστε να επιστρέψω στον Τομέα, την συνεργασία που έχουμε και την υπομονή που έδειξε ώστε να ολοκληρωθεί η παρούσα διατριβή, εις βάρος άλλων επαγγελματικών υποχρεώσεων. Επίσης θα ήθελα να ευχαριστήσω τον συνεργάτη μου Ιωάννη Τεγούλια, για τη βοήθεια του σε όλα τα τεχνικής φύσεως ζητήματα που προκύπτανε κατά καιρούς. Ευχαριστώ επίσης τους συνεργάτες μου, Δρ. Βασίλη Παυλίδη και Υποψήφιους Διδάκτορες Σοφιάδη Γιάννη και Καρυπίδου Μαρία-Χαρά για τις όμορφες συζητήσεις μας και το χρόνο που περάσαμε μαζί μέσα στο ίδιο γραφείο.

Ευγνωμονώ τους γονείς μου για τα εφόδια και τις αξίες που μου προίκισαν, τις αρετές και τα μειονεκτήματα που μου έσπειραν και την αμέριστη βοήθειά τους όλον αυτό το καιρό. Υπήρξαν δίπλα σε μένα και στην οικογένειά μου από την αρχή αυτής της προσπάθειας και όχι μόνο. Τους ευχαριστώ με όλη μου την καρδιά.

Το μεγαλύτερο ευχαριστώ πηγαίνει στην οικογένειά μου, στη γυναίκα και τον υιό μου. Τους ευχαριστώ για τις θυσίες που έκαναν για να ολοκληρωθεί η παρούσα διατριβή, την κατανόηση που έδειξαν στην απουσία μου, την υποστήριξη, την εμπιστοσύνη και για όλες τις όμορφες στιγμές που ζούμε. Η αξία της οικογένειας είναι ανεκτίμητη. Ευχαριστώ επίσης τους γονείς της για τη συμβολή τους στην ολοκλήρωση αυτής της διατριβής.





Η παρούσα Διδακτορική Διατριβή διερεύνησε τις αλληλεπιδράσεις ατμόσφαιρας – πυρός με τη βοήθεια ενός άμεσα συζευγμένου αριθμητικού μοντέλου (WRF-SFIRE), το οποίο αποτελεί συνδυασμό ενός αριθμητικού μοντέλου πρόγνωσης καιρού με ένα ημι-εμπειρικό μοντέλο διάδοσης του πυρός. Η αξιοποίηση των δυνατοτήτων του εν λόγω συστήματος επέτρεψε την ανάλυση των αναδράσεων ατμόσφαιρας-πυρός σε διαφορετικές χωρικές κλίμακες, από τη μέση κλίμακα και κατά τη διάρκεια πυρκαγιών με ακραία συμπεριφορά στον Ελλαδικό χώρο, έως τη μικροκλίμακα, μέσα από ιδεατά πειράματα με τη τεχνική Large Eddy Simulation (LES). Επιπρόσθετα, ελέγχθηκε η απόδοση του αριθμητικού συνδυασμού σε σύγκριση με παρατηρησιακά δεδομένα επιφανείας από την Εθνική Μετεωρολογική Υπηρεσία (EMY) και δεδομένα τηλεπισκόπησης από τους δορυφόρους Meteosat (SEVIRI), SENTINEL-2 (MSI), Aqua, Terra (MODIS) και Suomi-NPP (VIIRS).

Στο πρώτο μέρος της ερευνητικής διεργασίας μελετήθηκε η επίδραση των εκλυόμενων ροών θερμότητας του πυρός στις ιδιότητές του (ρυθμός διάδοσης, καμένη έκταση κτλ.) και στα χαρακτηριστικά της ατμοσφαιρικής ροής και της επαγωγικής στήλης θερμότητας (πλούμιο), αντίστοιχα. Πιο συγκεκριμένα, εκτιμήθηκε ο ρόλος της παραμέτρου *heat extinction depth* ή *e-folding depth* (z_{ex} , ύψος στο οποίο οι ροές θερμότητας αποκτούν το 36% της αρχικής τους τιμής), μέσα από οχτώ ιδεατά αριθμητικά πειράματα, τα οποία πραγματοποιήθηκαν με τη μέθοδο LES. Σύμφωνα με τα αποτελέσματα, η τιμή του z_{ex} επηρέασε την καθ' ύψος κατανομή των εκλυόμενων ροών αλλά επίσης και την ποσότητα της εκλυόμενης ενέργειας που «εισχωρεί» στο ατμοσφαιρικό μοντέλο. Όσο μεγαλύτερη ήταν η τιμή του z_{ex} τόσο μεγαλύτερο υπήρξε και το ποσοστό της ενέργειας που ήταν διαθέσιμο στο πρώτο θ επίπεδο του μοντέλου. Επιπρόσθετα, διαφορετικές τιμές z_{ex} κάτω από ίδιες αρχικές ατμοσφαιρικές συνθήκες είχαν ως αποτέλεσμα διαφορετικές καμένες περιοχές (σχήμα και έκταση). Αν και παρατηρήθηκαν διαφορές τόσο στη δομή όσο και στην ένταση τους, ο αριθμητικός συνδυασμός αναπαρήγαγε συγκεκριμένα χαρακτηριστικά της ατμοσφαιρικής ροής, όπως τη ζώνη σύγκλισης μπροστά από το μέτωπο και την εκ των όπισθεν καθοδική εισροή αέρα προς τη βάση της επαγωγικής στήλης θερμότητας σε όλα τα πειράματα. Εν γένει, η αύξηση της παραμέτρου z_{ex} οδήγησε σε μικρότερες χρονικά-μέσες ανωμαλίες της δυνητικής θερμοκρασίας, κοντά στο έδαφος αλλά και στην κορυφή του πλουμίου. Ωστόσο, τα μέγιστα των ανωμαλιών αυτών δεν ακολούθησαν κάποια γραμμικότητα και η εμφάνισή τους διέφερε χωρο-χρονικά ανάμεσα στα πειράματα. Όσον αφορά τα δυναμικά χαρακτηριστικά της ροής, διαφορές παρατηρήθηκαν τόσο στην ένταση όσο και στα μοτίβα της κάθετης συνιστώσας του στροβιλισμού (οριζόντιος στροβιλισμός) και της απόκλισης κοντά στην επιφάνεια, επηρεάζοντας το σχήμα της καμένης έκτασης και τη θέση της κεφαλής. Μικρές τιμές του z_{ex} οδήγησαν στην παραγωγή περισσότερο οργανωμένων και ενισχυμένων ζευγών στροβίλων, κυκλωνικής και αντικυκλωνικής φοράς αντίστοιχα, περιοχών έντονου οριζόντιου στροβιλισμού (θετικού ή αρνητικού) κατά μήκος των πλευρικών ορίων και έμπροσθεν της κεφαλής. Αντιθέτως στα πειράματα όπου η τιμή του z_{ex} ήταν μεγαλύτερη των 50 m, ο οριζόντιος στροβιλισμός ήταν λιγότερο οργανωμένος και παροδικός. Ο όρος του σωληνοειδούς στην εξίσωση του στροβιλισμού (οριζόντιος) βρέθηκε έως και δώδεκα φορές μικρότερος σε σύγκριση με τους υπόλοιπους όρους, ενώ ο όρος της οριζόντιας μεταφοράς συνείσφερε θετικότερα στην αύξηση του οριζόντιου στροβιλισμού. Ο όρος της κλίσης/συστροφής βρέθηκε μεγαλύτερος κατά τα πρώιμα στάδια της φωτιάς, όπου η παραγόμενη λόγω κατακόρυφης διάτμησης του ανέμου, ψ συνιστώσα του στροβιλισμού προσανατολίστηκε κατακόρυφα εξαιτίας της έντονης ανωμεταφοράς από την φωτιά επιφανείας.

Στο δεύτερο μέρος της ερευνητικής διεργασίας πραγματοποιήθηκε η συνοπτική ανάλυση, παρουσιάστηκαν οι επικρατούσες ατμοσφαιρικές συνθήκες στην επιφάνεια, διερευνήθηκε η

επίδραση της τοπογραφίας στη μέση ροή και στη συμπεριφορά του πυρός και ελέγχθηκε η επίδραση των παραμέτρων της ανάφλεξης (τοποθεσία, χρόνος, είδος) στη καμένη έκταση, κατά τη διάρκεια των γεγονότων της 23^{ης} Ιουλίου 2018, όπου εκδηλώθηκαν δύο πυρκαγιές με ακραία συμπεριφορά, σε Δυτική (περιοχή Κινέτα) και Ανατολική (περιοχή Μάτι) Αττική. Σύμφωνα με τη συνοπτική ανάλυση, η παρουσία ενός αυλώνα στην ανώτερη τροπόσφαιρα με θετική κλίση πάνω από την Κεντρική Μεσόγειο, η κίνησή του προς τα ανατολικά και η αλληλεπίδρασή του με τον υποτροπικό αεροχείμαρρο, οδήγησαν σε έντονη δυτική κυκλοφορία πάνω από τον Ελλαδικό χώρο. Ο αυτόματος μετεωρολογικός σταθμός στο Πεντελικό Όρος κατέγραψε ριπαίο άνεμο έως 25 m s^{-1} , μεταξύ 1230 και 1430 UTC, ενώ αρκετοί σταθμοί επιφανείας (συνοπτικοί και δευτερεύοντες) της Εθνικής Μετεωρολογικής Υπηρεσίας (EMY), στην ευρύτερη περιοχή της Αττικής, κατέγραψαν ριπές ανέμου μεγαλύτερες των 20 m s^{-1} , μεταξύ 1200 και 1730 UTC. Ο αριθμητικός συνδυασμός αξιολογήθηκε ως προς την θερμοκρασία και υγρασία του αέρα και την ταχύτητα του ανέμου με βάση τα δεδομένα των σταθμών επιφανείας της EMY, χρησιμοποιώντας τις μεθόδους χωρικής παρεμβολής Inverse Distance Weighting (IDW), Gressman και 4-grid point. Η απόδοση του κρίθηκε ικανοποιητική, αν και βρέθηκε να υπερεκτιμά τη θερμοκρασία στα 2 m και τη ταχύτητα του ανέμου στα 10 m, και να υποεκτιμά τη σχετική υγρασία στα 2 m. Η προσομοίωση της καμένης έκτασης και στα δύο γεγονότα υπό μελέτη ήταν σε σχετική συμφωνία με τη εκάστοτε πραγματική, ωστόσο και στις δύο περιπτώσεις υπήρξε καθυστέρηση στην ανάπτυξη της δυναμικής τους, με αποτέλεσμα να προκύψουν διαφορές ως προς την εξέλιξή τους χρονικά. Επιπλέον, η ανάλυση των αποτελεσμάτων της αριθμητικής προσομοίωσης υπέδειξε την παρουσία επαγόμενων κυμάνσεων λόγω ορογραφίας στην ευρύτερη περιοχή, μονοπάτια ατμοσφαιρικής ροής μεγάλης ταχύτητας στα υπήνεμα των ορεινών εμποδίων, παροδική εμφάνιση χαρακτηριστικών ενός τυρβώδους υδραυλικού άλματος στα κατάντη του Όρους Πεντέλη και κατακόρυφη μεταφορά ενέργειας και ορμής προς τα έδαφος, κατά τη διάρκεια εμφάνισης των μέγιστων ταχυτήτων ανέμου. Η τύρβη και οι δυναμικά ασταθείς συνθήκες στα υπήνεμα των Γεράνειων Ορέων (περιοχή Κινέτα) και του Πεντελικού Όρους (περιοχή Μάτι) συνέβαλαν στην αύξηση της κινητικής ενέργειας της ροής, ενώ το πεδίο του στροβιλισμού εισήγαγε επιπλέον δυναμικό εξαναγκασμό στους ρυθμούς εξάπλωσης των πυρκαγιών. Η επίδραση της ορογραφίας στην εκάστοτε πυρκαγιά βρέθηκε διαφορετική καθώς, η παρουσία των απομονωμένων Γεράνειων Ορέων οδήγησε σε θερμότερες και ξηρότερες συνθήκες, με ισχυρότερες ταχύτητες ανέμου στα κατάντη, ενώ το Όρος Πεντέλη είχε μικρότερη επίδραση στις ατμοσφαιρικές συνθήκες στην υπήνεμη πλευρά. Επιπλέον, τα πειράματα ευαισθησίας έδειξαν πως ο τύπος ανάφλεξης στο πυρικό μοντέλο μαζί με το ρυθμό εξάπλωσης κατά την ανάφλεξη επηρέασαν περισσότερο την εξάπλωση του πυρός κατά τα πρώτα στάδια της πυρκαγιάς στο Μάτι, σε σχέση με τις άλλες υπό διερεύνηση παραμέτρους. Τέλος, η κατηγοριοποίηση της καύσιμης ύλης δεν επηρέασε τόσο τους ρυθμούς εξάπλωσης κατά τα πρώτα στάδια της πυρκαγιάς όσο αργότερα.

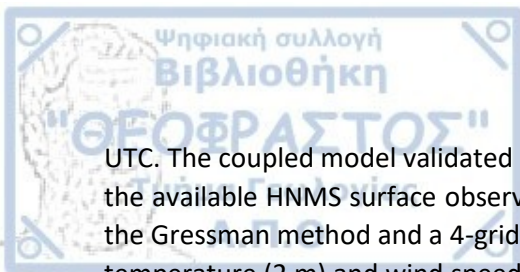


Abstract

The present PhD dissertation investigated several aspects of atmosphere-wildland fire interactions by utilizing an online coupled atmosphere – fire numerical model (WRF-SFIRE), which is a combination of a numerical weather prediction (NWP) model with a semi-empirical numerical fire spread model. Subsequently, this PhD dissertation exploited the capabilities of WRF-SFIRE modelling system across several spatial scales, from mesoscale analysis on fire weather conditions during high-impact fire events in Greece to microscale analysis on highly idealized experiments, in Large Eddy Simulation (LES) mode. Additionally, this manuscript addressed the performance of the coupled model by utilizing a number of surface observational data from the Hellenic National Meteorological Service (HNMS) and several EO data from the Meteosat second generation (SEVIRI), SENTINEL-2 (MSI), Aqua, Terra (MODIS) and Suomi-NPP (VIIRS) satellites, respectively.

The first study investigated the influence of the released heat fluxes from a surface fire on its characteristics (e.g. rate of spread, fire area), flow dynamics in the vicinity and plume properties. Specifically, the role of the extinction depth or e-folding depth parameter, z_{ex} (the height at which the fluxes are equal to 36% of their initial value), was assessed throughout eight highly idealized experiments, which were performed in LES mode. Results indicated that the choice of the z_{ext} parameter not only affected the vertical distribution of the fluxes but also the amount of the released energy from the surface fire. The higher the z_{ext} value, the higher the percentage of the released energy that resided on the first theta model level. Moreover, the calculated burn probabilities revealed that under identical initial atmospheric conditions but different e-folding depths discrepancies might occur in the resulted fire area. The coupled model was able to reproduce certain flow characteristics such as the convergence region ahead of the fire front and the descending rear inflow to the updraft's base, in all experiments albeit structural differences were observed. In general, an increase of the z_{ext} parameter led to weaker time-averaged potential temperature anomalies both close to the ground and in the top of the convective plume. However, the temporal peaks in theta anomalies did not follow any linearity and their occurrence varied both in time and space. The analysis on near surface dynamics revealed discrepancies in the patterns and the magnitude of vertical vorticity and divergence fields, in the shape of the fire perimeter and the location of the fire head between the experiments. Low e-folding depth values produced more organized and intense counter-rotating vertical vorticity pairs and regions of vorticity along the fire flanks and in front of the active fire head, whilst in the sensitivities with z_{ext} greater than 50 m, this vorticity was less organized and more transient. The vorticity equation budget analysis showed that the solenoidal term was up to twelve orders of magnitude less than the other terms. The horizontal advection of vertical vorticity contributed the most to the increase of vorticity, while the tilting/twisting term was dominant at the early stages of the fire, where the ambient shear-generated horizontal vorticity, ω_y , was oriented into vertical due to buoyant gradients from the surface fire.

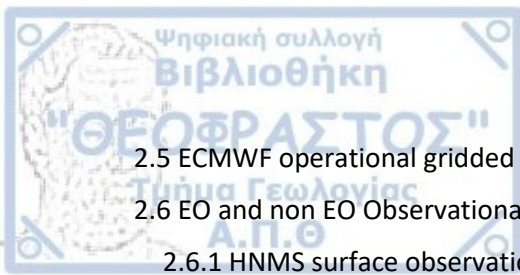
The second study analyzed the prevailing weather conditions on 23rd of July 2018, assessed the performance of the WRF-SFIRE modelling system, investigated the role of the complex terrain to the mean flow and fire behavior and examined the uncertainty of ignition features during two high-impact fire events that occurred in Attica Region, Central Greece (Mati and Kineta fire events). The synoptic analysis revealed the presence of a positively tilted trough over the Central Mediterranean, moving eastwards and interacting with the subtropical jet, resulting in a strong westerly flow over Greece. The AWS in Penteli Mt. recorded gusts reaching 25 m s^{-1} between 1230 and 1430 UTC, while several HNMS surface stations in the wider area recorded wind gusts exceeding 20 m s^{-1} between 1200 and 1730



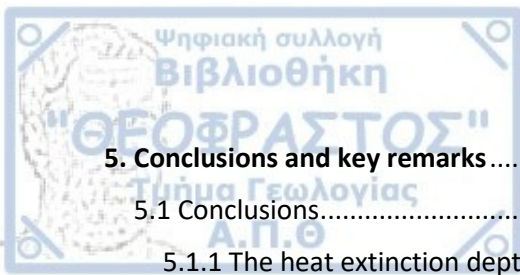
UTC. The coupled model validated in terms of temperature, relative humidity and wind speed against the available HNMS surface observations by applying the Inverse Distance Weighting (IDW) method, the Gressman method and a 4-grid point method. Although the model performed satisfactory, the air temperature (2 m) and wind speed (10 m) were overestimated, whilst the relative humidity (2m) was underestimated. The predicted fire perimeters were in satisfactory agreement with the observed ones, but there were time lags in the initial development of the fires' momentum and subsequently discrepancies on the temporal evolution of the modeled fires occurred. Moreover, simulations revealed the presence of induced orographic waves, paths of high winds on the lee-slopes, transient resemblance of a hydraulic jump downstream of Penteli Mt., while indicated a downward transport of energy and momentum during the maximum wind speed occurrences. The turbulent and dynamically unstable conditions on the lee-slopes of Gerania Mts. (Kineta) and Penteli Mt. (Mati) contributed to the flow kinetic energy, while vorticity provided additional forcing into the fire spread rates. Quite different influences of topography in each fire event were found, where the isolated Gerania Mts contributed to warmer, drier and windier conditions leeward, while Penteli Mt. had a lesser impact on atmospheric variables downstream. In addition, the sensitivity experiments showed that the type of ignition along with the rate of spread during ignition influenced the most the fire propagation at the early stages of the fire at Mati event. Finally, fuel description had a lesser impact on the simulated rate of spreads during the early stages of the fire but influenced its behavior later.



1. Introduction	5
1.1 A short overview of atmosphere – fire interactions	6
1.2 Wildfires in Greece	11
1.3 A review of fire danger/risk and drought indices, and fire danger rating systems.....	14
1.3.1 Munger Graphic Method.....	14
1.3.2 Angström Index (AI).....	15
1.3.3 Nesterov Index (NI)	15
1.3.4 McArthur Forest and Grassland Fire Danger Meters	16
1.3.5 Keetch-Byram Drought Index (KBDI)	17
1.3.6 Chandler Burning Index (CBI)	18
1.3.7 Fosberg Fire Weather Index (FFWI).....	19
1.3.8 Canadian Forest Fire Weather Index (CFFWI)	20
1.3.9 National Fire Danger Rating System (NFDRS).....	23
1.3.10 Haines Index (HI)	26
1.3.11 Fire Potential Index (FPI)	26
1.3.12 F index	27
1.3.13 Santa Ana Wildfire Threat Index (SAWTI)	29
1.3.14 Hot-Dry-Windy Index (HDWI).....	29
1.3.15 Additional European fire danger indices and methods.....	29
1.3.16 Fire danger rating system in Greece	30
1.4 Wildfire modelling.....	31
1.4.1 FIRETEC.....	33
1.4.2 WFDS	34
1.4.3 CAWFE	34
1.4.4 ARPS/DEVS-FIRE	34
1.4.5 ForeFire/Meso-NH.....	35
1.4.6 WRF-(S)FIRE	35
1.5 Motivation and Overview.....	37
2. Numerical models, observational data and methodology	39
2.1 Introduction.....	39
2.2 The Weather Research and Forecasting model	39
2.3 The Spread FIRE model.....	40
2.4 The online coupled WRF-SFIRE modelling system	41



2.5 ECMWF operational gridded analyses	43
2.6 EO and non EO Observational datasets	44
2.6.1 HNMS surface observations	44
2.6.2 Meteosat SEVIRI satellite observations.....	46
2.6.3 SENTINEL-2 satellite observations.....	46
2.6.4 Copernicus Emergency Management Service	46
2.6.5 MODIS Fire and Thermal Anomalies	47
2.6.6 VIIRS 375m active fire detection product	47
2.7 Methods of analysis.....	48
2.7.1 Vorticity and vorticity equation.....	48
2.7.2 Calculation of air density.....	50
3. The heat extinction depth concept: An application to the WRF-SFIRE modelling system.....	51
3.1 Introduction.....	51
3.2 Numerical modelling system and experimental setup.....	53
3.2.1 Domain configuration and model setup	53
3.2.2 Initial and lateral boundary conditions / fire ignition	56
3.2.3 Experimental design	57
3.3 Results	58
3.3.1 Fire fluxes into the atmospheric model	58
3.3.2 Impact of z_{ext} to pyric parameters	62
3.3.3 Impact of z_{ext} to atmosphere/plume properties.....	68
3.4 Discussion	96
3.5 Summary and conclusions.....	98
4. Numerical investigation of atmosphere fire interactions during extreme fire events in Attica region	101
4.1 Introduction.....	101
4.2 Description of the events	103
4.3 Data and numerical modelling system.....	103
4.4 Synoptic Analysis and Observational Data	108
4.5 Airflow modification and mountain waves	113
4.6 Numerical simulations.....	118
4.6.1 Model verification	118
4.6.2 Control experiment	121
4.6.3 Sensitivity experiments	134
4.7 Discussion	142
4.8 Summary and conclusions.....	144



5. Conclusions and key remarks	147
5.1 Conclusions.....	147
5.1.1 The heat extinction depth concept: An application to the WRF-SFIRE modelling system.	147
5.1.2 Numerical investigation of atmosphere-fire interactions during extreme fire events in Attica region	149
5.2 Key remarks.....	151
References	153
Acknowledgements	181
Appendix I	183
Statistical formulas.....	183
Spatial interpolation formulas.....	183
Meteorological variables.....	183
Appendix II	185
Tables	185
Figures	206
Appendix III	211
Figures	211





Chapter 1

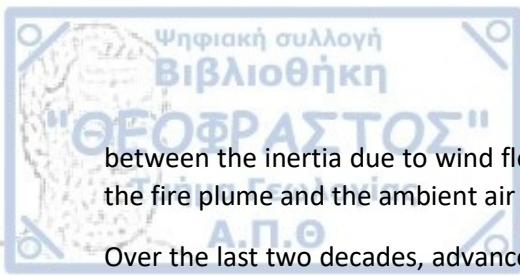
Introduction

Wildfires are known as natural phenomena and important features of many ecosystems (Bowman et al., 2009; Pausas et al., 2008). The significant increase in the number of fires and area burnt during the 2nd half of the 20th century has confirmed the perception that wildfires are a serious environmental and socioeconomic hazard for most Mediterranean-type ecosystems (Paschalidou and Kassomenos, 2016). Areas with Mediterranean-type climate, due to the combination of dry and warm climate, flammable vegetation and increased human activities, are extremely fire prone (Dimitrakopoulos et al., 2011b). Wildfires in the Mediterranean region have been linked to fuel accumulation, as a consequence of the abandonment of cultivated fields and afforestation policies, climate change and increased ignition sources (Moreira and Russo, 2007), while concerns have grown about how climate change and human activities might impact future fire regimes (Paschalidou and Kassomenos, 2016).

Wildfires can be characterized by the nature of their interaction with the local environment. The geometry and burning characteristics of the fuel bed, the properties of the atmosphere in the vicinity of the fire and the local topography define that environment, which is also known in the literature as the wildfire-triangle. The role of weather to fire activity is complex and varies over spatiotemporal resolutions with short-term variation affecting local fire behavior, and seasonal and inter-annual variations affecting fuel production and flammability over large areas as well as habitat type richness (Drakou et al., 2011; Falk et al., 2007; Trouet et al., 2009). Extreme weather results in large and intense fires, where in Mediterranean-type ecosystems extreme weather becomes an increasingly important forcing mechanism for large fires (Moritz, 1997), while the area burned by large fires (> 100 ha) is positively correlated with summer dryness and negatively correlated with summer wetness (Ganteaume and Jappiot, 2013). For example, the exceptionally hot and dry summer of 2007 was the most contributed factor in the extensive fires in Greece that burned approximately 190,836 ha in total and resulted to 67 life losses (Founda and Giannakopoulos, 2009). Unfortunately, on 23rd of July 2018, Greece faced another tragedy, where the high surface temperatures and low relative humidity values, the strong winds, along with the fuel conditions and the morphological features of the wider area of Rafina, East Attica region, Central Greece (wildland-urban interface, WUI), resulted in high fire propagation rates, minimum responses by the local civilians and authorities and on the aftermath, 103 life losses.

The combined effect of weather conditions and fuel characteristics (e.g. fuel moisture and loading) is expressed through several fire-weather indices, which are used to identify potential fire risk or danger¹. However, wildland fires include complex physical processes across different spatial and temporal scales. In this multiscale approach, heat transfer between the flame and the unburned fuel depends on two physical mechanisms, radiation from soot particles in the flame and convective heat transfer between the hot gases from the burning zone and vegetation located ahead of the fire front (Morvan, 2011). Which of the these two mechanisms is the most important depends on the competition

¹ Fire risk is defined as the chance that a fire might start, as affected by the nature and incidence of causative agents (Hardy, 2005). Fire danger refers to the assessment of the weather of climatic factors which determine the ease of ignition, rate of spread, difficulty of control and impact of a fire (Bedia et al., 2018). Fire hazard is referred as a fuel complex, defined by volume, type, condition, arrangement, and location that determines the degree of ease of ignition and the resistance to control (Hardy, 2005).



between the inertia due to wind flow and the buoyancy coming from the pressure gradient between the fire plume and the ambient air (Morvan et al., 2009, 2008).

Over the last two decades, advances on fire modelling and computational resources have resulted to the development of multi-scale models (Bakhshaii and Johnson, 2019; Papadopoulos and Pavlidou, 2011; Sullivan, 2009a, 2009b, 2009c). Fire behavior models, like BehavePlus (Andrews, 2014, 2007), FARSITE (Finney, 1998) etc. have shown significant development as well. These models are initialized by meteorological data, such as wind and air temperature, without any feedback to the atmospheric model. Subsequently, the lack of such a feedback mechanism, between the weather and fire models, is a major drawback of these fire behavior models.

The development and utilization of coupled atmospheric-fire behavior models is considered as a breakthrough in global research for innovative methods of predicting fire behavior. A significant range of the processes evolved during a wildfire can be simulated by coupling a mesoscale weather model with a fire propagation algorithm (Clark et al., 1996a, 1996b, 2004; Coen, 2013; Coen et al., 2013; Filippi et al., 2009; Mandel et al., 2011). Over the years, several prescribed burns and field experiments (Benech, 1976; Clements et al., 2019, 2018, 2008, 2007, 2006; Coen et al., 2004; Countryman, 1969; Hinzman, 2003) have provided valuable observational data. The latter were utilized for the evaluation and verification of the developed models (Filippi et al., 2013; Kochanski et al., 2013a), revealing their potentiality but also their weaknesses.

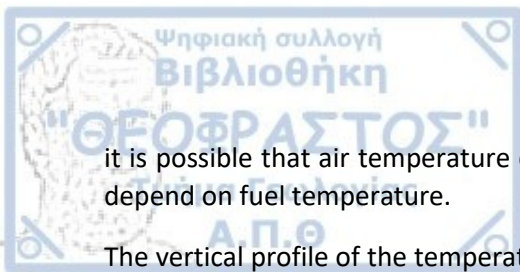
This chapter presents briefly some key factors on atmosphere – fire interactions (section 1.1) and provides information about wildfires in Greece (section 1.2), based on historical data from various sources. Section 1.3 reviews the most used fire danger indices and fire danger rating systems in the world, while section 1.4 elaborates on the advances in wildfire modelling and presents six state-of-the-art wildfire models. Section 1.5 quotes the motivation for the present PhD dissertation and provides the structural overview of this manuscript.

1.1 A short overview of atmosphere – fire interactions

Fire – atmosphere or vice versa interactions encompass the interactions between the atmosphere and the combustion process but also include a) the interactions between the fuels presently burning and the atmosphere and b) the interactions between the atmosphere and those fuels that will eventually burn in a given fire (Potter, 2012a). Also, fire – atmosphere interactions include energy and mass fluxes between living and dead vegetation and the atmosphere. During a wildland fire, these interactions produce perturbations in state variables like air temperature, humidity and wind speed, which are greater than those from other processes. This section elaborates shortly the rationale and the scientific discussion behind these interactions².

Over the years, several studies tried to relate air temperature with fire characteristics (the former is recognized as the dominant factor determining wildland fire behavior) but failed to explain the direct influence of surface air temperature to fire behavior. Potter (1996) found that air temperature at fire days differed significantly from temperatures on days shortly before or after the fire, but this result was robust only at certain locations. Van Wagner (1979) noted the non-linear effect of temperature on saturation vapor pressure, while earlier, McArthur (1966) argued that temperature effect on fuel moisture is much less than that of relative humidity. As Potter (2012a) mentioned in his review article,

² For a complete review of atmospheric interactions with wildfire, the interested reader is referred to Potter (2012a, 2012b).



it is possible that air temperature correlates with fire behavior due to the fact that these properties depend on fuel temperature.

The vertical profile of the temperature (known as lapse rate or stability) also influences fire behavior, while determines the structure of a fire's plume and its characteristics. An unstable profile increases the vertical mixing and the turbulence within the unstable region. In addition, stability is related to the development of fire whirls (Byram and Nelson, 1951). Arnold and Buck (1954) proposed that in the existence of an inversion, drier and windier air from above might flow downward, if the convective column penetrated the inversion, resulting in a sudden transition in fire behavior. Moreover, lapse rate is used in Haines Index (Haines, 1988) (see sub-section 1.3.10), in order to assess the atmospheric potential for large or erratic fires. Jenkins (2004) utilized Haines Index to show that boundary-layer depth and the presence or absence of an inversion layer above it are the key factors determining plume height and maximum updraft velocity. As Potter (2009a) summarizes, it is clear that temperature profile influences fire behavior by controlling a) turbulence as manifest in variable winds, b) rate of entrainment in the rising plume and c) the degree to which the energy released by the fire converts into kinetic energy of the updraft.

Regarding the air moisture, the first reference to the night-time humidity recovery was first done by (Gisborne, 1927a), while early studies (Bates, 1923; McCarthy, 1923; Munns, 1921) found that evaporation correlates well with fuel moisture, but was impractical to measure. On the other hand, some studies (McArthur, 1966; Van Wagner, 1979) used fuel moisture as a surrogate indicator of fire behavior. Vapor pressure, an indicator of the available water in the air, was found to negatively correlate with fire behavior, while dew-point depression or wet-bulb depression were also used to provide some correlations with the size of fires or fuel moisture. In general, atmospheric moisture influences fuel moisture, which in turns affects fire behavior or danger (Potter, 2012a).

Under unstable conditions, the moisture profile indicates the degree to which mixing and turbulence will decrease surface humidity (Foley, 1947), affecting fuel moisture and thus increasing fire intensity and spread. Jenkins (2004) found that a moist profile increased fire behavior as an entrainment parcel rose from a fire, while concluded that plume characteristics change only weakly as the 850 hPa dew-point depression varies from 4 to 15 °C. The concept of downdraft convective available potential energy (DCAPE) was employed by Potter (2005) in order to illustrate that a dry profile provides more potential for a downburst, where the liquid water required for such a downburst could come either from ambient air flowing into the fire plume or from the water produced during the combustion process.

The role of near surface wind in fire-atmosphere interactions was early recognized (Gisborne, 1928). In general, wind contributes to moisture exchange between the air and the fuels (Matthews, 2006; Van Wagner, 1979; Viney, 1991), affects the rate of spread (Albini, 1982; Baughman and Albini, 1980; McArthur, 1966; Rothermel, 1972; Viegas and Neto, 1991), carries embers that potentially cause spot fires and controls the fluxes of oxygen and combustion products at the flaming front (Potter, 2012a). Fire also affects near surface wind and flow characteristics around a fire.

Byram (1954) related wind profiles and fire behavior by examining the nearest available wind profiles during blow-up fires³. The most characteristic feature was a low-level jet with a maximum speed above 8 m s⁻¹ within 300 m of the fire's elevation. Steiner (1976) based his analysis on Byram's (1954) wind

³ According to the Glossary of Wildland Fire Terminology, a "blow-up" fire is defined as the "sudden increase in fireline intensity or rate of spread ... often accompanied by violent convection and may have other characteristics of a fire".

profiles. He suggested that the interaction of upwind convergence and the fire's updraft with the wind profile would have two distinct impacts. A negative wind shear with height would increase convergence at the fire, subsequently fanning the flames and increasing intensity, while a positive wind shear would produce net divergence on the downwind side of the fire, counteracting the surface convergence produced by the fire (Fig. 1.1).

Numerical experiments highlighted several effects of wind profile to fire behavior, as well. Wind speed influences the updraft strength and tilt, while impacts the generation of roll vortices (Heilman and Fast, 1992). Moreover, under favorable conditions the vertical shear and the fire updraft may interact to produce downstream vertical vortex pairs, which influence fire behavior (Clark et al., 1996b). In addition, the presence of a critical layer (zero wind) in the wind profile can lead to generation of new updraft cells upwind of the fire (Kiefer et al., 2009, 2008). The magnitude and type of shear in the above surface wind field affects fire propagation, while the magnitude of the convergence zone associated with the surface flow that propagates the fire front does not appear to be related directly to the strength of the fire-induced updraft (Kochanski et al., 2013c).

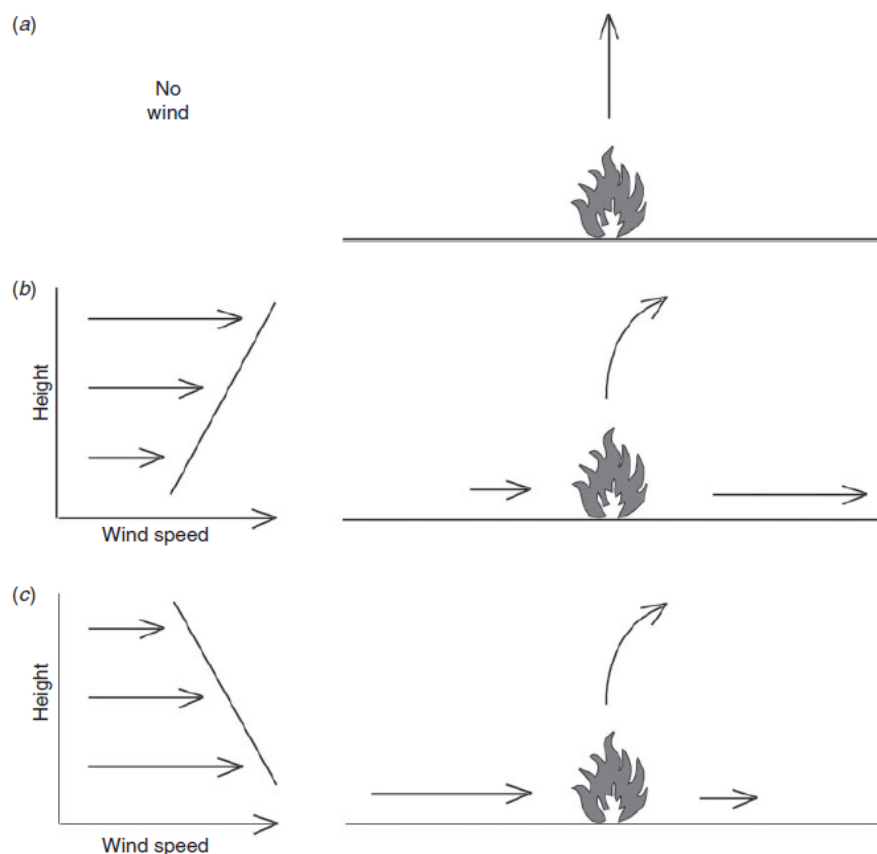


Fig. 1.1: Influence of vertical wind shear and fire-induced vertical mixing on convergence or divergence at the ground in the case of a) no wind, b) positive wind shear and c) negative wind shear. Originated from Steiner (1976). Adopted from Potter (2012a), his Fig. 8.

The most complex part of the fire-atmosphere interaction is perhaps the plume dynamics. Plume dynamics involve the visible updraft, with the invisible downdraft and horizontal circulations into and around the fire plume, the effects of sensible and latent heat fluxes from the fire and the generation of vortices (Potter, 2012b). The aforementioned vary very quickly in time and space. Numerous studies have demonstrated certain aspects on plume dynamics based on field experiments (Clements, 2010;

Clements et al., 2019, 2007; Coen et al., 2004; Countryman, 1969; Lareau and Clements, 2016; Palmer, 1981; Taylor et al., 1971, 1968; Wilson, 1969), radar data (Banta et al., 1992; Reid and Vines, 1972) and numerical experiments (Clark et al., 1996a; Cunningham et al., 2005; Kiefer et al., 2015; Kochanski et al., 2019; Mallia et al., 2018; Sun et al., 2006, 2009).

Potter (2012b) provided a conceptual model (Fig. 1.2) on airflow in and around a developed fire front, where a descending rear inflow "feeds" the fire and an accelerating updraft with a laminar portion lower and greater mixing above produces greatest vertical velocities. The plume is subject to vertical extension until it hits a stable layer, while velocity varies in time and space within the plume. In addition, multiple updraft cores may develop by a single fire and intensive turbulence exists throughout the circulation.

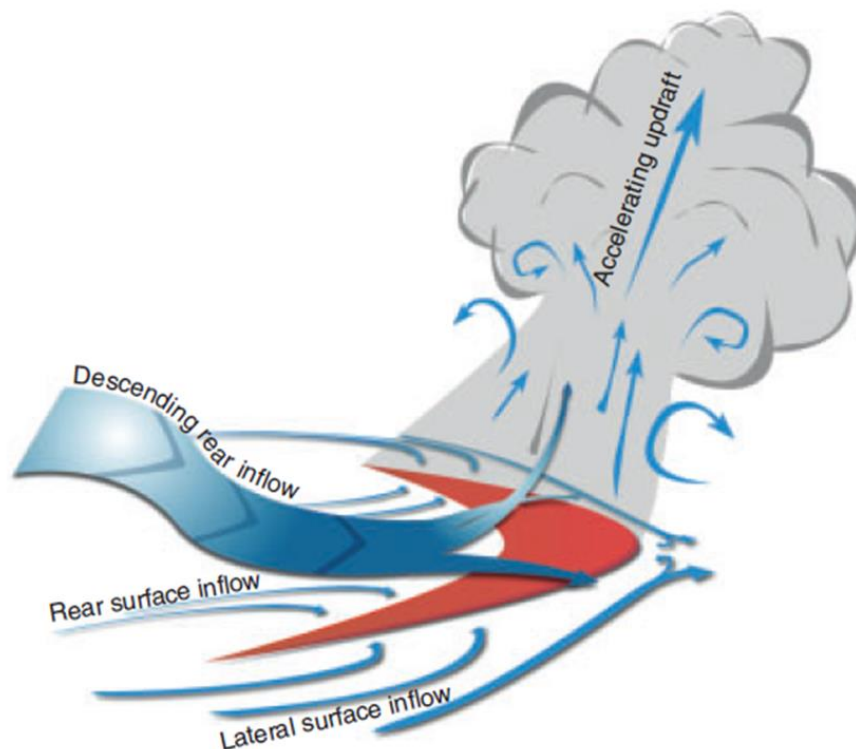


Fig. 1.2: Conceptual diagram of airflow in and around a developed fire front. Red swoosh indicates combustion zone, arrows indicate airflow and grey indicates visible smoke plume. Adopted from Potter (2012b), his Fig.6b.

Moreover, vortices (horizontal or vertical, short-lived, small scale or larger) may form due to the presence of the fire, affecting its behavior. They are more common under light winds, while persistent vertical vortices form ahead of the fire as the fire's updraft bends environmental wind shear vorticity upward. Descending air behind the fire would similarly bend horizontal environmental shear vortices downward behind the fire (Fig. 1.3a). In addition, horizontal buoyancy gradients created by the fire produce horizontal vortices, which then tilt into vertical vortices in the fire's updraft (Fig. 1.3b). These buoyancy-generated vortices develop right against the combustion region, where there is potential for them to be drawn into the fire on either the front or the rear of the head, but this vorticity may be less organized and more transient (Potter, 2012b). It must be emphasized that the vorticity due to tilting of ambient wind shear and the vorticity due to buoyancy gradients reinforce one another.

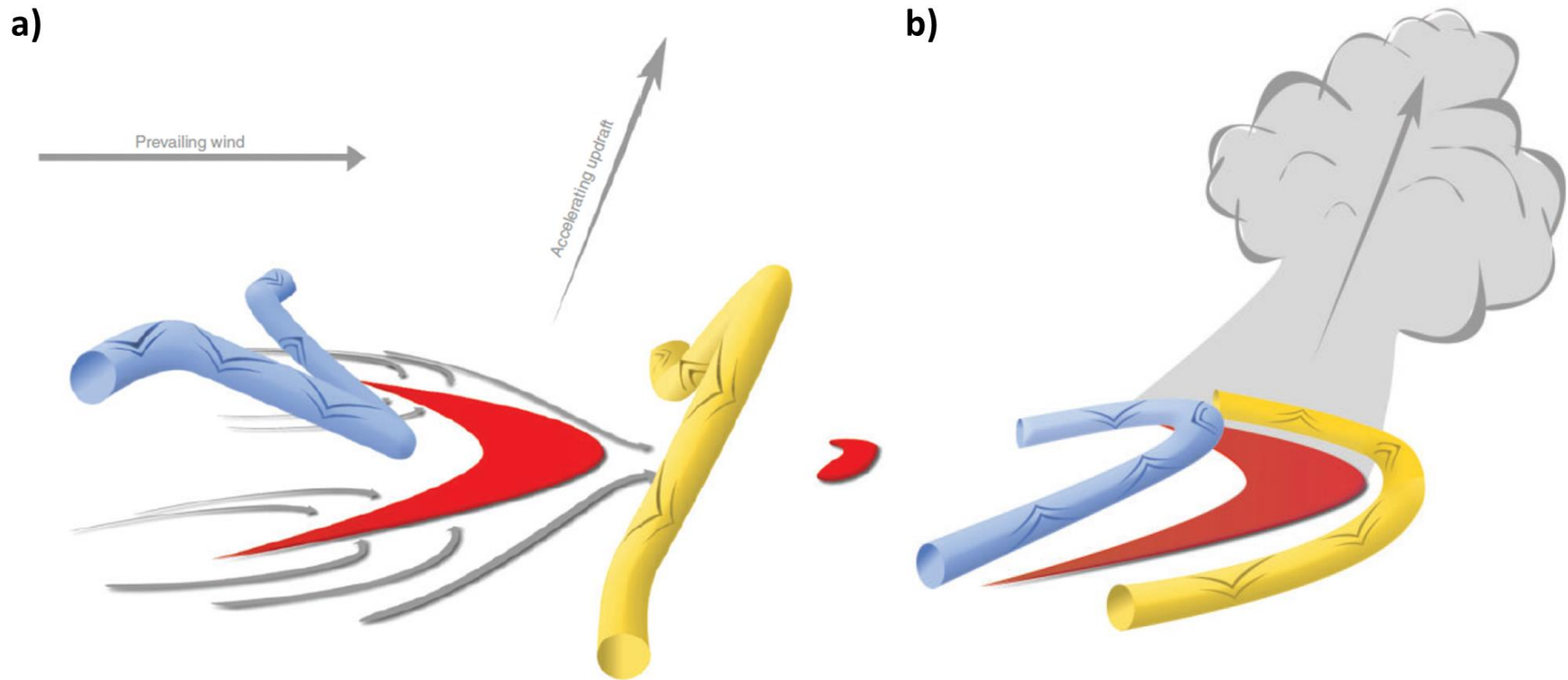


Fig. 1.3: Conceptual diagram of a) bending and tilting of vortices due to environmental wind shear around a developed fire front, when ambient wind speed increases with height and b) buoyancy-gradient generation of vorticity around a developed fire front. Arrows on vorticity tube surfaces indicate the direction of rotation. Adopted from Potter (2012b), his Figs. 8 and 9.

1.2 Wildfires in Greece

The climate in Greece is characterized as predominantly Mediterranean, with hot and dry summers, wet and moderate winters and extended periods of sunshine throughout most of the year. Thus, weather and climatic conditions regulate the wildfire activity, which presents a non-stationary time series. During the period 1961–1997, the number of fires showed an increasing trend, along with the burned area (at 95th confidence interval), where in total 17,926 wildland fires occurred in Greece, burning 603,615 ha (Dimitrakopoulos et al., 2011c). According to the records of Ministry of Environment and Energy, during the period 1980 - 1999, the year with the largest burned area was the 1988, albeit the highest number of fires were recorded in 1993 (Fig. 1.4).

The summer of 2007 (Fig. 1.5) was the worst year on record for forest fires, where extremely hot and dry weather conditions, combined with strong winds led to a disastrous upsurge of forest fires and wildfires (Knorr et al., 2011; Koutsias et al., 2012). Additionally, a significant increase on the number of fires and the burned areas was observed during the period 1980 – 2007 compared to the previous period 1960 – 1979, which resulted in three times larger burned areas in the 1980s, 1990s and 2000s against the 1960s and 1970s (Dimitrakopoulos, 2009). According to the publicly available data from the Hellenic Fire Service, for the period 2000 – 2018 (Fig. 1.6), on average, the most forest fires occur on August (389.8), while December presents the lowest number of fire events (59.6). For the same period, 2069.7 wildfires (forest or forested areas) per year occurred, 22429.6 ha year⁻¹ and 108.4 ha per fire incident were burned.

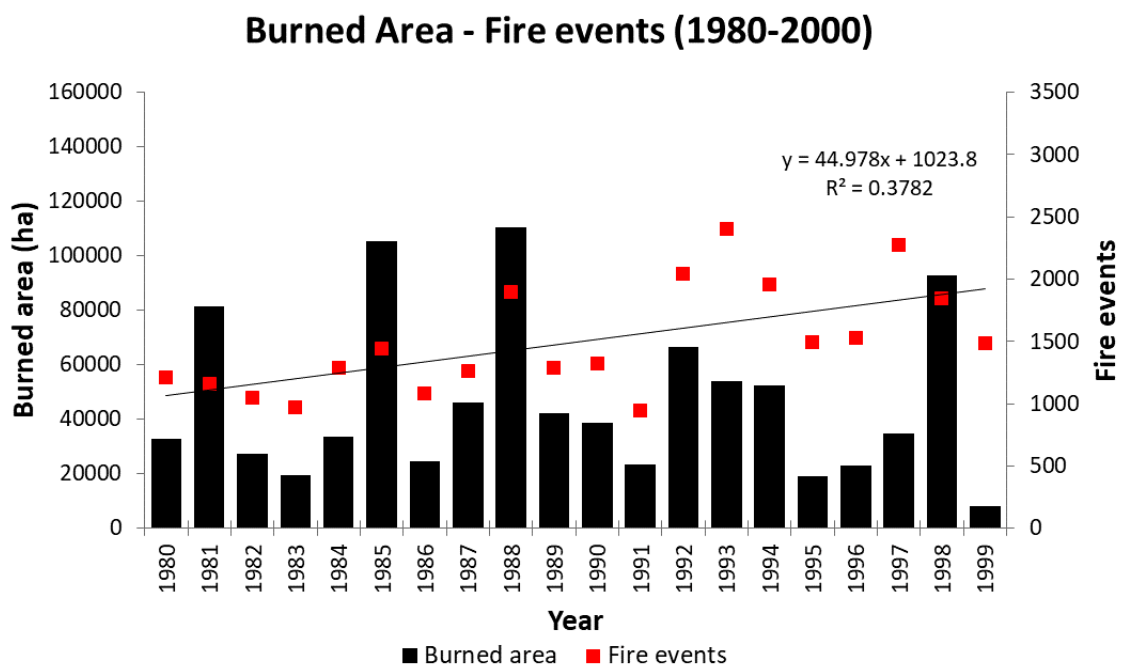


Fig. 1.4: Burned area (ha; black bars) and number of fire (red squares) in Greece (forests and forested areas), for the period 1980 – 1999, according to the records of Ministry of Environment and Energy.

Burned Area - Fire events (2000-2018)

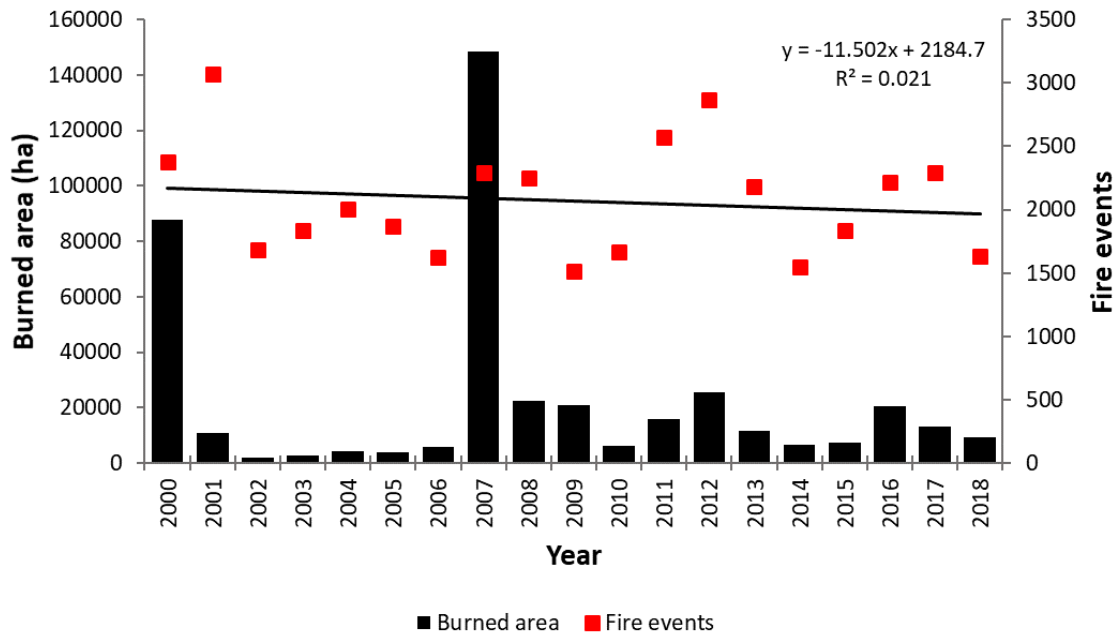


Fig. 1.5: Burned area (ha; black bars) and number of fire (red squares) in Greece (forests and forested areas), for the period 2000 – 2018, according to the records of the Hellenic Fire Service (https://www.fireservice.gr/el_GR/synola-dedomenon).

In Greece, fire season precipitation is the dominant factor coinciding with area burned, where extreme fires are controlled by precipitation rather than air temperature (Xystrakis et al., 2014). Very large fires (>1000 ha) occur under moderately low relative humidity, with strong prevailing winds and during heat waves (Dimitrakopoulos et al., 2011b). Regarding the synoptic circulation pattern over the wider Greek territory, the combination of a high atmospheric pressure system located N to NW of Greece, coupled with a lower pressure system located over the very Eastern part of the Mediterranean, an atmospheric pressure pattern closely linked with the local Etesian winds over the Aegean Sea, result to the most fire dangerous conditions (Paschalidou and Kassomenos, 2016). Moreover, the most fire-dangerous days were associated with anomalously low geopotential heights at 500 hPa and negative total water column anomalies, supporting the close link between droughts and wildfire activity (Paschalidou and Kassomenos, 2016). A positive correlation between the number of fires and area burned and the annual drought episodes was also found in Dimitrakopoulos et al. (2011c). Cyclonic conditions have also been significantly linked with fire development (Duane and Brotons, 2018), resulting to convective fires which spread by massive spotting (Duane et al., 2015).

Fig. 1.7 presents the spatial distribution of the burned areas in Greece, during the period 1984 – 2018, according to the diachronic inventory of forest fires of the National Observatory of Athens (Kontoes et al., 2013). The frequency of fire events over the same area is presented with different colors. As Fig. 1.7 depicts, a large portion of the burned areas is located in Central (Attica region, Evia) and Southern Greece (Peloponnese), while the islands of Thasos (A), Chios (B), Rodhes (C) and Zakynthos (D) have experienced large fires over this period.

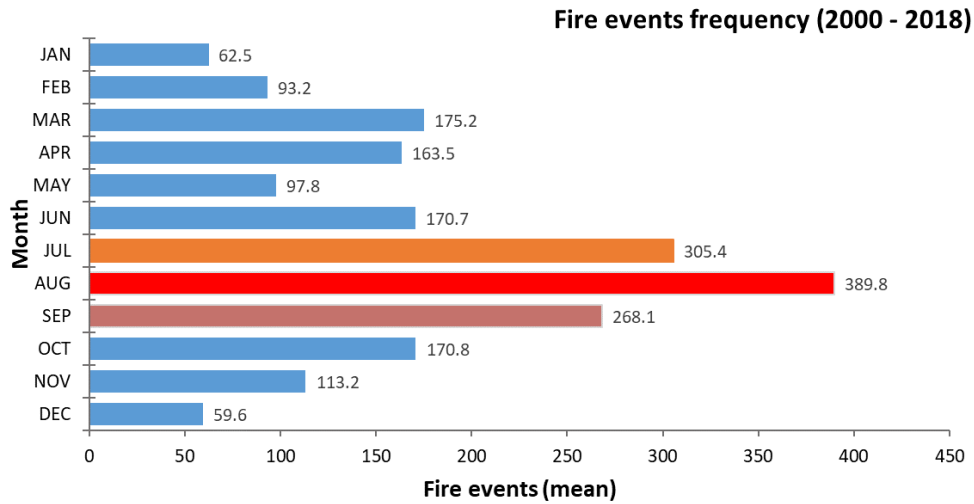


Fig. 1.6: Mean frequency of fire events per month in Greece (forests and forested areas), for the period 2000 – 2018, according to the records of the Hellenic Fire Service (https://www.fireservice.gr/el_GR/synoladedomemon).

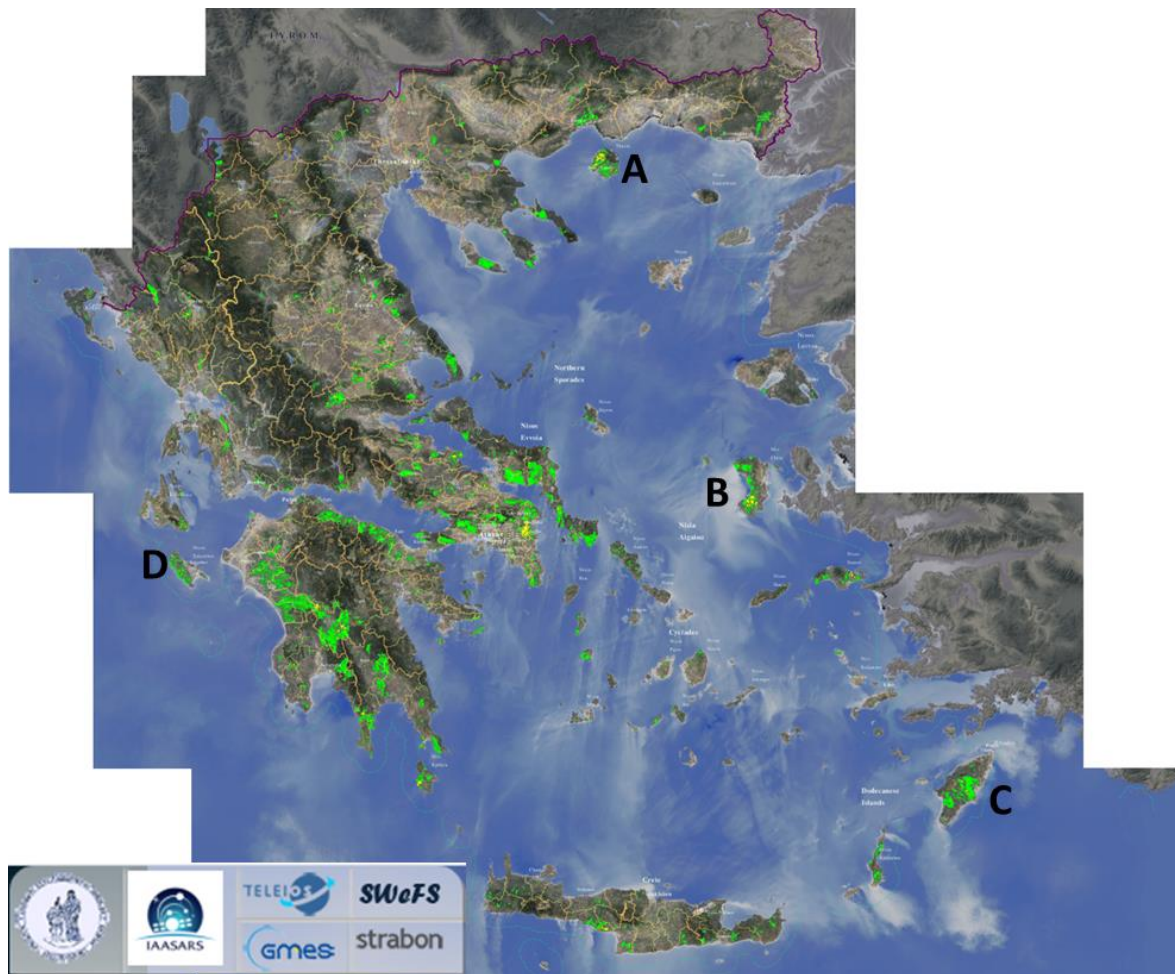
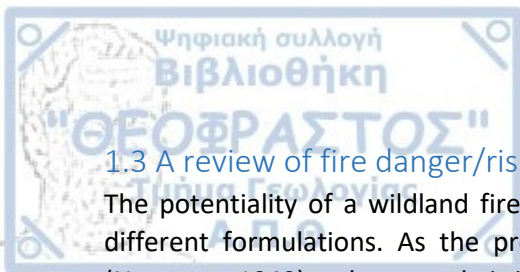


Fig. 1.7: Spatial distribution of burned areas (shaded polygons) in Greece from 1984 to 2018. Different colors are used to depict the number of times a fire has occurred in the same area. Green, yellow, orange, red and dark red colors indicate fire frequencies equal to one, two, three, four and five, respectively. Adopted from http://ocean.space.noa.gr/diachronic_bsm/.



1.3 A review of fire danger/risk and drought indices, and fire danger rating systems

The potentiality of a wildland fire occurrence is usually expressed as a single value, calculated by different formulations. As the probability of ignition is linked to the dryness of the vegetation (Nesterov, 1949), subsequently it is related to weather conditions (Reinhard et al., 2005). Simplified fire danger indices or more sophisticated fire danger rating systems use meteorological, climate and fuel information, in order to provide a measure of chance of a fire starting in a particular fuel, its rate of spread, intensity, flame height, spotting distance and difficulty to suppress (Sharples et al., 2009a). According to Chandler et al. (1983), fire danger is the resultant of constant and variable factors that affect the inception, spread and difficulty of control of fires and the damage they cause. Easily numerical quantified factors are the topographic features, fuel characteristics and weather variables, while random factors are often difficult to quantify, such as arson. Although incorporating all these factors into a single index that describes fire danger seems an impossible task, each developed fire index or fire danger rating system integrates a number of selected factors in order to assess fire danger.

Most of the fire and drought indices have been developed and employed in specific regions of the world (e.g. Eastern or Western Australia, Canada, United States of America). From the above, some of them have been modified, adopted and calibrated in order to be applicable in other regions (Arpaci et al., 2013; Dimitrakopoulos et al., 2011a; Elhag and Boteva, 2017; Kambezidis and Kalliampakos, 2016; Tatli and Türkeş, 2014). This section provides information on the most worldwide used fire danger or drought indices and fire danger rating systems, in chronological order of appearance⁴.

1.3.1 Munger Graphic Method

Munger (1916) introduced a graphic method of representing and comparing drought intensities, rather than a single index representing fire severity. He argued that precipitation, temperature and wind were so complexly interwoven that it seemed to be impossible to combine them and consider them jointly. Thus, he concluded that the most important factor that influences fire hazard in the Pacific Northwest was the infrequency of soaking rains, in other words the intensity of the droughts.

He assumed that a 30-day drought would be four times as intense as a 15-day drought, as probably fair assumption in the case of forest desiccation. To present his hypothesis that the intensity of a drought increased as the square of its duration, he represented this intensity by a right-angle triangle, whose height and base were both proportional to the duration of the drought (Fig. 1.8). The right-hand edges of the triangles marked the dates on which rain of 0.05 inch or more fell and the area of each triangle determined the severity of drought. With this simple graphic method, comparisons of the average for various localities could be made.

⁴ Additional indices exist in the bibliography, such as the German Baumgartner Index, the M68 Index, the Zhdanko Index and the Garrega Index, which are not elaborated in this manuscript, but are worth mentioning.

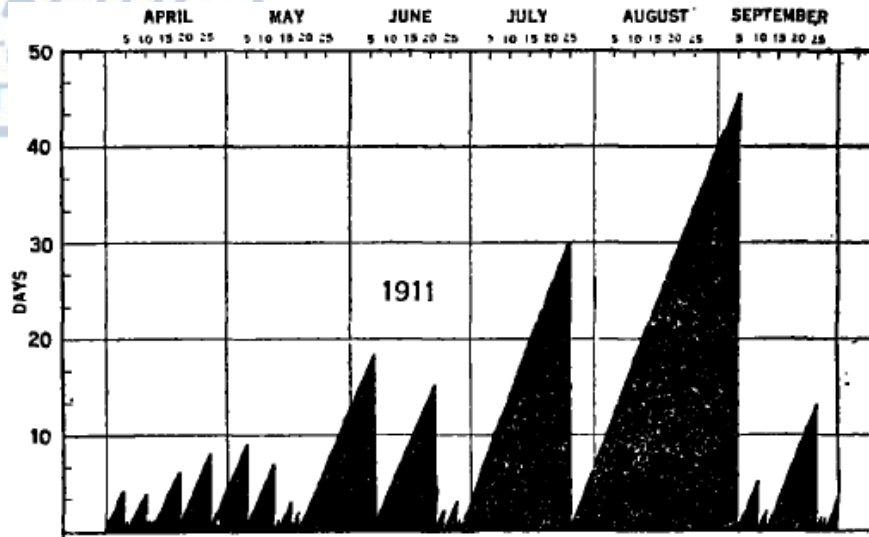


Fig. 1.8: Graphic representation of the drought intensities at Ashland, Oregon, during the summer of 1911. Ordinates and abscissae both represent duration of dry periods having less than 0.05 inch precipitation on any day (midnight to midnight). Adopted from Munger (1916).

1.3.2 Angström Index (AI)

Angström Index (Ångström, 1949, 1942) is calculated by combining temperature, humidity and expresses immediate fire danger. It was devised in Sweden and has been used all over the Scandinavia. The index is given by

$$I = \frac{H}{20} + \frac{27 - T}{10} \quad (1.1)$$

where H is the relative humidity (%) and T is the air temperature (°C).

According to Eq. 1.1, the Angström Index does not use a model for fuel moisture, nor does it accumulate the danger ratings over time. In this sense, it is a simple day-to-day fire danger indicator, with a pure climatic approach, which be good if there are rapid changes in weather situations, which increase the fire danger situation so quickly that fuel or soil moisture models are not able to capture that moment (Arpaci et al., 2013). Table 1.1 translates the values of AI into fire risk occurrence.

Table 1.1: Angström Index values regarding fire risk.

AI values	Fire risk
>4.0	fire occurrence unlikely/low
4.0 ≤ AI < 3.0	fire occurrence unfavorable/moderate
3.0 ≤ AI < 2.5	fire conditions favorable/high
2.5 ≤ AI < 2.0	fire conditions more favorable/very high
AI ≤ 2.0	fire occurrence very likely/extreme

1.3.3 Nesterov Index (NI)

The Nesterov Index (Nesterov, 1949) is a simple fire danger rating system that combines precipitation, temperature and dew-point temperature information into a single index, calculated as (Onderka and Melicherčik, 2010; Škvarenina et al., 2004)

$$NI = \sum_{i=1}^w (T_i - T_i^{dew}) T_i \quad (1.2)$$

where NI denotes the Nesterov Index, w is the number of days since the last rainfall exceeding 3 mm day⁻¹, T_i is the daily maximum air temperature (°C) and T_i^{dew} is the daily maximum dew-point temperature (°C). Once the daily rainfall, as cumulative value, exceeds 3 mm day⁻¹, the index resets to zero. The index is used primarily in Russia (McRae et al., 2006), Ukraine and in several countries of former Soviet Union (e.g. Slovenia). It was also employed in Austria, as possible candidate (Arpaci et al., 2013). A modified version of the index was applied in Portugal for forest fire risk estimation (Viegas et al., 1999), while other modified versions also exist (Groisman et al., 2007). Table 1.2 indicates NI values as a function of fire danger.

Table 1.2: Fire danger classes depending on the NI values (Škvarenina et al., 2004).

NI values	Fire danger rating
0 – 300	Minimal
301 – 1000	Low
1001 – 4000	Moderate
4001 - 10000	High
>10001	Extreme

1.3.4 McArthur Forest and Grassland Fire Danger Meters

The McArthur Mark 5 Forest Fire Danger Meter (McArthur, 1967) is widely used in eastern Australia, since its initial development, for dry-sclerophyll forest types. From that meter, an index referred to as the Forest Fire Danger Index (FFDI) is produced, which is the basis for the fire danger classification scheme (low, medium, high, very high or extreme), according to the value of FFDI, with respect to a number of threshold values (Sharples et al., 2009a). The formulation of the Mark 5 meter was performed by Noble et al. (1980) and is given by

$$FFDI = 2exp(-0.45 + 0.987\ln(DF) + 0.0338T - 0.0345H + 0.0234U) \quad (1.3)$$

where DF is the drought factor, which represents fuel availability and ranges from 1 to 10 (Griffiths, 1999), T is the dry-bulb temperature (°C), H is the relative humidity (%) and U is the wind speed (km h⁻¹) at 10 m above the ground surface. The DF factor is based on recent precipitation and on the Byram-Keetch Drought Index (BKDI), which is described below. Table 1.3 presents the different categories of FFDI according to its values.

Table 1.3: Fire danger classes depending on the FFDI values.

FFDI value	Fire danger rating
0 – 11	Low/Moderate
12 – 24	High
25 – 49	Very high
50 – 74	Severe
75 – 99	Extreme
>100	Catastrophic

The McArthur Mark 4 Grassland Fire Danger Meter (McArthur, 1966) and the McArthur Mark 5 Grassland Fire Danger Meter (McArthur, 1977) were developed and presented initially in the form of



circular slide rules⁵, in order to assist in prediction of fire behavior in grassland fuels in New South Wales and the Australia Capital Territory. The mark 4 meter is used by the Bureau of Meteorology and produces the Mark 4 Grassland Fire Danger Index (GFDI4), which relates to the expected severity of fire behavior and difficulty of suppression (Sharples et al., 2009a). The GFDI4 is formulated as (Purton, 1982)

$$GFDI4 = \exp(-1.523 + 1.027\ln(Q) - 0.009432(100 - C)^{1.536} + 0.02764T - 0.2205\sqrt{H} + 0.6422\sqrt{U}) \quad (1.4)$$

where Q is the quantity of fuel ($t\ ha^{-1}$), T is the dry-bulb temperature ($^{\circ}C$), H is the relative humidity (%), U is the wind speed ($km\ h^{-1}$) and C is the degree of grass curing (%), which describes long-term effects on the moisture content of grassland fuels. Curing is determined through the interaction of precipitation and temperature patterns with the growing cycles of individual grass species (McArthur, 1966), while Sharples et al. (2009) expressed Eq. 1.4 as,

$$GFDI4 = Q^{1.027} f(C) \exp(-1.523 + 0.02764T - 0.2205\sqrt{H} + 0.6422\sqrt{U}) \quad (1.5)$$

where the terms of fuel quantity and curing are multiplicative factors. The curing factor is given by

$$f(C) = \exp(-0.009432(100 - C)^{1.536}) \quad (1.6)$$

The McArthur Mark 5 Grassland Fire Danger Meter was designed to be more widely applicable than its predecessors (Noble et al., 1980), while the associated fire danger index is the mark 5 Grassland Fire Danger Index (GFDI5). The derived equation for the GFDI5 is given by (Noble et al., 1980)

$$GFDI5 = \begin{cases} 3.35W \exp(-0.0897m + 0.0403U), & m < 18.8 \\ 0.299W \exp(-1.686 + 0.0403U)(30 - m), & 18.8 \leq m < 30 \end{cases} \quad (1.7)$$

where W is the fuel weight ($t\ ha^{-1}$), U is the wind speed ($km\ h^{-1}$) and m is the fuel moisture content (%), which is given as a function of dry-bulb temperature, relative humidity and curing as

$$m = \frac{97.7 + 4.06H}{T + 6} - 0.00854H + \frac{3000}{C} - 30 \quad (1.8)$$

1.3.5 Keetch-Byram Drought Index (KBDI)

The Keetch-Byram Drought Index (Keetch and Byram, 1968) was specifically designed for fire potential assessment (Dimitrakopoulos and Bemmerzouk, 2003). It is a cumulative estimate of moisture deficiency (fire potential) based on meteorological parameters, where its number represents the net effect of evapotranspiration and precipitation in producing cumulative moisture deficiency in the upper soil layers. The index attempts to measure the amount of precipitation necessary to recharge the soil to field capacity and it is initialized when the soil is near saturation (close to field capacity). Soil saturation varies by geographic region but may be reached during prolonged precipitation (rainfall) events (Janis et al., 2002). Its formulation is given by (Dimitrakopoulos and Bemmerzouk, 2003)

⁵ Circular slide rules come in two basic types, one with two cursors, and another with a free dish and one cursor. The dual cursor versions perform multiplication and division by holding a fast angle between the cursors as they are rotated around the dial. The onefold cursor version operates more like the standard slide rule through the appropriate alignment of the scales. Source: https://en.wikipedia.org/wiki/Slide_rule#Circular_slide_rules.

$$dQ = \frac{(203.2 - Q)(0.968 \exp(0.0875T + 1.5552) - 8.3)dt}{1 + 10.88 \exp(-0.001736R)} \times 10^{-3} \quad (1.9)$$

where dQ is the daily addition to the moisture deficiency (mm), Q is the moisture deficiency index (mm) of the previous day reduced by the daily net precipitation (greater than 5.1 mm), T is the daily maximum temperature ($^{\circ}\text{C}$), R is the mean annual precipitation (mm) and dt is the time increment (day). If the KBDI is computed in daily basis then dt equals 1. If $T < 10$ $^{\circ}\text{C}$ then the KBDI value remains unchanged.

Several assumptions exist for the calculation of the KBDI (Dimitrakopoulos and Bemmerzouk, 2003; Keetch and Byram, 1968), such as a) the rate of moisture loss in a forested area will depend on the density of the vegetation cover in this area, b) an exponential curve, where the rate of moisture loss is a function of the mean annual rainfall, approximates the vegetation-precipitation (rainfall) relation, c) the rate of moisture loss from the soil is determined by evapotranspiration relations, d) the depletion of soil moisture with time is approximated by an exponential curve in which wilting-point moisture is used as the lowest moisture level and e) the depth of the soil layer where the drought event occurs is such that the soil has a field capacity of 20 cm (8 inches) of available water. In addition, Janis et al. (2002) argued that median annual precipitation could be more appropriate than mean annual precipitation, but they did not test this statement.

KBDI is an integral component of the US National Fire Rating System since 1988 (Burgan et al., 1998; Janis et al., 2002), it has been tested in Hawaiian islands (Dolling et al., 2005) and it is included in the Australian Fire Rating Systems (San-Miguel-Ayanz et al., 2003). Moreover, it has been in use at selected Mediterranean locations of Greece since 1990 (Dimitrakopoulos and Bemmerzouk, 2003) and in Central Europe, such as in Austria (Arpaci et al., 2013; Eastaugh and Hasenauer, 2014; Petritsch and Hasenauer, 2014). Table 1.4 presents drought classes and fire potential for relative KBDI levels (Dimitrakopoulos and Bemmerzouk, 2003; Janis et al., 2002).

Table 1.4: Drought classes and fire potential for relative KBDI levels.

KBDI values	Drought class	Fire potential
0-150	Very low	Minimal
150-300	Low	Predictable fire behavior
300-500	Moderate	Somewhat predictable fire behavior
500-700	High	Above 600 fire suppression is a significant undertaking
>700	Extreme	Unpredictable fire behavior with crowning and downwind spotting.

1.3.6 Chandler Burning Index (CBI)

The Chandler Burning Index (Chandler et al., 1983), originally designed for application at a monthly time-scale, combines relative humidity and air temperature into a single index, with no adjustment for fuel moisture. It has been applied to study fire weather in United States (McCutchan and Main, 1989) and globally (Le Page et al., 2010; Roads et al., 2008) and it is formulated as

$$CBI = \frac{124 \times [(110 - 1.373RH) - 0.54(10.2 - T)] \times 10^{(-0.0142RH)}}{60} \quad (1.10)$$

where RH is the relative humidity (%) and T is the temperature ($^{\circ}\text{C}$). If the CBI is calculated in daily basis, then the maximum daily temperature is considered, while at monthly time increments, average mean monthly values are considered (both in T and RH).

Assessments of the CBI (Le Page et al., 2010) revealed an inconsistent behavior over boreal regions during winter, when low relative humidity induces increased CBI values, while T is negative and the ground is covered by snow. Thus, Le Page et al. (2010) modified the index to take its minimum value when the air temperature was minimum by forcing relative humidity to 100%. Table 1.5 associates CBI values with fire danger. Moreover, examination of Eq. 1.10 revealed that the CBI is highly volatile in its expression of fire danger for all temperatures from 0 to 50 degrees Celsius for the range of 40% – 15% relative humidity.

Table 1.5: CBI values and their corresponding fire danger⁶.

CBI values	Fire danger
< 50	Low
50 – 75	Moderate
75 – 90	High
90 – 97.5	Very high
>97.5	Extreme

1.3.7 Fosberg Fire Weather Index (FFWI)

The FFWI (Fosberg, 1983) is an instantaneous index which represents expected flame length and fuel drying, assuming that fuel bed properties (e.g. moisture of extinction, surface area to volume ratio) are temporally and spatially constant (Goodrick, 2002). It is a nonlinear filter of dry-bulb temperature, relative humidity and wind speed data, which is designed to provide a linear relationship between the combined meteorological data and fire behavior characteristics (Goodrick, 2002; Sharples et al., 2009a). The formulation of FFWI is given by (Fosberg, 1983; Goodrick, 2002; Roads et al., 1991; Sharples et al., 2009a)

$$FFWI = \frac{n\sqrt{1 + U^2}}{0.3002} \quad (1.11)$$

where U denotes the wind speed (mph) and n is the moisture damping coefficient, which is calculated as

$$n = 1 - 2\left(\frac{m}{30}\right) + 1.5\left(\frac{m}{30}\right)^2 - 0.5\left(\frac{m}{30}\right)^3 \quad (1.12)$$

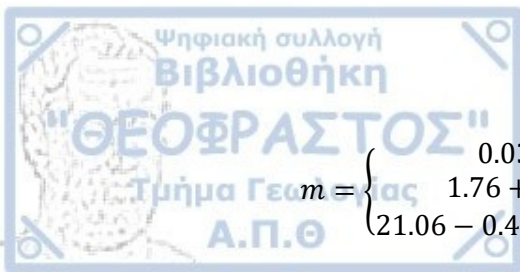
while m stands out for the equilibrium moisture content, which is formulated as a function temperature T (F) and relative humidity R (%), as (Roads et al., 1991)

$$m = \begin{cases} 0.03229 + 0.281073R - 0.000578RT, & R \leq 10\% \\ 2.22749 + 0.160107R - 0.01478T, & 10\% < R \leq 50\% \\ 21.0606 + 0.005565R^2 - 0.00035RT - 0.483199R, & R > 50\% \end{cases} \quad (1.13)$$

The index ranges from 0 to 100, where the upper limits have been set to give an index value of 100 if the moisture content is zero and the wind is 30 mph. If any number is larger than 100, it is set back to 100. Table 1.6 provides the classification of fire behavior according to FFWI values.

Simard (1968) provided another expression for the equilibrium moisture content. It was resulted from the regression analysis of data pertaining to the equilibrium moisture content of wood and is given by (Sharples et al., 2009b)

⁶ Source: http://www.sasquatchstation.com/Fire_Weather.php



$$m = \begin{cases} 0.03 + 0.2626R - 0.00104RT, & R < 10\% \\ 1.76 + 0.4601R - 0.0266T, & 10\% \leq R < 50\% \\ 21.06 - 0.4944R + 0.005565R^2 - 0.00063RT, & R \geq 50\% \end{cases} \quad (1.14)$$

FFWI was found to be highly correlated with fire occurrence in the north-east United States (Haines et al., 1983) and also, in south-west United States (Sharples et al., 2009a). FFWI has been applied to estimate the fire weather severity in the chaparral ecosystems of the Mediterranean-climate southern California during Santa Anna wind events (Moritz et al., 2010; Nauslar et al., 2018). In France, Barbero et al. (2019) used the FFWI in a modelling framework for resolving complex relationships linking weather-to-climate variability associated with the occurrence of large wildfires, while Kambezidis and Kalliampakos (2016) introduced a modification of the FFWI that included forest coverage to assess the fire risk in Northern Greece (Central, Eastern Macedonia, Thrace).

Table 1.6: Fire behavior characteristics according to FFWI values.

FFWI values	Fire behavior
0-20	Low risk/predictable
20-40	Moderate risk/somewhat predictable
40-60	High risk/ its suppression is a significant undertaking
60-80	Very high/uncontrollable
80-100	Extreme/erratic

Goodrick (2002) also modified the FFWI to take into account the impact of precipitation to the index, improving its relationship with the burnt area. He combined the FFWI with the fuel availability factor (FAF) which is a function of KBDI (dQ) and allows the fuel availability to increase rapidly as drought conditions become more severe, as,

$$mFFWI = FAF \times FFWI \quad (1.15)$$

where FAF was given by,

$$FAF = 0.000002dQ^2 + 0.72 \quad (1.16)$$

1.3.8 Canadian Forest Fire Weather Index (CFFWI)

The Canadian Forest Fire Weather Index (CFFWI) System (also known as FWI) was first issued in 1970, but its full potential was presented seventeen years later (Van Wagner, 1987), with analytical presentation of the system equations and numerical codes (van Wagner and Pickett, 1985). The system is based on the moisture content of three forest fuel classes plus the effect on fire behavior and consists of six components. The three primary sub-indices represent fuel moisture, while the two intermediate sub-indices represent fire behavior (rate of spread and fuel consumption) and the final index represents fire intensity (FWI), as energy output rate per unit length of fire front. Fig. 1.9 depicts the flow chart of the CFFWI System.

The CCFWI is digested with weather inputs in the form of air temperature ($^{\circ}\text{C}$), 24h-accumulated precipitation (mm), relative humidity (%) and wind speed (m s^{-1}) at 10 m above ground level. The four weather observational data are generally recorded daily at noon local standard time (LST) or 1300 local daylight time (LDT).

According to Van Wagner (1987), the Fine Fuel Moisture Code (FFMC) indicates the moisture content of the smallest forest fuels (surface litter, leaves, needles and small twigs) and is estimated from the

previous day's FFMC plus temperature, relative humidity, wind speed and 24-h precipitation, while it takes about 2–3 days to equilibrate under constant conditions. The Duff Moisture Code (DMC) represents the moisture content of the medium-sized surface fuels and duff layers (approximately 2–10 cm beneath the surface), it is calculated from the previous day's DMC, in conjunction with temperature, relative humidity and 24-h precipitation data and requires 12 days to equilibrate. The Drought Code (DC) indicates the moisture content of the largest surface fuels and deep duff layers (deeper than approximately 10 cm). It is also estimated from the previous day's DC, local noon temperature and 24-h precipitation with a longer period to lose its moisture, about 52 days (Van Wagner, 1987).

The Initial Spread Index (ISI) calculates the expected rate of fire spread, by combining the effects of wind and the FFMC on rate of spread without the influence of variable quantities of fuel. The Buildup Index (BUI) estimates the total amount of fuel available for combustion by combining the DMC and the DC fuel moisture codes. Finally, the ISI and BUI codes are used in the calculation of the Fire Weather Index (FWI). The latter is incorporated into the Daily Severity Rating (DSR), which accurately reflects the expected efforts required for fire suppression, emphasizing higher FWI values (Shabbar et al., 2011).

The CFFWI System been used by Canadian fire management agencies for more than forty years (Girardin and Wotton, 2009), in southern European countries (Bedia et al., 2015; Viegas et al., 1999) such as Italy (Good et al., 2008) and Greece (Dimitrakopoulos et al., 2011a; Elhag and Boteva, 2017; Good et al., 2008; Karali et al., 2014), in Australia (Kraaij et al., 2013), South Africa (Dowdy et al., 2009) and China (Tian et al., 2011). Moreover, the European Forest Fire Information System (EFFIS, <http://effis.jrc.ec.europa.eu>) utilizes the FWI in the EFFIS Danger Forecast module (San-Miguel-Ayanz et al., 2019), while in the United Kingdom, a modified version of the CFFWI is used by the name, Fire Severity Index (FSI). In addition, the CFFWI has been used for long term fire weather trends (Wallenius et al., 2011), climate variability studies (Shabbar et al., 2011) and possible future fire behavior under climate change (Mori and Johnson, 2013; Whitman et al., 2015), while its dependency to weather stations data makes the CFFWI system a good candidate for exploring the effects of inhomogenized versus homogenized data (Tsinko et al., 2018).

Fig. 1.10 displays examples of fire behavior in jack pine stands under different FWI values. Table 1.7 presents the classification of FWI values into fire danger classes appropriate for the Mediterranean environments, proposed by Dimitrakopoulos et al. (2011a), who evaluated the FWI module during two consecutive fire seasons in Crete, Greece. However, they pointed out that long-term studies are necessary to determine the precise range of each fire danger class according to fire occurrence data.

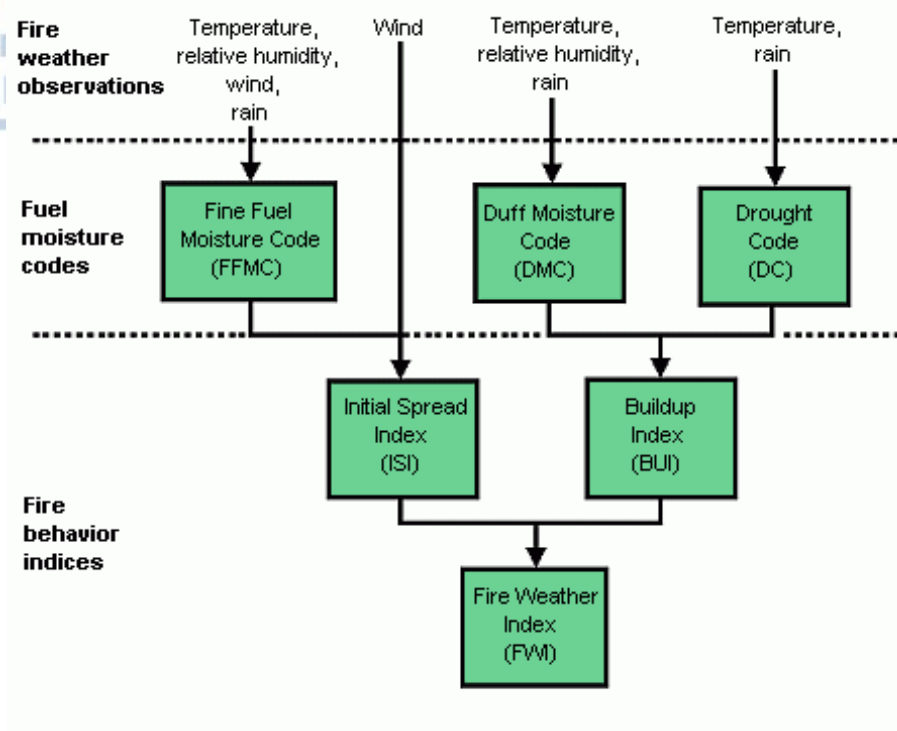


Fig. 1.9: The Canadian Forest Fire Weather Index (CFFWI) System and its six components. Adopted from <https://cwfis.cfs.nrcan.gc.ca/background/summary/fwi>.



Fig. 1.10: Examples of fire behavior in jack pine stands under different FWI values. Adopted from <https://cwfis.cfs.nrcan.gc.ca/background/examples/fwi>.

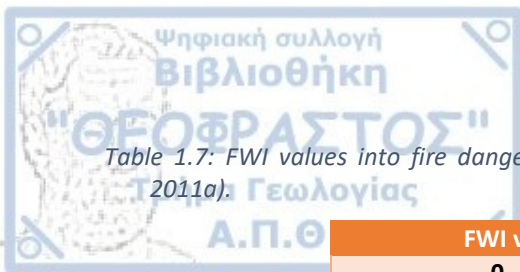


Table 1.7: FWI values into fire danger classes for the Mediterranean environments (Dimitrakopoulos et al., 2011a).

FWI values	Fire danger
0 – 38	Low
39 – 48	Moderate
49 – 60	High
>60	Extreme

1.3.9 National Fire Danger Rating System (NFDRS)

The National Fire Danger Rating System (NFDRS) was developed in the United States as a consistent interagency decision-support framework to provide a measure of the relative seriousness of burning conditions and threat of fire. It was first introduced in 1964, while it has been updated in 1972, 1978 (Deeming et al., 1977), 1988 (Burgan, 1988) and recently, in 2016⁷. The three significant changes in the latest version are a) the incorporation of the Growing Season Index (GSI)⁸ to compute live fuel moisture, b) the incorporation of the Nelson Model (Nelson Jr, 2000) to compute fine dead fuel moisture and c) the reduction of the number of fuel models in the NFDRS. Figs. 1.11 and 1.12 display the 78/88 NFDRS and 2016 NFDRS⁹ flow charts, respectively. The NFDRS combines fire weather observations and forecasts, a set of primary components and indices (see below), the Wildland Fire Assessment System (WFAS), the Weather Information Management System (WIMS) and Pocket Cards in order to assess fire danger.

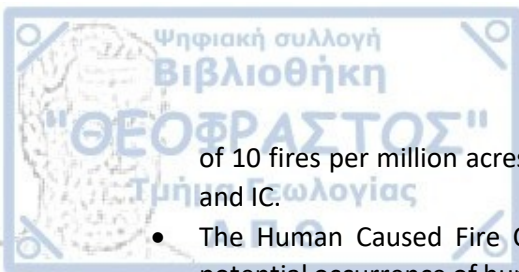
The primary NFDRS components and indices are:

- The Ignition Component (IC): The IC provides rating of the probability that a firebrand will cause a fire requiring suppression action. Expressed as a probability; it ranges on a scale of zero to 100. An IC of 100 means that every firebrand will cause an actionable fire if it contacts a receptive fuel. Likewise, an IC of zero would mean that no firebrand would cause an actionable fire under those conditions.
- The Spread Component (SC): The SC is a rating of the forward rate of spread of a headfire in ft min⁻¹.
- The Energy Release Component (ERC): The ERC is a number related to the available energy, Btu per unit area square foot, within the flaming front at the head of a fire. Daily variations in ERC are due to changes in moisture content of the various fuels present, both live and dead. Conditions producing an ERC value of 24 represent a potential heat release twice that of conditions resulting in an ERC value of 12.
- The Burning Index (BI): The BI is a number related to the contribution of fire behavior to the effort of containing a fire and is derived from a combination of SC and ERC. It is expressed as a numeric value closely related to the flame length in feet multiplied by ten. The computed BI values represent the near upper limit to be expected on the rating area. In other words, if a fire occurs in the worst fuel, weather, and topography conditions of the rating area, then these numbers indicate its expected fireline intensities and flame length.
- The Lightning Occurrence Index (LOI): The LOI is a numerical rating of the potential occurrence of lightning-caused fires. It is intended to reflect the number of lightning caused fires one could expect on any given day. The LOI is scaled such that a LOI value of 100 represents a potential

⁷ <https://www.nwcg.gov/sites/default/files/memos/eb-m-19-002.pdf>

⁸ <https://www.wfas.net/index.php/growing-season-index-experimental-products-96>

⁹ <https://sites.google.com/firenet.gov/nfdrs>



of 10 fires per million acres. It is derived from a combination of Lightning Activity Level (LAL) and IC.

- The Human Caused Fire Occurrence Index (MCOI): The MCOI is a numeric rating of the potential occurrence of human-caused fires. Similar to the LOI, this value is intended to reflect the number of human-caused fires one could expect on any given day. It is derived from a measure of daily human activity and its associated fire start potential, the human caused fire risk input, and the ignition component. The MCOI is scaled such that the number is equal to ten times the number of fires expected that day per million acres.
- The Fire Load Index (FLI): The FLI is a rating of the maximum effort required to contain all probable fires occurring within a rating area during the rating period. The FLI was designed to be the end product of the NFDRS – the basic preparedness or strength-of-force pre-suppression index for an administrative unit. It was to be used to set the readiness level for the unit. It focuses attention upon the total fire containment problem. Because the FLI is a composite of the various components and indexes of the NFDRS, including the local lightning and human caused fire risk inputs, the comparability of values varied significantly from one unit to another.
- The Keetch-Byram Drought Index (KBDI): The KBDI is not an output of the National Fire Danger Rating System itself but is often displayed by the processors used to calculate NFDRS outputs. The KBDI was described in section 1.2.5.

Fire Danger is expressed using these levels:

- **Low:** Fuels do not ignite readily from small firebrands although a more intense heat source, such as lightning, may start fires in duff or light fuels.
- **Moderate:** Fires can start from most accidental causes, but with the exception of lightning fires in some areas, the number of starts is generally low.
- **High:** All fine dead fuels ignite readily and fires start easily from most causes.
- **Very high:** Fires start easily from all causes and, immediately after ignition, spread rapidly and increase quickly in intensity.
- **Extreme:** Fires start quickly, spread furiously, and burn intensely. All fires are potentially serious.

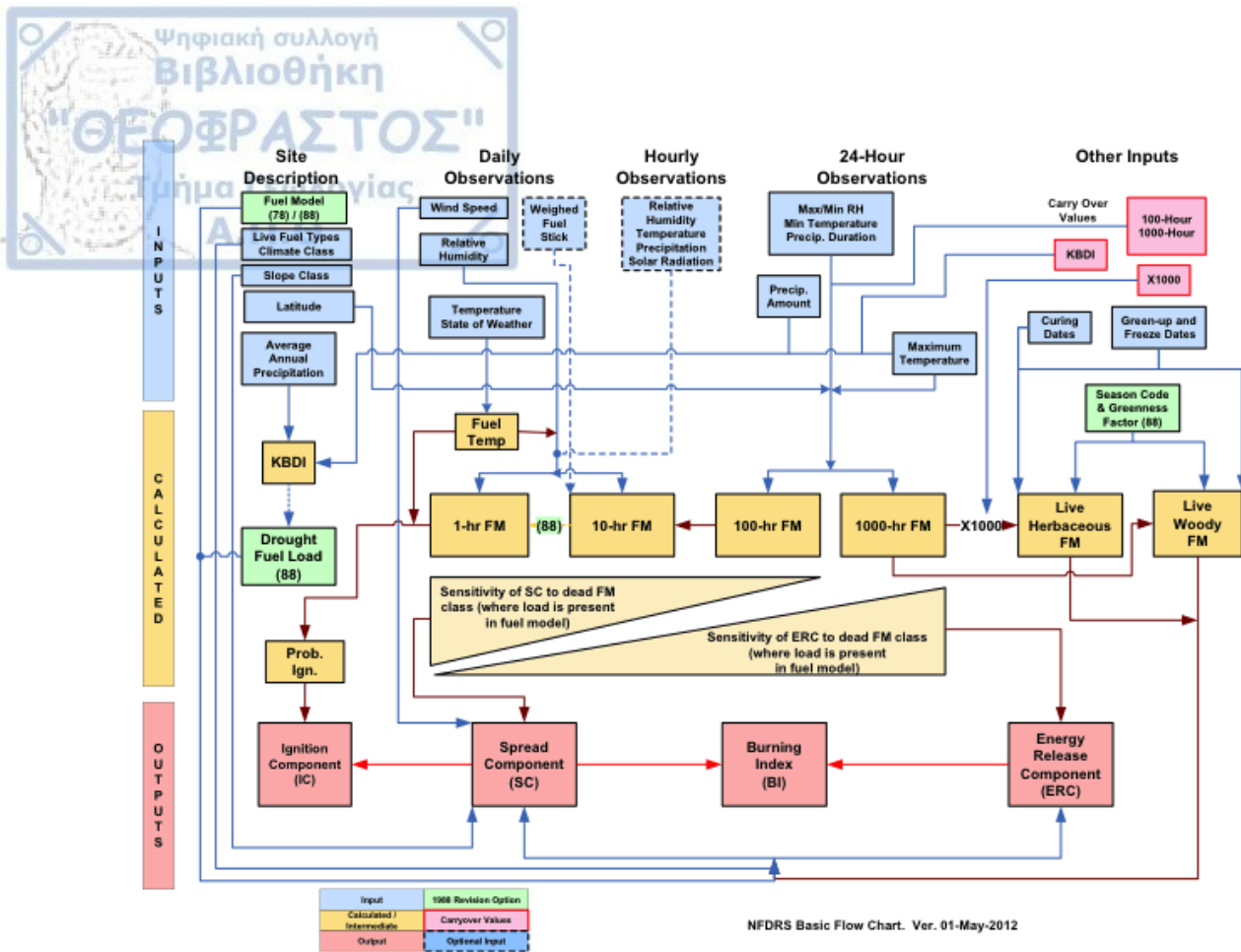


Fig. 1.11: Flow chart of the 78/88 version of the NFDRS. Adopted from <https://www.nwcg.gov/publications/pms437/fire-danger/background>.

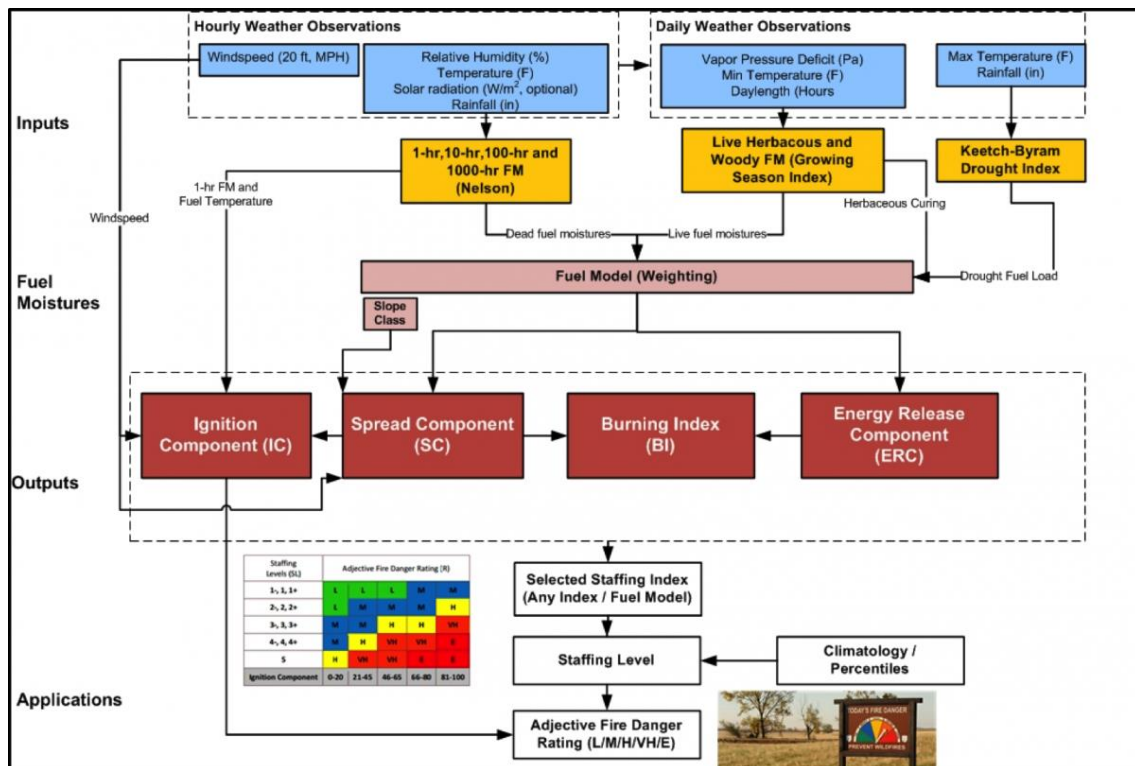


Fig. 1.12: Flow chart of the 2016 NFDRS. Adopted from <https://www.nwcg.gov/publications/pms437/fire-danger/background>.

1.3.10 Haines Index (HI)

The Haines Index (Haines, 1988), originally known as the Lower Atmospheric Severity Index (LASI), is used primarily in United States wildland fire management in order to show the atmospheric potential for large or erratic fires. Its conceptualization was based on the environmental lapse rate of a layer of air coupled with its moisture content (Haines, 1988). The HI comprises the stability component (A, the temperature difference between two prescribed pressure levels) and the moisture component (B, the dew point depression at a prescribed pressure level). The prescribed levels depend on the surface elevation (low, middle and high variant) at the location which the HI is applied (Haines, 1988; his Fig. 1). Each component's value corresponds to integers of 1, 2 or 3 and the summary (A+B) yields the final HI value from 2 to 6. Fire personnel generally consider a 5 or 6 value indicative of a need to be prepared for atypically high fire activity (Potter, 2018). Table 1.8 presents the pressure levels and threshold values for the Haines Index.

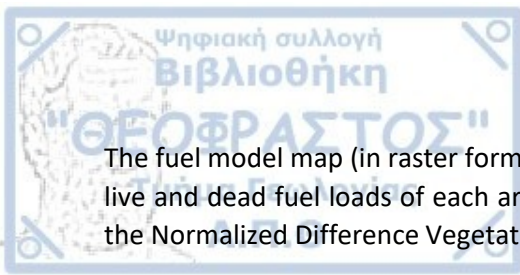
Table 1.8: Components of the Haines Index with their pressure levels and threshold values. T and T_D is the air temperature and dew point temperature ($^{\circ}\text{C}$), respectively, at the specific pressure level. After Potter (2018).

Component	Variant (elevation)						HI value
	Low		Medium		High		
Stability	$T_{950}-T_{850}$	<4	$T_{850}-T_{700}$	<6	$T_{700}-T_{500}$	<18	1
		4-8		6-11		18-22	2
		≥ 8		≥ 11		≥ 22	3
Moisture	$(T-T_D)_{850}$	<6	$(T-T_D)_{850}$	<6	$(T-T_D)_{700}$	<15	1
		6-10		6-13		15-21	2
		≥ 10		≥ 13		≥ 21	3

However, the validity of the Haines Index is questioned thoroughly in the work of Potter (2018), who examined several studies (McCaw et al., 2007; Saltenberger and Barker, 1993; Werth and Ochoa, 1993) of the HI performance. He concluded that, although the intent and logic going into the original Index development were sound and the effort employed what was then the state of the science, the resulting Index was unsound, including lacking quantitative fire data, while it is unclear whether it would more appropriately be revised or replaced. Its limitations are also acknowledged in Murdoch et al. (2012), who stated that the HI is most often used as an indicator of the potential for rapid-fire growth in plume-dominated fires, which typically occur in large fuel or forested regimes. Nevertheless other studies employed the HI into their analysis, such as the work of Tatli and Türkeş (2014), who evaluated the HI over the Mediterranean Basin for the period 1980 – 2010.

1.3.11 Fire Potential Index (FPI)

The Fire Potential Index (Burgan et al., 1998) model incorporates both satellite and surface observations in a single index that depicts fire potential, in the sense that the latter can be assessed if the moisture level of live and dead vegetation is reasonably represented. It was developed in United States in order to provide a method of estimating fire potential that was simpler to operate than the current U.S. National Fire Danger Rating System (NFDRS) (Burgan et al., 1998). The FPI model requires a) a fuel model map, b) a Relative Greenness (RG) map (Burgan and Hartford, 1993), indicating current vegetation greenness compared to historical maximum and minimum values and c) a 10-hour time lag dead fuel moisture map (Fosberg and Deeming, 1971). A 10-hour time lag fuel is defined as the dead woody vegetation in the range between 0.6 to 2.5 cm in diameter. The FPI ranges from 0 to 100.



The fuel model map (in raster format) consists of the standard NFDRS fuel types, where only the total live and dead fuel loads of each are required as additional information. The RG map is derived from the Normalized Difference Vegetation Index (NDVI) (Rouse et al., 1973), according to

$$RG = \frac{NDVI_0 - NDVI_{min}}{NDVI_{max} - NDVI_{min}} \times 100 \quad (1.17)$$

where $NDVI_0$ is the highest observed NDVI value for the 1-week composite period, $NDVI_{min}$ and $NDVI_{max}$ are the historical minimum and maximum NDVI values for a given pixel, respectively.

Burgan et al. (1998) provided a number of steps for the calculation of the FPI values and concluded into a single equation (their Eq. 10), which is not presented here for consistency reasons. A modified version of the FPI adopted to the European context was introduced by Sebastián López et al. (2002), where the FPI was given by

$$FPI = 100 \times (1 - Fm10hr_{cor}) \times (1 - Lr) \quad (1.18)$$

where the $Fm10hr_{cor}$ was the moisture content of the small dead fuels corrected by the solar heating and the extinction moisture content and Lr was the live ratio corrected by the RG (Eq. 1.17). The uncorrected $Fm10hr$ was empirically estimated as

$$Fm10hr = 1.28 \times m \quad (1.19)$$

where m was the equilibrium moisture content from Eq. 1.13. The uncorrected Lr was given by

$$Lr_{un} = 0.25 + 0.5 \times \left(\frac{NDVI_{max}}{NDVI_{absMax}} \right) \quad (1.20)$$

where the $NDVI_{max}$ represented the maximum NDVI in the considered 5-year period and the $NDVI_{absMax}$ was the overall maximum NDVI on any location in Europe during the same period. Their results showed the ability of the FPI to identify potential fire scenarios, albeit they recognized several lines of future work, such as optimization of interpolation methods, meteorological forecast and the introduction of new variables (e.g. wind patterns).

Schneider et al. (2008) proposed a new approach to the calculation of the RG based on the Visible Atmospherically Resistant Index (VARI) (Gitelson et al., 2002) and tested their FPI values (their Eq. 4) to the Southern California, against 12,490 fire detections from the MODIS active fire product using logistic regression. Moreover, Adelabu et al. (2020) employed a modified version of FPI calculation algorithm in South-Africa in order to provide a useful index of fire risk in the mountainous study area, from 2011 to 2014.

1.3.12 F index

The F index (Sharples et al., 2009a) is a combination of wind speed information and fuel moisture content, where the fire danger decreases as fuel moisture content increases, but increases as wind speed increases. It is given by

$$F = \frac{\max(U_0, U)}{FMI} \quad (1.21)$$

where U_0 is a wind speed threshold (1 km h^{-1}), U is the wind speed (km h^{-1}) and FMI is the fuel moisture content, which is calculated as (Sharples et al., 2009b)

$$FMI = 10 - 0.25(T - H) \quad (1.22)$$

where T is the air temperature (°C) and H is the relative humidity (%).

Sharples et al. (2009a) compared the F index with the FFDI (Eq. 1.3), GFDI4 (Eq. 1.4), GFDI5 (Eq. 1.7) and FFWI (Eq. 1.11), which are more mathematically involved fire danger indices. They showed that the F index is highly correlated with each of the four indices (their Table 2) and was able to produce similar results with them. However, they stated that under extreme fire weather conditions the agreement between the F index and the other indices was worst, but to its defense they acknowledged that the McArthur indices were developed in the absence of extreme fire weather. Table 1.9 presents the fire danger classification thresholds for F, along with the corresponding values of FFDI and GFDI4 indices, while Fig. 1.13 displays the fire danger rating monogram based on the F index, as proposed by Sharples et al. (2009a).

Table 1.9: Fire danger classification thresholds for F compared to FFDI and GFDI4, respectively (Sharples et al., 2009a).

Fire danger	F index	FFDI	F index	GFDI4
Low	0 – 0.7	0 – 5	0 – 0.5	0 – 2.5
Moderate	0.7 – 1.5	5 – 12	0.5 – 1.2	2.5 – 7.5
High	1.5 – 2.7	12 – 24	1.2 – 2.9	7.5 – 20
Very high	2.7 – 6.1	24 – 50	2.9 – 7.3	20 – 50
Extreme	> 6.1	50 – 100	> 7.3	50 – 200

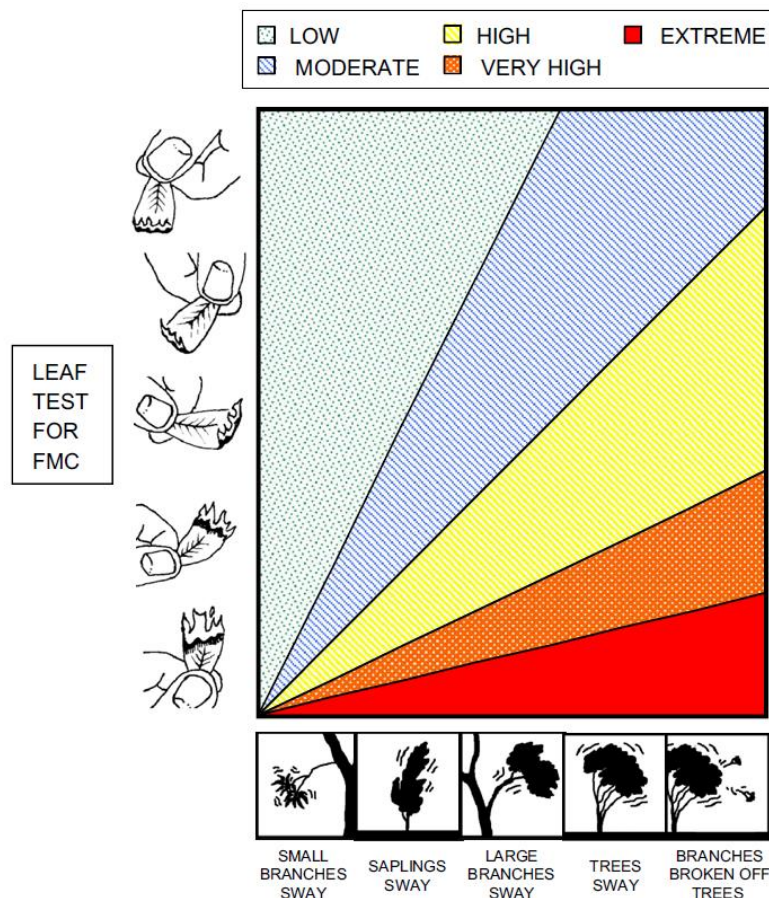


Fig. 1.13: Fire danger rating monogram based on the F index (Sharples et al., 2009a).

1.3.13 Santa Ana Wildfire Threat Index (SAWTI)

The Santa Ana Wildfire Threat Index (SAWTI) (Rolinski et al., 2016) is a tool for categorizing Santa Ana (California, USA) wind events with respect to anticipated fire potential, especially large fire potential (>100 ha). It combines meteorological and fuel moisture information into a single equation as

$$LFP = 0.001W_s^2 D_d \times FMC \quad (1.23)$$

where W_s is the 10 m sustained wind speed (mi h^{-1}), D_d is the near-surface (2m AGL) dew point depression ($^{\circ}\text{F}$), defined as $(T - T_d)$ and FMC is the fuel moisture component given by (Rolinski et al., 2016)

$$FMC = \left\{ 0.1 \left[\left(\frac{DL}{LFM} - 1 \right) + G_{ag} \right] \right\}^{1.7} \quad (1.24)$$

In Eq. 1.24, DL is the dryness level, LFM is the live fuel moisture and G_{ag} is the degree of green-up of the annual grasses. The interested reader is referred to Rolinski et al. (2016) for the analytical explanation and calculation of the aforementioned variables.

1.3.14 Hot-Dry-Windy Index (HDWI)

The Hot-Dry-Windy Index (HDWI) (Srock et al., 2018) was developed recently as an effort to isolate the effects of weather on wildland fire, such as the Angström Index (Eq. 1.1) and the Haines Index (Table 1.8). According to authors, the HDWI is a physical index that utilizes large scale information, as it is more spatially and temporally predictable, and conditions at these scales are often an adequate proxy for fire-scale variability. Given that the relative humidity alters the level of evaporation at different temperatures, the combined effect of the temperature and absolute moisture content on the fire environment is different. Taking the aforementioned into consideration, the HDWI is formulated as (Srock et al., 2018)

$$HDWI = U \times VPD(T, q) \quad (1.25)$$

where U is the wind speed (m s^{-1}) and VPD is the vapor pressure deficit (hPa), defined as

$$VPD(T, q) = e_s(T) - e(q) \quad (1.26)$$

where e_s is the saturation vapor pressure (hPa) and e is the vapor pressure (hPa). Both quantities are formulated in Appendix I. Practically the HDWI can be calculated at any point, but the authors advocated that a 500 m deep layer over the surface is sufficient in order to identify days on which synoptic-and meso-alpha-scale weather processes can contribute to especially dangerous fire behavior. However, they stressed out that additional analysis is required before HDWI can be used as an operational, decision-informing forecast tool.

1.3.15 Additional European fire danger indices and methods

In southern European countries, a number of fire danger indices and methods were developed mostly at the 1980s and early 1990s. Specifically, France, Italy, Portugal and Spain developed or adopted and calibrated their own fire danger rating systems, known as the French, Italian, Portuguese and Spanish Method, respectively. Viegas et al. (1999) evaluated these methods, along with the CFFDI in Southern

Europe and showed that the CFFDI and the Portuguese Method presented the best overall performance. Here, only a short description of each method is presented¹⁰.

The *French Method*, proposed originally by Sol (1989) and Drouet and Sol (1990), requires daily values of air temperature, relative humidity, cloud cover, wind velocity and an initial value of the water content of the soil (Viegas et al., 1999). Additionally, Carrega (1991) has proposed an index from a statistical analysis of meteorological parameters associated with fire occurrence in the French Riviera (Dimitrakopoulos et al., 2011a). The *Italian Method* (IREPI) (Bovio et al., 1984) estimates the loss of water in the soil due to actual evapotranspiration and combines it with the potential value of evapotranspiration in order to compute the danger index. It requires the daily average values of air temperature, relative humidity, wind and insolation, and cumulative precipitation.

The *Portuguese Method* is composed of a daily fire index and a cumulative index, the latter being a weighed sum of the daily indexes of the previous days, where the weighting factor is a function of precipitation. It's a modified version of the Nesterov Index (Eq. 1.2) and was employed by the Portuguese Meteorological Institute (Viegas et al., 1999). For the calculation of the daily index, it is necessary to measure the air temperature and relative humidity at 1200 LST. Wind speed and direction is taken into account in the final classification, according to local conditions (INMG, 1988). In addition, other studies explored the fire potential (Nunes et al., 2019) and fire hazard (Fernandes, 2009) over Portugal. The *Spanish Method* (ICONA, 1988) evaluates a probability of fire start, based on air temperature and relative humidity measured at 12.00 UTC.

1.3.16 Fire danger rating system in Greece

In Greece, the General Secretariat of Civil Protection produces daily fire risk thematic maps during the fire season (May-October). The production of the thematic maps (<https://www.civilprotection.gr/el/daily-fire-prediction-map>) is based on combined information (Issues No 2729/24-05-2013 and No 3841/29-05-2017) from several agencies and sources (e.g. Civil Protection Agency, Hellenic National Meteorological Service-HNMS, Hellenic Ministry of Environment and Energy, Hellenic Fire Service, Atmospheric Modeling and Weather Forecasting Group - National & Kapodistrian University of Athens).

The meteorological information is available primarily from the HNMS surface stations, while information on the current status of vegetation is provided through the exploitation of the NDVI, relative greenness (RG) and departure from average greenness parameters, respectively. In addition, the General Secretariat of Civil Protection calculates daily the FWI of the CFFWI system and the Ignition component (IC) of the NFDRS by utilizing gridded forecast data from numerical weather prediction models and/or geographical information systems (GIS). The final product is a thematic map in five fire risk classes (low, moderate, high, very high and extreme/on alert), which is available daily at approximately 1230 LT and it is valid for the next day. The map is disseminated on several agencies according to protocol and on the news, as well, which are obliged to present it to the public (https://www.civilprotection.gr/sites/default/gscp_uploads/gscp_20190624_0.pdf). Fig. 1.14 presents the fire risk on 23rd of July 2018, as it was issued on the 22nd of July 2018.

¹⁰ The author did not examine if the presented methods are currently in use (January 2020).

**ΧΑΡΤΗΣ ΠΡΟΒΛΕΨΗΣ ΚΙΝΔΥΝΟΥ ΠΥΡΚΑΓΙΑΣ ΠΟΥ ΙΣΧΥΕΙ ΓΙΑ
Δευτέρα 23/07/18**

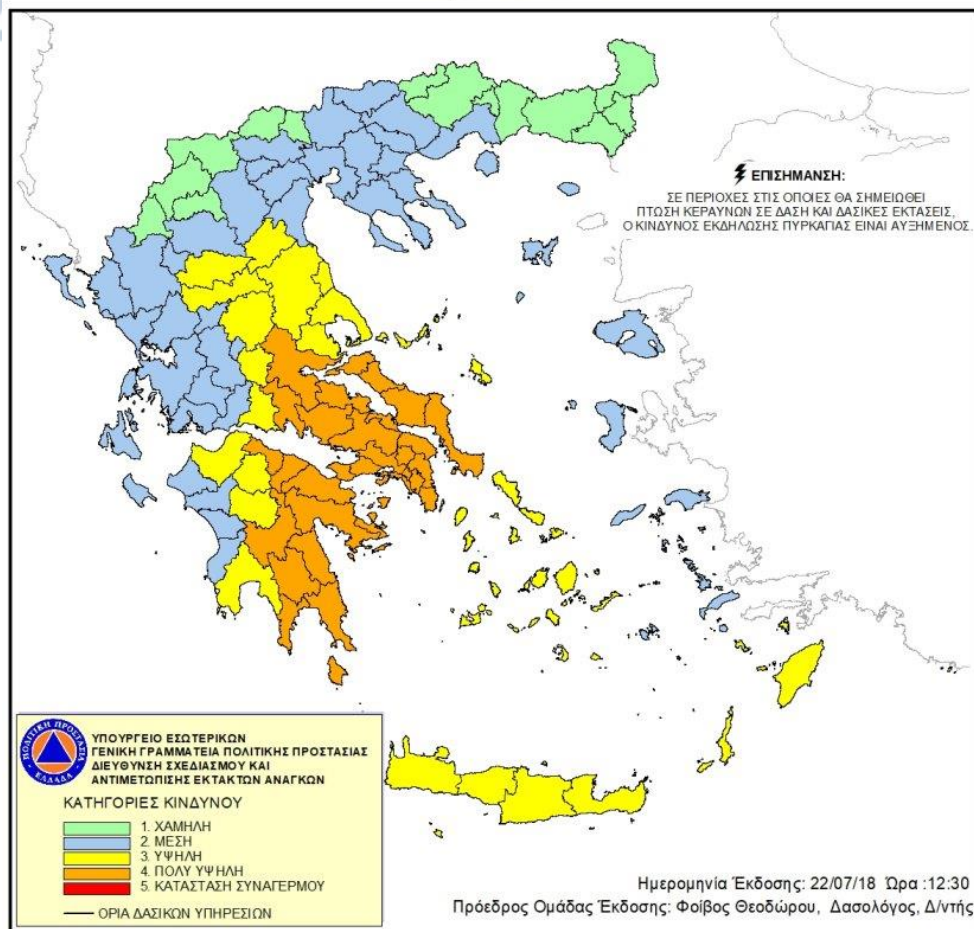
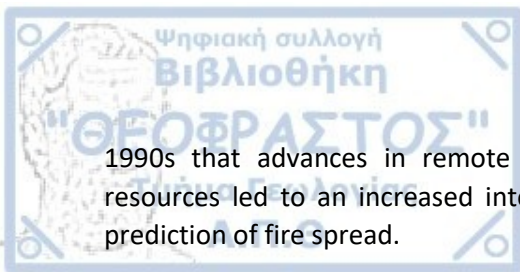


Fig. 1.14: Fire risk thematic map issued on 22/07/2018 by the Greek General Secretariat of Civil Protection, valid for 23/07/2018. Green, light blue, yellow, orange and red colors indicate low, moderate, high, very high and extreme (on alert) fire risk, respectively.

1.4 Wildfire modelling

Modelling the behavior of a wildland fires has been an active field of research since the 1920s (Sullivan, 2009a). From the early beginning, it became evident that the understanding of such phenomena and their potential behavior was through measurements, observations (Gisborne, 1929, 1927b) and theoretical considerations of the processes involved (Hawley, 1926). In the 1930s and 1940s, a physical approach¹¹ was incorporated to the measurement and modelling of the behavior of wildland fires (Curry and Fons, 1940, 1938; Fons, 1946), while in the 1950s several fire danger rating systems were emerged in the US, Canada and Australia. In the next twenty years (1950s and 1960s), research efforts in the field were associated and closely related with the effects of mass bombing and nuclear weapons (Chandler et al., 1963), albeit in the 1970s the lack of funding from the defense organizations did not advance the research of wildland fire behavior. In the 1980s, mostly land and fire management agencies and occasional journeyman mathematicians and physicists were interested in wildland fire behavior, where bigger and more achievable goals were introduced (Sullivan, 2009a). It was during the

¹¹ As physical approach here is considered the fundamental understanding of physics and chemistry involved in the combustion of biomass fuel and behavior of a wildland fire.



1990s that advances in remote sensing, geographical information systems and computational resources led to an increased interest on fire behavior modelling, specifically the spatiotemporal prediction of fire spread.

Early fire spread and flame length predictions were based on easily measured properties, such as fuel and surface weather variables. The fuel was divided into categories and the traditional approach was based on the heat from fuel consumption, albeit heat transfer mechanisms did not separate radiation and convection (Anderson, 1969; Van Wagner, 1967). Later, fuel categories in conjunction with topography and the wind were used for fire spread predictions (Brown, 1974) but the focus was on fire behavior more than the mechanisms of combustion and heat transfer (Bakhshaii and Johnson, 2019). At the same time, a more semi-mechanistic approach simplified the combustion and heat transfer into a simple flux equation (Byram, 1959; Rothermel, 1972), incorporating the heat released per unit mass of fuel during combustion and the mass loss rate during flaming combustion.

Weber (1991) provided a comprehensive review of fire behavior modelling prior to 1990, where models described as physical, empirical or statistical. Mell et al. (2007) elaborated on physical models and proposed a categorization scheme according to the component on which the model was focused (Fig. 1.15). In his series of papers, Sullivan (2009a, 2009b, 2009c) presented an extensive range of modelling work in wildland fire behavior during the period 1990-2007 and categorized the different methods of modelling. According to his convention, a physical model attempts to represent both the physics and the chemistry of fire spread (Table 1.10), while a quasi-physical model attempts to describe only the physics (Table 1.11). An empirical model contains only statistical in nature and no physical understanding (Table 1.12), with quasi-empirical models containing some form of physical framework on which the statistics are based (Table 1.13). Simulation models implement a pre-existing fire behavior model (Table 1.14), while mathematical analogue models utilize a mathematical precept rather than a physical one for the fire spread modelling (Table 1.15).

The new generation of wildfire models combine physical or empirical fire models with a numerical weather prediction (NWP) model or a computational fluid dynamics (CFD) model. The coupling depends on the approach (one-way or two-way¹²) and the spatiotemporal scales of phenomena that are resolved or parameterized. Thus, the models' physics and dynamics are strongly dependent on the scales of the target phenomena. As a wildfire is a multi-scale event (from combustion processes to synoptic scale forcing), physical parameterization in a particular scale of motion is required. Multi-scale models intend to assess the different levels of complexity in each scale. A coupled atmosphere-wildfire numerical system requires a significant amount of parameterization and filtering in order to represent the combined essence of a wildfire behavior over large domains (Bakhshaii and Johnson, 2019). Fire heat and moisture fluxes are physical parameterized in microscale (2 mm – 200 m), the convection and potential pyrocumulus activity are described in mesoscale (2 to 200 km), while synoptic scale drives the atmospheric forcing.

Next, a short description of the most common used new generation atmosphere-wildfire models is presented.

¹² In the one-way interaction model the atmospheric or CFD model “feeds” the fire model with input (e.g. wind direction and velocity), while in the two-way coupling, the fire model provides feedback, altering the atmospheric conditions in the vicinity of the fire.

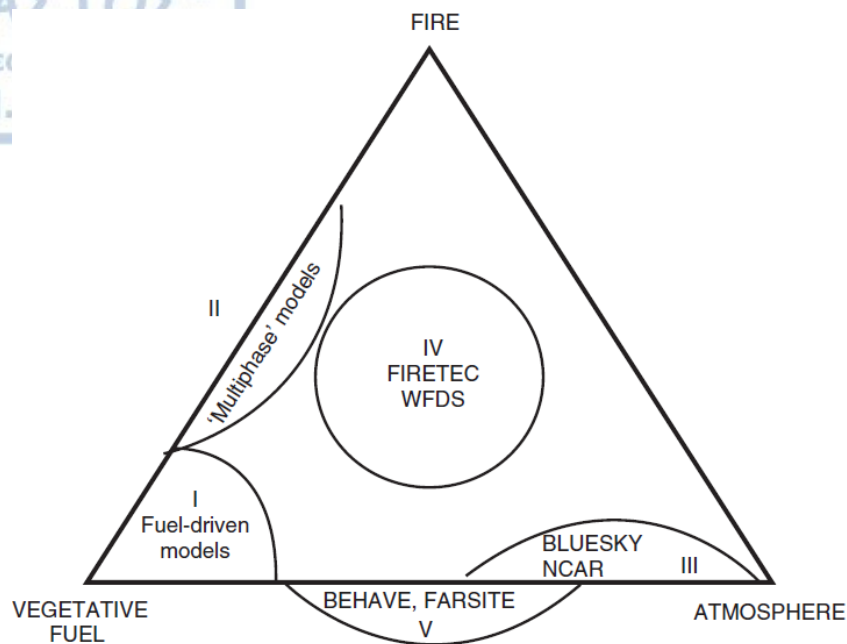


Fig. 1.15: The relationship of different wildland fire models. Each approach is located according to its emphasis on the atmosphere, vegetative fuel, and/or fire component(s) of the working model. Adopted from Mell et al. (2007), their Fig. 1.

Table 1.10: Physical models published in the literature during 1990-2007. Adopted from Sullivan (2009a).

Model (Year)	Origin	Dimensions	Plane
Weber (1991)	Australia	2	xy
AIOLOS-F (1994)	Greece	3	
FIRETEC (1997)	USA	3	
Forbes (1997)	Australia	1	x
Grishin	Russia	2	xz
IUSTI (1998)	France	2	xz
PIF97(1999)	France	2	xz
FIRESTAR (2001)	France	2	xz
LEMTA (2002)	France	2	xy
UoS (2002)	Spain	2	xy
UoC-R (2005)	USA	3	
WFDS (2007)	USA	3	

1.4.1 FIRETEC

FIRETEC (Linn et al., 2002), developed at the Los Alamos National Laboratory, New Mexico, USA, is a one-way physical coupled fire model, where the fire physics is an ensemble of average that is coupled to the atmosphere by HIGRAD (Reisner et al., 2000, 1998) at the scale of the fire model. HIGRAD adjusts the airflow to the terrain and topography and feeds FIRETEC, without updating the boundary conditions. The latter solves its system of equations using a finite volume numerical method, while structures smaller and larger than the resolved scale of the model are not represented explicitly. FIRETEC does not use empirical relations to the fire spread prediction and uses the Boussinesq approximation that ignores variation in the atmosphere. The model is computationally expensive and is limited to a small-eddy spatial (1 mm – 1 m, domain: 1 km²) and temporal (1 s – 2 h) scale.

1.4.2 WFDS

WFDS (Mell et al., 2007) stands for Wildland-urban interface Fire Dynamics Simulator and is an extension of the Fire Dynamics Simulator (FDS), developed at the U.S. National Institute of Standards and Technology (NIST). It is a fully three-dimensional physical one-way fire-atmosphere model that uses approximations to the governing equations of fluid dynamics, combustion and the thermal degradation of solid fuel. It differs from FIRETEC in terms of the physics of combustion (Bakhshaii and Johnson, 2019). WFDS is an open source large-eddy simulator (LES) that includes an approximation to analytically eliminating acoustic wave propagation. In addition, the model uses the level set method to simulate the fire front (Osher and Fedkiw, 2003), with no ability for wildfire forecasting in real-time. Although it utilizes a multi-mesh, the inner mesh feedback cannot update outside the boundary conditions and simultaneously adjust the coarse resolution values, adding potential limitations for simulating large wildfires (as multi-scale phenomena).

Table 1.11: Quasi-physical models published in the literature during 1990-2007. Adopted from Sullivan (2009a).

Model (Year)	Origin	Dimensions	Plane
ADFA I (1989)	Australia	1	x
TRW (1991)	USA	2	xy
Albini (1985, 1986, 1996)	USA	2	xz
UdC (1998)	France	2	xy
ADFA II (2002)	Australia, USA	2	xz
Coimbra (2004)	Portugal	2	xy
UoC-B (2005)	USA	2	xz

1.4.3 CAWFE

The Coupled Atmosphere-Wildland Fire-Environment (CAWFE) model (Clark et al., 1996b, 1996a, 2004) was developed at the National Center for Atmospheric Research (NCAR), Colorado, USA. In its early releases, CAWFE consisted of the Clark-Hall mesoscale atmospheric model coupled with a tracer-based fire spread model, while in the current version (Coen, 2013) a quasi-physical (or semi-physical) fire module is fully coupled to the atmospheric model. CAWFE can be initialized and boundary conditions updated with gridded atmospheric states from model forecasts or analyses. The model is based on the primitive equations of motion and thermodynamics, where wildland fire processes occur at scales several orders of magnitude smaller than the atmospheric grid size. CAWFE does not simulate flames, combustion chemistry or consumption of oxygen, but simulates the flaming front, rate of spread, post-frontal release and sensible and heat fluxes (both for surface and crown fires). CAWFE has the ability to run both in LES or in a multi-nesting mode, faster than real time (Coen et al., 2018).

1.4.4 ARPS/DEVS-FIRE

The Advanced Regional Prediction System (ARPS) serves as a tool for research and explicit prediction of convective storms and weather systems at meso-gamma scales (2 km) and was developed at the Center for Analysis and Prediction of Storms (CAPS), at the University of Oklahoma, USA (Xue et al., 2001, 2000). The DEVS-FIRE (Hu et al., 2012; Ntaimo et al., 2004) is a raster based fire spread model, which treats weather as an external input. As a result, the execution times in the ARPS/DEVS-FIRE system are longer. In addition, the lack of parallelism in the fire spread, fluxes and emissions solvers impacts computational times further. The coupling between ARPS and DEVS-FIRE is performed in the same framework as in FIRETEC and HIGRADs. Moreover, the newly implemented dynamic data assimilation methods showed that the simulation results can be improved (Dahl et al., 2015; Xue et al., 2012b, 2012a).

1.4.5 ForeFire/Meso-NH

The Meso-NH (Lafore et al., 1998) is non-hydrostatic mesoscale numerical model that utilizes the anelastic approximation for filtering acoustic waves. It was developed as a collaboration effort between the Centre National de Recherche Météorologique (CNRM) and the Laboratoire d' Aérologie in France. The fire propagation model (Balbi et al., 2009) is a quasi-physical model that predicts the fire front propagation as a radiating panel in the normal direction normal to the front. A Lagrangian front tracking method is used in the ForeFire fire propagation solver (Filippi et al., 2009). The coupling between Meso-NH and ForeFire is performed in the manner that the atmosphere's forcing applies in the fire model by a bilinear interpolation in space and time and the atmospheric model treats the feedback (imposed sensible and latent heat fluxes), at ground level. In addition, the radiation is treated explicitly by using fuel-dependent nominal values to estimate the heat fluxes and effective emitting temperature (Filippi et al., 2011).

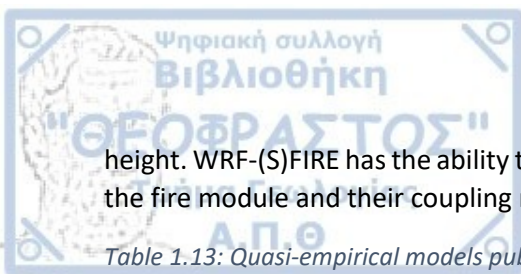
Table 1.12: Empirical models published in the literature during 1990-2007. Adopted from Sullivan (2009b).

Model (Year)	Origin	Field or laboratory ¹³	Fuel type
CFS-accel (1991)	Canada	Laboratory	Needles/excelsior
CALM Spinifex (1991)	Australia	Field	Spinifex
CFBP (1992)	Canada	Field	Forest
PWSTas (1995)	Australia	Field	Buttongrass
CALM Mallee (1997)	Australia	Field	Mallee/heath
CSIRO Grass (1998)	Australia	Field	Grass
Heath (1998)	Australia	Field	Heath/shrub
CALM Jarrah I (1999)	Australia	Laboratory	Litter
CALM Jarrah II (1999)	Australia	Field	Forest
UdTM Shrub (2001)	Portugal	Field	Heath/shrub
UdTM Pinaster (2002)	Portugal	Field	Forest
Gorse (2002)	Spain	Field	Gorse
Maquis (2003)	Turkey	Field	Maquis
Helsinki (2007)	Finland	Field	Forest/moss
CSIRO Forest (2007)	Australia	Field	Forest

1.4.6 WRF-(S)FIRE

The WRF-SFIRE (Mandel et al., 2014, 2011) and the WRF-FIRE (Coen et al., 2013) atmosphere-wildland fire models are essentially the same, albeit the former shares additionally features against the latter. The atmospheric model WRF is an upgrade of the 5th generation NCAR/Penn State Mesoscale Model (MM5) and the Advance Research WRF (ARW) solver (Skamarock et al., 2008) is applicable across scales ranging from 10s of meters to 10s of kilometers, including real-time forecast, research, coupled model applications, regional climate research and data assimilation. Its computation parallelization and modular structure is a tremendous advantage, where the fire module is based on the Rothermel's formulation (Rothermel, 1972) and is implemented as an added physics option. The fire module originates from CAWFE. The atmosphere-fire coupling is performed through passing wind, temperature and moisture values from the lowest model level to the fire module, which predicts the fire spread and in turn releases the fire emissions back to WRF assuming an exponential decay with

¹³ Empirical models further categorized into field or laboratory, based on the statistical analysis of observations. Distinction is made between observations of fire behavior in the strictly controlled and artificial conditions of the laboratory or in the field under more naturally occurring conditions.



height. WRF-(S)FIRE has the ability to run faster than real time. A more detailed description of the WRF, the fire module and their coupling method are presented in Chapter 2.

Table 1.13: Quasi-empirical models published in the literature during 1990-2007. Adopted from Sullivan (2009b).

Model (Year)	Origin	Field or laboratory	Fuel type
TRW (1991)	USA	Laboratory	Match splints
NBRU (1993)	Australia	Laboratory	Match splints
USFS (1998)	USA	Laboratory	Ponderosa/excelsior
Coimbra (2002)	Spain	Laboratory	Ponderosa
Nelson (2002)	USA	Laboratory	Birch sticks

Table 1.14: Simulation models published in the literature during 1990-2007. Adopted from Sullivan (2009c).

Model (Year)	Origin	Simulation type ¹⁴	Primary spread model
Ignite (1990)	Australia	Raster	McArthur (1967)
CSU (1991)	USA	Raster	Rothermel (1972)
FIREMAP (1992)	Portugal	Raster	Rothermel (1972)
NCAR/Clark model (1996)	USA	Vector-raster hybrid	Rothermel (1972)
SiroFire (1996)	Australia	Vector	McArthur (1967); Cheney et al. (1998)
Thrace (1997)	Greece	Raster	Rothermel (1972)
Prolif (1997)	France	Vector	Rothermel (1972)
FARSITE (1998)	USA	Vector	Rothermel (1972)
PYROCARD (1999)	New Zealand	Raster	Rothermel (1972)
FIREMASTER (2001)	Australia	Vector	McArthur (1967)
PdM (2002)	Italy	Raster	Rothermel (1972)
FireStation (2002)	Portugal	Raster	Rothermel (1972)
Prometheus (2004)	Canada	Vector	FCFDG (1992)
UWA (2006)	Australia	Raster	Cheney et al. (1998)

Table 1.15: Mathematical analogues models published in the literature during 1990-2007. Adopted from Sullivan (2009c).

Reference	Origin	Mathematical type
Catchpole et al. (1989)	Australia	Markov chain
Beer (1990)	Australia	Percolation ¹⁵
Bak et al. (1990)	USA	Cellular Automata (CA) ¹⁶
Clarke et al. (1994)	USA	Cellular Automata (CA)
Watt et al. (1995)	Australia	Ordinary Differential Equation (ODE) ¹⁷

¹⁴ Representation of the fire follows in general two approaches. In raster implementation, the fire is treated as a group of mainly contiguous independent cells whose state is unburnt, burning or burnt, that grow in number. In vector formulation, the fire is treated as a closed curved of linked points, where the propagation of the fire is carried out using some form of expansion algorithm.

¹⁵ In mathematics, percolation is a theory of transport through a randomly distributed medium. More on percolation theory and its application to wildland fire behavior, on Sullivan (2009c).

¹⁶ Cellular automata (CA) are formal mathematical idealization of physical systems in which space and time are discretized and physical quantities take on a finite set of values (Wolfram, 1983). Each cell of space is in one of a finite number of states at any one time. In general, CAs are implemented as a lattice (i.e. 2-D) but can be of any dimension. CA methods include organized criticality, diffusion-limited aggregation, local rules, fuzzy logic, stochastic, discrete event system and circuit calculus. More on CA and their applications to wildland fire behavior, on Sullivan (2009c).

¹⁷ The most common ODE method is that of the reaction-diffusion equation, which is comprised of the reaction term that generates energy and the diffusion term in which the energy is dissipated. The general solution is that of a wave. More on reaction-diffusion term and its application to wildland fire behavior, on Sullivan (2009c).



Duarte (1997)	France	Cellular Automata (CA)
Méndez and Liebot (1997)	Spain	Ordinary Differential Equation (ODE)
Margerit and Sero-Guillaume (1998)	France	Ordinary Differential Equation (ODE)
Karafyllidis (1999)	Greece	Generic algorithms
McCormick et al. (1999)	USA	Neural network
Mrz et al. (1999)	Slovenia	Cellular Automata (CA)
Hargrove et al. (2000)	USA	Cellular Automata (CA)
Li and Magill (2000)	Australia	Cellular Automata (CA)
Nahmias et al. (2000)	France	Percolation
Ricotta and Retzlaff (2000)	Italy	Percolation
Caldarelli et al. (2001)	Italy	Percolation
Muzy et al. (2002)	France	Cellular Automata (CA)
Achtemeier (2003)	USA	Cellular Automata (CA)
Dunn and Milne (2004)	Australia	Cellular Automata (CA)
Favier (2004)	France	Percolation
Ntaimo et al. (2004)	USA	Cellular Automata (CA)
Vakalis et al. (2004)	Greece	Cellular Automata (CA)

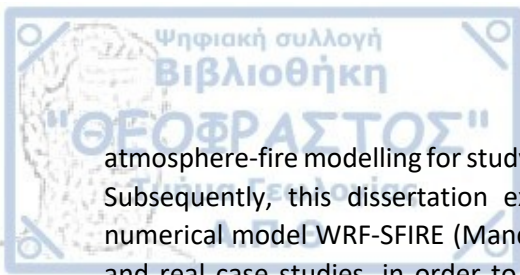
1.5 Motivation and Overview

Wildland fires are considered as a major problem to the natural environment, with great social and economic impacts. Since the 1980s, an almost exponential increase of forest fires and burnt areas is recorded in Greece, as during severe droughts, the annual burnt areas have exceeded 100,000 hectares (Dimitrakopoulos, 2009). The total burnt areas during 1983 to 2008 period corresponded to 10.3% of the country (Tzagari et al., 2011), while according to the Hellenic Fire Service, on average, 2070 forest fires were recorded yearly, during the period 2000 – 2018. Moreover, many economic and social activities, such as tourism, apiculture, logging, etc., are based on forests and their ecosystems. Many of these environments are adjacent to urban and / or tourist areas and they receive more and more pressure from land use changes.

Weather is the most variable and less predictable factor in the vicinity of a fire, while it can affect the fuel properties and fire behavior overall (Potter, 2012b, 2012a; Whiteman, 2000). As a wildfire event is a cascade of physical processes over different spatial and temporal scales, the challenge lies on the development of fire models that can resolve or parameterize as many as possible of these phenomena. Over the last two decades, significant advances have been made on the development of coupled atmosphere–fire numerical models for simulating wildland fire behavior, which can be proved valuable tools for fire behavior prediction and fire suppression planning. However, calibration and evaluation of such models are required prior to their utilization, while very fine resolution static data (e.g. topography height, fuel data) are of paramount importance for the accurate representation of the morphological features of the area of interest.

In Greece, the exploitation of such a modelling tool is imperative more than ever, due to the large number of forest fires breakouts every year, with devastating results. Unfortunately, the lack of an operational online coupled tool in Greece became more evident, in the tragic events on 23rd of July 2018, albeit efforts have been made since then to deploy such a system (Giannaros et al., 2019; Lagouvardos et al., 2019). Although many Greek researchers have utilized several approaches in fire modelling in recent years, the vast majority shares a common point; the one-way coupling between weather and fire models (Filippopoulos, 2012; Iliopoulos, 2013).

Thus, the motivation of this dissertation lies on the aforementioned statements but also on a simple question, which is expressed as “what is the level of effectiveness by utilizing an online coupled



atmosphere-fire modelling for studying various aspects of atmospheric interactions with wildland fire". Subsequently, this dissertation explores the capabilities of the online coupled atmosphere-fire numerical model WRF-SFIRE (Mandel et al., 2014, 2011) through a number of idealized experiments and real case studies, in order to investigate several aspects of the atmospheric interactions with wildland fires, across different scales.

This manuscript consists of five chapters, in total. Chapter 2 describes the numerical models and the observational data employed in this dissertation, while provides a short description of the methodology evolved in the analysis of the results on the following chapters. Chapter 3 investigates the online coupling between the atmospheric and fire model through highly idealized sensitivity experiments. A user-defined parameter sets the height in which the released energy fluxes from the surface fire are equal to 36% of their original value, controlling the depth of affected atmospheric layer and affecting the surface dynamics, the fire and the plume properties. Chapter 4 presents two real case studies, in which the coupled model is applied in order to investigate a) the meteorological conditions prior to the ignition and during the extreme fire events, b) the role of the topography in the overall fire behavior and c) the performance of the WRF-SFIRE during these extreme fire events. Finally, in Chapter 5 the conclusions and key remarks are presented.



Numerical models, observational data and methodology

2.1 Introduction

This chapter introduces the numerical models and their coupled modelling system, the global gridded analyses, the available surface and satellite observational data and the methods of analysis utilized in the current PhD thesis. Section 2.2 briefly presents the Weather Research and Forecasting (WRF) model, section 2.3 introduces the Spread FIRE (SFIRE) model, while section 2.4 describes the online coupled WRF-SFIRE modelling system. Section 2.5 discusses the operational gridded analyses of European Centre of Medium Range Weather Forecasts (ECMWF). In section 2.6, the Hellenic National Meteorological Service (HNMS) surface observations at Attica region, the Meteosat SEVIRI and Sentinel-2A L1C products, the Copernicus EMS (Emergency Management Service) – Mapping platform, the MODIS (Moderate Resolution Imaging Spectroradiometer) Fire and Thermal Anomalies and the Visible Infrared Imaging Radiometer Suite (VIIRS) products are presented. Finally, section 2.7 enumerates the equations and methods of analysis applied in this manuscript.

2.2 The Weather Research and Forecasting model

The Weather Research and Forecasting (WRF) model is a numerical weather prediction (NWP) and atmospheric simulation system designed for both research and operational applications. It features two dynamical cores (the ARW and NMM solver) and a data assimilation system, while its software framework has facilitated such extensions and supports efficient, massively-parallel computation across a broad range of computing platforms (Powers et al., 2017). The model serves a wide range of meteorological applications across scales from tens of meters to thousands of kilometers. During the last decade, the advent of more powerful and efficient High Performance Computing (HPC) infrastructure has led to the utilization of WRF to a number of climate applications as well (e.g. Coppola et al., 2018; Davin et al., 2019; Katragkou et al., 2015; Knist et al., 2018, 2017; Pavlidis et al., 2019). WRF has the ability to run as a global model as well. Other tailored WRF systems include air chemistry (WRF-Chem; Fast et al., 2006; Grell et al., 2005), hydrology (WRF-Hydro; Gochis et al., 2015), fire weather (WRF-Fire; Coen et al., 2013), tropical cyclones (HWRF; Tallapragada et al., 2014), solar and wind energy (WRF-Solar; Jimenez et al., 2016) applications, Large-Eddy-Scale (WRF-LES) and high latitude and ice sheets modelling (Polar WRF; Bromwich et al., 2013, 2009; Hines and Bromwich, 2008). WRF has a large worldwide community of registered users, while it shares an online portal at <https://www.mmm.ucar.edu/weather-research-and-forecasting-model>.

The Advanced Research WRF (ARW, v3) solver (Skamarock et al., 2008) integrates the fully compressible, non-hydrostatic Euler equations in flux form (conservative for scalar variables). The equations are formulated using a terrain-following hydrostatic-pressure vertical coordinate (Laprise, 1992), on a staggered Arakawa C –grid and are integrated by a 2nd or 3rd order Runge-Kutta time-split scheme, with smaller time step for acoustic and gravity waves. In addition, 2nd to 6th order advection options in horizontal and vertical are available for the spatial discretization of the equations. WRF comes with a vast number of physics suites regarding the microphysical, planetary boundary layer,

cumulus, surface and radiation (shortwave and longwave) processes. The ARW solver has been developed in large part and is maintained by NCAR's Mesoscale and Microscale Meteorology Laboratory, while on 8th of June 2018, the version 4 (Skamarock et al., 2019) has been released, with major updates, additional features, improvements and bug fixes in almost all the components of the modelling system. The interested reader is pointed to <https://www2.mmm.ucar.edu/wrf/users/> portal for addition information about the WRF-ARW model and its current released version.

The WRF-ARW has been employed by the Department of Meteorology and Climatology (<http://meteo.geo.auth.gr>), School of Geology, Aristotle University of Thessaloniki in Greece, since 2009. It has been used for operational weather forecasting (<http://meteo3.geo.auth.gr/WRF/home.html>), educational and research purposes (Bampzelis et al., 2015; Karacostas et al., 2018; Kartsios et al., 2014a, 2014b, 2015, 2017; Katragkou et al., 2015, 2017; Krestenitis et al., 2017; Pavlidis et al., 2019; Pytharoulis et al., 2015, 2016; Pytharoulis, 2018; Pytharoulis et al., 2018; Stolaki et al., 2012; Tegoulis et al., 2014a, 2014b, 2017). In this manuscript, the WRF-ARW v3.4.1 has been utilized (Skamarock et al., 2008; Wang et al., 2012) in the performed simulations.

2.3 The Spread FIRE model

The Spread FIRE (SFIRE) module is a 2-dimensional semi-empirical fire spread model that was developed based on the level set method (Osher and Fedkiw, 2003) and consists of numerical algorithms specifying the fire spread rate and the heat fluxes. It originates from the NCAR's CAWFE (Clark et al., 1996b, 1996a, 2004) code. Here, only a brief description of the governing equations is provided. For more information, the complete description of the model and its components can be found in Mandel et al. (2011).

The fireline propagation is based on a modified (Rothermel, 1972) fire spread rate formula expressed by,

$$S = R_0 (1 + \phi_w + \phi_s), \quad (2.1)$$

where, R_0 is the spread rate absence of wind, and ϕ_w and ϕ_s is the wind and slope factor, respectively. At any point, the normal component of the wind vector and terrain gradient are used in the determination of the spread rate (in the normal direction outside to the fire region).

The fuel burning is formulated assuming exponential decrease of the fuel fraction, where the default coefficients (e.g. fuel weight) are applied from the CAWFE code. The average sensible and latent heat flux density ($W m^{-2}$) released in time interval ($t, t+\Delta t$) are computed by,

$$\phi_h = \frac{F(t) - F(t + \Delta t)}{\Delta t} \frac{1}{1 + M_f} w_l h \quad (2.2)$$

and

$$\phi_q = \frac{F(t) - F(t + \Delta t)}{\Delta t} \frac{M_f + 0.56}{1 + M_f} L w_l, \quad (2.3)$$

respectively. In Eqs. 2.2 and 2.3, $F(t)$ denotes the fuel fraction as a function of time, M_f is the fuel particle moisture content, w_l is the total fuel load ($kg m^{-2}$), h is the fuel heat contents of dry fuel ($J kg^{-1}$) and L is the specific latent heat of condensation of water at 0 °C. Mandel et al. (2011) note that the

speed of burning is independent of the wind speed and fuel moisture, while many factors that influence the spread rate are not accounted for.

The fire propagation by the level set method is governed by the partial differential equation

$$\frac{\partial \psi}{\partial t} + S \|\nabla \psi\| = 0, \quad (2.4)$$

where $\psi = \psi(\mathbf{x}, t)$ is the level set function and S is the fire spread from Eq. 2.1. The burning region at time t is represented by ψ as the set of all points $\mathbf{x} = (x, y)$ such that $\psi(\mathbf{x}, t) \leq 0$. The fireline is defined as $\nabla \psi = 0$. The 2nd order Runge-Kutta method is responsible for advancing the fire region in time. Once the fuel fraction is calculated, Eqs. 2.2 and 2.3 compute the heat fluxes. For the computation of fuel fraction, the fire mesh cells are divided into 4 subcells C_j , in which the level set function is interpolated bilinearly to the vertices of the subcells. Fig. 2.1 provides a graphical illustration of the aforementioned method.

The ignition mechanism supports both point ignition and line ignition (drip-torch ignition). Once a node is ignited, the normal fire propagation algorithm takes over from that node. It must be mentioned that it is best to choose ignition points from fire model mesh nodes. Otherwise, if the ignition rate of spread is low, it may take a long time for the fire to reach mesh nodes, and nodes at different but small distances from the ignition line may ignite at times that are not intended.

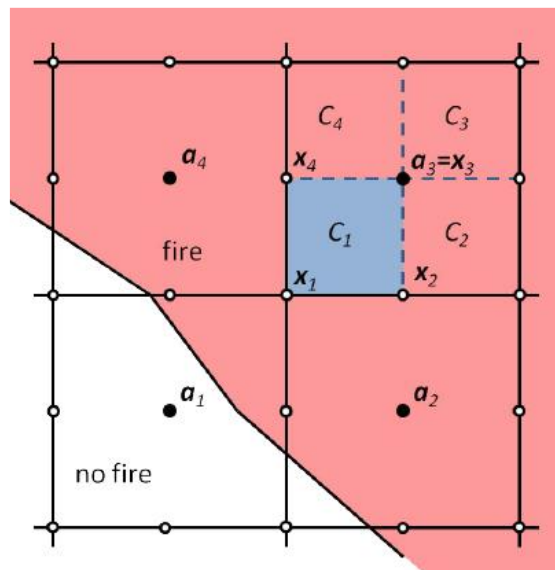


Fig. 2.1: Division of fire mesh cells into subcells for fuel fraction computation. The level set function ψ and the ignition time t_i are given at the centers $\alpha_1, \dots, \alpha_4$ of the cells of the fire grid. The integral over the cell C with the center α_3 is computed as the sum of integrals over the subcells C_1, \dots, C_4 . While the values of ψ and t_i are known at $\alpha_3 = \mathbf{x}_3$, they need to be interpolated to the remaining corners x_1, x_2, x_4 of the subcell C_1 from their values at the points $\alpha_1, \dots, \alpha_4$. After Mandel et al. (2011), their Fig. 2.

2.4 The online coupled WRF-SFIRE modelling system

The WRF-SFIRE modelling system (Mandel et al., 2011) consists of the Weather Research and Forecasting (WRF) model with the Advanced Research WRF (ARW) solver, coupled with the fire spread model (SFIRE) module. Both models were briefly described in Sections 2.2 and 2.3, respectively. The coupling is performed in every WRF's integration time step, where the wind is inserted in the fire

module and the latter outputs the heat flux from the fire into the lowest levels of the atmosphere, which in turn influences the atmospheric properties in the vicinity. The system facilitates additional features, such as a fuel moisture model (Mandel et al., 2014), a fuel-moisture-data-assimilation system (Vejmelka et al., 2016), the coupling with the atmospheric chemistry and aerosols schemes in WRF-Chem (Kochanski et al., 2019, 2016) and a data-assimilation method for initialization of the fire from a given fire perimeter (Mandel et al., 2012). The code is available through the Open Wildland Fire Modelling (OpenWFM) environment at <http://openwfm.org>, where new developments, improvements and bug fixes are available. Additionally, a subset of the SFIRE's features is distributed in the regular WRF releases by the WRF-Fire (Coen et al., 2013) designation. Fig. 2.2 illustrates the interactions between WRF, SFIRE and WRF-Chem models.

As Fig. 2.2 shows, the near surface wind (from the lowest WRF's mass/theta vertical level) is entered as input into the fire module in each WRF's time step, following two different methods. In the first option, the wind is interpolated horizontally from the atmospheric mesh to the fire mesh and then vertically to a given "midflame" height (Baughman and Albini, 1980), z_f , above the terrain height. The vertical interpolation is performed following the ideal logarithmic wind profile, while the z_f depends on each fuel category.

In the second method and after the horizontal interpolation step, the vertical interpolation is supported by the use of wind reduction factors (Baughman and Albini, 1980), where the latter determine the vertically interpolated wind (in the calculated "midflame" height) from wind measured at a reference height ($z_{ref} = 6.096$ m), by assuming the ideal logarithmic wind profile. Which one of the methods is the best to use depends upon the height of the first WRF's theta level, z_1 . If $z_1 < z_{ref}$ then the first option is preferred. The second option can be also used in this case, as it is much cheaper computationally, but the actual wind profile information under the z_{ref} may be lost. Both methods produce the same results if the vertical resolution is coarse that $z_1 \geq z_{ref}$. For more information about the vertical interpolation methods the interested reader is pointed to Mandel et al. (2011), Section 5.2 and to https://www.openwfm.org/wiki/Vertical_wind_interpolation.

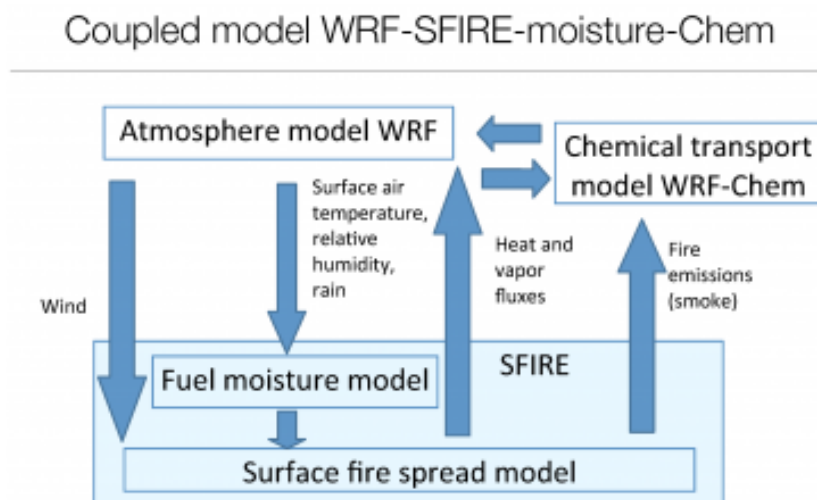


Fig. 2.2: Schematic illustration of the interactions between the different models in WRF-SFIRE modelling system. Adopted from <http://openwfm.org>.

The fire module is called in the 3rd step of the Runge-Kutta method in WRF-ARW, where the interpolated wind is used for the calculation of the fire spread rate according to Eq. 2.1, along with the terrain gradient, which is computed from the terrain height at the best available horizontal resolution. Then, the fire spread model updates the level set function, advances the Eq. 2.4 to the next time step, sets the time of ignition for any ignited nodes, updates the fuel fraction and calculates the heat flux densities in each fire grid point from Eqs. 2.2 and 2.3. The last step involves the averaging of the resulting heat densities over the fire cells that make up one WRF grid cell and their insertion into the WRF.

The heat fluxes are inserted into the atmospheric model into a layer above the surface by assuming an exponential decrease with height. The sensible heat flux density is inserted as additional source term to the differential equation of potential temperature, equal to the vertical divergence of the heat flux (Mandel et al., 2011) as,

$$\frac{d(\mu\theta)}{dt}(x, y, z) = R_{\theta}(\Phi) + \frac{\mu(x, y)\varphi_h(x, y)}{\sigma\rho(x, y, z)} \frac{\partial}{\partial z} \exp\left(-\frac{z}{z_{ext}}\right), \quad (2.5)$$

while the latent heat flux density is inserted into the source term of the vapor concentration by

$$\frac{d(\mu q_m)}{dt}(x, y, z) = R_{q_m}(\Phi) + \frac{\mu(x, y)\varphi_q(x, y)}{L\rho(x, y, z)} \frac{\partial}{\partial z} \exp\left(-\frac{z}{z_{ext}}\right). \quad (2.6)$$

$R_{\theta/q_m}(\Phi)$ are the components of the source terms (tendencies), σ and L represent the specific heat and latent heat of the air, respectively, φ_h and φ_q are the averaged fluxes over the fire cells that make up one atmosphere model cell from Eqs. 2.2 and 2.3, ρ is the air density, μ is the hydrostatic component of the pressure differential of dry air between the surface and the top of the computational domain and z_{ext} is the heat extinction depth parameter or e-folding depth. The latter controls the height in which the heat fluxes are equal to $\sim 36\%$ (e^{-1}) of their original value upon insertion from the fire model. Chapter 3 of this manuscript addresses the choice of the e-folding depth, its impact to the vertical distribution of the heat fluxes and consequently to flow dynamics in the lowest levels of WRF and its role to the overall fire behavior.

2.5 ECMWF operational gridded analyses

In Chapter 4, the operational gridded analyses of the European Centre of Medium Range Weather Forecasts (ECMWF) are utilized for the synoptic analysis of the extreme fire events under investigation. The operational analyses are gridded products available from the ECMWF Integrated Forecasting System (IFS, Bechtold et al., 2008; Benedetti et al., 2009; Buizza et al., 2007; Drusch et al., 2009; Morcrette et al., 2009, 2008; Rabier et al., 2007). The IFS consists of a) an atmospheric model run at various resolutions appropriate to the forecast length, b) an ocean wave model, c) an ocean model including a sea ice model, d) a land surface model including a lake model, e) a data analysis system (4D-VAR) and f) perturbation techniques for generation of the ensembles. Fig. 2.3 displays the various IFS components and their exchange sequences. The retrieval of the gridded analyses performed under the CY45R1 operational configuration of the IFS (HRES), at pressure levels up to 10 hPa, with $0.1^\circ \times 0.1^\circ$ (latitude-longitude) grid spacing.

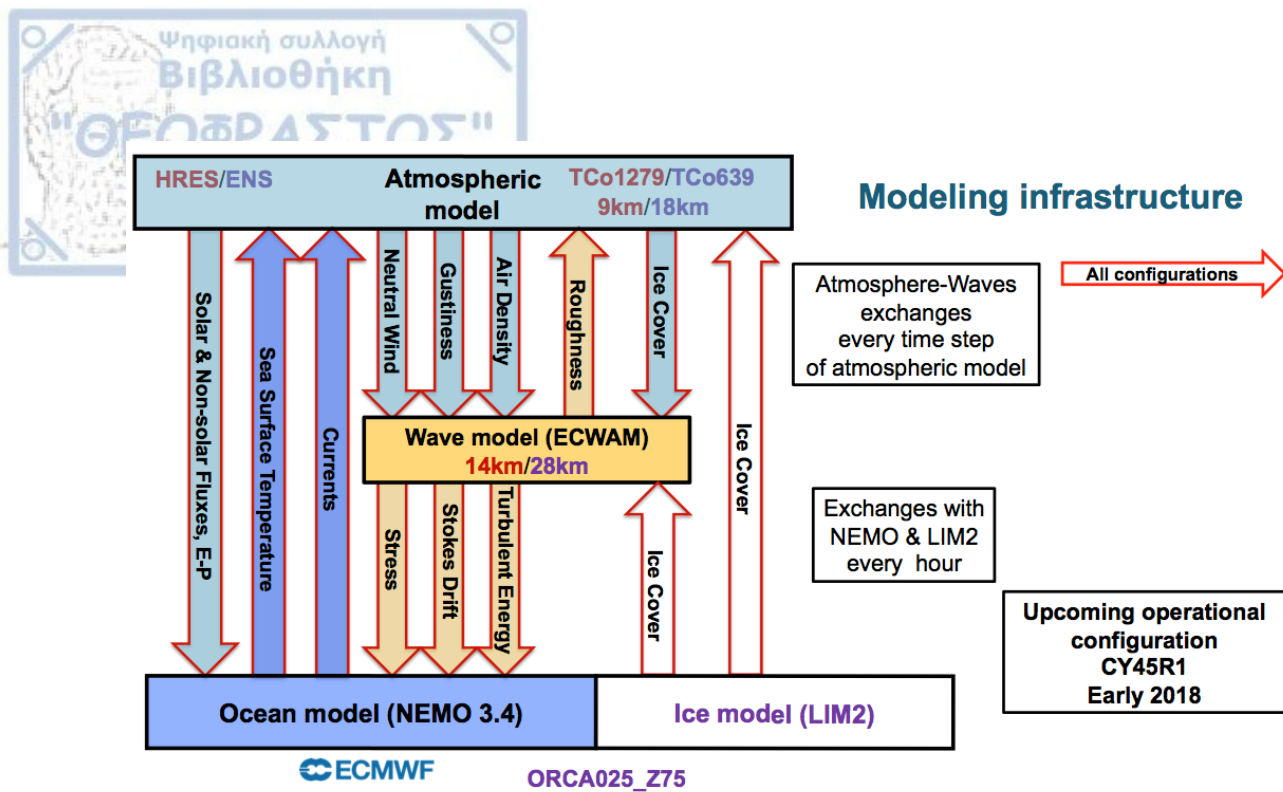


Fig. 2.3: Exchange of physical quantities between the atmospheric, ocean wave and ocean. Adopted from <https://confluence.ecmwf.int//display/FUG/2+The+ECMWF+Integrated+Forecasting+System++IFS>.

2.6 EO and non EO Observational datasets

2.6.1 HNMS surface observations

For the verification of the WRF-SFIRE model results in Chapter 4, surface observations at Attica region were obtained from the Hellenic National Meteorological Service (HNMS). The record data consist of 2 m air temperature (°C) and relative humidity (%), 10 m wind speed (knots) and direction (degrees), wind gust speed at last 10 min and 3 hrs (knots) and daily precipitation (mm). The HNMS operational observations span from 22nd (00Z) to 24th (12Z) of July 2018 at 30 min intervals, while at least half of them are part of the World Meteorological Organization (WMO) network. Fig. 2.4 depicts the locations of the 12 available HNMS surface observations, along with their WMO identification number.

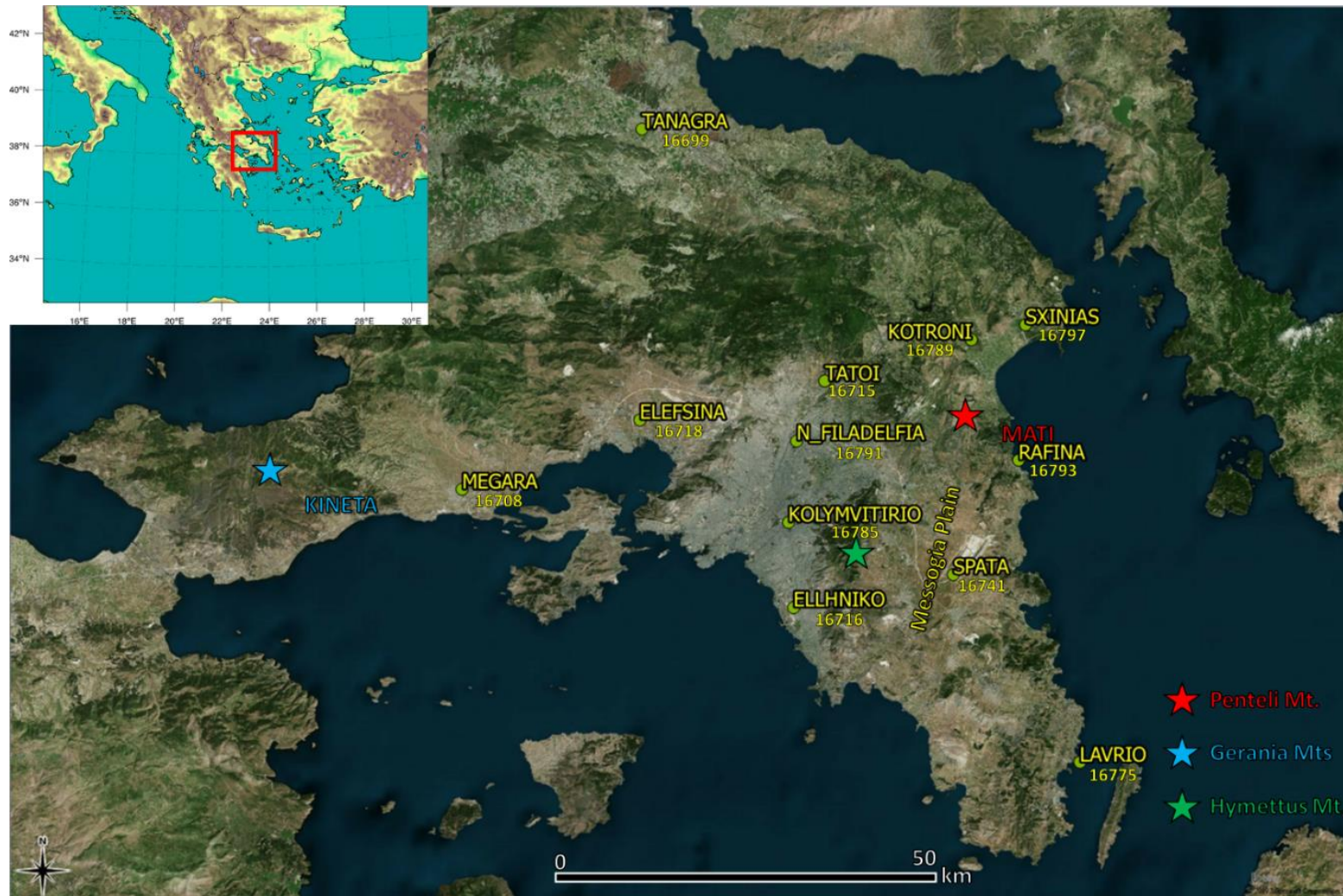
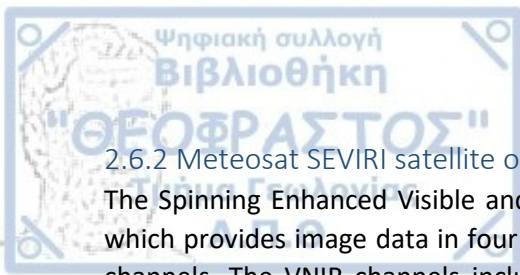


Fig. 2.4: Locations of the HNMS surface observations that are utilized for verification purposes in Chapter 4.



2.6.2 Meteosat SEVIRI satellite observations

The Spinning Enhanced Visible and Infrared Imager (SEVIRI) is a 50 cm optical imaging radiometer, which provides image data in four Visible and Near InfraRed (VNIR) channels and eight InfraRed (IR) channels. The VNIR channels include the High-Resolution Visible (HRV) channel, which contains 9 broadband detection elements to scan the Earth with a 1 km sampling distance at Sub Satellite Point (SSP), helping weather forecasters in detecting and predicting the onset or end of severe weather. All the other channels (including the IR channels) are designed with 3 narrow band detection elements per channel, to scan the Earth with a 3 km sampling distance, providing information about the temperatures of clouds, land and sea surfaces. The instrument is onboard the Meteosat-11 Second Generation (MSG) geostationary satellite, orbiting at 36.000 km above the equator, positioned at 0°E and providing full disc imagery every 15 minutes. The MSG meteorological satellites developed by the European Space Agency (ESA) in close co-operation with the European Organisation for the Exploitation of Meteorological Satellites (EUMETSAT). In this manuscript (Chapter 4), the panchromatic visible (0.4 to 1.1 μm) Meteosat SEVIRI images (0°E) from the NERC Satellite Receiving Station at Dundee University were retrieved and examined from <http://www.sat.dundee.ac.uk>.

2.6.3 SENTINEL-2 satellite observations

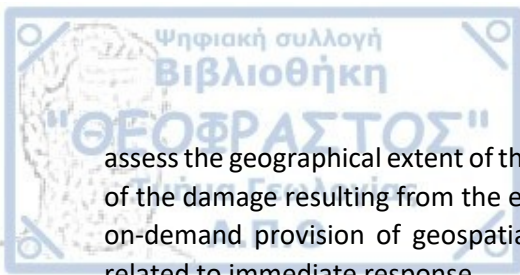
SENTINEL-2 is a European wide-swath, high-resolution, multi-spectral imaging mission of twin satellites (Sentinel-2A, Sentinel-2B), which operate simultaneously, phased at 180° to each other, in a sun-synchronous orbit at a mean altitude of 786 km. The coverage limits are from between latitudes 56° south and 84° north. Each of the satellites carries the Multi-Spectral Instrument (MSI). The MSI works passively, by collecting sunlight reflected from the Earth. New data is acquired at the instrument as the satellite moves along its orbital path. The incoming light beam is split at a filter and focused onto two separate focal plane assemblies within the instrument; one for Visible and Near-Infra-Red (VNIR) bands and one for Short Wave Infra-Red (SWIR) bands. The optical design of the MSI telescope allows for a 290 km Field Of View (FOV).

For interpretation purposes in Chapter 4 of this manuscript, the Level-1C (L1C) True and False color images from the Sentinel-2A satellite were retrieved through the EO Browser of the Sentinel-Hub portal (<https://www.sentinel-hub.com/explore/eobrowser>). The Level-1C product is composed of 100 x 100 km² tiles and additionally includes Cloud Masks and ECMWF data, such as total column of ozone, total column of water vapour and mean sea level pressure. The interested reader can find additional information at <https://sentinel.esa.int/web/sentinel/missions/sentinel-2/overview>.

2.6.4 Copernicus Emergency Management Service

The Copernicus Emergency Management Service (EMS) uses satellite imagery and other geospatial data to provide free of charge mapping service in cases of natural disasters, human-made emergency situations and humanitarian crises throughout the world (<https://emergency.copernicus.eu/mapping/ems/service-overview>). Copernicus EMS - Mapping is provided during all phases of the emergency management cycle, where the maps are produced in two temporal modes, the Rapid Mapping and the Risk and Recovery Mapping.

The Rapid Mapping consists of the provision of geospatial information within hours or days from the activation in support of emergency management activities immediately following a disaster. Standardised mapping products are provided: e.g. to ascertain the situation before the event (reference product), to roughly identify and assess the most affected locations (first estimate product),



assess the geographical extent of the event (delineation product) or to evaluate the intensity and scope of the damage resulting from the event (grading product). Risk and Recovery Mapping consists of the on-demand provision of geospatial information in support of Disaster Management activities not related to immediate response.

In the deadly fire events on 23rd of July 2018 at Attica region, the Copernicus EMS was activated delivering delineation and grading products both for Gerania and Rafina fire events (event EMSR300, <https://emergency.copernicus.eu/mapping/list-of-components/EMSR300>). Fire scars in shape file format from the final grading product were used in the verification process of the WRF-SFIRE modeled burnt area.

2.6.5 MODIS Fire and Thermal Anomalies

The Moderate Resolution Imaging Spectroradiometer (MODIS) is onboard the Terra and Aqua satellites, as a part of NASA's Earth Observing System (EOS) and began collecting data in February 2000 and June 2002, respectively. Both satellites are in a circular sun-synchronous polar orbit, at 705 km above Earth's surface. The MODIS instruments deliver oceanic, atmospheric and terrestrial data products. Among terrestrial products is the Thermal Anomalies/Fire product, which is based on a fire detection algorithm originated from Kaufman et al. (1998) and improved by Giglio et al. (2003), with special 1 km resolution. The algorithm uses brightness temperatures derived from the fire channels at 4 and 11 μm and identifies pixels with burning fires at the time of the satellite overpass. Each pixel is assigned to one of the six classes (missing data, cloud, water, non-fire, fire or unknown).

A daytime pixel is assigned as potential fire when $T_{4\mu\text{m}} > 310 \text{ K}$, $\Delta T = T_{4\mu\text{m}} - T_{11\mu\text{m}} > 10 \text{ K}$ and the reflectance at $0.86 \mu\text{m}$ is less than 0.3. The nighttime pixels must fall into the following, $T_{4\mu\text{m}} > 305 \text{ K}$ and $\Delta T > 10 \text{ K}$. An estimation of the fire radiative power (FRP) is also available in the MODIS Thermal Anomalies/Fire product given by,

$$FRP = A_s \beta (T_f^8 - T_b^8), \quad (2.7)$$

where, A_s is the nominal MODIS pixel area evaluated at the scan angle s , β is equal to $4.34 \times 10^{-19} \text{ W m}^{-2} \text{ K}^{-8}$, T_f is the 4 μm brightness temperature of the fire pixel and T_b is the mean 4 μm brightness temperature of the background pixel. A quantification of the MODIS FRP measurement uncertainty is presented in (Freeborn et al., 2014). In Chapter 4, the Collection 6 MODIS L3 fire product was utilized.

2.6.6 VIIRS 375m active fire detection product

The Visible Infrared Imaging Radiometer Suite (VIIRS) aboard the Suomi National Polar-orbiting Partnership (S-NPP) satellite (in a sun-synchronous orbit) delivers key Environmental Data Records (EDRs) and the Active Fires Application Related Product (ARP). The VIIRS acquires 375 m (I-bands) and 750 m (M-bands) data. The VIIRS 375 m data are comprised of five distinct single-gain channels extending from the visible to thermal infrared spectral region. The VIIRS active fire detection algorithm is based on the MODIS Fire and Thermal anomalies (Giglio et al., 2003; Kaufman et al., 1998) product but differences in spatial resolution, sampling and spectral characteristics led to a new adaptation of the original algorithm (Schroeder et al., 2014). Fig. 2.5 illustrates the significant improvement in VIIRS 375 m fire detection product against the 1 km Terra/MODIS (left) and Aqua/MODIS (right) products, during a fire in southern Brazil, on March 2013.

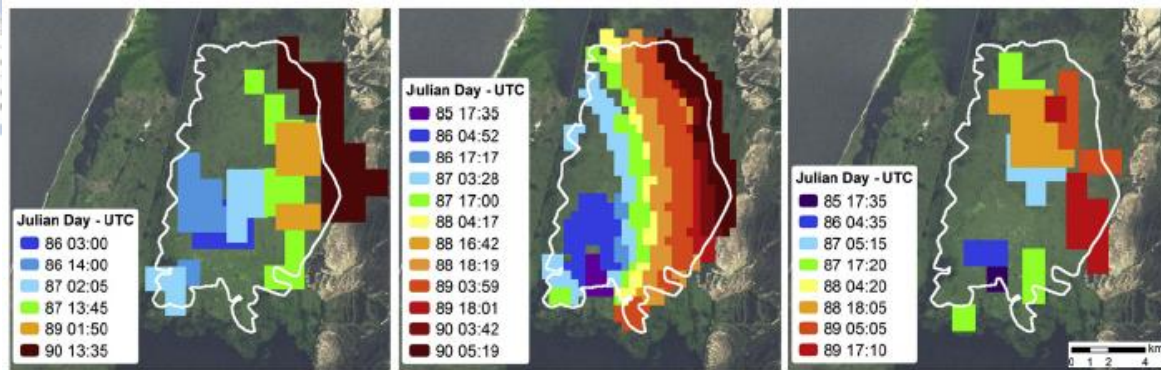


Fig. 2.5: Daily fire spread mapped by 1 km Terra/MODIS (left), 375 m VIIRS (center), and 1 km Aqua/MODIS (right) data for a wildfire at the Taim Ecological Reserve in southern Brazil (-32.7°lat , -52.55°lon). The data cover the period beginning on 26 March 2013 (Julian day 85) and ending at the approximate time of the Landsat-7 data acquired at 13:15UTC on 31 March 2013. The white vector outline represents the burned area mapped using the 30 m Landsat-7 data. Adopted Schroeder et al. (2014), their Fig. 9.

2.7 Methods of analysis

2.7.1 Vorticity and vorticity equation

The flow dynamics can be influenced and/or altered in the vicinity of a fire. Dynamic fire behavior can occur by vorticity generation (Sharples et al., 2013, 2015; Simpson et al., 2013; 2014), flow attachment to the surface (Edgar et al., 2015), or interaction between separate fire fronts, e.g. junction fires (Thomas et al., 2017). Vorticity and circulation are the two primary measures of rotation in a fluid. While circulation (a scalar integral quantity) is a macroscopic measure of rotation for a finite area of the fluid, vorticity (vector field) describes the microscopic rotation at any point in the fluid (Holton, 2004; Karacostas, 2008). Here, the definitions of vorticity and vorticity equations are provided, since in the analysis of the results, both in Chapter 3 and 4, the aforementioned quantities are utilized.

Vorticity is a vector field defined by the curl of the velocity (in Cartesian coordinates),

$$\vec{\omega} = \nabla \times \vec{V} = \begin{vmatrix} \hat{i} & \hat{j} & \hat{k} \\ \frac{\partial}{\partial x} & \frac{\partial}{\partial y} & \frac{\partial}{\partial z} \\ u & v & w \end{vmatrix} = \underbrace{\left(\frac{\partial w}{\partial y} - \frac{\partial v}{\partial z} \right)}_{(\omega_x)} \hat{i} + \underbrace{\left(\frac{\partial u}{\partial z} - \frac{\partial w}{\partial x} \right)}_{(\omega_y)} \hat{j} + \underbrace{\left(\frac{\partial v}{\partial x} - \frac{\partial u}{\partial y} \right)}_{(\zeta)} \hat{k}, \quad (2.8)$$

where u , v and w the three components of the wind vector. If the wind vector refers to the absolute velocity, then we take the absolute vorticity \mathbf{w} from Eq. 2.8, whereas if we consider the relative velocity (wind velocity relative to Earth's rotation), then Eq. 2.8 gives the relative vorticity \mathbf{w} . The difference between absolute and relative vorticity is planetary vorticity, known as Coriolis parameter, f ($\sim 10^{-4} \text{ s}^{-1}$). In this manuscript, only the relative vorticity is considered.

The vertical component of relative vorticity is designated by the Greek letter ζ . In the Northern Hemisphere, regions of positive (negative) ζ are associated with cyclonic (anticyclonic) rotation. In the remainder of this manuscript, ζ is referred to as relative vorticity.

The time evolution of vorticity, in the vicinity of a fire, can be derived by applying Eq. 2.8 to the Navier-Stokes equations of an adiabatic motion to get,

$$\frac{\partial \vec{\omega}}{\partial t} + (\vec{V} \cdot \nabla) \vec{\omega} = (\vec{\omega} \cdot \nabla) \vec{V} - \vec{\omega} (\nabla \cdot \vec{V}) + \frac{1}{\rho^2} \nabla \rho \times \nabla p + \nabla \times \left(\frac{\nabla \cdot \vec{\tau}}{\rho} \right) + \nabla \times \vec{B} \quad (2.9)$$

(A) (B) (C) (D) (E) (F)

The second left-side term (Eq. 2.9A) describes the advection of vorticity by the wind. The first term of the right-hand (Eq. 2.9B) is the tilting term, which describes how velocity gradients transform vorticity from one axis to another, while the second right-hand term (Eq. 2.9C) characterizes how flow convergence (divergence) stretches (compresses) the vortices and increases (decreases) the magnitude of vorticity. The solenoidal term or baroclinic (Eq. 2.9D) quantifies the generation of vorticity in conditions where the pressure and density gradients are not parallel. During a fire, the intense heating results in horizontal temperature gradients that are not aligned with the vertical static pressure gradient, leading to rotational motions to restore balance (Forthofer and Goodrick, 2011). The fourth right-hand term (Eq. 2.9E) describes the generation of vorticity due to viscous shear stress, produced by the surface drag. Finally, in the last right-hand term (Eq. 2.9F) vorticity changes due to gravity or buoyance forces. Although Tohidi et al. (2018) present a review on the state of knowledge concerning the fluid dynamics of fire whirls, they provide a comprehensive illustration of vorticity evolution processes in their Fig. 2, which is adopted also here (Fig. 2.6).

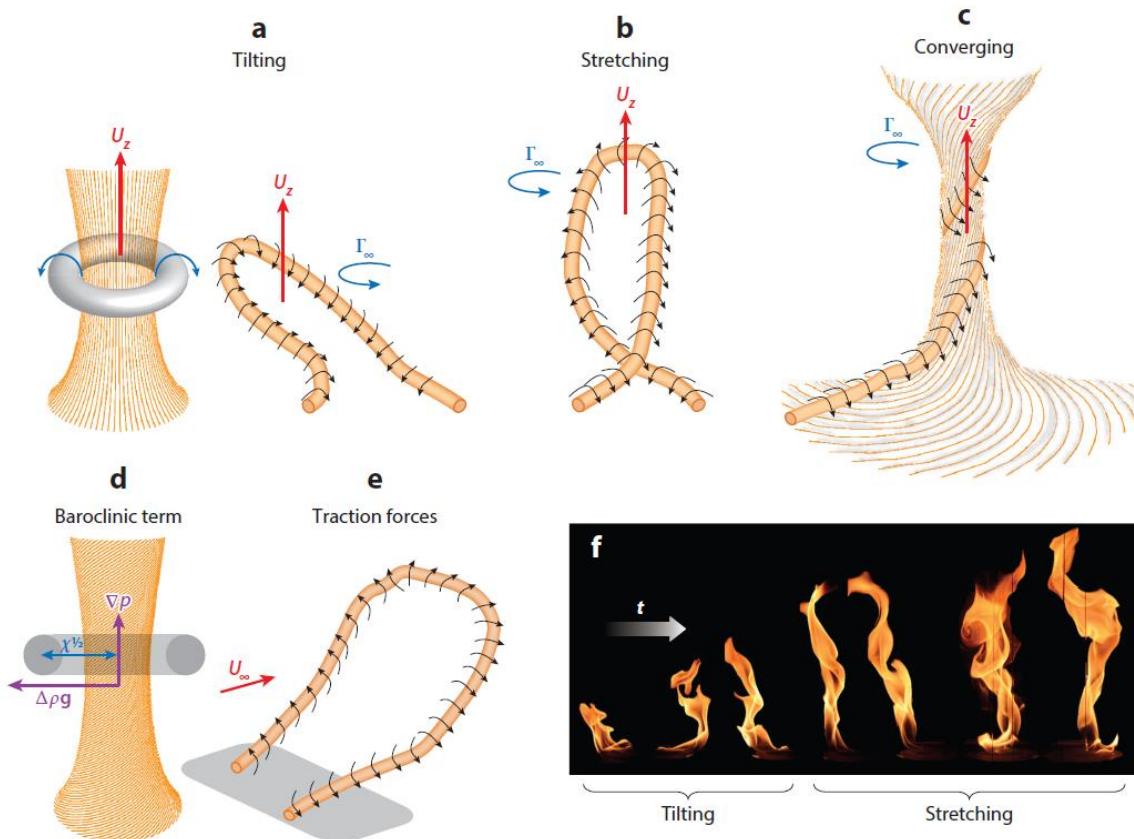


Fig. 2.6: Schematic diagrams of vorticity evolution processes: (a) tilting, (b) stretching, (c) converging, (d) the baroclinic term, and (e) traction or body forces evolving the vorticity field. Panel f shows the evolution of the flame sheet over time as a pool fire transitions into a fire whirl and demonstrates the presence of tilting and stretching under controlled laboratory conditions. Γ denotes circulation. Adopted from Tohidi et al. (2018), their Fig. 2.



The horizontal divergence, δ , is defined as,

$$\delta = \nabla_h \cdot \vec{V}_h = \frac{\partial u}{\partial x} + \frac{\partial v}{\partial y}. \quad (2.10)$$

In the Northern Hemisphere, $\delta > 0$ (divergence) is associated with anticyclonic (clockwise) rotation while $\delta < 0$ (convergence) with cyclonic (counterclockwise) rotation.

2.7.2 Calculation of air density

WRF did not provide air density as an output variable in version 3.4.1. However, the aforementioned is not true for example in version 3.8.1 or 4.1.2. The calculation of the solenoidal term (Eq. 2.9D) requires the air density (kg m^{-3}) which is approximated by,

$$\rho(i, j, k) = \frac{\text{pres}(i, j, k) \cdot 100}{R_a \cdot T_v(i, j, k)}, \quad (2.11)$$

where pres is the air pressure (hPa), R_a is the mass-specific gas constant for dry air ($287.058 \text{ J kg}^{-1} \text{ K}^{-1}$) and T_v is the virtual temperature or density temperature (K), given by

$$T_v(i, j, k) = T(i, j, k) \cdot (1 + 0.622 \cdot r(i, j, k)), \quad (2.12)$$

where T is the air temperature (K) and r is the water vapor mixing ratio (kg kg^{-1}).



The heat extinction depth concept: An application to the WRF-SFIRE modelling system

3.1 Introduction

During a wildland fire, complex physical and chemical processes are involved across different spatiotemporal scales. Fire - atmosphere interactions include energy and mass fluxes between living and dead vegetation and the atmosphere, that occur on time scales approximately on the order of 10^2 to 10^5 s and spatial scales on the order of 10^2 to 10^5 m (Potter, 2012a). Complex mechanisms such as degradation by drying and pyrolysis of vegetation, multiple interactions between turbulence and a number of phenomena (combustion, drag forcing due to vegetation, radiative heat transfer) are accounted for the behavior of wildfires (Morvan, 2011).

Due to the wide range of physical scales involved in a wildland fire, it is not possible to develop models that analyze all scales. According to Mell et al. (2007), simulations of wildfires require models for both the fire-fuel interaction and the fire-atmosphere interaction. The fire-fuel interaction involves gas generation by solid fuel pyrolysis, the subsequent combustion of the fuel gases, and the resulting heat flux back to the solid fuel, driving continued pyrolysis and fire spread. The fire-atmosphere interaction involves the response of both the fire and its plume to the ambient winds, and the response of the atmosphere to the buoyant fire plume. Also, this two-way coupling can alter the orientation and geometry of the fire plume, influencing the distribution and intensity of the net heat flux to the solid fuel, and the downwind transport of firebrands and smoke. At larger spatiotemporal scales, the interaction of the fire plume with the atmosphere can result in atmospheric processes such as pyrocumulus formation. At even larger scales, diurnal cycles in humidity and temperature, and synoptic weather patterns, can influence the behavior of the fire and its smoke plume.

Sun et al. (2006) focused on the interactions between the fire flame and the fuel and between the fire flame and the plume and the ambient atmosphere by utilizing two fluid dynamics numerical wildfire models. In their work they evaluated the fire-plume properties simulated with the Fire Dynamics Simulator (FDS; McGrattan, 2004), an explicit and computational demanding tool and the Clark coupled wildfire model (Clark et al., 1996a), which was based on a simplified physical approach regarding the fire spread formula and the coupling between the atmospheric and fire model. For more information on the different approaches on modelling wildland fires, the reader is pointed to the first chapter of this manuscript.

Their evaluation was carried out using observational data from the Meteotron experiment (Benech, 1976), while one of the key findings of their study was that, the less explicit and less computational Clark model was sensitive to the method by which the energy from the fire was inserted into the lowest part of the atmosphere. By depositing the released sensible fluxes over a relative large layer above the fire, underestimation of near-surface properties over the fire (e.g. temperature excess and vertical velocity) was observed, while an abrupt and discrete spike in convective buoyancy fluxes was found when the released fluxes were inserted into the first 10m above surface.

The released energy fluxes from a wildland fire alter the thermodynamic characteristics of the fire-plume, where sensible and latent heat fluxes add momentum to the air parcels aloft the combustion zone, triggering convection. In wildland fire-atmosphere modelling, the parameterization of the heat exchange between the fire and the lowest levels of the atmosphere is of paramount importance, as different approaches of how the heat fluxes and water vapor fluxes are inserted into the atmospheric boundary layer can result to different fire-plume properties and thus fire behavior.

As physically detailed, fire-atmosphere coupled and computationally intensive models such as FIRESTAR (Morvan and Dupuy, 2004, 2001), FIRETEC (Linn et al., 2007, 2002) and WFDS (Mell et al., 2007) are beyond the scope of this manuscript, this chapter focuses on the atmosphere-fire coupling between available mesoscale atmospheric models with 2-D fire simulators. In recent years, this approach has demonstrated potentiality, as some of the complex phenomena occurring in wildland fires are being captured by this type of models, which are able to run faster than real time (Filippi et al., 2018, 2013; Kochanski et al., 2016, 2013b, 2013a).

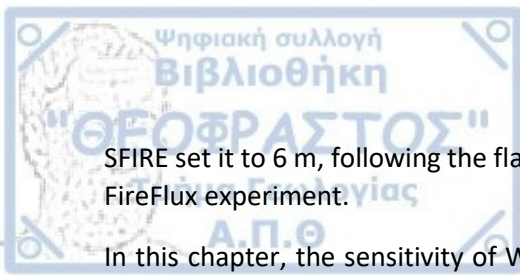
In their coupled atmosphere – fire numerical model (MesoNH/ForeFire), Filippi et al. (2009) use an externalized surface model in order to introduce the fire feedback to the atmosphere, while a fire rate of spread (RoS) model is adopted to advect the fire front. Feedback from the fire to the atmosphere is provided by generating three different surface matrices from the wildfire model to force the atmospheric model at the first ground level, a) sensible heat fluxes ($W m^{-2}$), b) flux of water vapor ($kg m^{-2}$) and c) radiant temperature (K). The numerical system was evaluated with observational data coming from the FireFlux experimental burn (Clements et al., 2008, 2007) that took place on 23 February 2006 at the Houston Coastal Center, resolving relatively well the atmospheric coupling induced by the fire, both in terms of amplitude and the general behavior of the fire-induced winds (Filippi et al., 2013).

In WRF-SFIRE (Mandel et al., 2011) modelling system, the sensible and latent heat fluxes from the fire are inserted as forcing terms in the differential equations of the atmospheric model into a layer above the surface, where an exponential decrease with height is assumed, following Eq.(3.1).

$$F(\vec{x}, t) = F(x, y, t) \exp\left(-\frac{z}{z_{ext}}\right). \quad (3.1)$$

As described in Chapter 2, section 2.4, the sensible heat flux is inserted as an additional source term to the equation for the potential temperature θ , equal to the vertical divergence of the heat flux according to Eq (2.5), while, the latent heat flux is digested into the source term of vapor concentration q_m , following Eq (2.6).

The altitude in which the heat fluxes decay is controlled through the heat extinction depth parameter (z_{ext}), a variable with a default value of 50 m, which can be adjusted through the namelist.input file. The aforementioned formulation is originally used by Clark et al. (1996a, b) and it was rewritten for WRF variables in Patton and Coen (2004). During the FROSTFIRE research project (Fastie et al., 2002; Hinzman, 2003), Coen et al. (2004) showed that the fire affected the air in its vicinity approximately 50 m above the fire (updrafts & temperature perturbation), suggesting the e-folding extinction depth of 50 m (where the variables' value is equal to ~36% of its original value). Nevertheless the FROSTFIRE experiment was conducted in a boreal forest of interior Alaska, burning mostly black spruce, leaving the hardwoods standing. Moreover, in the CAWFE modelling system (Coen, 2013), the evolution of the Clark et al. (1996a,b) model, a very similar to WRF-SFIRE approach is used in order to distribute the released heat fluxes into the atmosphere, where for grass and crown fires the extinction depth is set to 10 m and 50 m, respectively. On the contrary, Kochanski et al. (2013a) in their validation of WRF-



SFIRE set it to 6 m, following the flame length of 5.1 m estimated by Clements et al. (2007), during the FireFlux experiment.

In this chapter, the sensitivity of WRF-SFIRE model to the choice of different heat extinction depths (z_{ext}) is evaluated, in order to investigate its role to the overall fire behavior. Although it was not accounted in their simulations, Moisseeva and Stull (2019) pointed out potential implications in the choice of the different e-folding depths. Since there is no widely accepted value for z_{ext} , its value remains an active field of research, due to strongly dependency on fuel properties, flame length, fire intensity and the environment of the fire (Sun et al., 2006).

In section 3.2, the model configuration is described, section 3.3 presents the results from the numerical experiments, section 3.4 discusses, while section 3.5 concludes this study.

3.2 Numerical modelling system and experimental setup

3.2.1 Domain configuration and model setup

The non-hydrostatic Weather Research and Forecasting model with the Advanced Research dynamic solver (WRF-ARW Version 3.4, Skamarock et al., 2008; Wang et al., 2012) was utilized and configured in turbulence-resolving large-eddy-simulation (LES) mode. In LES mode, the model runs at a few to approximately 100 m horizontal grid resolutions in order to resolve turbulent eddies and circulations within the atmospheric boundary layer. Although WRF-ARW is a mesoscale numerical weather prediction system, it has the capability to reproduce structures of the daytime boundary layer (Moeng et al., 2007) in LES mode, but with some limitations (Gibbs et al., 2014), depending on the application.

Several studies (Jenkins et al., 2011; Kartsios et al., 2014a, 2014b; Kochanski et al., 2013a, 2013c; Moisseeva and Stull, 2019; Simpson et al., 2016, 2014, 2013a; Thomas et al., 2017) focusing on atmosphere-fire interactions have demonstrated that WRF in LES mode can reproduce several aspects of the coupling between fire evolution and atmospheric dynamics. Here, a single 3-D domain was configured, with a west-east and south-north extent of 7.5 km and a uniform and flat terrain. In comparison to Kartsios et al. (2014b), the model top was placed at 10 km, as it was observed that when the fire-plume reaches the upper boundary of the domain, it alters the fire dynamics at surface (additional experiments that are not included in this manuscript). The horizontal grid discretization was 50 m for the atmospheric and 5 m for the fire model (1/10 grid to sub-grid ratio), respectively.

In vertical, a hyperbolically stretched grid with 80 levels (at mass/theta points; 81 levels staggered in Z axis) was derived from Eq. 3.2,

$$z_{nw}(k) = -1 \cdot \frac{\left\{ \tanh \left[z_{scale} \left(\frac{k-1}{kde-1} - 1 \right) \right] \right\}}{\tanh(z_{scale})}, \quad (3.2)$$

where z_{scale} equals 2.03, k corresponded to each vertical level and kde was the number of total vertical staggered levels (81). Thus, a computational domain of 1,846,881 grid points (151 x 151 x 81; (x,y,z) staggered; 1,800,000 grid points unstaggered) was defined. In addition, the fire surface model was consisted of 2,280,100 grid points (1510 x 1510; x,y staggered). The first theta level was placed at 5.8 m above surface, while the minimum vertical distance between mass levels was 11.9 m (between 1st and 2nd level) and the maximum was 444 m at the top of the domain (Appendix II, Table B.1). Fig 3.1 displays the values of sigma coordinates (on model levels), along with the height at mass points, where thermodynamic variables like temperature and pressure are calculated. According to Fig. 3.1, 34

vertical levels lie in the first 1 km, assuring very high vertical resolution inside the boundary layer. Coen (2018) pointed out that grid aspect ratio (the ratio of the vertical grid resolution to the horizontal grid resolution) plays important role in fire modelling, since sharp buoyancy gradients across narrow fire lines and convective updrafts are the source of fire-induced motions. While the accuracy of the numerical solutions is maintained when the grid aspect ratio is approximately equal to 1, Sullivan et al. (2011) suggested that the aspect ratio in convective and turbulence simulations should lie between 1 and 5. Thus, at ~ 1 km height, dz was equal to horizontal grid spacing (50m), gradually increased to ~ 250 m above 5 km height.

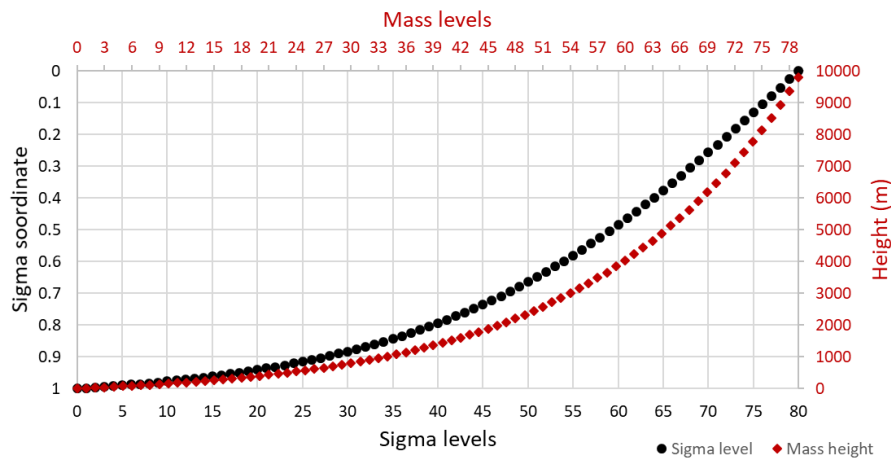


Fig. 3.1: Sigma coordinates (black circles) and mass points as function of height (red diamonds) in the configured 3-D domain.

The model time step integration was set to 0.1 s (smaller than the recommended 0.3 s) in order to prevent numerical instabilities using the available third-order Runge-Kutta scheme. In addition, a secondary time step (1/12 s of the primary time step) for acoustic and gravity wave modes was used, based on previous studies (Kartsios, 2013; Moeng et al., 2007; Simpson et al., 2013a; Yamaguchi and Feingold, 2012). Although best practices for WRF-LES simulations include cycling boundary conditions (Coen, 2018; Coen et al., 2013) where the flow leaving the domain re-enters upwind as inflow, in the case of fire simulations this is not reasonable as thermal and momentum perturbations and smoke by the fire would be introduced back to the domain. Also, Moeng et al. (2007) mentioned that cycling boundary conditions are not ideal when turbulent eddies are generated from different sources near the domain boundaries (e.g. existing topography or different land use properties). Thus, open boundary conditions were applied on the lateral boundaries, following similar configurations from the literature (referred on the previous paragraph).

Diffusion was calculated by evaluating the mixing terms in physical space ($dff_opt = 2$), while turbulence was parametrized by a 3-D prognostic 1.5 order turbulence closure ($km_opt = 2$). Fine tuning on the computation of the eddy viscosities in the prognostic TKE closure scheme (Skamarock et al., 2008) was achieved by setting the diffusion coefficient, C_x , equal to 0.1, following Cunningham et al. (2005) and Moeng et al. (2007). In addition, a nonlinear backscatter and anisotropy (NBA) subfilter-scale (SFS) stress model (Mirocha et al., 2010; $sfs_opt = 2$) was applied in order to remove the effects of the scales within the turbulence cascade on the resolved component of the flow. Also, 5th and 3rd order centered finite differences schemes were chosen for horizontal and vertical advection (momentum and scalar), respectively. A Rayleigh damping scheme (Klemp et al., 2008) with a 10 s damping coefficient (0.1 s^{-1} in inversed timescale; $damp_opt = 2$) was employed to the upper 3 km

layer of the domain, while a vertical velocity damping flag was activated in order to prevent violations of the CFL (Courant–Friedrichs–Lewy) condition. In addition, passive tracers were enabled (tracer_opt = 2) in order to simulate smoke from the surface fire.

Regarding the parametrization of the physical processes, the MM5 surface layer scheme (Jiménez et al., 2012) and the 5-layer surface model (SLAB 5-layer MM5 model; Dudhia, 1996) were activated, while the rest of the physics schemes were disabled. Moreover, surface heat and moisture fluxes along with model-computed friction velocity, u^* , from the Monin–Obukhov similarity theory were enabled (isfflx = 1).

A Mediterranean shrubland (maquis) fuel model, named Evergreen-sclerophyllous shrublands (1.5 up to 3.0m; Dimitrakopoulos, 2002) was assigned into the entire two dimensional fire grid of the SFIRE model. Despite the fact that Anderson’s thirteen (13) fuel categories (Anderson, 1982) are considered as the default configuration (Appendix II, Table B.2), a more representative fuel model was inserted, with custom values based on actual field measurements from Greece. According to Dimitrakopoulos (2002), the Evergreen-sclerophyllous shrublands fuel model is characterized by maximum values of fire-line intensity and rate of spread, while it relatively corresponds to Anderson’s fuel model 6 (Dormant brush, hardwood slash; personal communication with Prof. Dimitrakopoulos). The properties of the fuel model are presented in Table 3.1.

Table 3.1: Pyric properties of the Evergreen-sclerophyllous shrublands (Dimitrakopoulos, 2002) fuel model. The identifiers are as used in Mandel et al. (2011).

Symbol	Description	Identifier	Value
α	Wind adjustment factor	windrf	0.78
z_f	Fuel wind height (m)	fwh	3.0
z_o	Fuel roughness height (m)	fz0	0.2834
w	Fuel weight (s)	weight	3.4
w_l	Total fuel load (kgm^{-2})	fgi	4.908
δ_m	Fuel depth (m)	fueldepthm	2.18
σ	Fuel particle surface-area-to-volume ratio (m^{-1})	savr	1600
M_x	Moisture content of extinction (%)	fuelmce	0.35
ρ_p	Ovendry fuel particle density (kgm^{-3})	fueldens	32
S_T	Fuel particle total mineral content	st	0.0555
S_E	Fuel particle effective mineral content	se	0.010
h	Fuel heat contents of dry fuel (Jkg^{-1})	cmbcnst	17433000
M_f	Fuel particle moisture content	fuelmc_g	0.016

Wind from the atmospheric mesh is interpolated horizontally and vertically to the fire mesh in order to enter the Rothermel’s spread rate formula (Rothermel, 1972), as described briefly in Chapter 2, section 2.4. The vertical interpolation obeys, in general, the logarithmic profile (Mandel et al., 2011), while a number of available options control the interpolation mode. The simpler and cheaper option of interpolating first vertically to different heights on the fire mesh and then horizontally (fire_wind_log_interp = 1, fire_use_windrf = 2) was chosen, by utilizing the wind reduction factors from Baughman and Albin (1980). Using the fuel roughness height (fz0) and wind adjustment factor (windrf) from Table 3.1, the interpolation height was automatically set by the code to ~ 3.1 m, following Eq. 26 in Mandel et al. (2011). Even though the first theta level was set to ~ 5.8 m (below the BEHAVE

reference height of 6.096 m), the choice of this method could potentially affect the actual wind profile under the reference height, as noted in section 2.4.

The fire spread model was also coupled with a simple fuel moisture model (Mandel et al., 2014), which provides fuel moisture to the SFIRE from the WRF, altering the fuel moisture contents of the 4 available fuel classes (1, 10, 100 and 1000 h lag time). The Evergreen-sclerophyllous shrublands model was assigned proportionally to the first two classes (10% at 1 h and 90% to 10 h lag time), while the moisture model was integrated at every main time step. The default coefficients (rain-wetting lag time, saturation moisture content, saturation rain intensity and threshold rain intensity) were used, as they have been calibrated based on the Canadian fire-danger rating system (Mandel et al., 2014; van Wagner and Pickett, 1985).

3.2.2 Initial and lateral boundary conditions / fire ignition

Vertical profiles of potential temperature (K), water vapor mixing ratio (g kg^{-1}), and longitudinal and meridional wind components (m s^{-1}) as a function of height were applied as lateral boundary conditions by a single 1-D input sounding. The ideal atmosphere was constructed based on the Atmospheric Boundary Layer (ABL) profiles from Stull (1994). According to Fig. 3.2, neutral conditions dominated the first 1.5 km, a thick (300 m) temperature inversion layer (16.6 K km^{-1}) was located just above in order to control the height of the ABL, while aloft, the potential temperature was increasing with a rate of 4.6 K km^{-1} until the top of the domain (10 km). The water vapor mixing ratio was decreasing non-linearly from 12 g kg^{-1} to 6.25 g kg^{-1} until the upper inversion boundary, further decreasing to 0.1 g kg^{-1} (linearly) and it became equal to 0.08 g kg^{-1} at 10 km. Moreover, a westerly uniform wind profile, which varied with height, was adopted following Eq. 3.3:

$$U(z) = \begin{cases} 4 \cdot 10^{-4} z + 1.98, & 25 \leq z \leq 5000 \\ 2 \cdot 10^{-3} z - 6.05, & 5000 < z \leq 10000 \end{cases}, \quad (3.3)$$

where $U(z)$ in m s^{-1} and z is the height (m). According to Eq. 3.3, the westerly flow near the surface was 2 m s^{-1} with a positive linear-sheared background wind profile up to 5000 m, where the wind speed reached 4 m s^{-1} . From that height and until the top of the domain, the flow intensified linearly to 14 m s^{-1} . The surface pressure was 1015 hPa, while the skin surface temperature and the mean soil temperature were set to 304 K and 299.7 K, respectively.

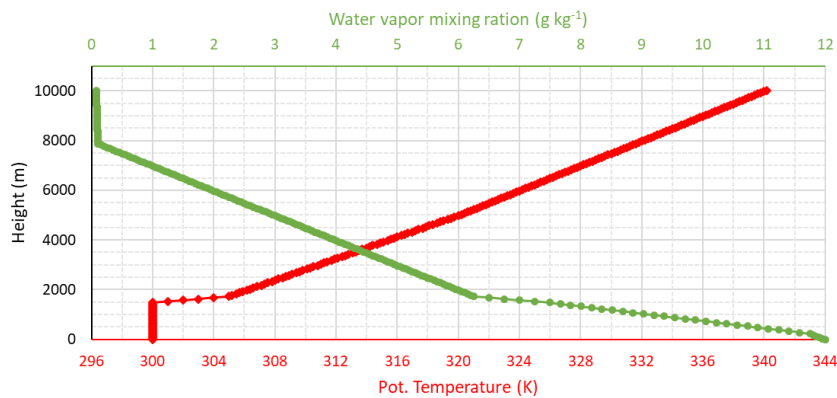


Fig. 3.2: Vertical profiles of potential temperature (K, red diamond line) and water vapor mixing ratio (g kg^{-1} , green circle line) acted as lateral boundary conditions.

The first 30 min were considered as spin-up period, allowing the atmospheric model to develop and equilibrate the boundary layer turbulence with the external forcing. Similar spin-up periods appear in the LES configurations of Moeng et al. (2007) and Yamaguchi and Feingold (2012) and in fire simulations with WRF-FIRE by Coen et al. (2013) and Simpson et al. (2013). In addition, some studies used a shorter time period (20 min) as spin-up time (Simpson et al., 2016, 2014; Thomas et al., 2017).

The fire ignited 30 s after the spin-up period (1830 s since model initialization), at a point 1850 m east and 3750 m north from the domain's lowest left corner, which corresponds to a grid point (x,y) with indexes (370,750) on the fire mesh. From that fire grid point and until the fire reached all the fire nodes inside a 10 m radius (fire_ignition_ros), the fire spread with an ignition rate of spread (fire_ignition_ros) of 0.1 m s^{-1} . The latter was modified from its default value (0.01 m s^{-1}), following the findings of Cunningham and Linn (2007) and the configurations of Kochanski et al. (2013a,b,c). At Appendix II (Table B.3), the input_sounding file is also provided for completeness.

3.2.3 Experimental design

In order to evaluate the role of heat extinction depth to the fire – atmosphere interactions, eight (8) experiments were performed, controlling how the released sensible and latent heat fluxes from the fire are inserted into the lower levels of the WRF model. For the purposes of this study, fire – atmosphere interactions involve a) the response of the released energy on surface or near surface variables (e.g. fire rate of spread, wind speed, air temperature) in the vicinity of the fire and b) the effect of fire plume into the ambient atmosphere and vice versa.

The control experiment (CNTRL hereafter) utilized the model and domain configuration as described in the two previous sub-sections, where the default value of 50 m was deployed in the code for the extinction depth parameter (z_{ext} hereafter). The rest seven (7) sensitivity experiments used the exact model setup as in CNTRL but the z_{ext} was changed accordingly to the following values, 5 (ext005m), 10 (ext010m), 15 (ext015m), 25 (ext025m), 75 (ext075m), 100 (ext100m) and 200 m (ext200m).

The model was integrated in the National HPC facility - ARIS – under the projects LESinFIRE (PA001010) and COrFIRE (PR002009), in MPI communication mode, using 160 cores (2 Intel Xeon E5-2680v2 processors at 2.8 GHz per node, 20 cores per node, 8 nodes with Infiniband interconnection) in each simulation. The forecast horizon was set to 2.5 hours, while the simulations wall clock time was ~8.5 hours. Output files were saved every 5 min, and the required total storage was approximately 500GB. Fig. 3.3 displays the execution time (s) as a function of core number according to the results of the performed benchmarking on HPC ARIS for 1 hour simulated time.

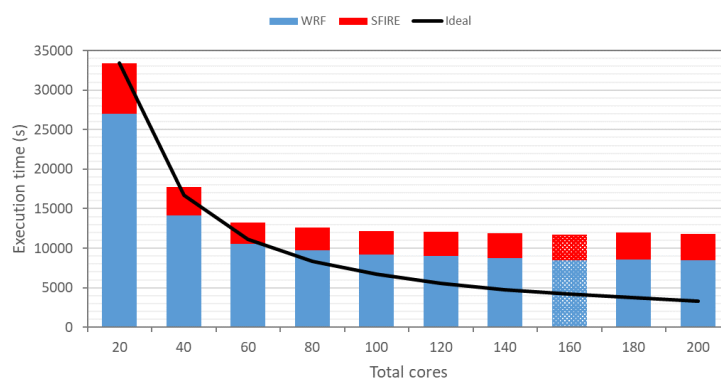


Fig. 3.3: Execution time (s) of WRF-SFIRE on MPI mode, in HPC ARIS, as a function of core number. The simulation wall clock time was 1 hour.

3.3 Results

In this section, the model results from the 8 experiments are presented. A unique code name is assigned in each experiment, which corresponds to the value of the extinction depth parameter (z_{ext}) used in the sensitivity. The naming convention of each experiment dictates the letters "ext" to be followed by the value of z_{ext} (3 digits), ending with the letter "m", e.g. ext005m for z_{ext} equal to 5 m. The experiment with the default z_{ext} value, 50 m, is referred as CNTRL. Due to excessive local heating of the atmosphere in the column above the fire, vertical violations of the CFL (Courant–Friedrichs–Lewy) condition were encountered and some of the simulations did not reach the forecast horizon (2.5 hours). Thus, for the analysis, a subset of the data was used from each model run, particularly the first forecast hour since the ignition of the fire, which was available in all simulations, unless it is mentioned otherwise.

3.3.1 Fire fluxes into the atmospheric model

According to Eq. 3.1, the released fluxes from the fire model are distributed vertically in a layer above surface into WRF, following an exponential decay with height. From Eq. 3.1 and based on the average height of the theta levels (Fig. 3.1), theoretical percentage flux values relative to ground ones, as a function of mass levels, were calculated for each experiment (Fig. 3.4). As Fig. 3.4 shows, for $z_{ext} = 5$ m, at 1st theta level, only ~31.4% of the heat fluxes from the surface is entering into WRF, while they are decaying rapidly on the next 4 levels aloft. On the other hand, for $z_{ext} = 200$ m, approximately 97% of the ground heat fluxes are inserted into the 1st theta level and reach half of their initial intensity (50%) at 10th mass level (~137 m). The calculated values in Fig. 3.4, can be found in the Appendix II (Table B.4).

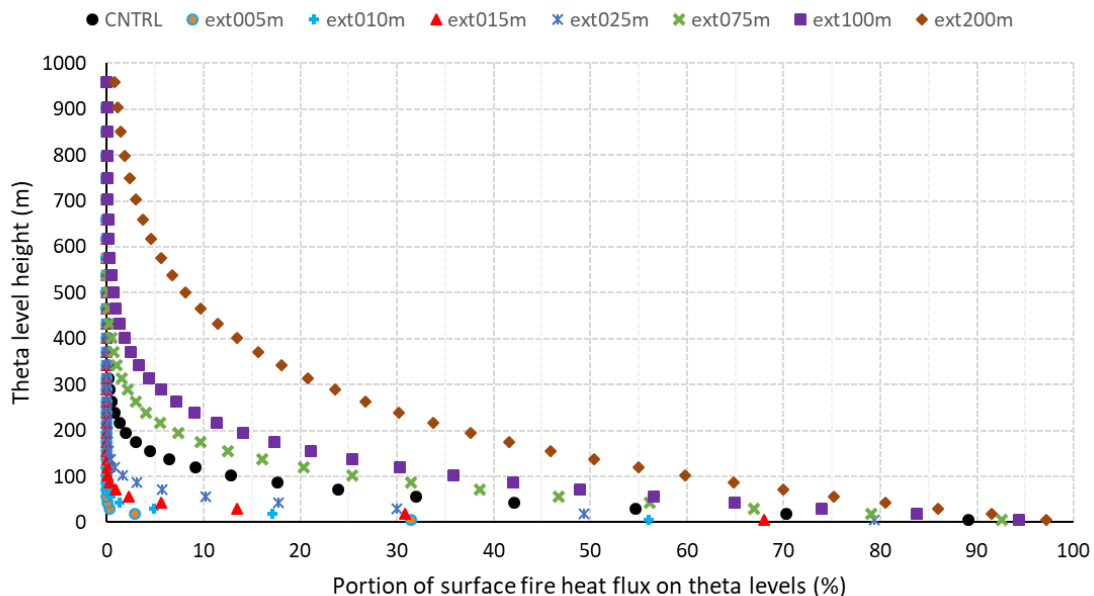


Fig. 3.4: Portion of heat flux from the surface fire that resides on every theta level up to ~1000 m above surface, for each experiment (black dots, CNTRL; orange dots, ext005m; cyan crosses, ext010m; red triangles, ext015m; blue asterisks, ext025m; green xs, ext075m; purple squares, ext100m; brown rhombi, ext200m).

Fig. 3.5 depicts the relative frequency distribution of the temperature tendency ($K s^{-1}$, red solid line) and humidity tendency (or vapor concentration; blue dashed line) as a function of altitude in each simulation, which correspond to the vertical divergence of the sensible and latent heat fluxes from the ground fire, respectively. At all available times within the first forecast hour after ignition and for each grid point in the 3-D domain, the height in which a single value of temperature and humidity tendency existed, it was considered as valid for the calculations of the distribution. Each distribution is consisted of 40 bins, with 250 m intervals.

In the CNTRL experiment (Fig. 3.5a), approximately 50% of the ground released heat fluxes (grid points with a valid flux value), in the first hour since ignition, lie below 750 m, while the surface fire adds energy, momentum and humidity to the ambient atmosphere until ~ 4000 m agl. Moreover, Fig. 3.5a suggests that the height of the fire heat fluxes follows an exponential decrease in vertical but this feature is arbitrary due to the higher density of the model levels near the surface (Eq. 3.2, Fig. 3.1). By setting the z_{ext} value equal to 5 m (Fig. 3.5b), almost 73% (77%) of the sensible (latent) heat fluxes are concentrated in the first 250 m and the maximum injection height is at 417 m agl. According to Eq. 3.1 and Fig. 3.4, at 5 m only 36% of the initial flux values exist, which is below the average height of the 1st theta level (~ 5.8 m). At 10 m ($2 \times z_{ext} = 5$ m), the fluxes are equal to 13.5% of their original value. Since the 2nd theta level is located at ~ 18 m, the released fluxes are underestimated, as only a small portion is entering into WRF. In addition, when doubling the z_{ext} parameter (10 m, Fig. #3.5c), the maximum height in which the fluxes from the fire reside is doubled (~ 823 m) and only $\sim 5\%$ is located above 750 m agl.

A linear behavior regarding the maximum injection height seems to follow the choice of the z_{ext} parameter, as a three times increase (Fig. 3.5d) results in approximately three times higher heights (~ 1240 m), with $\sim 62\%$ of the distribution lying below 500 m. The same behavior is depicted when z_{ext} is equal to five (Fig. 3.5e), fifteen (Fig. 3.5f) and twenty times (Fig. 3.5g) of the z_{ext} initial value ($z_{ext} = 5$ m). Differences appear only in the shape of the corresponding distributions, where the higher the z_{ext} value the more elongated the tail. Finally, in the ext200m sensitivity experiment (Fig. 3.5h), $\sim 52\%$ of the flux values are located in the first 1500 m above surface, while the fire fluxes are distributed almost up to the top of the computational domain, which clearly acts as an upper limit to them. If the aforementioned linear behavior applies also in this case, then the fluxes might be artificially distributed up to 16000 m.

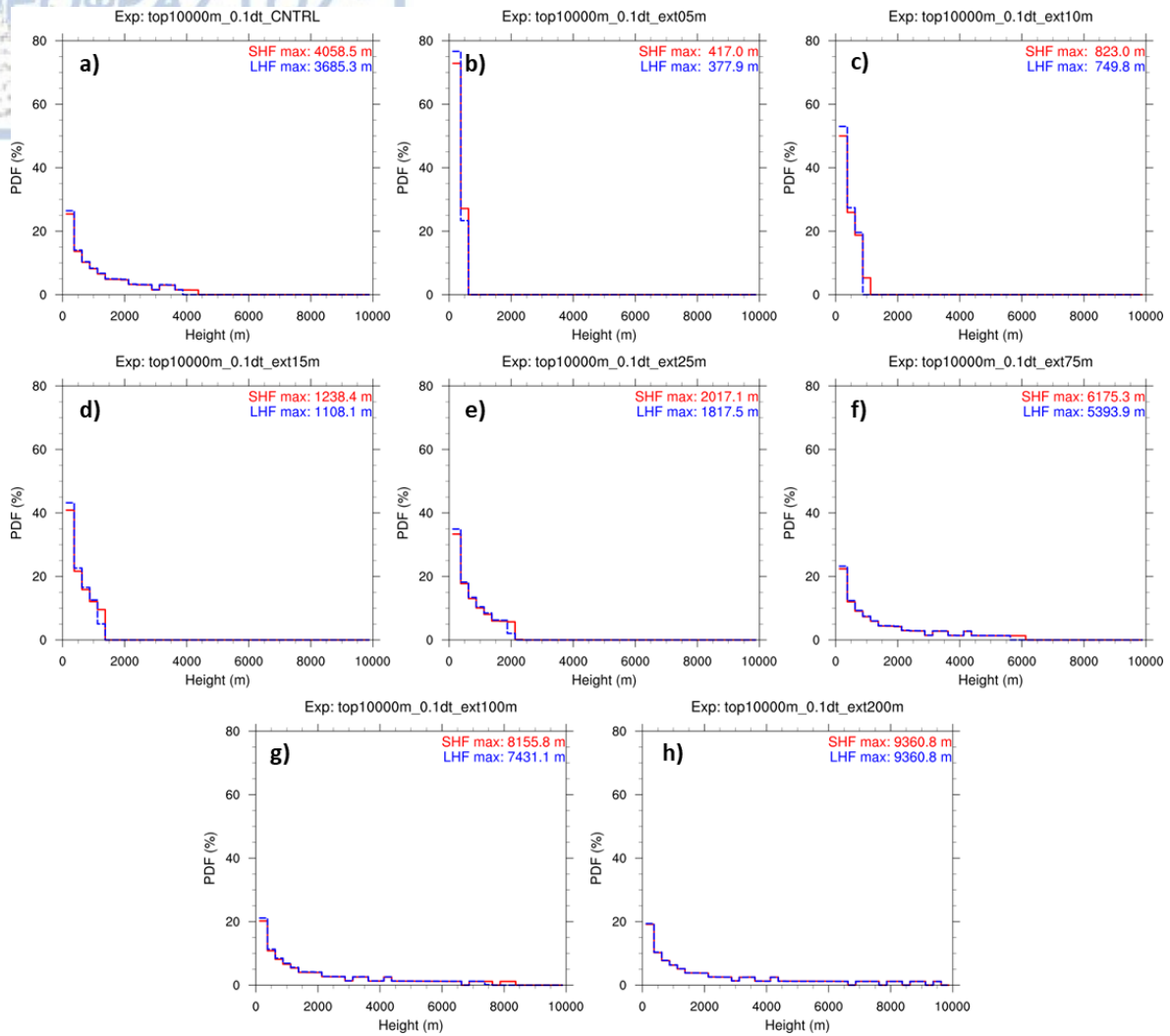


Fig. 3.5: Vertical distribution of the released sensible (red solid line) and latent (blue dashed line) heat fluxes from the fire as function of height for each experiment. The heights are calculated at all theta levels of the 3-D WRF domain with valid flux values (non-missing), within the 1st forecast hour since ignition. See text for further details.

Fig. 3.6 shows how the concept of exponential heat flux decrease (Eq. 3.1) within WRF domain affects the actual values of the released fire fluxes in vertical, as a function of z_{ext} parameter. As the quantitative comparison of the fluxes themselves was not desired, normalized values of the sensible heat fluxes were calculated and plotted against height. Each graph in the panel plot (Fig. 3.6), depicts values of the Eq. 2.5 rightmost term, at all grid points of the 3-D domain with valid data and at all available model output (every 5 min), while the different dot colors correspond to minutes since ignition.

According to Fig. 3.6a, in the CNTRL experiment, the highest sensible heat flux values are located in the first theta level and are recorded in the early beginning of the fire (black dots), approximately at 5 minutes after the fire ignition. Also, lower but significant values (cyan dots) stand out at 10 minutes and half-strength values (olive dots) are met at 30 minutes, related with temporal peaks of the surface heat fluxes (will be discussed later). The vertical profiling of the CNTRL fire fluxes displays a smoothly decreasing of their values, where the exponential fitting is evident. Moreover, the flux values at 1st theta level agree with ~89% of the surface flux values at each valid grid point (Fig 3.4). In addition, the

height of a single theta level is increasing as the corresponding flux value is increasing due to the buoyance response. The higher the theta level, the more pronounced the effect. With z_{ext} equal to 5 m (Fig. 3.6b), high heat flux values lie on the first theta level, with the highest value being recorded at 60 minutes since ignition. However, an abrupt decrease on their values is shown on the 2nd theta level, while very low flux values are located aloft. This feature is attributed to the fact that only $\sim 31\%$ of the released fluxes from the surface fire are inserted into the 1st theta level (5.8 m) and $\sim 3\%$ into the 2nd theta level (Fig. 3.4). Worth of noting is also the height variation of the 2nd theta level, during the period of analysis (1 hr).

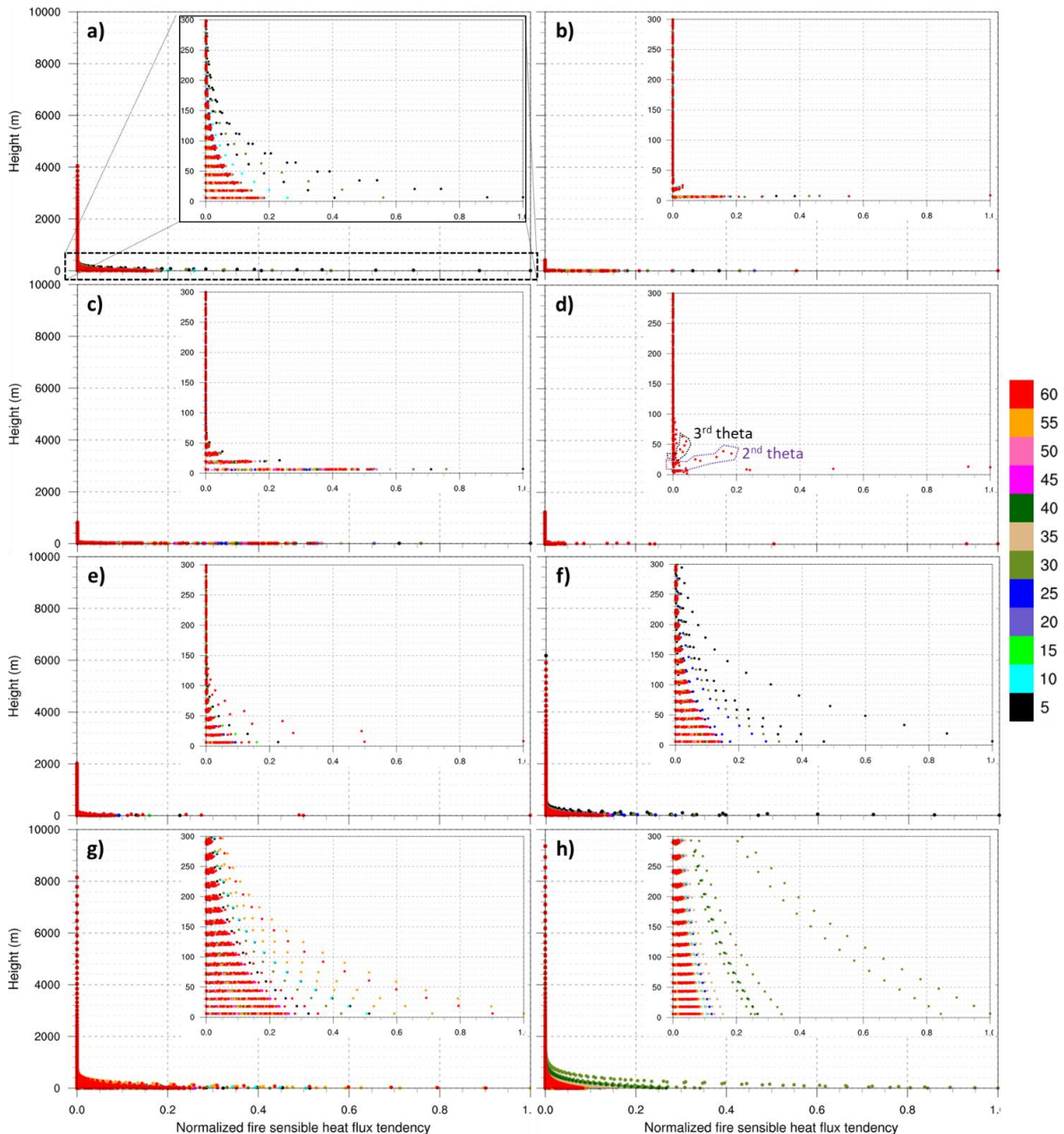
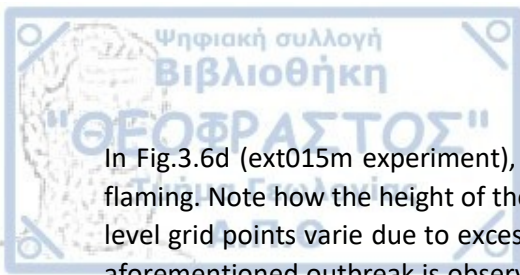


Fig. 3 6: Normalized sensible heat flux from surface fire as a function of height (theta levels) for a) CNTRL, b) ext005m, c) ext010m, d) ext015m, e) ext025m, f) ext075m, g) ext100m and h) ext200m experiments. In each plot in the panel, the area encompassed by the black dashed frame is shown enlarged for clarity. Different dot colors correspond to minutes since ignition ($T+5 - T+60$).



In Fig.3.6d (ext015m experiment), high heat flux values are dominating at 60 minutes after the fire flaming. Note how the height of the 2nd (purple dashed polygon) and 3rd (black dashed polygon) theta level grid points varie due to excessive local heating from the surface and the resulted updrafts. The aforementioned outbreak is observed only in this sensitivity simulation, albeit less intense outbreaks exist also in ext005m, ext025, ext100m and ext200m experiments. Moreover, intense heat fluxes have been produced and exponentially distributed in vertical, during the first 5 minutes of the fire in ext075m experiment, while in ext100m, high flux values are recorded mostly in the period between 30 and 60 minutes since ignition. For the ext200m simulation, high and moderate heat fluxes appear in two clusters at 30 minutes after fire initialization, where they exponentially decrease with height.

3.3.2 Impact of z_{ext} to pyric parameters

As an online-coupled atmosphere-fire model, the different energy budget above the ground fire must influence the modeled fire behavior in terms of predicted Rate of Spread (ROS), total burnt area, fire-line intensity and surface heat fluxes. Wind speed directly affects the spread model, while air temperature, relative humidity and precipitation modify the fuel moisture content, altering its flammability. In addition, for the interpretation of the results, some limitations of the Rothermel model (Rothermel, 1972) must be taken into consideration. The most important aspect is that the effects of wind and slope on the rate spread are based on fuel dependent coefficients, fitted at certain height (mid-flame wind speed), where wind speed calculations are performed if the fire was not there (Filippi et al., 2013, 2009).

3.3.2.1 Rate of Spread

In the box-and-whisker diagram (Fig. 3.7), the predicted ROS ($m s^{-1}$), greater than $0.06 m s^{-1}$, is presented for each model run. For the CNTRL simulation, the median (average) ROS is equal to $0.27 (0.37) m s^{-1}$, the interquartile range (IQR = $Q75 - Q25$) is $\sim 0.4 m s^{-1}$, while the maximum ROS is found to be $1.3 m s^{-1}$ (mild outlier, between the inner fence, $IF2 = 1.12 m s^{-1}$ and the outer fence, $OF2 = 1.71 m s^{-1}$). Kochanski et al. (2013c) found spread rates of $\sim 1.2 m s^{-1}$ at the early stages of the fire propagation in their simulations, while Mell et al. (2007) reported spread rates between 0.4 to $1.5 m s^{-1}$, as ambient winds were increased from 1 to $5 m s^{-1}$. In addition, Morvan (2011) presented various rate of spreads (his Fig. 6), as a function of $10 m$ wind speed, obtained from numerical simulations with different fully physical wildland fire models, which were ranging from ~ 0.1 to $6.4 m s^{-1}$. In Linn and Cunningham (2005), spread rates lied between 0.27 and $1.37 m s^{-1}$, as the ambient wind speeds were increased.

Worth of noting is the distinguished box-and-whisker plot of predicted ROS in ext015m sensitivity experiment, where the maximum produced ROS is equal to $5.97 m s^{-1}$. The median (average) ROS, the standard deviation and the interquartile range are $0.63 (1.54), 1.72$ and $2.59 m s^{-1}$, respectively. It must be mentioned that, the fire spread code has an upper limit in the predicted ROS, which is equal to $6 m s^{-1}$ and potentially acted as a “cap” to the numerical calculations. However, there are no outliers (mild or extreme), while the 95th quartile is equal $5.15 m s^{-1}$, declaring a fast forward fire front propagation in this experiment.

Although the interquartile range in ext075m run is the smallest (IQR = $0.25 m s^{-1}$) compared to all experiments, this simulation presents the second largest ROS maximum ($3.84 m s^{-1}$) and range ($3.77 m s^{-1}$). Note also the significant amount of outliers, which range from 0.73 to $1.1 m s^{-1}$ and 1.11 to $3.84 m s^{-1}$, for the mild (circles) and extreme (asterisks) ones, respectively. In addition, in the ext200m

sensitivity, the maximum ROS is equal to 2.24 m s^{-1} , while the outliers (mild and extremes) are related with values beyond 1.06 m s^{-1} . To conclude with, the choice of the z_{ext} parameter strongly influences the simulated ROS mostly due to variations in the near surface winds speed, which are produced by the online feedback between the fire and the ambient atmosphere. The descriptive statistics of the simulated ROS in each experiment are shown in Table 3.2.

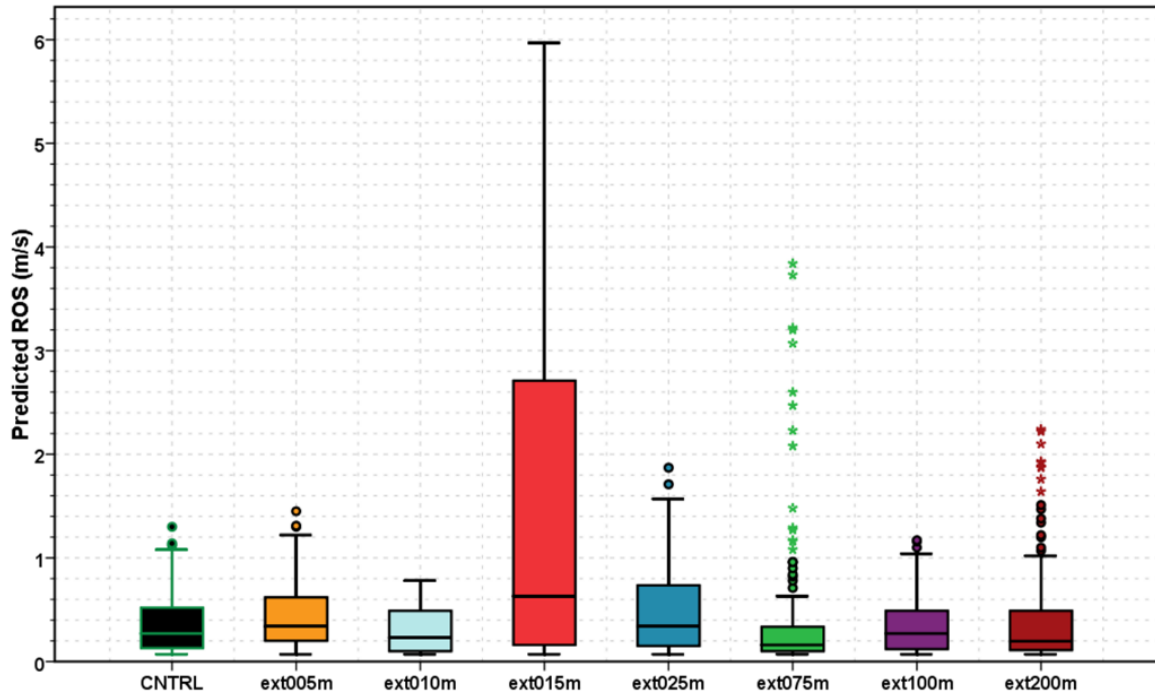


Fig. 3.7: Box-and-whisker plots of the predicted rate of spread (m s^{-1}) in each sensitivity experiment.

Table 3.2: Descriptive ROS statistics for each sensitivity experiment. The 95% confidence intervals were calculated using the bootstrap method (1000 samples).

	CNTRL	ext005m	ext010m	ext015m	ext025m	ext075m	ext100m	ext200m
Mean	0.373 ± 0.026	0.431 ± 0.023	0.292 ± 0.027	1.544 ± 0.132	0.491 ± 0.042	0.468 ± 0.070	0.331 ± 0.023	0.362 ± 0.025
Median	0.270	0.340	0.230	0.630	0.340	0.160	0.270	0.195
Mode	0.090	0.070	0.080	0.080	0.120	0.070	0.090	0.070
Std. Deviation	0.293	0.297	0.213	1.717	0.423	0.774	0.260	0.405
Variance	0.086	0.088	0.045	2.948	0.179	0.599	0.068	0.164
Skewness	1.114 ± 0.217	1.005 ± 0.192	0.712 ± 0.302	1.000 ± 0.187	1.178 ± 0.238	2.863 ± 0.218	1.262 ± 0.210	2.562 ± 0.150
Kurtosis	0.417 ± 0.430	0.678 ± 0.381	-0.773 ± 0.595	-0.251 ± 0.371	0.750 ± 0.472	7.932 ± 0.433	1.185 ± 0.417	7.249 ± 0.300
Range	1.230	1.380	0.710	5.900	1.800	3.770	1.100	2.170
Maximum	1.300	1.450	0.780	5.970	1.870	3.840	1.170	2.240
Percentiles								
	1	0.070	0.070	0.070	0.070	0.070	0.070	0.070
	5	0.080	0.080	0.070	0.080	0.080	0.070	0.070
	10	0.090	0.110	0.070	0.090	0.090	0.080	0.080
	25	0.130	0.200	0.100	0.150	0.140	0.115	0.110

	50	0.270	0.340	0.230	0.630	0.340	0.160	0.270	0.195
	75	0.525	0.620	0.490	2.740	0.740	0.350	0.500	0.490
	90	0.856	0.817	0.610	4.320	1.146	1.230	0.676	0.717
	95	1.002	1.008	0.684	5.145	1.368	2.574	0.911	1.322
	99	1.258	1.365		5.949	1.864	3.814	1.167	2.144

3.3.2.2 Fire area

The predicted ROS is correlated with the fire perimeter and controls the rate of growth of the burnt area. Large spread rates lead to faster growing burnt areas and thus to more intense fires. Fig. 3.8 depicts the fire area (ha) as a function of time, in each experiment. In addition, the first twenty minutes of the fire area time-series (30 to 50 minutes) are displayed enlarged in the graphic plot. At the very first minutes (30 to ~33 min) of the fire, the burnt area grows at the same rate in all experiments. From this point and in the next three minutes, deviations in growth rates start to occur, where in ext005m, ext010m, ext015m and ext025m sensitivity runs the burnt area increases almost equally and faster than in the other four experiments, where $z_{\text{ext}} \geq 50$ m. However, at nine minutes (39 min) since ignition, ext100m (magenta solid line) presents the largest growth rate and the largest burnt area (~1.2 ha), while at the same time period, the fire area in ext200m (purple solid line) seems to increase linearly and very slowly, hardly reaching 0.3 ha. Moreover, the ROS maxima in the ext100m sensitivity run are occurring during the aforementioned period (33 to 39 min).

At 50 minutes since model initialization (20 minutes from the fire ignition), the ext100m and ext200m simulations present the largest and the smallest burnt areas (~2.74 and 1.27 ha, respectively), the ext015m (red solid line) and ext075m (dark green solid line) model runs produce equal fire areas (~2.35 ha), while for the rest of the experiments, the burnt area lies between 2.13 to 2.22 ha. As the distribution of the released fire heat fluxes in vertical varies in each experiment, the feedback between the fire and the atmospheric column aloft is different, which in turn affects the wind field near the surface. This is evident in fire growth rates of the ext200m simulation, where the fire area increases from 1.27 ha, at 50 min, to 6.0 ha, at ~61 min, which corresponds to an average growth rate of 0.43 ha min^{-1} . Up to the end of the analysis, the ext200m's fire area expands almost linearly at a steady rate (0.4 ha min^{-1}).

During the second half of the analyzed period (60 to 90 min into the simulation), all the experiments except ext200m sensitivity run, produce approximately equal fire growth rates with temporal variations. However at around 90 min, an abrupt increase in ext015m's fire area is observed and is related with the production of high heat fluxes from the ground fire (as it will be discussed later), while a second but smoother growth is shown in ext005m (orange solid line) experiment. Finally, the burnt area after 1 hour from the onset of the fire was 14.2, 16.3, 15.1, 17.4, 14.8, 14.9, 15.8 and 18.0 ha for the CNTRL, ext005m, ext010m, ext015m, ext025m, ext075m, ext100m and ext200m experiments, respectively.

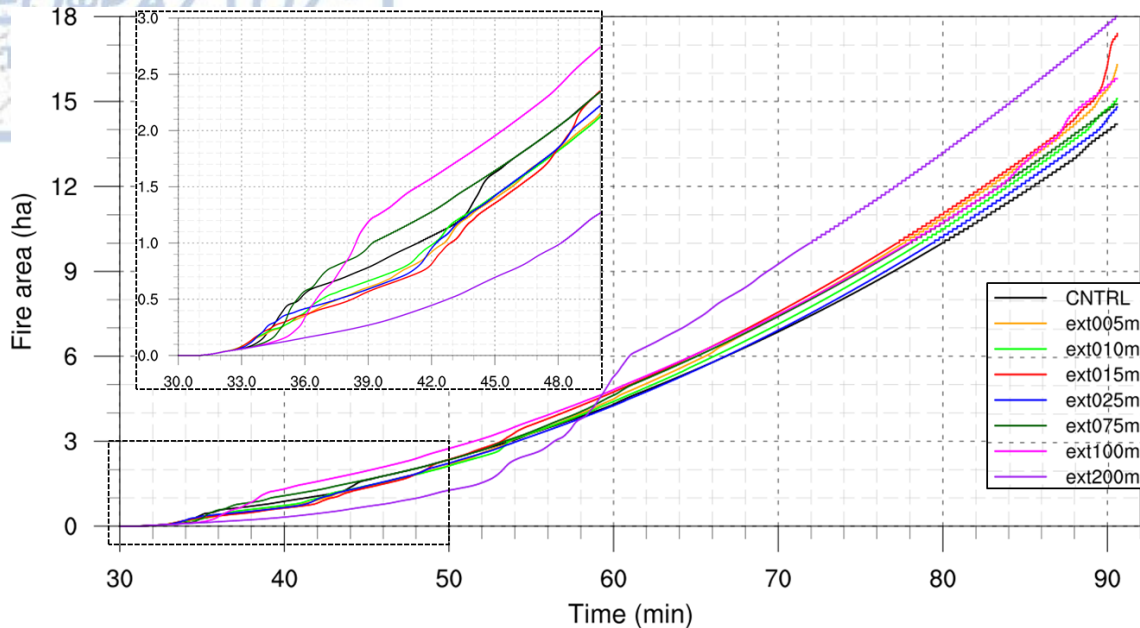


Fig. 3.8: Burnt area (ha) as a function of time (min) since model initialization in each sensitivity experiment. The first twenty minutes of the time-series are shown enlarged (encompassed by the black dashed boxes).

The effect of different z_{ext} values on fire spread and burnt area can be also illustrated by calculating the burn probabilities from the eight experiments. Fig. 3.9 depicts the resulting probabilities (%) at every fifteen minutes since fire ignition. Each color in the plots represents a burn probability equal to 12.5 %, which corresponds in a single experiment. Thus, the light blue color means that only one simulation burned that area, while the dark red color means that all experiments burned that area. Even though the sample of eight experiments is not large enough, as the central limit theorem dictates, Fig. 3.9 provides an insight on the uncertainty in fire propagation and burned area as the z_{ext} changes.

Fig. 3.9a shows that at 15 min since the initialization of the fire, the fire will propagate eastwards up to a certain point, but there is a 12.5% chance that it will spread on its flanks, towards north (light blue area). Here, the northwards propagation is produced in ext100m simulation. At 30 min since fire ignition, there is 100% probability that the fire will move towards east-southeast, up to 150 m (in west-east direction) from the ignition point (1850 m in west-east direction, from the west boundary of the domain). At the same time, there is 50 % chance that the fire will spread further towards southeast, while there is 12.5% chance that the fire will spread faster towards southeast, until ~ 2200 m in west-east direction (350 m from ignition point). The faster spread rates are presented in ext200m experiment, as it is shown in Fig. 3.8. After fifteen minutes (Fig. 3.9c), it is evident that the fire will spread on its flank and on its backside, growing almost proportionally. The east-southeast propagation is maintained (dark red area), but there is also a chance, equal to 12.5 %, that the burned area obtains an elongated shape moving further eastwards (light blue; due to ext200m simulation). At 90 min into the simulations (Fig. 3.9d), the fire will continue to grow in all directions (albeit with no equal spread rates), whilst the northeast flank will become the most active fire front. Six out of eight simulations (75% probability) present a northeast fire propagation, while there is a 12.5 % chance of an abrupt increase in spread rates along the northeast flank (due to ext015m contribution).

Since only the first hour from the fire initialization is analyzed and discussed, up to this point for all experiments, the discrepancies in space are not very large. However, significant larger deviations exist beyond the first hour, for example at one at half hour (1.5 hr) since fire ignition. According to Fig. 3.10a,

the burn probability from the five model runs (CNTRL, ext025m, ext075m, ext100m and ext200m) that reached up to this time, shows that there is 20% possibility of a northwestwards spread, which produces approximately a doubled area (light blue), in comparison to the commonly burnt area in all five experiments. The aforementioned area is predicted in the ext025m simulation.

Fig. 3.10b depicts the calculated burn probabilities at simulations' forecast horizon (2.5 hr since model initialization), where only four out of eight experiments (CNTRL, ext075m, ext100m and ext200m) reached the target time. Note the different sub-domain extent in y direction, compared to Fig. 3.10a. Here, a clearly northward-burnt area expansion (25% chance) is shown, due to the ext200m run contribution. Nevertheless, the fire area in the remaining member is very similar and there is 100% possibility that the fire will burn an almost elliptical area after 1.5 hour (dark red area).

Although the meteorological forcing in all experiments is identical, the produced deviations in fire spread rates and burnt area are attributed to the different available energy budget in the atmospheric column above the surface fire. As a result, the fire-induced winds, produced by the atmosphere-fire interactions, are responsible for the presented variability, verifying that the WRF-SFIRE is capable of reproducing such processes, albeit they are affected by the z_{ext} parameter. In full sample plots (Fig. 3.9), the 12.5% probability range shows the possible margin error for the non-coupled operational fire spread models that do not take into account the feedback between atmosphere and fire. For smaller samples (Fig. 3.10), the margin error is higher. Thus, probabilistic fire predictions may be required in order to evaluate the predicted fire behavior. In an analogous statement ended up Kochanski et al. (2013c), who in their study pointed out the importance of a range of predictions for the future fire behavior and its spread, as different ambient wind shears led to a range of fire spread rates and burnt areas.

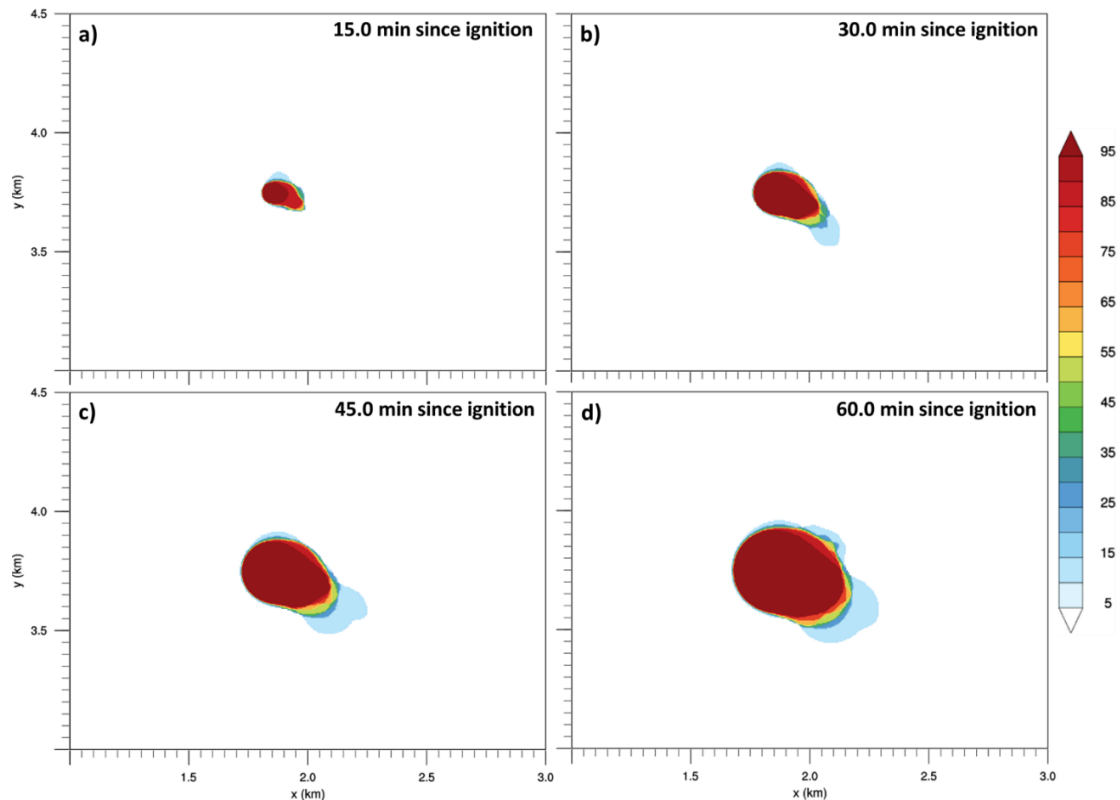


Fig. 3.9: Burn probabilities (%) based on the eight sensitivity simulations at a) 15 min, b) 30 min, c) 45 min and d) 60 min since fire ignition. A sub-area of the entire domain is illustrated for visualization purposes.

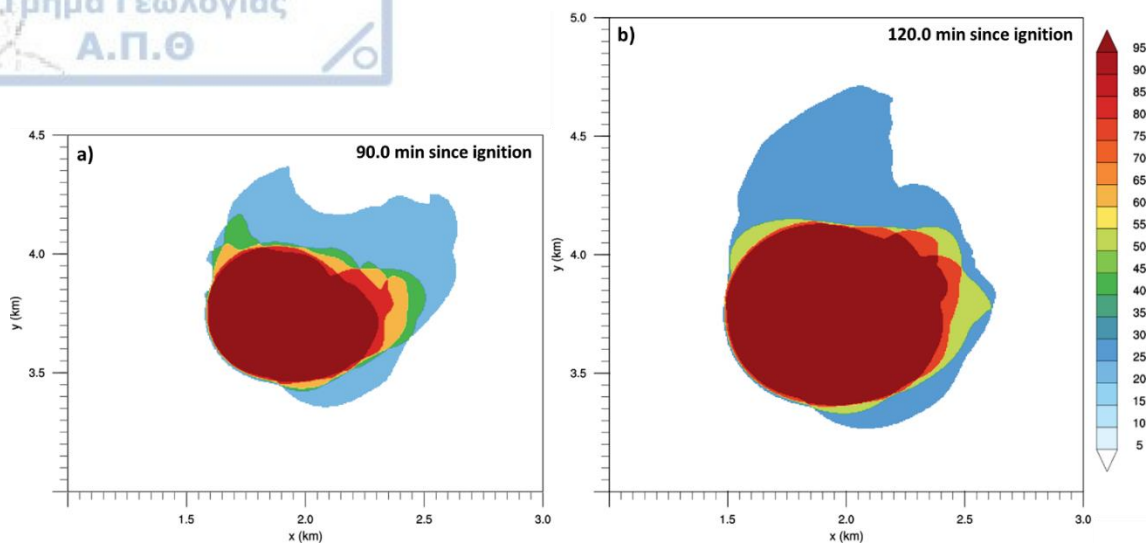


Fig. 3.10: Burn probabilities (%) based on a) five out of eight experiments (CNTRL, ext025m, ext075m, ext100m and ext200m), at 90 min since ignition and b) four out of eight experiments (CNTRL, ext075m, ext100m and ext200m), at 120 min since ignition. Note the different sub-domain extent in y direction, compared to the left plot.

3.3.2.3 Fire heat release rate at surface

The rate of spread and the growth rate of the fire area are driven by the fire heat release rates, in every integration step of the WRF-SFIRE modelling system. Fig. 3.11 displays the instantaneous combined sensible and latent heat release rate on the 2-D fire grid mesh, at 0.1 s intervals, in each experiment. The parameterization of the combustion in SIFIRE model dictates that the so called “power of the fire” is increasing when there is sufficient fuel ignition to replace the mass loss of the previously ignited fuel. According to Fig. 3.11, in the CNTRL experiment, the maximum fire heat output lies below 7,600 MW and it is produced at the end of the analyzed period. Although there are temporal peaks, mostly at the first 15 minutes since fire ignition, the CNTRL fire heat output is gradually increasing as more and more fire grid cells are being ignited, a feature that is observed almost in each experiment. The aforementioned peaks are responsible for the temporal increase in the fire area growth rate (Fig. #, enlarged frame, black solid line), at ~34 min and ~44 min since model initialization, respectively.

In ext005m sensitivity run, the largest heat release rates (> 7,000 MW) are met at the very end of the analyzed period (~90 min into the simulation) with a maximum of ~33,000 MW, which result to faster fire spread and higher fire area growth rates, as it is depicted in Fig. 3.8 (purple solid line). In addition, the ext010m and ext025m simulations produce the highest heat output at approximately 60 min since fire ignition, but their values are below 11,000 MW and 9,800 MW, respectively. Also, the temporal peak at ~53 minutes into the simulation, in ext010m run, is responsible for the short temporal increase in the fire area growth rate, in Fig. 3.8 (green solid line). The most erratic fire behavior occurs in ext015m sensitivity run, where the maximum heat output is located between 89 and 90 min since model initialization and is equal to ~41,000 MW, almost four times higher than the corresponding maxima in the ext010m and ext025m simulations. The response to this amount of released energy is the abrupt increase in the fire spread rate and subsequently to the fire area growth rate (Fig. 3.8, red solid line), which resulted to a southeastwards fire expansion (Fig. 3.9d).

In ext100m and ext200m sensitivities, the maximum heat output is ~14,200 MW and ~13,100 MW, respectively. Despite their proximity, they occur in different time frames, resulting in different responses into the fire rate-of-spread. In ext200m model run, heat release rates higher than 8,000 MW are produced for approximately three minutes (between ~59 to ~61 min since initialization), while the corresponding period in ext100m is only one minute. Thus, the increased burnt area growth rate of the ext200m run, in Fig. 3.8 (purple solid line) is linked to the large amount of sensible and latent heat release, between 51 and 60 min into the simulation.

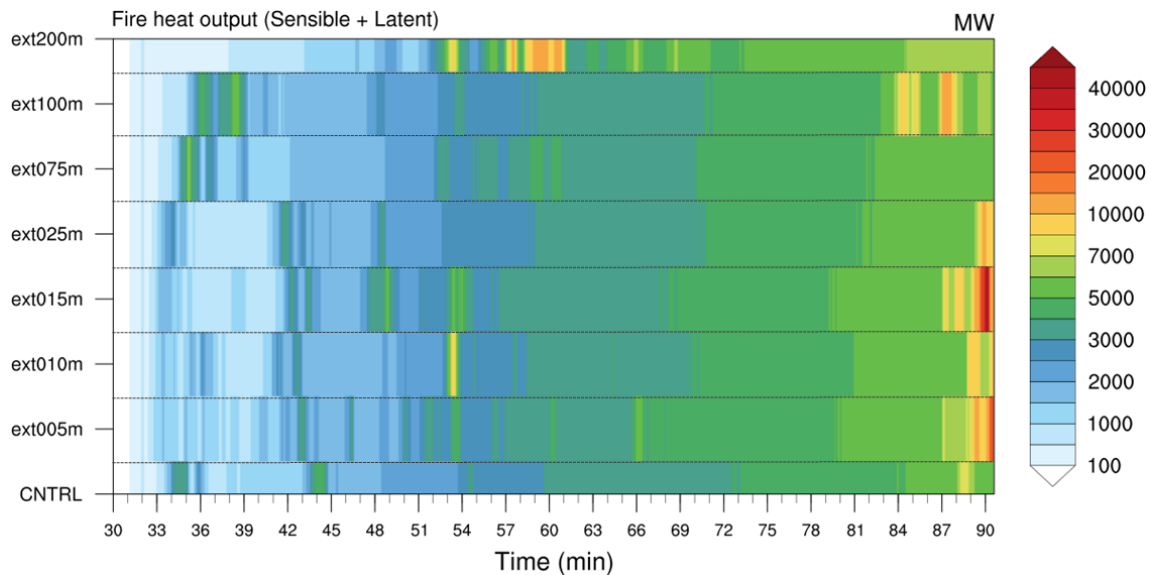


Fig. 3.11: Combined sensible and latent heat release rate (MW) from the 2-D SFIRE model, in each experiment.

3.3.3 Impact of z_{ext} to atmosphere/plume properties

3.3.3.1 Airflow characteristics

According to the conceptual illustration of airflow in and around a developed fire front, as it presented in Potter (2012b) and discussed in Chapter 1 (section 1.1) of this manuscript, a descending rear inflow feeds the fire with fresh air and additional oxygen, the surface inflow at the flanks creates convergence ahead and additional downward motions, whilst buoyancy produces strong updrafts and turbulence aloft.

In Fig. 3.12, flow lines at 60 min since ignition from the CNTRL experiment are illustrated, at different points of view. The upper limit in Fig. 3.12's plots is placed around 2 km. The construction of the flow visualization was carried out in VAPOR (Visualization and Analysis Platform for Research, v.2.6.0; Clyne et al., 2007), while a major update in the software took place in 2019 (Li et al., 2019). VAPOR performs a numerical integration of the 3-D wind field in a specified volume, where the integration starts at "seed points" and tracks the successive positions in the volume. The establishment of the seed points can be done by three different ways and by choosing a flow type. Here, the "steady" flow type was chosen, which means that the vector field does not change during the flow integration.

Fig. 3.12 presents some common flow characteristics from the literature and introduces new features as well. At surface, the convergence regime ahead of the fire is evident, as streamlines converge downwind of the fire-front. Moreover, the descending rear inflow observed by Banta et al. (1992) and Palmer (1981) and illustrated by Potter (2012b) in his Fig. 6, is demonstrated clearly in Fig. 3.12a,d.

Although it is not shown, a closer examination of the rear inflow lines revealed that the flow starts to descend approximately from the bottom of the inversion (~1500 m) layer and during its descent splits in two parts. The first one reaches close to the ground and enters into the active fire-front from behind, while the second one creates and sustains the clockwise longitudinal vortex above the left flank of the fire area (Fig. 3.12d). The right horizontal vortex (Fig. 3.12c,d) is rotated clockwise as well and it is not related with the descending rear inflow. However, it causes strong downward motions at the area to the right of the fire, where the descending air converges in front of the combustion zone. In addition, these vortices are persistent and are not a transient feature, whilst their intensification occurs at the late stages of the fire.

It must be mentioned that the previously presented horizontal vortices must not be confused with the counter rotating horizontal vortex pair presented in Haines and Smith (1987), in which the boundary layer vorticity causes rollup of the vortex tubes and subsequently plume bifurcation. Both vortices rotate clockwise and originate outside and upwind of the fire plume, near the left boundary of the domain. Moreover, the left horizontal vortex acts as inflow to the front of the half upper part of the fire plume, while the flow from the right horizontal vortex interacts mostly with the surface (see in Appendix II, Figs. B.1 and B.2). In addition, smaller but transient horizontal vortices are located to the left and above the main left vortex, near the boundaries. Although it is beyond the scope of this manuscript and may be addressed more properly in a future study, the presence of the fire plume must play important role to the dynamical characteristics of these vortices and how they interact with the near surface flow and plume dynamics. A possible mechanism is the reorientation of the shear-generated horizontal vorticity in the ambient atmosphere due to the presence of fire plume and the convergence that occurs in vertical. Other contributing factors can be the stability profile of the atmosphere, the wind vertical profile or even the presence of the inversion layer aloft.

The ascending updraft is vertically tilted (Fig. 3.12b) by the weak wind shear and the streamlines easily reach and even penetrate into the inversion layer. Entrainment of ambient air into the fire plume is observed mostly upwind of the main updraft and directly behind it, at all heights (see in Appendix II, Fig. B.3), but there is also a region of descending air from above and to the right (> 2 km), that enters into the upper portion of the fire plume. Clements (2010), by constructing the vertical profiles of rate of heat gain from high frequency thermocouple measurements, found a region of strong cooling (approximately -37 and -44 kW m⁻²) between 10 and 15 m above the ground, due to the strong entrainment that occurred behind the fire front and plume. As it is pointed in Potter (2012b), the heights at which entrainment occurs at various rates need further investigation and only field measurements can contribute positively to this question.

All the above depict the complexity and non-linearity of the interactions between a surface fire and the atmospheric flow. Given the uncertainty that is introduced by several assumptions in the model input data and parametrization schemes, analysis and interpretation of the results must be carefully performed. The next sub-sections try to shed some light upon the basic key parameters that are being affected by the tuning of the fire-released energy into the atmosphere, as it is controlled by the model's z_{ext} parameter.

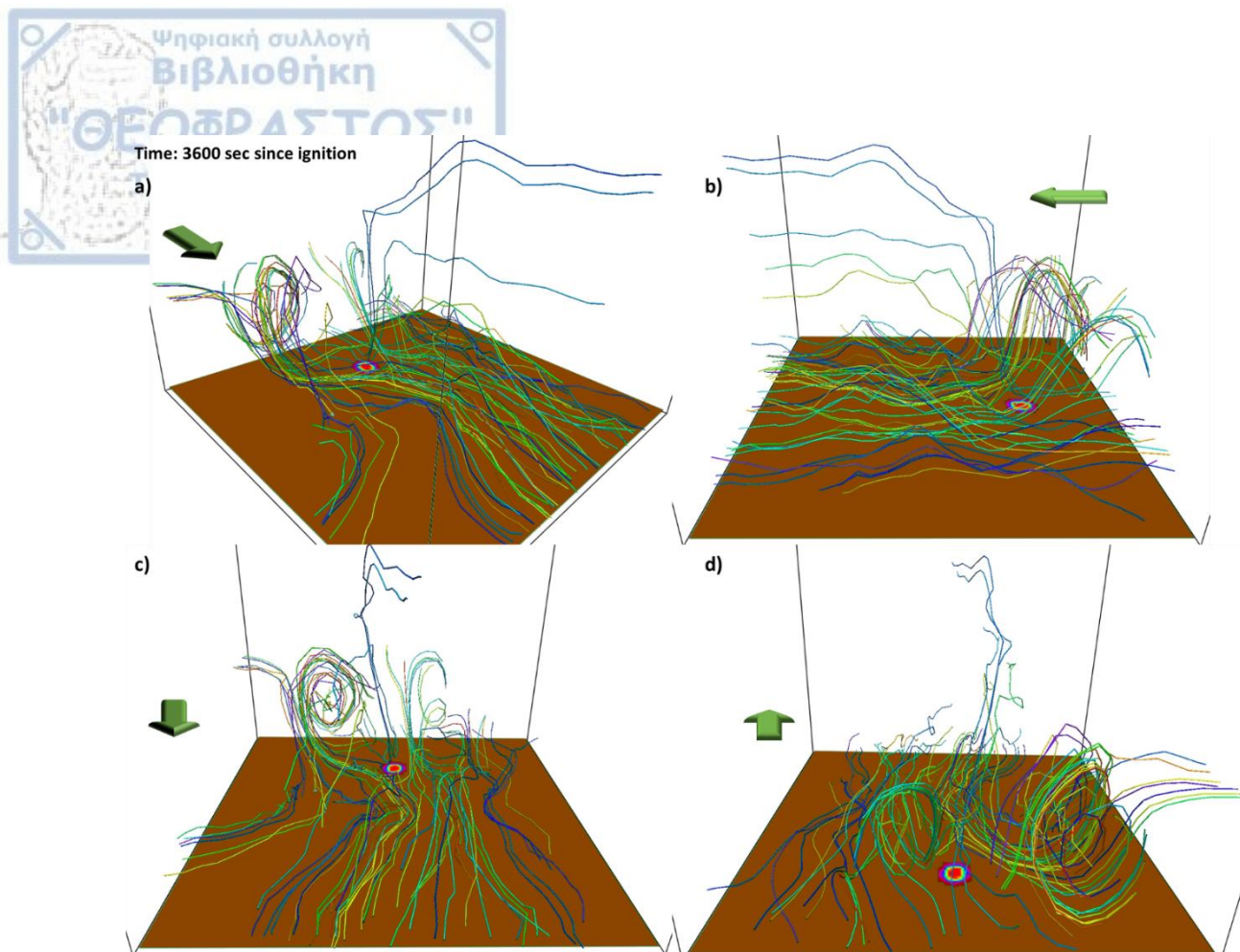


Fig. 3.12. Streamlines at 60 min since ignition, for the CNTRL experiment at different points of view. At surface, the fire area is shown with different colors according to the remaining fuel. The brown color corresponds to unignited fuel. The green arrow indicates the ambient wind (westerlies). Created in VAPOR using 60 random seeds (flow type steady).

3.3.3.2 Vertical velocities

The energy released from the fire, as sensible and vapor heat fluxes, results in heating and moistening of the air above. As the heated and lighter air parcels ascent due to buoyancy and pressure gradients, an endless cycle of upward and downward motions occur. Under certain conditions, the vertical velocity induced by fire can easily reach tornado strength values. The IR video imagery analysis (Coen et al., 2004) during the FROSTFIRE experiment revealed instantaneous upward velocities of 60 m s^{-1} and downward velocities of 30 m s^{-1} . During the field validation experiment FireFlux (Clements et al., 2007), the recorded updrafts and downdrafts reached speeds of nearly 5 m s^{-1} . A couple of decades earlier, Countryman (1969) analyzed the obtained data from Project Flambeau (Bush et al., 1969), where in his figures the maximum recorded updraft velocity was 7.3 m s^{-1} (his Fig. 37), whilst the maximum recorded downdraft exceeded 30 m s^{-1} (his Fig. 40). Moreover, Banta et al. (1992) estimated maximum vertical velocities of 15 m s^{-1} , by utilizing both Doppler radar and lidar equipment. All the above measurements, albeit they were performed under very different situations (both in environmental and technological terms) set the basis for the analysis and evaluation of any atmosphere-fire model results.

Fig. 3.13 and Fig. 3.14 depict the maximum updraft (left column) and downdraft (left column) over time and model level, for CNTRL (Fig. 3.13a, b), ext005m (Fig. 3.13c, d), ext010m (Fig. 3.13e, f) and ext015m (Fig. 3.13g, h), ext025m (Fig. 3.14a, b), ext075m (Fig. 3.14c, d), ext100m (Fig. 3.14e, f) and ext200m (Fig. 3.14g, h) experiments. In addition, the attached scatter plots in each subplot depict

upward vertical velocities greater than 4 m s^{-1} (red dots) and downward motions greater than 2 m s^{-1} (blue dots) as a function of height, during the first hour since fire ignition. According to Fig. 3.13a, the maximum updraft velocity in CNTRL experiment exceeds 26 m s^{-1} and it is recorded at $\sim 900 \text{ m agl}$, at 15 min since ignition. Moreover, values greater than 20 m s^{-1} are concentrated in a limited spatial area, which corresponds to the early stages of the fire. In vertical, strong updrafts ($> 20 \text{ m s}^{-1}$) are met between ~ 600 to 1200 m agl , while a second local maximum of vertical velocities, between 15 and 20 m s^{-1} , lies in a layer from ~ 1400 to $\sim 1800 \text{ m agl}$. An analogous vertical distribution of upward velocities was presented in (Reid and Vines, 1972) where their radar based analysis of the smoke puffs revealed higher velocities around 2 km , then decreasing up to the plume top.

The strongest simulated downdraft is 6.7 m s^{-1} (Fig. 3.13b) and it is observed at the base of the inversion layer ($\sim 1985 \text{ m}$), at 50 min since ignition. Fig. 3.13b also suggests that the strongest downdrafts ($> 5 \text{ m s}^{-1}$) are located around the fire plume, whilst a line of moderate downward velocities is displayed downwind of the fire. This feature is associated with the horizontal advection and intensification of the prior existed turbulent eddies, during the early stages of the fire. Specifically, the aforementioned line is simulated at 45 min into the simulation, at all experiments, and a possible explanation of this feature might be the additional kinetic energy that is added into the computational domain due to the surface fire and the generated fire plume dynamics. Moreover, the downward velocity regimes upwind of the fire area are associated with the horizontal vortices discussed in the previous sub-section (3.3.3.1), a feature that is persistent in all experiments and is illustrated in Fig. 3.13a,b,c,d,e,f,g,h and Fig. 3.14a,b,c,d,e,f,g,h, respectively.

Although the maximum upward vertical velocity in ext005m sensitivity run (Fig. 3.13c) is almost equal to the CNTRL's value (26.1 m s^{-1}), it is observed lower, at $\sim 576 \text{ m agl}$. In general, ext005m run produces more intense updrafts, with greater spatial expand and with multiple local maxima during the analyzed period, indicating transient and localized extreme vertical motions, in response to temporal peaks in fire heat output (Fig. 3.11). Moreover, stronger downdrafts than in CNTRL experiment are simulated in this model run (Fig. 3.13d), where the maximum downward vertical speed is 7.3 m s^{-1} and is located downwind of the fire, at $\sim 1882 \text{ m agl}$ (at 50 min since fire initialization).

In ex010m sensitivity, the higher vertical velocities are seen (Fig. 3.13e) mostly at the center of the fire area and slightly to its western (back) portion, showing that strong updrafts dominate at the early minutes of the fire rather than later. The maximum vertical velocity is equal to 24.2 m s^{-1} , is located at $\sim 1283 \text{ m agl}$ and is observed at 25 min since fire ignition. Another feature worth of noting is that the regime of strong updrafts ($> 20 \text{ m s}^{-1}$) is observed higher and in a $\sim 200 \text{ m}$ deep layer, located at $\sim 1200 \text{ m agl}$. Regarding the downward motions, two regions of high downward vertical velocities are illustrated (Fig. 3.13f), one at the left (north) and one at the right (south) flank of the fire perimeter, respectively. The spatial pattern of the downdrafts seems to encompass the updrafts area (Fig. 3.13e), where higher downward speeds ($> 6 \text{ m s}^{-1}$, orange shaded contours) are produced at the northern region, but they are more localized than at the southern area.

The sensitivity run ext015m presents the most interesting results regarding the simulated vertical motions and their corresponding magnitude. According to Fig. 3.13g, strong updrafts with values greater than 20 m s^{-1} (red shaded contours) exist in several atmospheric grid cells above the western portion of the burnt area, whilst their vertical distribution deviates clearly from the CNTRL's experiment and the actual measurements in Reid and Vines (1972). The attached scatterplot in Fig. 3.13g shows that the highest vertical velocities are produced close to the ground, where values greater than 20 m s^{-1} are met up to 400 m agl and in a layer between 1000 m and 1600 m above surface. The maximum updraft velocity is found equal to 34.3 m s^{-1} (not shown in Fig. 3.13g attached scatter plot), on $\sim 120 \text{ m agl}$, at 60 min since ignition and it is associated with the release of very high heat fluxes

during that time window (Fig. 3.11) and the responsive high fire area growth rates (Fig. 3.8, red solid line).

The aforementioned characteristics correspond to a common term in fire literature known as “blow-up fire”. The first introduction of the term was done by Byram (1954), who described a blow-up fire as a fire “which suddenly and often unexpectedly multiplies its rate of energy output many times”. In his review article, Potter (2012) states that according to the Glossary of Wildland Fire Terminology, a blow-up fire is defined as “the sudden increase in fireline intensity or rate of spread of a fire ... often accompanied by violent convection and may have other characteristics of a fire storm”.

The conservation of mass and momentum in WRF equations dictates that another air parcel must replenish this violent upward vertical motion of the air. Subsequently, the maximum downdraft velocity is found equal to 11.4 m s^{-1} , on $\sim 43 \text{ m}$ agl and at 60 min since ignition, as it is depicted in Fig. 3.13h (dark red dot at $\sim 2 \text{ km}$ east and $\sim 4 \text{ km}$ north of the bottom-left domain corner) and in the attached scatterplot. Note that the atmospheric grid cells with the maximum updraft and downdraft speeds are located at neighboring cells. Moreover, significant downward velocities with values greater than 7 m s^{-1} are observed mostly southeast of the fire area, while in vertical, the downdrafts present their maxima at around 2 km. Finally yet importantly, strong upwards motions ($> 4 \text{ m s}^{-1}$) reach up to 3 km agl, higher than in any other experiment, as a result of the aforementioned “blow-up”.

In ext025m model run, strong upward motions ($> 16 \text{ m s}^{-1}$) dominate all over the surface fire (Fig. 3.14a), with temporal peaks greater than 18 m s^{-1} located above the western portion of the burnt area. The maximum updraft velocity is equal to 20.8 m s^{-1} , on $\sim 960 \text{ m}$ agl, whilst it is predicted at 85 min into the simulation (55 min since flaming of the fire). In vertical, upward motions greater than 18 m s^{-1} are observed almost at all model levels up to 1600 m agl, a feature that is only met in this sensitivity run. Moreover, a cluster of increased vertical velocities close to the ground (up to $\sim 200 \text{ m}$ agl), with a peak of approximately same magnitude ($\sim 19 \text{ m s}^{-1}$) as the maximum vertical speed, stands out in Fig. 3.14a scatterplot, and are related with the temporal peak in fire heat output during the first 8 minutes since fire ignition (Fig. 3.11). The maximum downdraft velocity in this sensitivity is 7.8 m s^{-1} and is located at $\sim 1882 \text{ m}$ agl (at 60 min since fire ignition). Apart from the main area with downward velocities greater than 6 m s^{-1} , also localized downdrafts are shown to the south (Fig. 3.14b).

The maximum upward velocity in the ext075m sensitivity (Fig. 3.14c) is equal to 20.7 m s^{-1} and is found at $\sim 800 \text{ m}$ agl, at 45 min after the fire ignited. The vertical distribution of the updraft velocities is similar to the CNTRL’s one, albeit the region with the highest velocities presents lower values than in the CNTRL experiment. Moreover, an extended area of intense downward motions is depicted downwind of the updrafts area (Fig. 3.14d), with a peaking value of 7.5 m s^{-1} , at $\sim 2093 \text{ m}$ above surface.

In ext100m model run, two regimes of intense upward motions (Fig. 3.14e) are illustrated, which correspond into two different periods into the simulation. The northern region is related with the temporal peak in fire output at the early stages of the fire (during the first 10 minutes), while the southern regime is the response to the high heat release rates at the last 5 minutes of the analyzed period (55 – 60 min since fire flaming). The above two maxima are clearly shown in the vertical distribution of the upward velocities (Fig. 3.14e scatterplot), where the lower local maximum (in terms of height) is linked with the southern region and the other one with the northern area, in which the maximum upward velocity (22.6 m s^{-1} , at $\sim 1144 \text{ m}$ agl, at 10 min since ignition) is predicted. Moreover, the maximum downward velocity is equal to 7.3 m s^{-1} and is simulated at the height of $\sim 1882 \text{ m}$ above surface, at 75 min into the simulation.

"Blow-up" conditions are predicted also in the ext200m sensitivity, where according to Fig. 3.11, high heat release rates from the surface fire, between 23 min and 32 min after the fire ignited, result in high ROS (the outliers in Fig. 3.7) and subsequently, high fire area growth rates (Fig. 3.8, purple solid line). The response of the atmosphere to the released energy is translated into strong updrafts (Fig. 3.14g), which are located just ahead and above of the fire-front, as the ambient shear wind tilt the fire plume in vertical. According to Fig. 3.14g, there is a region of intense upward motions, with speeds greater than 20 m s^{-1} , where inside lies the maximum value of 29.8 m s^{-1} , on $\sim 1018 \text{ m}$ above surface. The maximum updraft velocity is recorded at 30 min since fire ignition, whilst the vertical examination of the updraft velocities (Fig. 3.14g scatterplot) reveal a deep layer of $\sim 800 \text{ m}$ depth, where the upward speeds are greater than 20 m s^{-1} . Worth of noting are also a) the cluster of high updrafts close to ground and b) the deviation of a number of grid points from the mean model height, a feature that is clearly presented only in this sensitivity. Both features are associated with the intense heating from the surface, which was described earlier. In addition, high downward velocities exist downwind of the updrafts area, where the highest velocities are observed (Fig. 3.14h). The peak value is equal to 8.9 m s^{-1} , the highest among the experiments, it is observed at 80 min into the simulation and on $\sim 1985 \text{ m}$ above surface. Moreover, downward velocities, greater than 2 m s^{-1} , extend up to $\sim 3 \text{ km}$ as in the CNRTL experiment, however they present much higher values in the layer above 2 km .

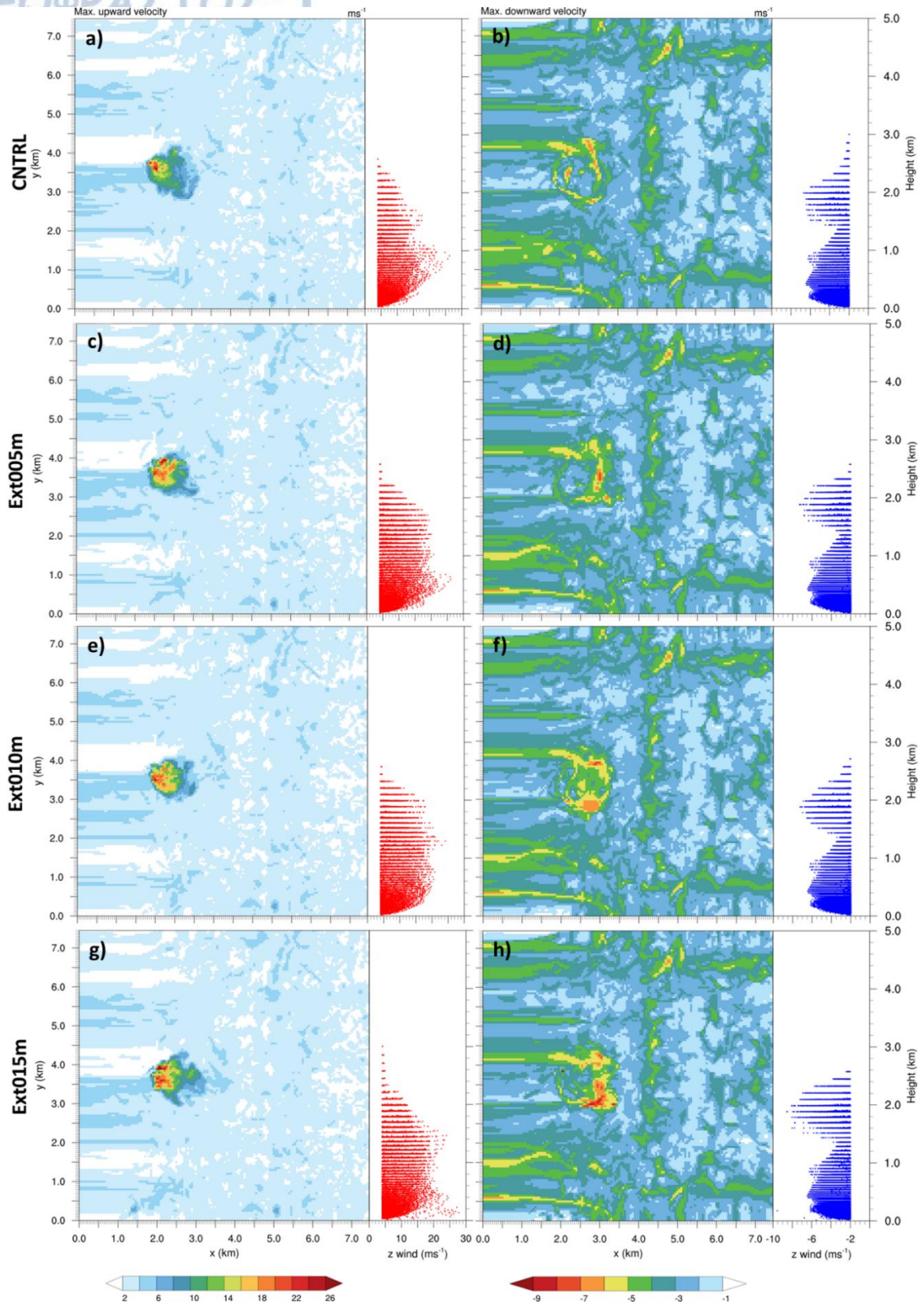


Fig. 3.13: Maximum updraft (left column) and downdraft (left column) velocity ($m s^{-1}$, shaded contours) over time and model level, for CNTRL (a, b), ext005m (c, d), ext010m (e, f) and ext015m (g, h) experiments. The attached scatter plots depict vertical velocities greater than $4 m s^{-1}$ (red dots) and less than $-2 m s^{-1}$ (blue dots) as a function of height, during the first hour since fire ignition.

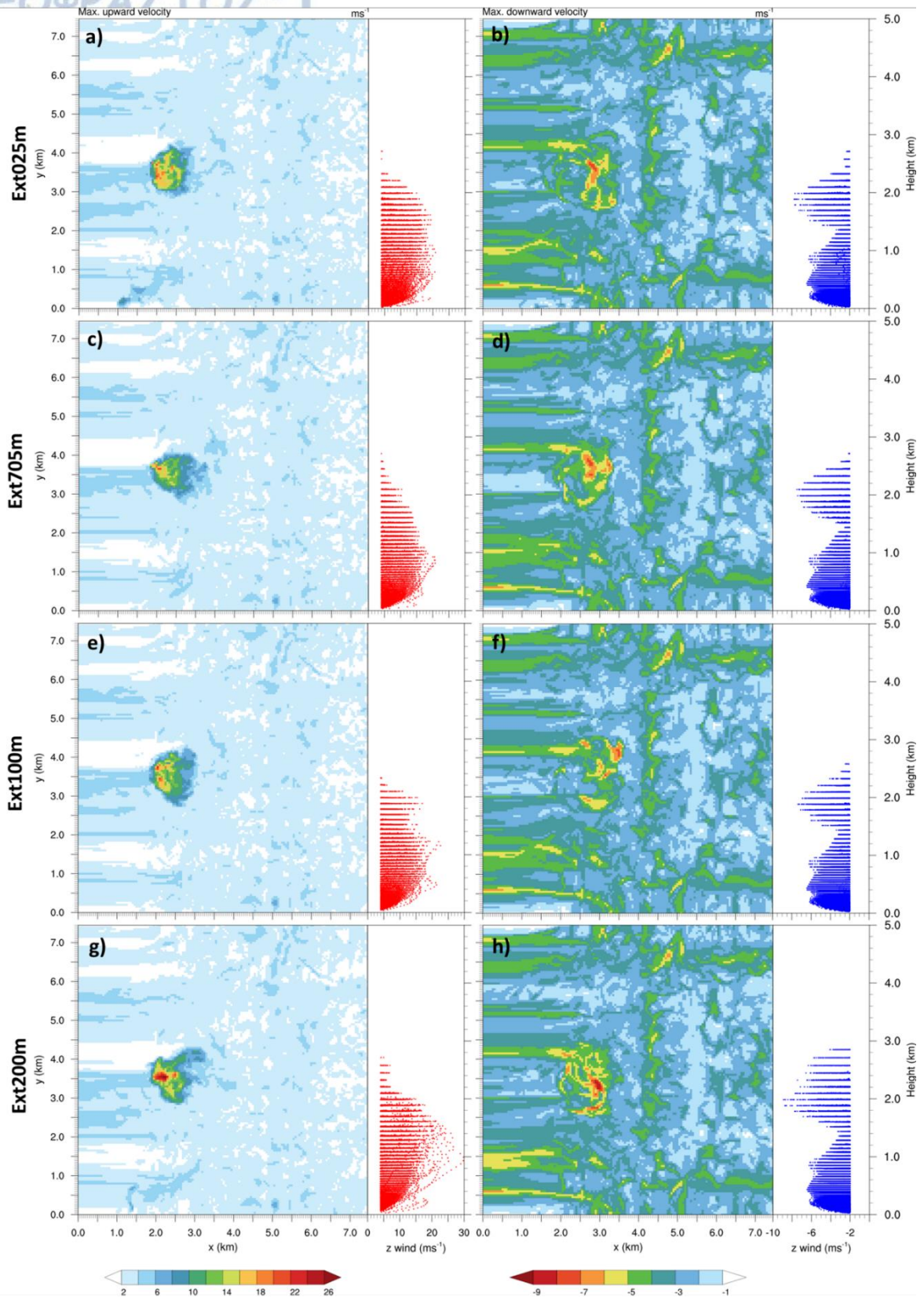


Fig. 3.14: As in Fig. 3.13, except for ext025m (a, b), ext075m (c, d), ext100m (e, f) and ext200m (g, h) experiments.

3.3.3.2.1 Vertical velocities and airflow features at 90 min

Fig. 3.15 and Fig. 3.16 display the direct volume rendering (DVR) of vertical wind component (m s^{-1}), airflow (streamlines), vertical cross section of water vapor mixing ratio (kg kg^{-1}) along x axis and potential temperature (K) vertical cross section along y axis, for CNTRL (Fig. 3.15a), ext005m (Fig. 3.15b), ext010m (Fig. 3.15c), ext015m (Fig. 3.15d), ext025m (Fig. 3.16a), ext075m (Fig. 3.16b), ext100m (Fig. 3.16d) and ext200m (Fig. 3.16d) experiments, at 60 min since fire ignition. For the DVR z-wind field, upward motions greater than 5 m s^{-1} (green shading) and downward motions greater than 3 m s^{-1} (blue shading) are illustrated, while the streamlines are colored based on vertical velocity values. At surface, the fire heat fluxes on the atmospheric grid cells are also depicted. The top of the depicted domain is located at $\sim 3500 \text{ m}$ above surface.

According to Fig. 3.15a, updraft velocities greater than 5 m s^{-1} are simulated from the surface up to the inversion layer, with multiple updraft cores. The main updraft is slightly tilted due to the wind shear profile and resides over the right flank of the fire area, narrowing close to the ground and expanding higher. In addition, a new updraft is developing above the northeast (right from the reader's point of view) region of the fire area, where at surface, the fire front produces the higher fluxes. Strong downward motions (blue shading) are observed around the "young" updraft as a response to the explosive pyro-convection, at the top of the main updraft and at the descending parts of the right (left from the reader's point of view) horizontal vortex, which advect drier air from above to lower altitudes. The descending streamline of the inflow, upwind of the fire area is also evident.

In ext005m experiment (Fig. 3.15b), the main updraft is consisted by a single column of ascending air, which penetrates into the inversion layer, while at its top, strong downward motions surround the column, mostly upwind. The descending inflow from behind circulates around the main updraft and converges in front of the fire, close to the surface. The sensitivity run ext010m (Fig. 3.15c) produces also a single updraft column, almost vertically oriented, but the strong downdrafts inside the inversion layer are simulated all around to the main updraft. Note also the two streamlines aloft and left of the updraft's core (right from the reader's point of view), and how they bounce as they descend downwind of the fire due to strong turbulence.

Two distinct updraft cores exist in ext015m simulation (Fig. 3.15d), close to the ground. A weaker to the left (east) and a stronger to the right (northeast) according to the reader's point of view, which collocates with the surface grid cells of maximum fire heat release. The two updrafts merge aloft, producing downward motions with multiple cores ($> 3 \text{ m s}^{-1}$), while at the top of the plume, vertically extended regions with strong downdrafts surround the main updraft column. At surface, the inflow originally upwind of the fire area, turns to the north (right from the reader's point of view) flank, curves, converges and finally enters into the strongest (right) updraft core. This feature illustrates how the convective column may act as an obstacle to the flow, an idea that was first introduced by Countryman (1964). Under certain conditions, a pair of counter-rotating lee vortices can form downwind of the column, due to the bending and tilting of the vortices (Countryman, 1969; Potter, 2012b).

In ext025m experiment (Fig. 3.16a), multiple updraft cores coexist close to the ground and merge higher, producing a single updraft column, as well. The strongest core is observed above the east forwarding fire front. While upward velocities greater than 5 m s^{-1} are not observed inside the inversion layer at this time frame and also seems to appear until the bottom of the inversion, however strong downdrafts are simulated within. Note, how the downward motions vertically extend around and aloft of the updraft column, while the streamlines descent on the downwind side.

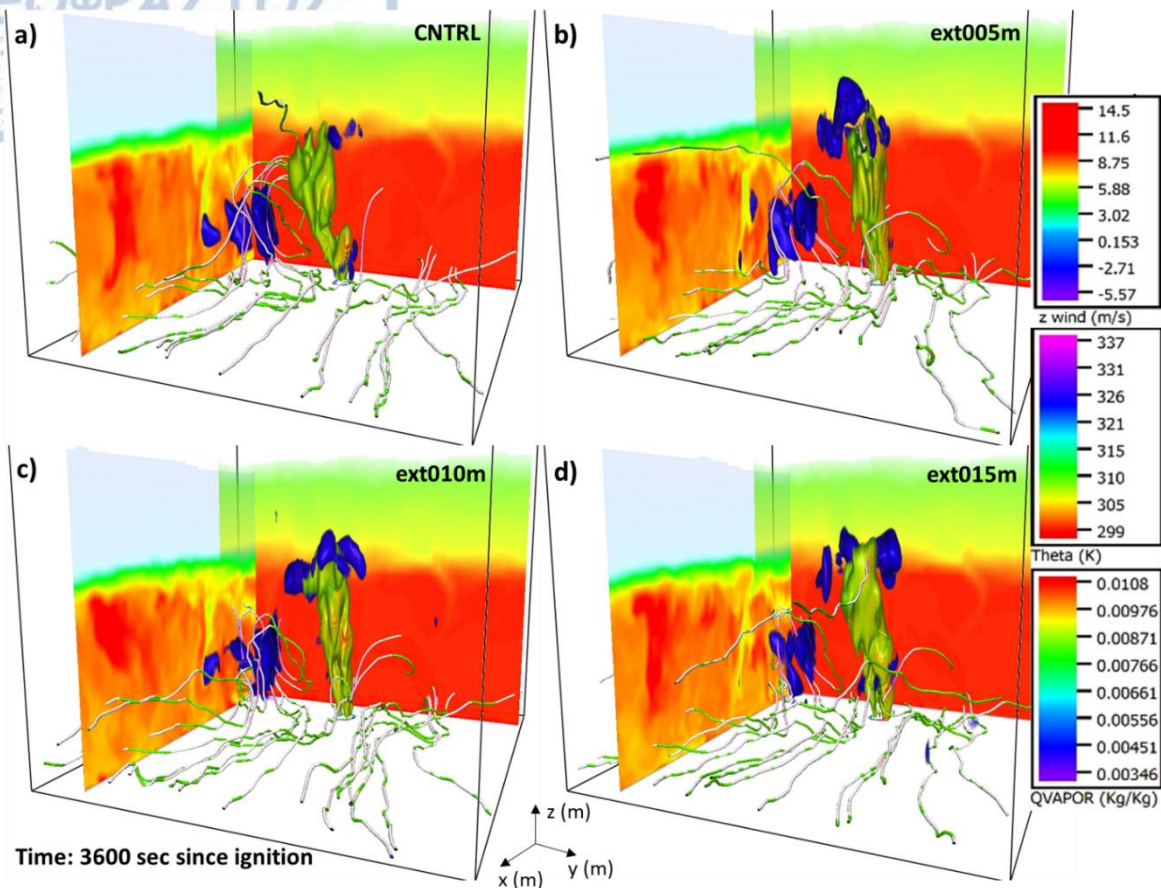


Fig. 3.15: Direct volume rendering (DVR) of vertical wind component ($m s^{-1}$), airflow (streamlines), vertical cross section of water vapor mixing ratio ($kg kg^{-1}$) along x axis and potential temperature (K) vertical cross section along y axis for a) CNTRL, b) ext005m, c) ext010m and d) ext015m experiments, at 60 min since fire ignition. For the DVR z-wind field, upward motions greater than $5 m s^{-1}$ (green shading) and downward motions greater than $3 m s^{-1}$ (blue shading) are illustrated. Streamlines are colored based on vertical velocity values and created using 16 random seeds (flow type steady). The top of the depicted domain is at $\sim 3500 m$ above surface. Created in VAPOR.

A different DVR of the vertical velocity variable is shown in ext075m simulation (Fig. 3.16b), where the absence of a single and coherent updraft column is evident, a feature that was illustrated and discussed in all previous experiments, with z_{ext} less than $75 m$. Here, the regime of strong vertical motions (greater than $5 m s^{-1}$) is consisted of a single narrow column near the surface, which expands as the height increases. Upon expansion, multiple updraft cores are observed and regions of weaker updrafts are present inside the wider area of the fire plume. In addition, the upward velocities with values greater than $5 m s^{-1}$ barely reach the bottom of the inversion layer. At lower heights, distinct downdraft cores are located left (right from the reader's point of view) of the updraft region, while aloft downward velocities (greater than $3 m s^{-1}$) are simulated above and slightly behind of the left (right from the reader's point of view) portion of the updraft regime. Moreover, the vertical wind shear tilts the fire plume relative to the ground, a feature that is attributed to the lower vertical speeds as the height increases (scatterplot from the Fig. 3.14c). Previously numerical studies (Sharples et al., 2013; Simpson et al., 2014, 2013a) have demonstrated that the background winds can tilt an intense pyroconvective column. In combination with downwind atmospheric dynamics and high turbulence near the fire, favorable conditions for spotting can emerge as well. It must be said that the WRF-SFIRE modelling system does not include such spotting mechanism.

Although the z wind DVR in ext100m sensitivity (Fig. 3.16c) presents similar morphological features with the ext075m experiment (absence of a single updraft column, multiple updraft cores and blended regions of weak upward motions), it is extended higher and into the inversion layer, while the downdraft cores are simulated only aloft and in front of the updrafts' regime. Moreover, the flow from the right (left from the reader's point of view) clockwise horizontal vortex converges close to the ground and downwind of the fire area, a feature that was also appeared in the CNTRL experiment. Regarding the ext200m simulation (Fig. 3.16d), strong updraft motions penetrate the inversion layer and coexist with strong downdraft cores. Regimes of weaker upward motion (less than 5 m s^{-1}) are also observed in the main fire plume. Last but not least, two different updraft cores are illustrated close to the ground and are associated with the two active fire regions at surface.

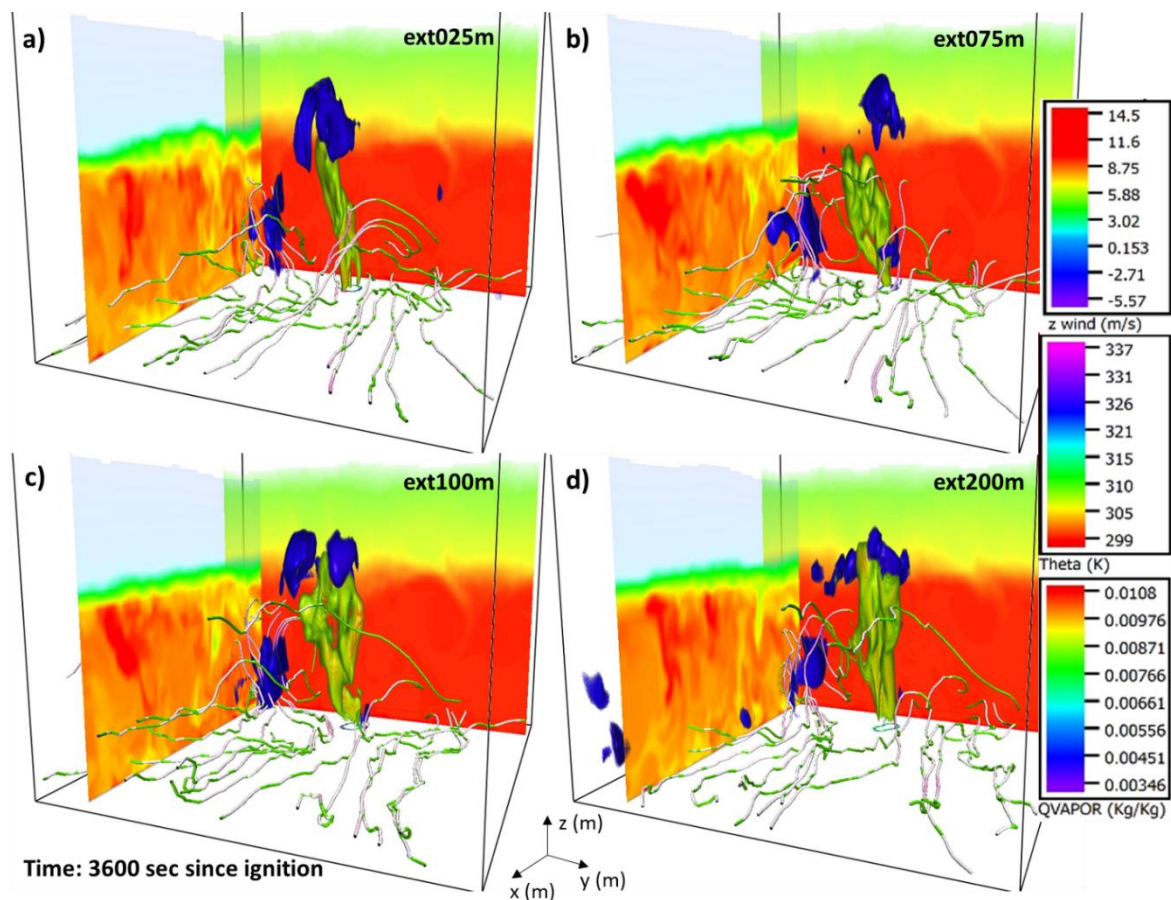


Fig. 3.16: As in Fig. 3.15 but for a) ext025m, b) ext075m, c) ext100m and d) ext200m experiments.

3.3.3.3 Potential Temperature Anomaly

The heat releases from the surface fire directly affect the potential temperature in the vicinity. Depending on the background winds, the temperature profile and stability conditions, potential temperature anomalies can reveal how the fire heat fluxes alter the energy budget close to the ground and aloft. As previously discussed (Section 3.1), the sensible heat fluxes from the fire model are inserted as additional source term to the equation for the potential temperature θ , equal to the vertical divergence of the heat flux. The z_{ext} parameter controls the vertical distribution of the fluxes but set limitations to the portion of the originally emitted fluxes that enter into the atmospheric domain, as shown earlier (sub-section 3.3.1).

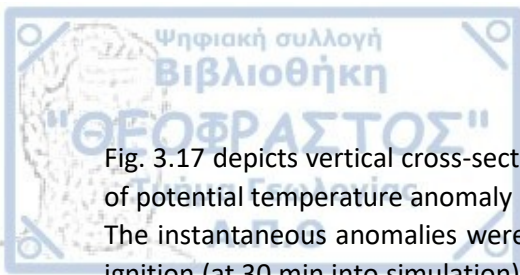


Fig. 3.17 depicts vertical cross-sections along x axis and through the center of the WRF-SFIRE domain of potential temperature anomaly (K), averaged from 5 to 60 min since ignition, for each experiment. The instantaneous anomalies were calculated based on the potential temperature field prior to the ignition (at 30 min into simulation) and then were averaged over time. In addition, the minimum and maximum time-averaged potential temperature anomalies along the y axis were considered. If the absolute value of the minimum time-averaged theta anomaly was greater than the corresponding maximum along y axis, then every grid point in y direction was assigned with this value, else the maximum value was considered. Thus, the choice of the y index of the cross-section point do not change the resulting plot. The contour fill pattern corresponds to theta anomalies between -0.5 to 0.5 K.

According to Fig. 3.17, the perturbation in potential temperature field due to the surface fire heat fluxes is greater close to the ground and diminishes as the height increases, in all experiments. In addition, the penetration of the convective column into the inversion layer and the vertical circulations result in the cooling of the aforementioned layer. The cooling is attributed to the advection of colder air from above (strong downward motions as discussed in sub-section 3.3.3.2) and to the adiabatic expansion and cooling of the rising air due to the decrease in air pressure as altitude increases. As the simulations were performed in a highly idealized configuration, with no any microphysics scheme active, it is hard to estimate if the adiabatic processes can lead to condensation.

In general, an increase of the z_{ext} parameter leads to weaker time-averaged potential temperature anomalies both close to the ground and in the top of the convective plume. However, the temporal peaks in theta anomalies do not follow any linearity and their occurrence varies both in time and space. In all experiments, the absolute minimum potential temperature anomaly occurred at 1st theta level (~5.8 m), while the maximum theta anomaly is met at 1st theta model level only in the CNTRL, ext005m, ext010m, ext015 and ext025m experiments. For the ext075m, ext100m and ext200m sensitivity runs, the maximum theta anomaly is located at 6th (~71.5 m), 11th (~155.7 m) and 9th (~119.5 m) mass level, respectively. Table 3.3 summarizes and presents the minimum and maximum time-averaged potential temperature anomaly from Fig. 3.17, the minimum and maximum theta anomaly values, the mass model level and the time of their occurrence.

Table 3.3: Minimum and maximum time-averaged potential temperature anomaly (K) in each experiment along with theta anomaly minimums and maximums, theta model level and time of occurrence.

Experiments	Time-averaged theta anomaly (K)		Theta anomaly (K)					
	Minimum	Maximum	Minimum	Theta model level	Time since ignition (min)	Maximum	Theta model level	Time since ignition (min)
CNTRL	-3.8	12.9	-33.3	1 st	5	52.7	1 st	5
EXT005M	-7.4	34.1	-87.2	1 st	60	142.1	1 st	60
EXT010M	-5.3	28.9	-36.0	1 st	25	65.5	1 st	5
EXT015M	-9.9	28.6	-207.3	1 st	60	372.2	1 st	60
EXT025M	-7.0	19.2	-32.7	1 st	60	128.4	1 st	60
EXT075M	-3.9	11.2	-19.0	1 st	5	66.6	7 th	5
EXT100M	-4.0	7.2	-21.8	11 th	55	22.6	1 st	55
EXT200M	-3.0	6.1	-27.2	9 th	30	48.7	1 st	30

In the CNTRL experiment (Fig. 3.17a, Table 3.3), the minimum time-averaged potential temperature anomaly is -3.8 K and is located in the inversion layer, whilst the maximum time-averaged theta anomaly is 12.9 K (above the surface fire). The absolute minimum and maximum potential temperature anomaly are found equal to -33.3 K and 52.7, respectively, at 5 min since ignition and at 1st mass level (almost in neighboring grid cells). Moreover, Fig. 3.17a indicates that maximum time-averaged theta anomalies above 5 K exist up to 300 m above surface and the background wind can alter the downwind theta profile up to 1 K. In addition, downwind of the fire and close to the surface, the negative theta anomalies are dominating, albeit their values are less than 0.5 K. The latter is true for all experiments.

Worth of noting is the minimum and maximum potential temperature anomalies in ext015m sensitivity, where their corresponding values are equal to -207.3 K and 372.1 K, respectively. Both extremes are occurring at 60 min since ignition (Table 3.3), at 1st theta model level and at neighboring grid cells. This feature is associated with the high amount of released heat fluxes from the surface fire (sub-section 3.3.2.3) at this time frame and its "blow-up" characteristics that discussed earlier (sub-section 3.3.3.2). Examination of the minimum and maximum theta anomaly in x-y plane, at 60 min since the fire's flaming revealed that aloft the active firefront there is a region of high positive theta anomalies (> 50 K), whilst on its surroundings high negative anomalies ($> |-50|$ K) exist (see Appendix II, Fig. B.4). Although the model setup and the domain configuration was different than in this study, Simpson et al. (2014) computed time-averaged theta anomalies up to 19 K above their ridge line fire, by utilizing the WRF-FIRE model (Coen et al., 2013). However, they did not mention any negative instantaneous theta anomalies. In addition, evaluation of the highly tuned WRF-SFIRE with field observations (Kochanski et al., 2013a) from the FireFlux experiment (Clements et al., 2007) showed good agreement between model and observational vertical temperature structure of the fire plume, with no intense cooling being reported.

Despite the lack of any immediate reports on potential temperature anomalies in other model simulations, this feature is consistent in all experiments, albeit it varies in space, time and intensity. Moreover, the minima and maxima coincide in time, for all experiments but one (ext010m) and in vertical, for almost all the simulations (except ext075m, ext100m and ext200m model runs), revealing the need for further investigation and interpretation of this mechanism. Whether is an arbitrary effect or a physical process is subject to future work.

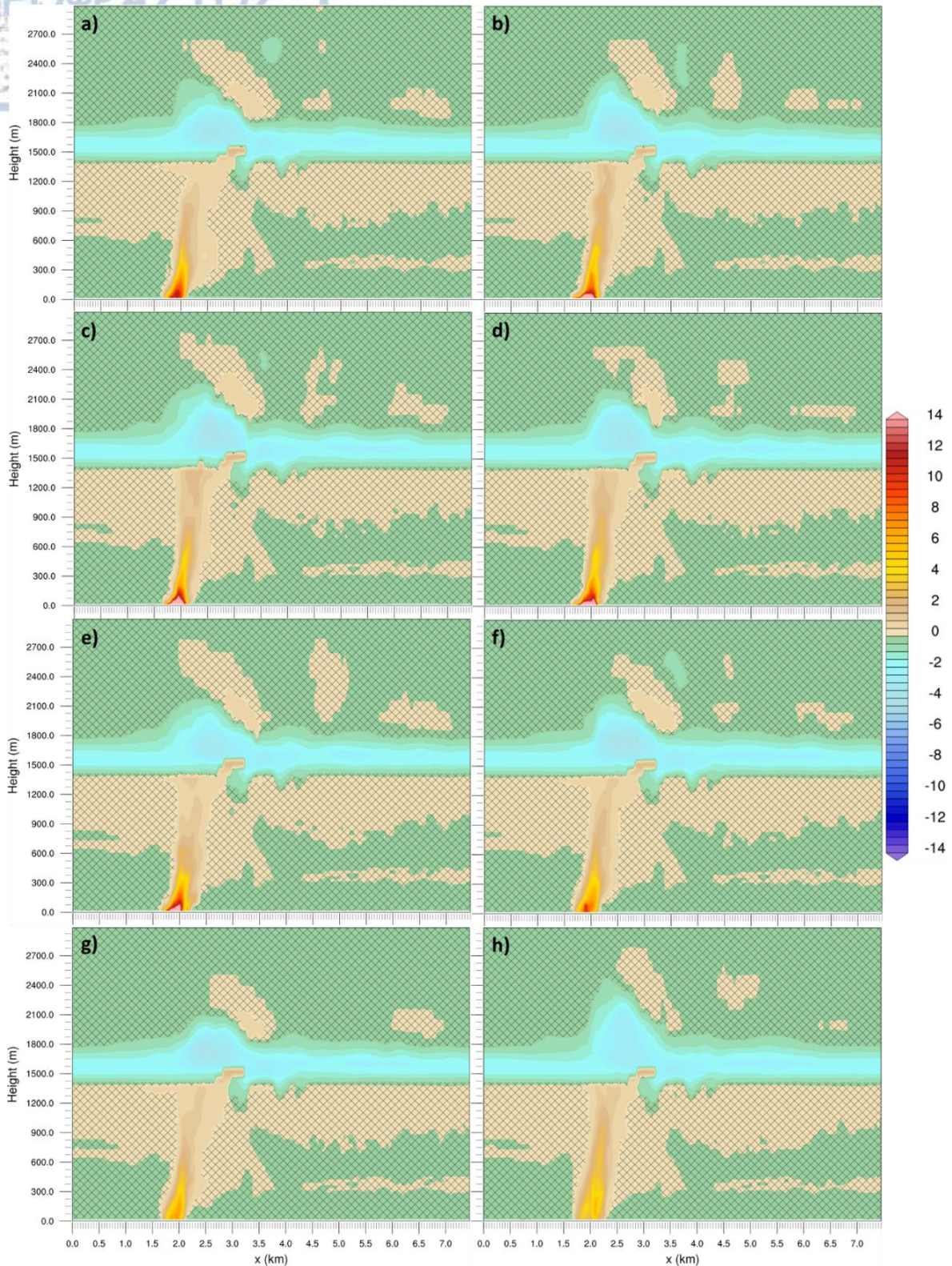


Fig. 3.17: Vertical cross-section along x axis through the center of the WRF-SFIRE domain of potential temperature anomaly (in 0.5 K intervals, shaded contours), averaged from 35 to 90 min into simulation, for a) CNTRL, b) ext005m, c) ext010m, d) ext015m, e) ext025m, f) ext075m, g) ext100m and h) ext200m experiments. The contour fill pattern corresponds to values between -0.5 to 0.5 K. See text for further details.

3.3.3.4 Modeled plume properties

A fire plume can act as indicator on how the released energy from a fire is distributed into the atmosphere. Proper model evaluation requires an number of observational datasets and field experiments that are carefully analyzed (Sun et al., 2006). For example, the FireFlux (Clements, 2010; Clements et al., 2008, 2007) and the FireFlux II (Clements et al., 2019) field experiments are two of the most detailed and well documented prescribed burns with a vast amount of data suitable for model evaluation and validation. Due to the highly idealized nature of the simulations performed, such comparison is not possible and it is far from the scope of this study. However, an evaluation on how the different input method (through changes in z_{ext} parameter) of the fire heat fluxes into the WRF atmospheric domain alter the fire plume properties can be achieved by determining the portion of each plume, in which the calculations and comparisons lie, according to the classic plume theory (Batchelor, 1954; Morton et al., 1956; Zeldovich, 1937).

Following the approach in Sun et al. (2006), the radial profile of vertical velocity w in the plume was assumed to have a normal distribution (McCaffrey, 1983) and the portion of the plume with vertical velocities (upward motions),

$$w > \frac{w_{\text{max}}}{1.38}, \quad (3.4)$$

where w_{max} is the maximum vertical velocity in the plume, was considered for the calculations. From the plume's definition (Eq. 3.4), time-mean plume averaged vertical velocity (m s^{-1}), plume radius (m) and area (ha), mass flux ($\text{m}^3 \text{s}^{-1}$), water vapor (g kg^{-1}) and temperature ($^{\circ}\text{C}$) excesses were calculated, as a function of height, for each simulation. The term excess is referring to the difference of the calculated variables between inside and outside of the defined plume, according to Eq. 3.4. The mass flux was calculated following,

$$M_F = \bar{w}\pi R^2, \quad (3.5)$$

where \bar{w} is the plume averaged vertical velocity and R is the plume radius. The plume mass flux is originated from the classical idealized plume theory (Hunt and van den Bremer, 2011; Morton et al., 1956). The plume radius was calculated from the plume area, since the latter was considered as a perfect circle on the horizontal plane, in each theta model level.

Table 3.4 presents the mean, minimum and maximum values of the time-mean plume-averaged variables that are utilized in the current analysis. In average, the ext015m sensitivity run produces the most intensive updraft speeds ($11.0 \pm 0.9 \text{ m s}^{-1}$), and the highest water vapor ($0.744 \pm 0.196 \text{ g kg}^{-1}$) and temperature ($12.1 \pm 3.9 \text{ }^{\circ}\text{C}$) excesses due to "blow-up" conditions at the end of the analyzed period. In addition, the absolute maximum temperature excess is presented also in this sensitivity run and is equal to $373 \text{ }^{\circ}\text{C}$. The plumes in CNTRL and ext200m experiments show almost equal spatial expansion (in x-y plane) in average and additionally, the ext200m plume mass flux is the highest ($241.0 \pm 39.4 \cdot 10^3 \text{ m}^3 \text{ s}^{-1}$) among the simulations. In general, the experiments with z_{ext} less than 50 m produce narrowed plumes with strong updrafts, whilst the plumes in the experiments with z_{ext} greater or equal to 50m are more horizontally expanded and present weaker updraft speeds in their cores. In Appendix II (Table B.5), the calculated descriptive statistics for each plume variable and experiment are presented.

Fig. 3.18 displays the differences in time-mean plume averaged vertical velocity (m s^{-1}), radius (m), area (ha), mass flux ($10^3 \text{ m}^3 \text{ s}^{-1}$), water vapor excess (g kg^{-1}), temperature ($^{\circ}\text{C}$), maximum temperature ($^{\circ}\text{C}$) and absolute maximum temperature excesses ($^{\circ}\text{C}$) between the CNTRL experiment and each sensitivity simulation, up to 2 km above ground level. Regarding the plume averaged vertical velocities (Fig. 3.18a), there is clearly a clustering at lower altitudes, where in sensitivity runs with z_{ext} less than 50 m

(ext005m, ext010m, ext015m and ext025m runs), simulated plume vertical velocities are higher than in CNTRL, a) close to the ground and up to ~ 1 km agl, and b) lower, in ext100m and ext200m experiments. For the ext075m run, positive differences are shown in the layer between ~ 200 m and ~ 470 m agl, whilst negative differences lie from the surface and up to ~ 200 m, and in the layer between 500 m and 1000 m above ground level. Above ~ 1 km and up to 2 km, all sensitivities produce higher plume vertical velocities, except in ext100m model run (magenta dashed line), where plume vertical velocity is essentially equal (in fact slightly smaller) to the CNTRL's one, at ~ 1500 m above surface. The ext015m sensitivity produces the most intensive updraft velocities (red dashed line) relative to CNTRL, with peak values being presented in a 100 m deep layer, between ~ 100 m and 200 m above ground level. The maximum positive difference is depicted also in this sensitivity run and is equal to 5.4 m s^{-1} , at ~ 90 m above surface. On the contrary, the maximum negative difference is equal to -2.6 m s^{-1} and it is presented in ext200m experiment (~ 140 m agl).

Table 3.4: Average, minimum and maximum values of the time-mean plume-averaged variables.

Variables		CNTRL	ext005m	ext010m	ext015m	ext025m	ext075m	ext100m	ext200m
w (m s^{-1})	Mean	8.3 \pm 0.9	10.6 \pm 0.9	10.5 \pm 1.0	11.0 \pm 0.9	9.6 \pm 0.8	8.4 \pm 0.9	8.1 \pm 0.9	8.0 \pm 0.9
	Min	0.7	1.2	1.1	1.5	1.1	0.6	0.6	0.5
	Max	11.8	13.7	13.8	14.3	12.7	11.4	11.2	11.7
R (m)	Mean	86.7 \pm 7.6	78.4 \pm 7.7	75.0 \pm 8.2	76.8 \pm 7.8	78.9 \pm 6.8	84.9 \pm 6.6	86.0 \pm 8.2	86.8 \pm 6.1
	Min	51.3	48.9	47.1	48.2	47.8	52.9	52.0	51.2
	Max	136.4	138.7	126.0	138.5	128.2	124.2	144.0	138.8
A (ha)	Mean	2.8 \pm 0.5	2.3 \pm 0.5	2.1 \pm 0.5	2.2 \pm 0.5	2.3 \pm 0.4	2.7 \pm 0.4	2.8 \pm 0.6	2.8 \pm 0.4
	Min	0.9	0.8	0.8	0.8	0.8	1.0	1.0	0.9
	Max	7.0	6.5	6.2	6.7	6.1	6.0	7.3	6.5
MF ($10^3 \text{ m}^3 \text{ s}^{-1}$)	Mean	235.3	239.4	219.8 \pm 4	227.9	217.0	232.4	241.7	241.0
	Min	± 38.2	± 45.4	6.7	± 40.8	± 35.1	± 40.9	± 48.4	± 39.4
	Max	509.8	563.9	633.8	482.1	416.3	549.6	566.2	494.1
r (g kg^{-1})	Mean	0.433	0.626	0.597	0.744	0.564	0.487	0.470	0.430
	Min	± 0.158	± 0.178	± 0.18	± 0.196	± 0.18	± 0.18	± 0.194	± 0.156
	Max	-0.081	0.049	-0.003	-0.016	-0.122	-0.159	-0.172	-0.030
T ($^{\circ}\text{C}$)	Mean	2.283	2.449	2.272	2.342	2.238	2.712	2.705	2.355
	Min	5.4 \pm 1.3	9.4 \pm 3.0	8.9 \pm 2.6	12.1 \pm 3.9	8.3 \pm 2.5	5.2 \pm 1.2	4.6 \pm 1.0	4.1 \pm 0.7
	Max	-1.8	-2.1	-2.1	-2.2	-1.9	-2.3	-2.6	-1.6
T max ($^{\circ}\text{C}$)	Mean	13.0	47.0	35.7	53.7	29.3	11.0	9.6	7.4
	Min	10.9 \pm 1.9	24.1 \pm 8.1	13.6 \pm 3.3	57.4 \pm 25.6	21.7 \pm 8.5	12.9 \pm 3.1	11.2 \pm 2.1	16.0 \pm 3.9
	Max	0.9	0.6	0.1	0.2	0.6	0.6	0.3	0.9
T AbsMax ($^{\circ}\text{C}$)	Mean	22.4	143.3	48.8	373.0	129.3	37.2	22.5	42.3
	Min	16.4 \pm 3.8	24.3 \pm 8.1	15.7 \pm 4.4	57.7 \pm 25.6	22.3 \pm 8.5	17.7 \pm 5.3	12.7 \pm 2.2	23.4 \pm 4.6
	Max	0.9	0.6	0.1	0.2	0.6	0.6	0.3	0.9
Max	53.1	143.3	66.0	373.0	129.3	66.5	22.5	48.6	

Since plume radius (Fig. 3.18b) was calculated based on the plume area field (Fig. 3.18c), the differences in vertical profiles of each sensitivity, relative to CNTRL experiment, present similar shape and behavior. The ext200m sensitivity produces larger plume area and essentially plume radius (purple dashed line) than the CNTRL experiment, between ~ 120 m to ~ 660 m agl (with maximum plume radius positive difference equal to 15.0 m, at ~ 260 m agl), while aloft, the ext100m (magenta dashed line, Fig. 3.18b,c) plume is bigger than in CNTRL, at two distinct layers (from ~ 960 m to ~ 1150 m agl and in a ~ 200 m deep layer, between ~ 1500 m and ~ 1700 m agl). In addition, in the layer between ~ 1200 m and ~ 1300 m agl, all experiments present thinner plumes than in CNTRL, which coincide with the regime of higher vertical velocities in this layer (Fig. 3.18a).

The vertical profiles of mass flux (Fig. 3.18d) present mostly negative discrepancies up to ~1200 m agl (except the MF profile, in ext200m sensitivity) compare to CNTRL's one and positive differences aloft. The ext010m mass flux shows opposite behavior below ~1100 m agl, where the most negative difference lies (equal to $-125.3 \cdot 10^3 \text{ m}^3 \text{ s}^{-1}$, at ~800 m agl) and aloft, where the most positive deviation is located (equal to $190.0 \cdot 10^3 \text{ m}^3 \text{ s}^{-1}$, at ~1360 m agl). Worth of noting is also the mass fluxes in the layer between ~1200 m and ~1300 m agl, in which the ext015m, ext025m and ext200m sensitivities produce the largest negative differences in vertical against CNTRL. This is reasonable, since the calculation of MF is based on plume radius and plume-averaged vertical velocity, according to Eq. 3.5, which also present the largest negative differences in this layer and for these experiments, as discussed previously.

Close to the ground and specifically up to ~18 m agl, all simulations but two (ext100m and ext200m) produce higher water vapor plume excesses than CNTRL (Fig. 3.18e). The ext015m plume is enriched with additionally 1.0 kg kg^{-1} water vapor (red dashed line) at 1st theta model level (~5.8 m agl), which decreases as the height increases, due to higher released latent heat fluxes from the surface fire. Moreover, positive excesses exist above ~1800 m agl, and up to 2000 m above ground level.

In all sensitivities, discrepancies on plume temperature excesses occur up to ~600 m agl (Fig. 3.18f), while aloft the differences become essentially zero against to CNTRL's vertical profile. At approximately 5.8 m agl (1st theta level), the ext015m simulation presents the highest positive difference in plume temperature excess (equal to $43.8 \text{ }^\circ\text{C}$) compared to the CNTRL's corresponding value ($9.9 \text{ }^\circ\text{C}$), while in ext200m, the average plume temperature is lower than in CNTRL, by $5.6 \text{ }^\circ\text{C}$. The experiments with z_{ext} less than 50 m (ext0{05,10,15,25}m), produce higher temperatures inside the plume and over a 600 m deep layer above surface, which result in higher buoyancy and pressure gradient forces and thus, higher vertical velocities (Fig. 3.18a). In addition, the maximum time-mean temperature excess difference is found equal to $350.6 \text{ }^\circ\text{C}$ (ext015m). In Appendix II (Tables B.6, 7, 8, 9, 10, 11, 12, 13), the absolute values of the time-mean plume-averaged vertical profiles (vertical velocity, plume radius and area, mass flux, water and temperature excess) are presented also for completeness.

Sun et al. (2006) compared time-mean plume-averaged measurements of temperature, at 10 m agl, from the Metatron (Benech, 1976) fire experiment with the Clark coupled model (Clark et al., 1996a) results. They found temperature excesses of $4.7 \text{ }^\circ\text{C}$ and $19.32 \text{ }^\circ\text{C}$, respectively, depending on how the sensible heat from the fire was put into the lower layer in the atmospheric model. The aforementioned dependency is also valid in the current study, where it is clearly demonstrated that the plume properties are altered by the choice of e-folding depth. However, estimations on which z_{ext} value is the most appropriate for use are not possible at this point, since the goal is to emerge and demonstrate the sensitivity of the e-folding approach, which is employed in the WRF-SFIRE modelling system.

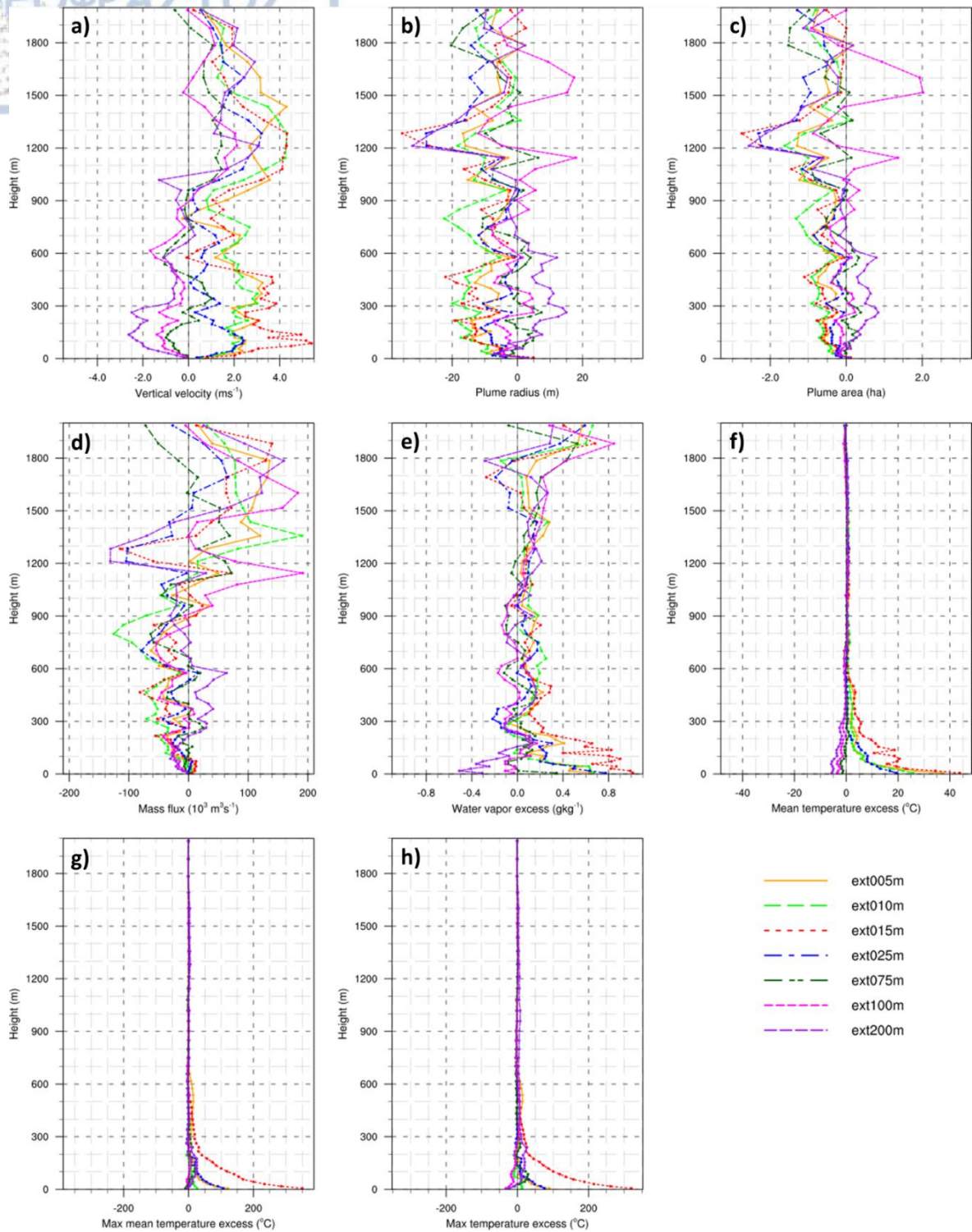


Fig. 3.18: Differences in time-mean plume averaged a) vertical velocity ($m s^{-1}$), b) radius (m), c) area (ha), d) mass flux ($10^3 m^3 s^{-1}$), e) water vapor excess ($g kg^{-1}$), f) temperature ($^{\circ}C$), g) maximum temperature ($^{\circ}C$) and h) absolute maximum temperature ($^{\circ}C$) excesses, between CNTRL experiment and each sensitivity simulation.

3.3.3.5 Near surface dynamics

3.3.3.5.1 Results at the end of initial steady state (30 min)

At 30 min since ignition, fire propagation is characterized by a steady rate in all experiments but one (ext200m), as Fig. 3.8 suggests. To understand how the different e-folding depths of the fire released

energy alter the near surface flow dynamics, the vertical component of vorticity vector, ζ (Eq. 2.8), and horizontal divergence, δ (Eq. 2.10), were calculated on the fire grid ($dx = dy = 5$ m), at 3.1 m agl. This level corresponds to the calculated "midflame" height (Baughman and Albin, 1980), in which the WRF horizontal winds are vertically interpolated to the fire mesh, according to the methodology presented in Section 3.2.

Fig. 3.19 and Fig. 3.20 depict the relative vorticity, ζ (left column) and divergence, δ (right column), at 30 min since fire flaming, for CNTRL (Fig. 3.19a, b), ext005m (Fig. 3.19c, d), ext010m (Fig. 3.19e, f), ext015m (Fig. 3.19g, h), ext025m (Fig. 3.20a, b), ext075m (Fig. 3.20c, d), ext100m (Fig. 3.20e, f) and ext200m (Fig. 3.20g, h) experiments. In addition, curl vectors indicate the airflow, at 3.1 m agl, while the dark red contour line represents the fire perimeter. Negative (positive) ζ values refer to clockwise (counterclockwise) rotation of flow parcels. Positive (negative) δ values signifies divergence (convergence) of flow parcels.

Overall, discrepancies exist in the patterns and magnitude of vorticity and divergence fields, in the shape of fire perimeter and the location of fire head. In the CNTRL experiment, a counterclockwise and clockwise vortex pair (Fig. 3.19a) is present ahead of the fire front, whilst strong convergence is evident (Fig. 3.19b) in front and just above the fire front (maximum equal to -0.171 s⁻¹). These flow features shape the fire front into a near bow-shaped or parabolic form, which are in line with the findings of previous numerical studies. Depending on the distance between the active portion of the fire front and the convergence region ahead, sharp or more rounded fire front shapes are observed in each experiment, which affect also the spread rates. Flow convergence is also depicted in the area behind the fire head, acting as inflow to base of the updraft (not shown).

Clark et al. (1996b) introduced and discussed the role of convergence region ahead of the fire front, as potential mechanism for "dynamic fingering", in which the horizontal components (ω_x, ω_y) of vorticity are tilted towards the vertical, increasing the wind speed in the direction of fire spread. Cunningham and Linn (2007) and Mell et al. (2007) presented similar fire front shapes in their numerical grass fire experiments. Kochanski et al. (2013c) evaluated the response of flow dynamics to fire propagation under different vertical wind shear profiles and found convergence patterns similar with the ones in this study.

The horizontal oriented vorticity that develops from the ambient vertically wind shear (generation of vorticity due to viscous shear stress, 4th right-side term of the vorticity equation (Eq. 2.9E), is oriented vertically by the fire's buoyant flow. Thus, along the north flank of the fire (Fig. 3.19a), positive ζ values exist, while at south flank, high negative ζ values are presented inside of the fire perimeter and positive ζ values on the outside. The patterns of vertical component of vorticity vary in each experiment and seems to be affected by the geometry of the fire line and the near surface flow. Thomas et al. (2017) pointed out also the latter and they concluded that both the bulk surface flow and the vertical vorticity contributed to the dynamic fire propagation presented in their simulations.

Church et al. (1980) discussed three types of vortices, based on the observations of the generated plume during the Meteotron experiment (Benech, 1976) and described the mechanisms leading to the generation of these vortex types. The tilting and stretching of horizontal components of vorticity presented in the environmental wind field was among the aforementioned mechanisms, accompanied by a graphical illustration (their Fig. 9). Cunningham et al. (2005) used WRF in LES mode and discussed a number of vortex characteristics, such as horizontal vortices over the fire's flanks. In their review article, Forthofer and Goodrick (2011) mentioned that likely the drafting to a buoyant plume develops also a shear layer near the ground, generating horizontal vorticity that can be oriented vertically. Potter (2012b) presented a conceptual model of bending and tilting of vortices due to environmental wind

shear (his Fig. 8) and buoyancy-gradient generation of vorticity around a fire front (his Fig. 9). In addition, similar ζ vorticity structures along the fire flanks are presented in the numerical simulations of Kochanski et al. (2013c), under different low-level environmental vertical wind shear.

Low e-folding depth values (Fig. 3.19c,e,g, Fig. 3.20a) produce more organized and intense counter-rotating vertical vorticity pairs and regions along the fire flanks and in front of the active fire head, whilst in the sensitivities with z_{ext} greater than 50 m (Fig. 3.20c,e,g), this vorticity is less organized and more transient. The above suggests that vorticity generation due to horizontal buoyancy gradients dominates over bending and tilting of horizontal vortices due to environmental wind shear, as higher updraft velocities are encountered in experiments with low z_{ext} values.

Among all experiments, ext200m produces the most interesting ζ vorticity features (Fig. 3.20g) at this time frame, as the fire is characterized by "blow-up" conditions, accompanied by fast propagation rates, strong induced surface wind speeds and vertical motions. The resulted fire area is almost doubled compared to the rest experiments, as previously presented in sub-section 3.3.3.5.1, where an extended region of positive ζ vorticity lies (maximum of 0.15 s^{-1}) upwind of the active fire head and is collocated with trails of negative ζ vorticity values downwind (of similarly strength, -0.13 s^{-1}). This counter-rotating vortex pair induces surface winds that advance the fire front at higher spread rates, whilst it maintains its structural form at 10 m agl (not shown). Aloft, the fire plume is consisted of pairs of counter-rotating vortices.

Time: 1800 sec since ignition

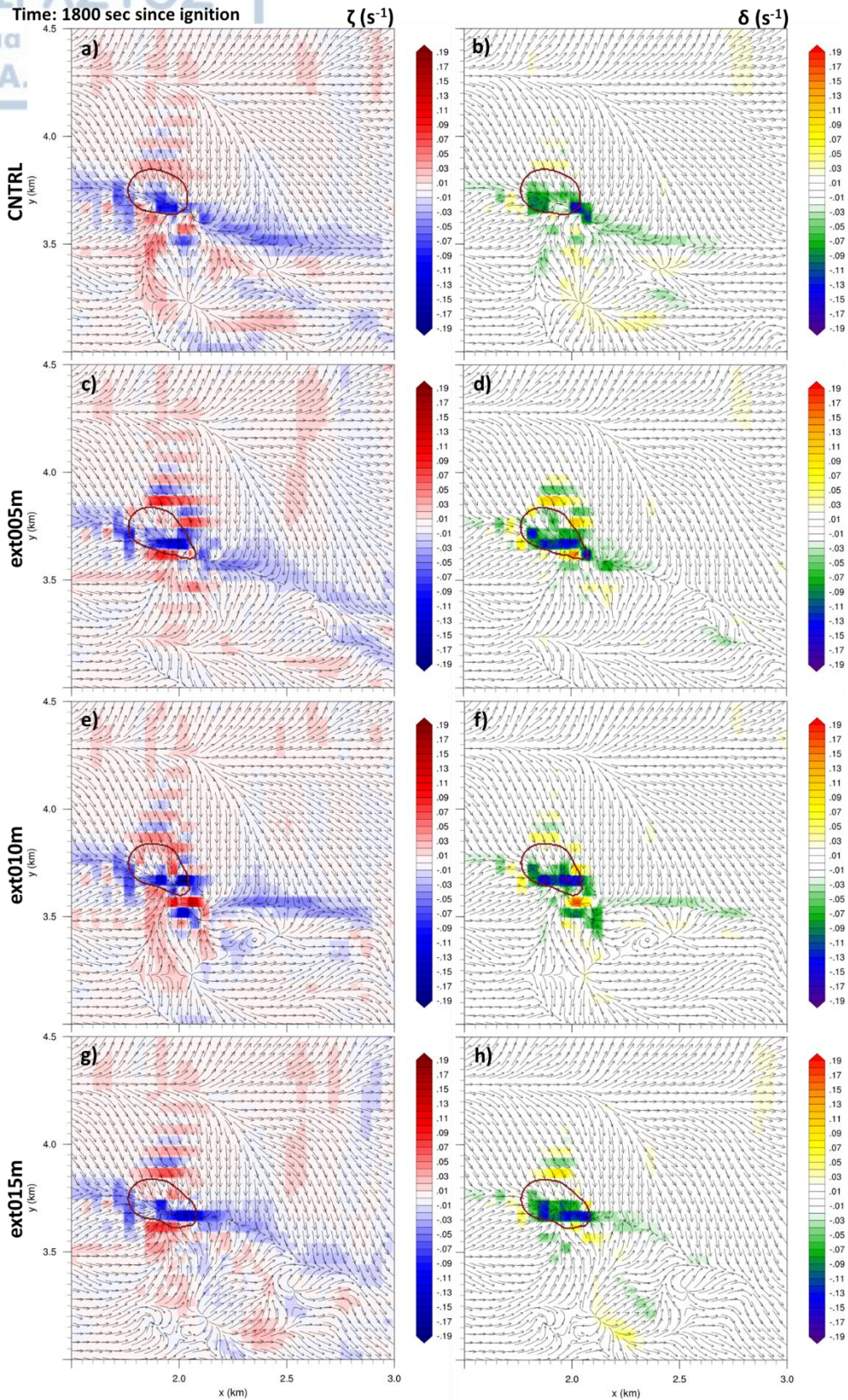


Fig. 3.19: Relative vorticity ζ (s^{-1} , left column) and horizontal divergence δ (s^{-1} , right column), at 30 min since ignition and 3.1 m agl, for CNTRL (a, b), ext005m (c, d), ext010m (e, f) and ext015m (g, h) experiments. Curl vectors indicate the airflow at 3.1 m agl. Fire perimeter is indicated with the dark red contour line. See text for further details.

Time: 1800 sec since ignition

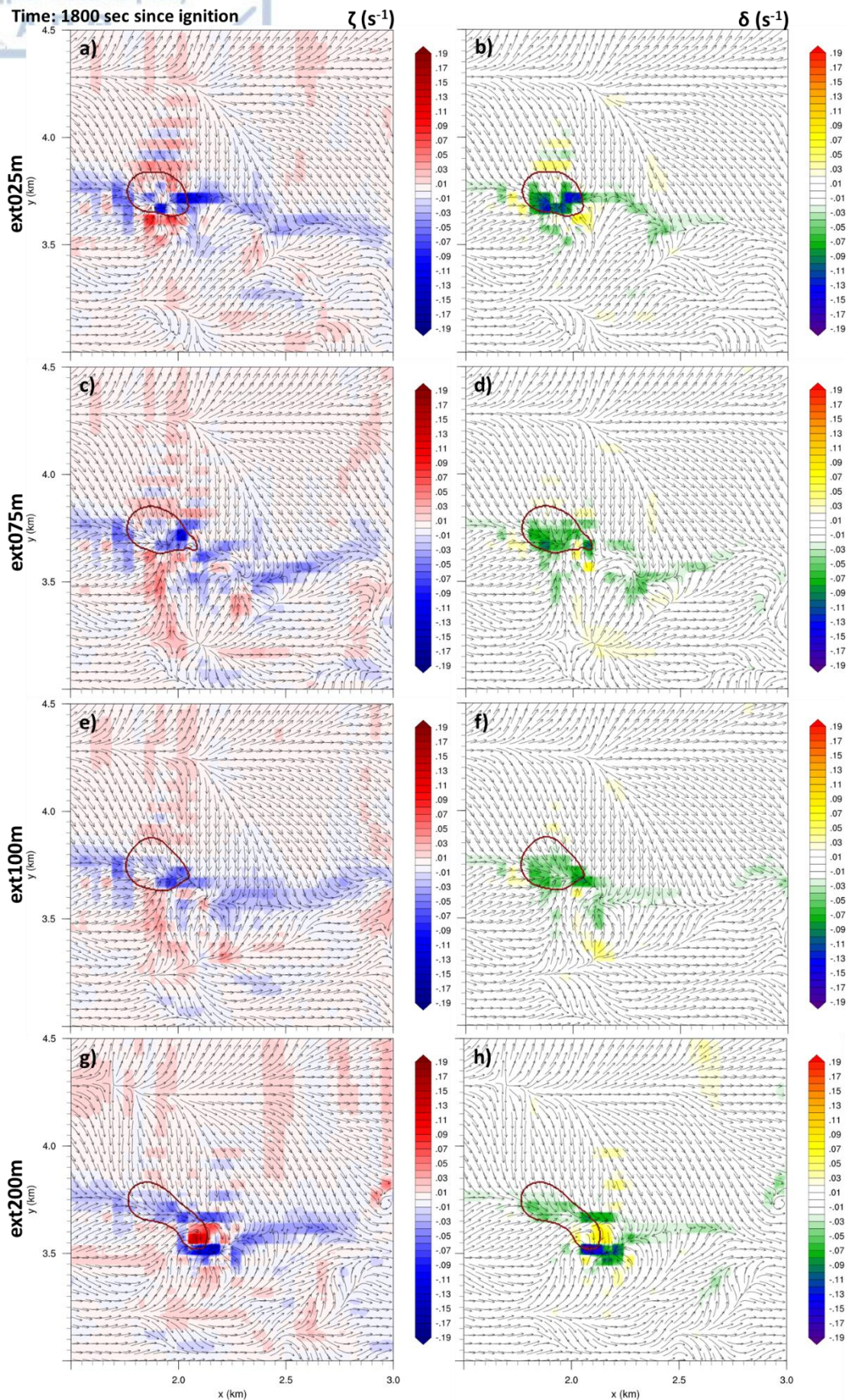


Fig. 3.20: As in Fig. 3.19, except for ext025m (a, b), ext075m (c, d), ext100m (e, f) and ext200m (g, h) experiments.

3.3.3.5.2 Vorticity equation in horizontal plane

Fire plume dynamics involve the development and growth of vortical structures, such as fire whirls and horizontally roll vortices, which can potentially lead to erratic fire behavior under favorable conditions. Vorticity equation (Eq. 2.9) is the most appropriate tool in order to understand and evaluate the flow dynamics during a wildland fire. According to Eq. 2.9, the vorticity at any point changes due to the advection (horizontally and vertically) of vorticity, the tilting of vorticity from one axis to another, the stretching and intensification by convergence and/or the generation of vorticity from non parallel pressure and density gradients, buoyancy and/or wind shear.

The rate of change of the relative vorticity, ζ , in a frictionless flow and in height Cartesian coordinates is expressed as,

$$\begin{aligned} \frac{\partial \zeta}{\partial t} = & -\vec{V} \cdot \nabla \zeta - \zeta (\nabla_h \cdot \vec{V}_h) + \left(\frac{\partial \vec{V}_h}{\partial z} \times \nabla_h w \right) \cdot \hat{k} + \frac{1}{\rho^2} \nabla_h \rho \times \nabla_h p \\ = & \underbrace{\left(-u \frac{\partial \zeta}{\partial x} - v \frac{\partial \zeta}{\partial y} \right)}_{(A)} - \underbrace{w \frac{\partial \zeta}{\partial z}}_{(B)} - \underbrace{\zeta \left(\frac{\partial u}{\partial x} + \frac{\partial v}{\partial y} \right)}_{(C)} + \underbrace{\left(\frac{\partial u}{\partial z} \frac{\partial w}{\partial y} - \frac{\partial v}{\partial z} \frac{\partial w}{\partial x} \right)}_{(D)} + \frac{1}{\rho^2} \underbrace{\left(\frac{\partial \rho}{\partial x} \frac{\partial p}{\partial y} - \frac{\partial \rho}{\partial y} \frac{\partial p}{\partial x} \right)}_{(E)}, \quad (3.6) \end{aligned}$$

where u , v and w the three components of the wind vector, ρ is the air density (kg m^{-3} , calculated from Eq. 2.11), p is the air pressure (Pa) and subscript h indicates a quantity or operation in the horizontal plane.

For each numerical experiment, the relative vorticity and the vorticity equation terms were estimated at different heights above surface (50, 100, 200, 600 m agl), at 5 min intervals. The first level (50 m) was chosen equal to the CNTRL's e-folding depth, the rest two rather randomly and the latter was the mean height in which the average plume vertical velocities from the plume analysis (sub-section 3.3.3.4) presented maximum values, in almost all experiments. Only the horizontal (Eq. 3.6A) and vertically (Eq. 3.6B) advection term, the convergence (Eq. 3.6C), tilting (Eq. 3.6D) and solenoidal (Eq. 3.6E) terms were accounted for the calculations, while Coriolis and earth radius effects were neglected. All components of the wind field were considered on theta points (at the center of each WRF grid cell). For the calculation of the vertical derivatives, the wind components are interpolated vertically at 25 m intervals. All derivatives were calculated by applying second-order centered finite differences. Computations took place in NCL (NCAR Command Language) by calling externally a number of Fortran functions, created for the purposes of the current analysis.

An analogous methodology is utilized in Matsangouras et al. (2016, 2014) regarding tornadogenesis over complex terrain in Greece and in Pytharoulis et al. (2016), where the influence of topography on the dynamical processes of a precipitation and lightning event is investigated. Sharples et al. (2015) provided a theoretical analysis of the vorticity equation for windward and lee slope fires producing pyrogenic vorticity, while Thomas et al. (2017) estimated each vorticity equation term in order to examine how the vertical vorticity was generated in their modelled junction fires.

Fig. 3.21 depicts time series of simulated maximum values of relative vorticity, ζ (s^{-1}) and vorticity equation terms of horizontal (Hadv, Eq. 3.6A) and vertical (Vadv, Eq. 3.6B) advection, convergence (Conv, Eq. 3.6C) and tilting/twisting (Tilt, Eq. 3.6D) at 5 min intervals, for CNTRL experiment, at 50 m (Fig. 3.21a) and 200 m agl (Fig. 3.21b), respectively. Although the solenoidal term was calculated it is not illustrated as it was found up to twelve orders of magnitude less than the other terms.

At 50 m agl (Fig. 3.21a), ζ peak values are encountered at 35 min (0.063 s^{-1}) and at 55 min (0.087 s^{-1}) since fire ignition. The tilting/twisting term is dominant at the early stages of the fire (up to 15 min), as the ambient horizontal vorticity is oriented vertically due to the presence of the fire, while the horizontal advection term contributes the most to the increase of relative vorticity. The vertical advection term is almost equal to the tilting/twisting term, in the period between 20 to 60 min after the fire's flaming. In addition, the convergence term (Eq. 3.6C) starts to increase after the first half of the analyzed period, with peak value equal to 0.41 s^{-1} (55 min) and the absolute ζ peak value can be attributed to this term, since the generation of vorticity from the baroclinic term (Eq. 3.6E) is negligible. It must be mentioned that the buoyancy gradients from the surface fire and the ambient wind shear must be considered as constant sources of new vorticity. Higher maximum ζ values are presented at 200 m agl (Fig. 3.21b), but the temporal evolution is similar to the corresponding one at 50 m agl, except that the relative vorticity peaks one hour after the fire ignition (0.14 s^{-1}). At this level, horizontal advection of vorticity is dominating over the other terms, with peak value equal to $0.63 \text{ s}^{-1} \text{ m}^{-1}$, at 60 min.

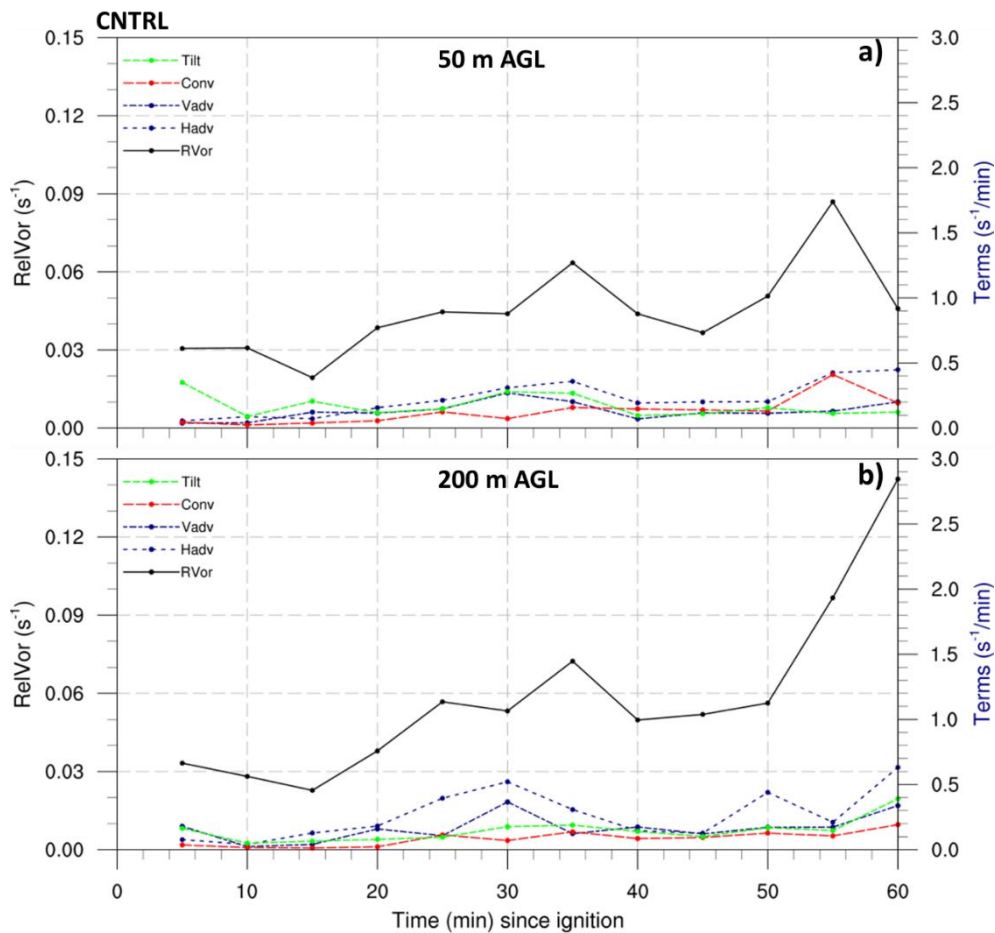


Fig. 3.21: Maximum relative vorticity (s^{-1}) and vorticity equation terms ($\text{s}^{-1} \text{ m}^{-1}$) of horizontal (Hadv) and vertical (Vadv) advection, convergence (Conv) and tilting/twisting (Tilt) as a function of time since fire flaming, for CNTRL experiment, in a box of $1.5 \text{ km} \times 1.5 \text{ km}$ over the fire area (1.5 km to 3 km west-east, 3 km to 4.5 km south-north), at a) 50 m agl and b) 200 m agl.

In ext015m sensitivity run, “blow-up” conditions are simulated at 60 min since ignition. At this time stamp, all the vorticity equation terms, under examination, increase their maximum values significantly at 200 m agl (Fig. 3.22) and lower (50 m and 100 m agl). The relative vorticity is advected vertically the most ($2.83 \text{ s}^{-1} \text{ m}^{-1}$), since at this layer, the vertical velocities are maximized. This value is the highest encountered among all experiments, regarding the vertical advection term. Also, the tilting/twisting term intensifies the vortices by increasing its absolute maximum value by $\sim 725\%$, between 55 min ($0.22 \text{ s}^{-1} \text{ m}^{-1}$) and 60 min ($1.84 \text{ s}^{-1} \text{ m}^{-1}$) since ignition, while the convergence term presents the lower peak value ($0.91 \text{ s}^{-1} \text{ m}^{-1}$) and increase (337%), at the same period. Moreover, the solenoidal term (not presented) amplifies its maximum values up to four orders at this time frame (max $1.22 \cdot 10^{-8} \text{ s}^{-1} \text{ m}^{-1}$, at 50 m agl), at 50 m, 100 m and 200 m agl, respectively, but still its values are eight times less than the other terms. The latter is in line with the findings of Clark et al. (1996b), where they concluded that the solenoidal source term is at least an order of magnitude smaller than the tilting/twisting term during the occurrence of an intense vertical rotor. In Appendix II (Figs. B.5 and B.6), the time series of relative vorticity and vorticity equation terms at each level and for each experiment are presented for completeness.

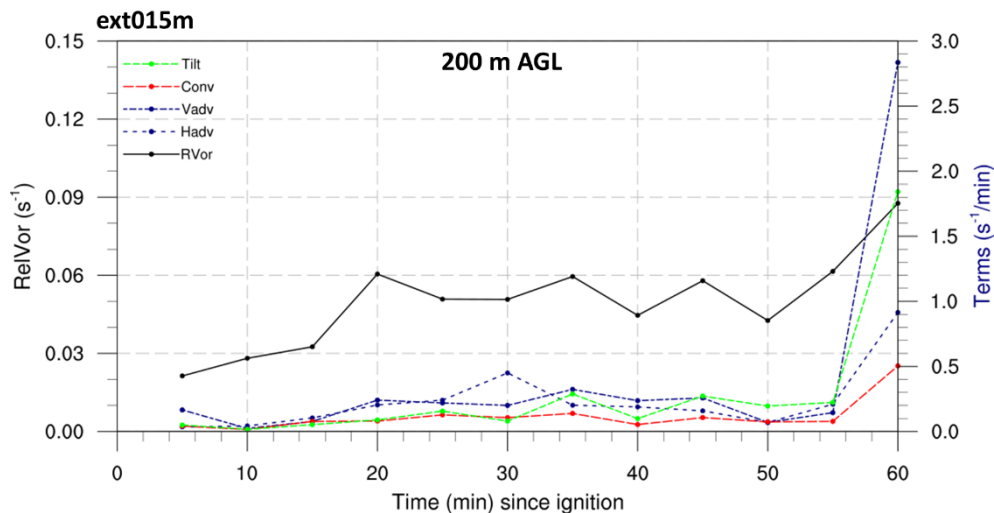
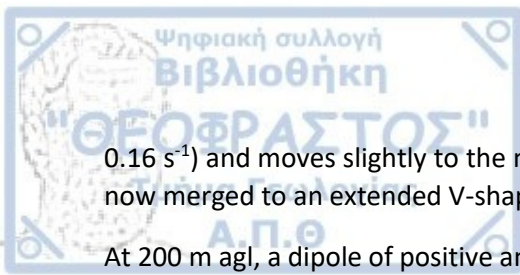


Fig. 3. 22: As in Fig. 3.21, but for ext015m experiment, at 200m agl.

According to Eq. 3.6, the relative vorticity tend to increase (decrease), at any location, if the terms' summary is positive (negative), while the maximum increase (decrease) is obtained when all the terms contribute positively (negatively). As the aforementioned is usually the exception to the rule, Fig. 3.23 and Fig. 3.24 try to illustrate the spatial behavior of each vorticity equation term, at 60 min since fire flaming, at 50 m and 200 m agl, respectively.

As the active fire front advances north-west, the relative vorticity and the vorticity equation terms patterns between the two heights significantly differ. At 50 m agl (Fig. 3.23a), the flow in the plume rotates clockwise (max. 0.096 s^{-1}) at sideways and along the fire head, whilst two counter-clockwise vortices (max. 0.1 s^{-1}) are observed behind and in front of the fire head. It seems that this structure is two counter-rotating vortex pairs, which are vertically extended down to the surface, as this pattern is also observed at 3.1 m and 10 m agl (not shown). At 200 m agl (Fig. 3.24a), the rightmost anti-cyclonic vortex is consisted of three smaller vortices, the region with negative ζ values at 50 m agl above the fire line is now comprised of positive ζ values, while the leftmost vortex intensifies its strength (max. -



0.16 s^{-1}) and moves slightly to the north. In addition, the separated cyclonic vortices 150 m below are now merged to an extended V-shaped region with maximum value equal to 0.088 s^{-1} .

At 200 m agl, a dipole of positive and negative horizontal ζ vorticity advection is observed (Fig. 3.24b), with maximum values equal to $0.91 \text{ s}^{-1} \text{ m}^{-1}$ and $0.89 \text{ s}^{-1} \text{ m}^{-1}$, respectively. As it was previously discussed, vertical advection is more pronounced at 200 m agl (min. $-1.62 \text{ s}^{-1} \text{ m}^{-1}$, max. $2.83 \text{ s}^{-1} \text{ m}^{-1}$; Fig. 3.24c) than at 50 m agl (min. $-1.09 \text{ s}^{-1} \text{ m}^{-1}$, max. $0.96 \text{ s}^{-1} \text{ m}^{-1}$; Fig. 3.23c) due to higher vertical velocities. Negative values of the convergence term indicate that the flow either diverges under $\zeta > 0$ or converges under $\zeta < 0$. The flow divergence (convergence) compresses (stretches) the vortices, resulting in decreased (increased) relative vorticity. At 50 m agl (Fig. 3.23d), the convergence term contributes mostly negatively (max. $0.82 \text{ s}^{-1} \text{ m}^{-1}$) to the increase of relative vorticity, while aloft (Fig. 3.24d) positive and negative contributions of approximately same magnitude exist (-0.55 and $-0.5 \text{ s}^{-1} \text{ m}^{-1}$, respectively). Regarding the tilting term, horizontal vorticity is oriented vertically mostly at 200 m agl (Fig. 3.24e), where the dominance of positive values is evident. Although the solenoidal term is at least eight orders of magnitude less than the other terms, its patterns in both levels indicate sources and sinks of relative vorticity, which are more spatially expanded at 50 m agl, due to its proximity to the surface fire.

ext015m

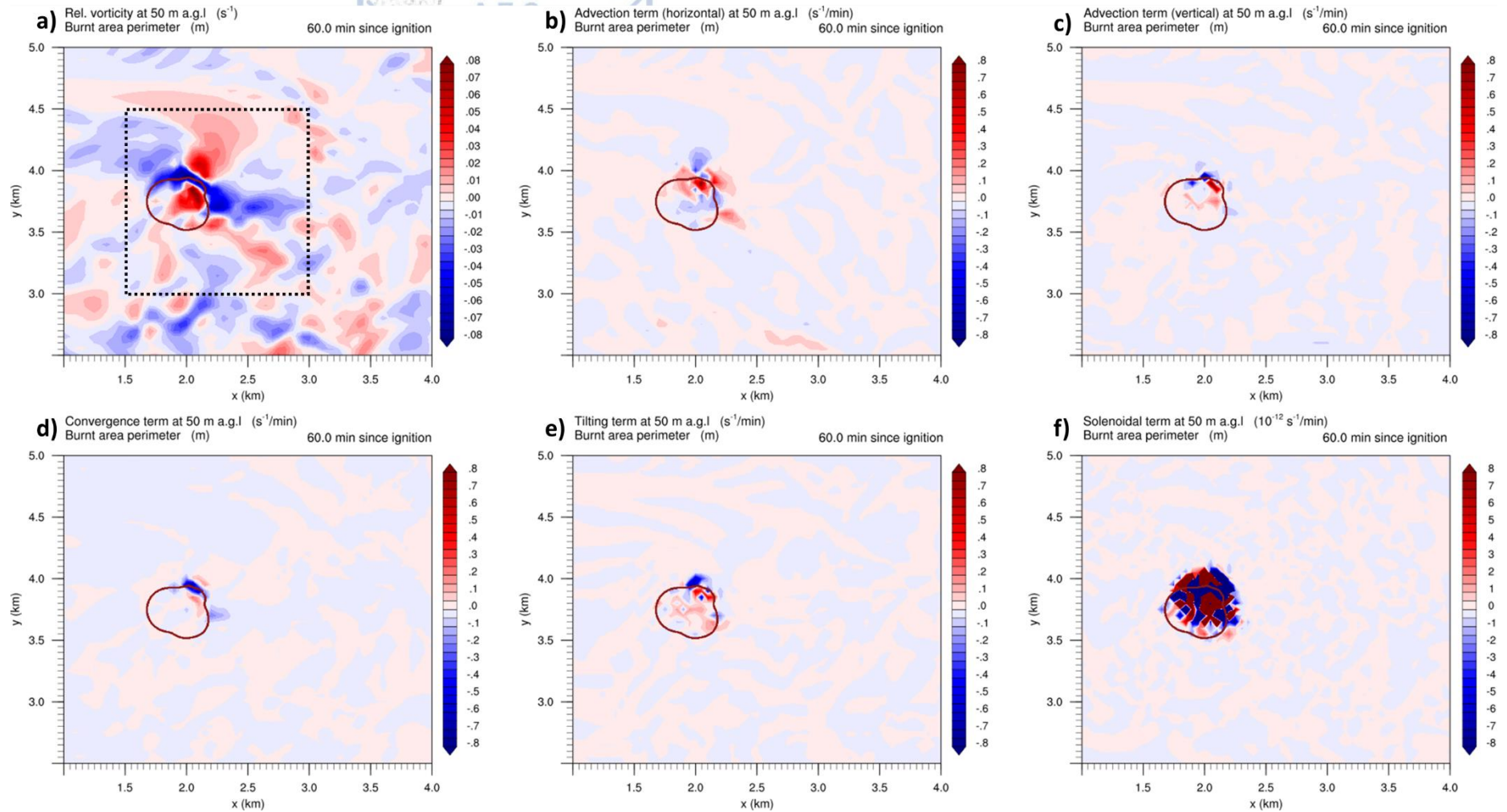


Fig. 3.23: Horizontal cross sections of a) relative vorticity (s^{-1}) and vorticity equation terms ($s^{-1} m^{-1}$) of b) horizontal and c) vertical advection, d) convergence, e) tilting/twisting and f) solenoidal, at 50 m agl, for ext015m experiment, at 60 min since fire ignition. The dark red contour line represents the fire perimeter at surface. The dashed black box encompasses the area in which the minimum and maximum values of each term were obtained (Fig. 3.21a,b, Fig. 3.22).

ext015m

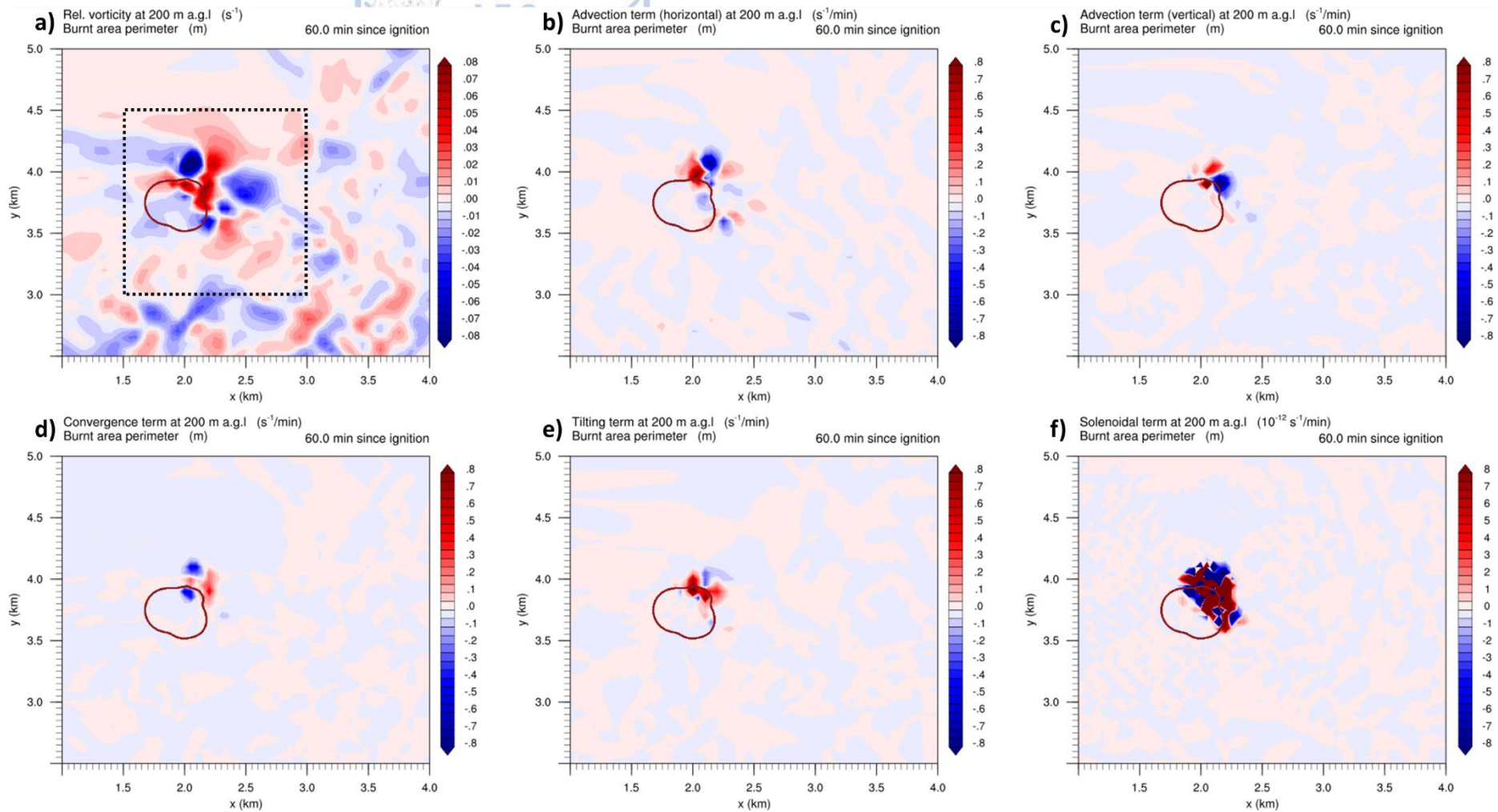


Fig. 3.24: As in Fig. 3.23, but at 200 m agl.

3.4 Discussion

This chapter presented a sensitivity study on how the released energy from a surface fire is vertically distributed via the e-folding depth concept into the lowest layers of the atmospheric domain, in WRF-SFIRE modelling system. Through a number of highly idealized numerical experiments in LES mode, the impact of different extinction depth values on a) the fire properties, b) near surface flow characteristics and c) atmosphere-fire interactions is investigated.

In WRF-SFIRE, the online coupling between the fire and the atmosphere is established by inserting the released heat fluxes from the fire to the lowest levels of the atmosphere, assuming an exponential decrease with height. The height where the fluxes are equal to the 0.36 of their initial value is constant in the code, but can be adjusted by the user. This concept originates from the Clark coupled atmosphere-fire model (Clark et al., 1996a), along with its default value of 50 m, albeit the authors did not provide any information upon its selection. Limited observational data (Coen et al., 2004) seem to encourage this choice, but a highly idealized study (Kochanski et al., 2013a) implied that it should be equal to the length of flames. Sun et al. (2006) pointed out the importance of a realistic extinction depth and its dependence on several parameters such as the fire intensity, flame height, burning fuel and the environment of the fire. They provided also an estimation by applying the Beer's law formula.

Whether this approximation is appropriate for parametrizing the energy distribution vertically or another formulation must be used, is something to be considered. The analysis showed that steady state propagation rates or "blow-up" conditions can be modelled under identical initial conditions by only changing a single constant. To its defence though, Cunningham et al. (2005) also included an exponential decay with height of the fire heat sources (theirs Eqs. 3.10 and 3.11), assuming a "scale height" of 25 m, as their extinction depth parameter. However, in their results, Moisseeva and Stull (2019) discussed potential limitations arising from the choice of heat extinction depth parameter mostly based on the preliminary results of the current analysis that were presented in Kartsios et al. (2017).

In addition, the horizontal and vertical discretization in atmospheric and fire model, respectively, and its influence on e-folding depth, is another factor that must be considered and examined. Simpson et al. (2014) investigated the impact of horizontal and vertical grid spacing to the formation of vorticity-driven lateral fire spread (VLS) and found certain discrepancies to the upslope and lateral rates of spread between high and coarser spatial resolutions, but they did not use different extinction depths to my knowledge. The latter could be the next step of the current analysis, in order to evaluate more thoroughly this interaction.

According to Skamarock (2004), the wavelength below which the simulated spectrum begins to decay relative to the natural spectra is defined as the "effective resolution" of a simulation. The author discussed how the energy at small-scale turbulence contains 10-100 times less energy than nature (his Fig. 3) in a 10 km WRF simulation and how the model damping affects the model spectral. In addition, he pointed out the dependence of the finest resolved scale motions on the formulation and tuning of implicit and explicit model filters. Coen (2018) provided a comprehensive discussion about energy dissipation during fire motions arising from buoyancy, stressing out the importance of model filters adjustment, the utilization of less dissipative closure schemes or the configuration in a LES mode in fire modelling.

In this study, the WRF-SFIRE modelling system was configured in LES mode and a 3rd order time integration scheme was utilized, while horizontal and vertical diffusion in physical space was treated by computing the eddy viscosities through a 1.5 order prognostic turbulence kinetic energy (TKE) closure. Moreover, tuning of the subgrid-scale stress tensor was performed through the Nonlinear

Backscatter and Anisotropy (NBA) filter (Mirocha et al., 2010), which is more appropriate when the buoyancy is important in the prognostic turbulent kinetic energy equation. Thus, a question rises, if the available 6th order spatial filter on coordinate surfaces (Kniewel et al., 2007; Skamarock et al., 2008; Xue, 2000) performs better in the explicitly treatment of the spatial diffusion or an alternative diffusion scheme must be adopted in the WRF code.

Since WRF is a fully compressible model, the prognostic equation for density requires very small time steps, thus increasing the computational cost, mainly because the acoustic waves are not filtered as in the anelastic set of equations in the Clark (Clark et al., 1996a), CAWFE (Coen, 2013) and MesoNH/ForeFire (Filippi et al., 2009) models. The basis of anelastic approximation is to speed up artificially the sound waves to infinity phase speed, so that every point in the atmosphere feels the impact of a perturbation simultaneously. Thus, the determination of the pressure is an implicit problem since it can not be solved point-by-point (explicitly) but for all grid points simultaneously. The latter practically means that pressure (actually its perturbation) is a diagnostic variable rather than a prognostic one, while the exclusion of the sound waves permits larger time steps and faster integrations times, but extreme temperature deviations truncate the most extreme vortices that might be produced (Coen, 2018). Sun et al. (2006) provided a short presentation of the anelastic approximation in the context of combustion-induced convection, as it was applied in the Clark model following the approach of Ogura and Phillips (1962), while they pointed out the model's inability to simulate fire convection without losing some vorticity production. On the contrary, in WRF and at each time step, mass continuity to machine error is not assumed, which potentially leads to numerical instability and early termination of the simulation, as it happened in the four out of eight experiments of the current study and apparently limited the analysis to a shorter time period. To the interested reader, Coen, (2018), also presents some pros and cons between compressible and anelastic systems.

Although the spin-up period prior to ignition was in line with other LES studies regarding fire modelling, it is believed that it was not enough in order to develop and equilibrate the boundary layer turbulence with the external forcing. Near the surface, the fire ignited under a well-mixed boundary layer, albeit near the west domain boundary, the flow was influenced strongly by the initial lateral conditions. Due to vertical wind shear, this influence was advanced eastwards at higher altitudes. Additional testing indicated that the spin-up time could be up to one hour since model initialization, albeit the impact of initial conditions was diminished and the model created its own weather. In a recent study upon buoyant rise and dispersion of smoke due to wildfires by Moisseeva and Stull (2019), a spin-up period of total of 2 h 23 min is utilized in order to achieve a well-mixed and developed boundary layer. Even though this was a very long spin-up time, it certainly added some extra validity to their results.

The Rothermel's rate of spread (RoS) model was formulated under the assumption that slope and wind effects are based on empirical fuel dependent coefficients, fitted to mid-flame height as the if the fire was not there. This clearly sets some limitations to the online feedback between the fire and the ambient atmospheric environment, as the feedback on the fire is from the wind that is influenced by the fire (Mandel et al., 2011). Different RoS formulas, such in Meso-NH/ForeFire (Filippi et al., 2009) or in CAWFE could potentially lead to a more realistic representation of the atmosphere-fire coupling close to the surface. Other possible limitations that inherit errors could be the disturbance of the assumed logarithmic profile due to strong heat fluxes and the horizontal wind interpolation method followed in this study. In addition, the Monin-Obukhov similarity theory may not fully apply in fire modelling, as the horizontal homogeneity is not satisfied (Mandel et al., 2011). Strong indicator of the aforementioned is the calculated diagnostic T2 variable, in which strong cooling was observed in the neighboring to the fire atmospheric grid cells.

3.5 Summary and conclusions

Eight highly idealized simulations were performed in order to investigate how the e-folding depth of the released sensible and latent heat fluxes from a surface fire into the lowest atmospheric computational domain of the WRF-SFIRE modelling system are affecting the evolution of the modelled fire. Since the vertical distribution of the fire's energy is not resolved explicitly in the coupled model but is parametrized by assuming an exponential decay with height, an assessment of the aforementioned formulation is necessary. Thus, in the control (CNTRL) experiment, the default extinction depth (z_{ext}) of 50 m was utilized, while in the rest seven sensitivity runs z_{ext} values equal to 5, 10, 15, 25, 75, 100 and 200 m were employed, respectively. Also, due to excessive local heating of the atmosphere in the column above the fire, vertical violations of the CFL (Courant–Friedrichs–Lewy) condition were encountered and the ext005m, ext010m, ext015m and ext025m sensitivities did not reach the forecast horizon (2.5 hours).

The analysis revealed that the choice of the z_{ext} parameter not only affects the vertical distribution of the fluxes but also the amount of the released energy from the surface fire. The higher the z_{ext} value, the higher the percentage of the released energy that resides on the first theta model level. For z_{ext} equal to 5 m it was found that only ~31.4% of the heat fluxes from the surface fire was entering into WRF (at 1st theta level), while for $z_{ext} = 200$ m, approximately 97% of the ground heat fluxes were inserted into the 1st theta level. Moreover, the results indicate that the height of the sigma levels can lead to further underestimation of the amount of the fire's energy that enters into the WRF domain, in the case where the z_{ext} value is lower than the first theta (mass) level. Since in real simulations the 1st theta level is usually much higher than in the experiments of this study, the latter must be taken into consideration upon configuration of the fire model. In addition, a linear behavior regarding the maximum injection height as a function of z_{ext} parameter was found.

In the surface, the ext15m sensitivity run produced the fastest advancing fire fronts, as rates of spread (ROS) equal to 5.97 m s^{-1} were simulated only in this experiment. The average ROS was 1.54 m s^{-1} , while in the rest experiments, the corresponding values were not greater than 0.5 m s^{-1} . The temporal evolution of the predicted fire area was in line with the temporal ROS peaks and found different in each experiment. Although in the ext200m run, the low ROS resulted to low fire area growth rates during the first 20 min since ignition, this simulation produced the largest burnt area (18.0 ha). At the end of the analyzed period (60 min since ignition), the ex015m model run presented the second largest fire area (17.4 ha), while the CNTRL experiment predicted the smallest (14.2 ha).

The calculated burn probabilities revealed that under identical initial atmospheric conditions but different e-folding depths discrepancies may occur in the resulted fire area, but the most profound deviations were found beyond the analyzed period, at 120 min since fire flaming, by utilizing only the available model results (CNTRL, ext075m, ext100m and ext200m). Consistent with Kochanski et al. (2013c), probabilistic fire predictions may be required in order to evaluate the predicted fire behavior.

The so called "power of the fire" was also examined, revealing differences in the released energy from the surface fire both in time and magnitude between experiments. The ext015m presented the highest temporal heat output peak (~41,000 MW), which led to erratic fire behavior and "blow-up" conditions at the end of the analyzed period. At the same time window, the maximum heat output in the ext005m run was found equal to ~33,000 MW, causing CFL violations and early termination of the simulation. In ext200m model run, heat release rates higher than 8,000 MW (max. ~13.100 MW) are produced in the middle of the analysis, resulting to high fire area growth rates.

The coupled WRF-SFIRE model was able to reproduce certain flow characteristics from the literature (Banta et al., 1992; Palmer, 1981; Potter, 2012b) such as the convergence region ahead of the fire front

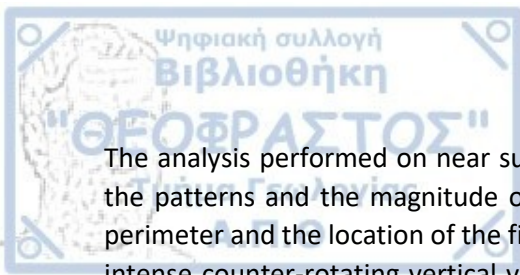
(Clark et al., 1996b, 1996a) and the descending rear inflow to the updraft's base. The interactions between the ambient environment and the surface plume resulted into the formation of two main longitudinal horizontal vortices, which acted as inflow to the front of the half-upper part of the fire plume or interacted mostly with the surface. A possible mechanism is the reorientation of the shear-generated horizontal components of vorticity (ω_x , ω_y) in the ambient atmosphere due to the presence of fire plume and the convergence that occurs in vertical, while the stability profile of the atmosphere or even the presence of the inversion layer aloft could also have contributed to their formation.

The highest vertical velocities were simulated in the ext015m experiment (max. 34.3 m s^{-1}) as a response to the high amount of released energy from the ground, but one should keep in mind the relatively small frequency of the model outputs (every 5 minutes). Thus, higher values could be encountered. The latter is in line with the IR video imagery analysis (Coen et al., 2004) during the FROSTFIRE experiment, which indicated instantaneous upward velocities of 60 m s^{-1} . The strongest downdrafts were also met in the ext015m sensitivity (max. 11.4 m s^{-1}), at $\sim 43 \text{ m agl}$. Both maximums (upward and downward velocities) were encountered during the blow up conditions, at 60 min since ignition. In addition, the vertical distribution of upward velocities in almost all experiments (except in ext025m) resembled that in Reid and Vines (1972), where higher velocities were presented around 2 km agl and were decreasing up to the plume top.

The direct volume rendering (DVR) of vertical wind component, at 60 min since ignition, showed that due to weak vertical wind shear and the strong updraft speeds, the convective column was characterized by a single column of ascending air and almost no tilting, mostly in experiments with z_{ext} less than 50 m. The strongest downdraft cores were located at the inversion layer, which acted as an upper limit to the strong convection. The absence of a single updraft column, multiple updraft cores and blended regions of weak upward motions are some common features in the experiments with $z_{\text{ext}} > 50 \text{ m}$.

In general, an increase of the z_{ext} parameter leads to weaker time-averaged potential temperature anomalies both close to the ground and in the top of the convective plume. However, the temporal peaks in theta anomalies do not follow any linearity and their occurrence varies both in time and space. In all experiments, the absolute minimum potential temperature anomaly occurred at 1st theta level ($\sim 5.8 \text{ m}$), while the maximum theta anomaly is met at 1st theta model level only in the CNTRL, ext005m, ext010m, ext015 and ext025m experiments. For the ext075m, ext100m and ext200m sensitivity runs, the maximum theta anomaly is located at 6th ($\sim 71.5 \text{ m}$), 11th ($\sim 155.7 \text{ m}$) and 9th ($\sim 119.5 \text{ m}$) mass level, respectively. Strong negative potential temperature anomalies were observed in ext015m (max. 207.3 K) and less intense minima in the rest experiments, revealing the need for further investigation and interpretation of this mechanism.

Time-mean plume-averaged properties were calculated in each sensitivity run and compared with the CNTRL's corresponding values, up to 2 km agl. Negative differences in plume vertical velocities were calculated in ext075m, ext100m and ext200m up to $\sim 1 \text{ km agl}$ and positive aloft, while positive differences were observed in ext005m, ext010m, ext015m and ext025m experiments up to 2 km agl. In the layer between $\sim 1200 \text{ m}$ and $\sim 1300 \text{ m agl}$, all experiments presented thinner plumes than in CNTRL, which coincided with the regime of higher vertical velocities in this layer. The vertical profiles of mass flux presented mostly negative discrepancies up to $\sim 1200 \text{ m agl}$ (except in ext200m sensitivity) compare to CNTRL's one and positive differences aloft. Close to the ground and specifically up to $\sim 18 \text{ m agl}$, all simulations but two (ext100m and ext200m) produced higher water vapor plume excesses than CNTRL, while discrepancies on plume temperature excesses occurred up to $\sim 600 \text{ m agl}$. Aloft the differences became essentially zero against to CNTRL's vertical profile.



The analysis performed on near surface dynamics at 30 min since ignition revealed discrepancies in the patterns and the magnitude of vertical vorticity and divergence fields, in the shape of the fire perimeter and the location of the fire head. Low e-folding depth values produced more organized and intense counter-rotating vertical vorticity pairs and regions along the fire flanks and in front of the active fire head, whilst in the sensitivities with z_{ext} greater than 50 m, this vorticity was less organized and more transient.

The vorticity equation budget analysis showed that the solenoidal term, which generates vorticity, was up to twelve orders of magnitude less than the other terms. During the “blow-up” conditions in ext015m sensitivity run, the latter amplified its strength up to four orders, in line with the findings of Clark et al. (1996b), where the vertical advection term presented the highest maximum among the other terms. In CNTRL experiment and at 50 m agl, the horizontal advection of vertical vorticity contributed the most to the increase of vorticity, while the tilting/twisting term was dominant at the early stages of the fire, where the ambient shear-generated horizontal vorticity, ω_y , was oriented into vertical due to buoyant gradients from the surface fire.



Chapter 4

Numerical investigation of atmosphere-fire interactions during extreme fire events in Attica region

4.1 Introduction

Extreme fire events are usually associated with atmospheric conditions at different spatial and temporal scales (Pereira et al., 2005) and are characterized by their duration (Amraoui et al., 2015), severity and the socioeconomic impact on the aftermath. Weather and climate define the favorable conditions in which these fire events may occur, affecting fuel properties such as fuel moisture and fuel accumulation.

The Mediterranean basin had experienced some of the most devastated fires in the last two decades, for example, the large fires of 2003 and 2005 in Portugal and on 2006 in Spain (Amraoui et al., 2013). The summer of 2007 was the worst year on record for forest fires in Greece, where extremely hot and dry weather conditions, combined with strong winds led to a disastrous upsurge of forest fires and wildfires, evidence of a synergy of fuel and weather (Knorr et al., 2011; Koutsias et al., 2012).

Moreover, the severity of fire events related to climate or weather extremes (Founda and Giannakopoulos, 2009; Tolika et al., 2009) from one hand and fuel accumulation and previous fire history (Minnich, 2001) from the other, has been investigated (Keeley and Fotheringham, 2001; Minnich, 2001). Under strong human pressure, the relationship between fire regimes and natural vegetation may be altered, even the climatic conditions are not favorable for fire occurrence (Vázquez et al., 2002). According to Moriondo et al. (2006), climate change will increase the fire risk over Mediterranean countries due to the increase in the number and the length of seasons with fire risk but most importantly because of the increase of extreme events.

A number of fire danger indices (presented in Chapter 1 of this manuscript), which combine meteorological and fuel information into a single value, have formulated the severity of a potential wildland fire or its suppression difficulty (Dowdy et al., 2009). Many of them are part of fire danger rating systems around the globe, such as the Canadian Forest Fire Danger Rating System (CFFDRS; Van Wagner, 1987) and the US National Fire Danger Rating System (NFDRS; Deeming et al., 1977). In the Eastern Australia, the McArthur Forest Fire Danger Index (FFDI; McArthur, 1967) is used while in the western parts, the Forest Fire Behavior Tables (FFBT; Sneeuwjagt and Peet, 1985) were established. In the framework of the European Forest Fire Information System (EFFIS, <http://effis.jrc.ec.europa.eu>), the EFFIS Danger Forecast module (San-Miguel-Ayanz et al., 2019) forecasts forest fire danger in Europe, part of North Africa and the Middle East, on the basis of the Canadian Fire Weather Index (FWI; Van Wagner, 1987; Van Wagner et al., 1985). Also, many European countries (mostly at south) use their own fire danger rating systems. For example, in Greece, the General Secretariat of Civil Protection produces daily fire risk thematic maps during the fire season (May-October), while the Spanish National Forestry Service uses the Spanish forest fire index or the recently adopted FWI in its system (Mestre et al., 2009). Dimitrakopoulos et al. (2011) provided a comprehensive presentation of the most established fire danger rating systems worldwide.



In the Mediterranean region, past rural areas have turned into secondary homes, enlarging the wildland urban interface (WUI). The majority of fire events is reported also there, while about 80% of the total burnt area in Europe concerns areas in this region. Among the natural, social and economic impacts, human casualties (civilians and firefighting crews) are the worst outcome in a fire event. During the period 1982-2007, the number of victims in Portugal and Spain was 110 and 186, respectively (Viegas, 2009), while in Greece 78 civilian lost their lives in the tragic events of the summer of 2007 (177 in total during 1980-2007). However, on 23rd of July 2018, the Greek nation faced another tragedy, where 103 civilians entrapped and lost their lives (directly or on the aftermath) due to extreme weather conditions, which led to aggressive fire behavior.

Although the impact of topography into atmospheric flow and fire behavior have been described (Butler et al., 1998; Conedera et al., 1998; Haines and Lyon, 1990; Millán et al., 1998; Miller and Schlegel, 2006; Rothermel, 1993; Sharples, 2009; Sharples et al., 2012; Simpson et al., 2013, 2014, 2016), the role that mountain meteorological phenomena play on overall fire behavior is still an active field of research. In general, fire-propagation modelling assumes that a fire spreads at quasi-steady fire spread (Thomas et al., 2017), under a certain set of environmental conditions. Dynamic or extreme fire behavior can occur due to spatial and temporal variations in meteorological conditions and variations in fuel spatial distributions. As a result, the safety of the fire fighting forces and civilians may be compromised unexpectedly. In a complex terrain and under low wind speeds (McCutchan and Fox, 1986), the uneven surface heating due to slope and aspect variations can affect the local weather conditions and fire behavior. Sharples (2009) provided a brief description of the key mountain meteorological phenomena that affect fire behavior (bushfires) such as, dynamic channeling, foehn winds, low-level jets and mountain waves.

Durrán (1990) presented the fundamentals of the atmospheric motions occurring in a gravity wave forced by mountains (mountain wave), and introduces downslope windstorms along the lee slope. Helmis et al. (2000) analyzed the results of an experimental study of downslope winds at Hymettus Mountain at Attica region, Greece and compared the observations with the Hydraulic-Like Theory (Long, 1955, 1953). Also, Koletsis et al. (2009) through numerical simulations showed that certain conditions such as the presence of a cross-barrier flow, a stable layer above mountain top and a critical level affected the wind speeds on the lee side during a wind event at northwest Greece. In literature, both observational and numerical studies (Clark and Peltier, 1984; Doyle and Durrán, 2004; Doyle and Jiang, 2006; Durrán and Klemp, 1987; Fudeyasu et al., 2008; Klemp and Lilly, 1975; Peltier and Clark, 1979; Sun, 2013) have been applied in order to investigate the flow structure of severe downslope winds associated with mountain waves. However, the linkage between mountain waves and fire behavior has been addressed to a smaller degree (Nauslar et al., 2018; Sharples et al., 2010; Simpson et al., 2013) and this was one of the motivations for this study.

The first aim of this chapter is to present the two fire events that took place on 23rd of July 2018 at Attica region in Greece and to analyze the prevailing weather conditions in the wider area. The synoptic/mesoscale analysis revealed the presence of mountain waves. Thus, the second aim is to investigate the interaction between the complex terrain and atmospheric flow, and how the latter affected the overall fire behavior.

In section 4.2, the two fire events are presented, while in section 4.3 the analysis and observational data, the numerical model and the methodology employed are described. Section 4.4 presents the synoptic analysis and the weather conditions according to the available surface observations. In section 4.5, the existence of mountain waves in the airflow is discussed, while in section 4.6 the results of the numerical experiments are presented. Finally, section 4.7 discusses and section 4.8 summarizes and concludes the findings of this study.

4.2 Description of the events

On 23rd of July 2018 two wildfires broke out at Attica region (Central Greece), under strong westerly - northwesterly flow, high temperatures and low values of relative humidity. According to the National Observatory of Athens (NOA), wind gusts exceeded 27 m s^{-1} at several sites of Attica that day, while the Automated Weather Station (AWS) in Penteli Mt. (close to the fire event) recorded gusts reaching 25 m s^{-1} between 1230 and 1430 UTC (Lagouvardos et al., 2019). At approximately 09:03 UTC (12:03 LT), a wildfire was reported in Gerania Mts., at "Aeras" location, north west of Kineta settlement (KINETA fire from now on), at regional unit of West Attica. The wider area is part of the European Network of Protected Areas – Natura 2000 (http://ec.europa.eu/environment/nature/natura2000/data/index_en.htm). According to the records of the Hellenic Fire Service, ground and air fire fighting forces were mobilized immediately (47 vehicles, 150 fire fighters, 4 Canadair aircrafts, 7 helicopters). The settlements of Galini, Maroula and Panorama were evacuated, while the fire was active until the late hours of the 25th of July 2018, totally burning two settlements (Panorama I-II and Galini), while Kineta settlement was partially burnt.

Nearly 4.5 hours later, at 13:49 UTC (16:49 LT), a fire-spot was reported at Kallitehnoupolis settlement (Ntaou) on Penteli Mt. (Municipality of Rafina), at East Attica regional unit (MATI fire onwards). Unofficial reports (e.g. video footage) presented that the fire ignition time was 8 minutes prior to the officially reported time (13:49 UTC), while at the first hours of the event, the Hellenic Fire Service was declaring 13:57 UTC as ignition time. The fire-fighting operation initially consisted of 60 fire fighters, 39 vehicles, 2 ground forces teams, 3 Canadair aircrafts and 1 helicopter, but quickly became evident that the air forces were unable to operate due to the strong wind field. Under such extreme windy conditions, the fire spread fast towards east through Kallitehnoupolis, Neos Voutzas, and Rafina settlements, where it finally stopped at the coastal area of Mati in less than 2 hours. In addition, the fuel type (mostly Mediterranean pine species such as *Pinus halepensis*) and fuel loading of the area, assisted the intensification of the event. Dimitrakopoulos and Panov (2001) quantified the chemical and physical properties of several dominant species in the eastern Mediterranean Basin. They found that *Pinus halepensis* presents high mean values of surface area-to-volume ratio (leaves, 62.49 cm^{-1}) and relatively low mean particle density (leaves, 0.29 g/m^3), thus high heat and moisture exchange rates (Brown, 1970) and lower thermal conductivity, meaning faster ignition times (Anderson, 1970), respectively. The aforementioned, in conjunction with the special morphology of the area (wild-urban interface) and the narrow streets resulted to minimal response times by the inhabitants and the local authorities. The tragic aftermath was 103 loss of lives (the majority of them were entrapped by the fire), the settlements of Neos Voutzas, Rafina, Mati and Kokkino Limanaki burnt with over 1500 structures and vehicles burnt or damaged, while parts of electricity, water supply and telecommunication networks greatly affected. According to the Hellenic Fire Service, the fire was totally suppressed the next day (24th of July 2018). During the events of the 23rd of July 2018, Hellenic authorities requested assistance through the European Community Civil Protection Mechanism.

4.3 Data and numerical modelling system

For the purposes of this study, available surface observations, satellite imagery, data from the Copernicus Emergency Management Service - Mapping, global model analyses and regional model simulations were utilized. Also, time series of available surface observations at Attica region (Fig. 4.1b) were obtained from the Hellenic National Meteorological Service (HNMS). The record data consist of 2m air temperature ($^{\circ}\text{C}$) and relative humidity (%), wind speed (m s^{-1}) and direction (degrees), wind

gust speed at last 10 min and 3 hrs ($m s^{-1}$) and daily precipitation (mm) and span from 22nd (00Z) to 24th (12Z) of July 2018 at 30 min intervals. In addition, panchromatic visible (0.4 to 1.1 μm) Meteosat SEVIRI images (0°E) from the NERC Satellite Receiving Station at Dundee University were examined, in order to distinguish key features of the synoptic flow and cloud formations. Also, burnt areas, in shape file format (.shp), were extracted from the Copernicus EMS (Emergency Management Service) – Mapping platform (event EMSR300, <https://emergency.copernicus.eu/mapping/list-of-components/EMSR300>), while Sentinel-2A L1C images (True and False color) were used as additional information (only for the KINETA event). Moreover, the MODIS (Moderate Resolution Imaging Spectroradiometer) Fire and Thermal Anomalies product acquired from the Terra (MOD14) and Aqua (MYD14) satellites (Giglio et al., 2003) with spatial resolution of 1 km and the 375 m I-band data from the Visible Infrared Imaging Radiometer Suite (VIIRS) on Suomi NPP satellite (Schroeder et al., 2014) were retrieved for interpretation and validation purposes.

Synoptic analysis was carried out by employing the operational gridded analyses of European Centre of Medium Range Weather Forecasts (ECMWF) at pressure levels up to 10 hPa, with $0.1^\circ \times 0.1^\circ$ (latitude-longitude) grid spacing. At this grid resolution, synoptic and sub-synoptic scale features of the flow are resolved properly but certain flow characteristics (e.g. mountain waves) with wavelengths smaller than ~ 9 km are not captured.

The numerical modelling system WRF-SFIRE (Mandel et al., 2011, 2014) was adopted in order to simulate the two fire events under high fire weather severity. In Chapter 2, section 2.4 a brief introduction to the system is provided. The version 3.4.1 of the WRF-ARW model (Wang et al., 2012) was utilized as the available release in the WRF-SFIRE distribution. WRF-SFIRE has been positively evaluated and implemented both in real and idealized cases (Dobrinkova et al., 2011; Farguell et al., 2017; Jordanov et al., 2012; Kartsios et al., 2017, 2014b, 2014a, Kochanski et al., 2013a, 2013b, 2013c; Kochanski et al., 2016; Peace et al., 2011; San Jose et al., 2015; Simpson et al., 2013, 2014).

The domain setup (Fig. 4.1a) consisted of three, 2-way telescoping nests, which covered parts of Southeast Italy, South Balkans, Greece and West Turkey (d01, 308 x 239 x 39 grid points), Central Greece and Peloponnese (d02, 259 x 193 x 39 grid points) and Attica region (d03, 283 x 205 x 39 grid points), of horizontal grid sizes 5 km, 1.67 km and 0.55 km, respectively. In vertical, 39 sigma levels, up to 50 hPa were manually defined, with increased resolution in the boundary layer. The first theta level (where variables like temperature and humidity are calculated) located at approximately 10 m above terrain height. The fire module was activated in the innermost domain (d03), where the surface fire mesh had a refinement ratio 1:20, which corresponds to ~ 27.77 m horizontal fire-grid cell size. Initial and boundary conditions for the outer domain were extracted from the ECMWF operational analyses ($0.1^\circ \times 0.1^\circ$ lat.-long.), at 6-hourly intervals. Model initialization was placed at 00Z on 23rd of July 2018, almost 9 hours prior to the fire ignition at Gerania Mts. (KINETA event), while the simulation time window was 36 hours. Model output was available every 5 minutes, at hourly intervals and every 3 hours for the finer (d03), intermediate (d02) and the coarser (d01) domain, respectively. The first 6 simulated hours were considered as model “spin-up” and were not included into the analysis. The spin-up time is of paramount importance in order the model to derive a valid physical state (Ulmer and Balss, 2016) and it has been considered in several numerical modelling studies (e.g. Koletsis et al., 2016; Matsangouras et al., 2016; Pytharoulis, 2018; Pytharoulis et al., 2018, 2016; Weiss et al., 2008; Yair et al., 2010).

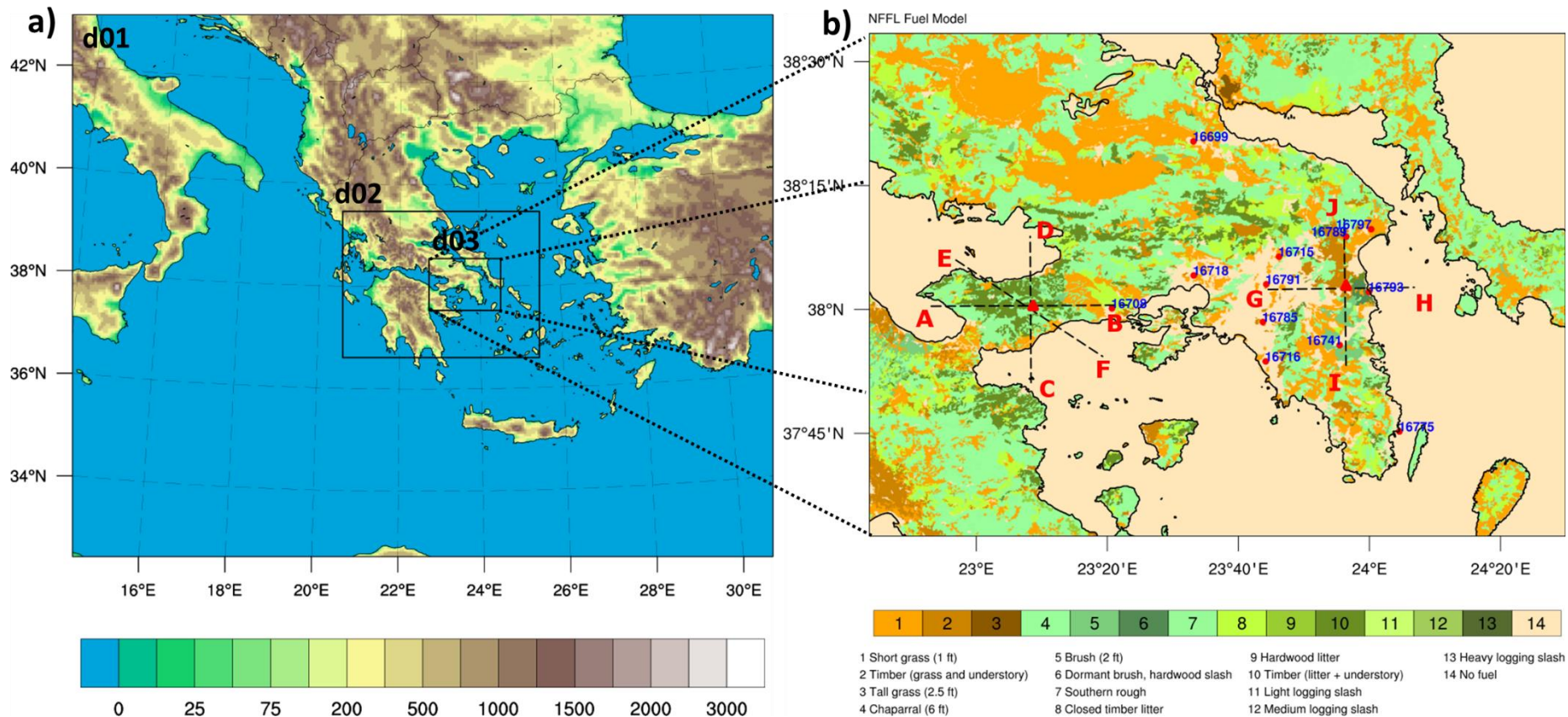


Fig. 4.1. a) Domain configuration with topography (shaded) and b) innermost domain (d03) extent, NFFL fuel spatial distribution (shaded), locations of HNMS surface stations (red dots) along with their corresponding WMO code and fire ignition points (red triangles) at KINETA and MATI events. The dashed lines indicate the locations of the cross-sections in Section's 4.6 figures (Figs. 4.12, 4.13, 4.13).

The wind field from the atmospheric model has been inserted to the spread rate formula by first vertically interpolated to common height (6.096 m), using the roughness length values from land use and then multiplied by prescribed wind reduction factors (Baughman and Albini, 1980; Mandel et al., 2011). Although a number of options, which control the process of the wind digestion to the fire model, are available, the aforementioned choice was based on its simplicity and computational efficiency. Additional information on the different methods of wind digestion from WRF to SFIRE model can be found on Chapter 2 of this manuscript. The heat fluxes from the fire assumed to exponentially decrease with height through the heat extinction depth formulation. As the 1st theta model level was placed at approximately 10 m agl, the default value of 50 m was used as e-folding depth. The role of the latter to the fire behavior was addressed in the previous chapter (Chapter 3) of this manuscript. Also, the fuel-moisture model (Mandel et al., 2014) was activated, allowing proper responses between fuel moisture and atmospheric conditions, while fire emissions were available as passive tracers (smoke).

Land use representation was based on CORINE Land Cover (CLC) 2006 data (100 m x 100 m) mapped and interpolated to the 1km-resolution IGBP-MODIS vegetation classification. Moreover, a soil texture map for Europe at 1 km based on the HWSD (Harmonized World Soil Database) v1.2 was inserted to the model as additional information (Josipa et al., 2014). The SFIRE demands very fine spatial resolution topographical and fuel data, in order to represent accurately the sub-grid variability in topography and fuel composition. Thus, the Shuttle Radar Topography Mission data (SRTM v3, 30 m x 30 m, 1 arc-sec, Farr et al., 2007; NASA JPL, 2013) were retrieved, properly converted and digested into the innermost domain (d03) and the fire model. The horizontal resolution of the SRTM dataset is approximately equal to the fire-grid discretization, ensuring properly calculated slope gradients (Mandel et al., 2011). Description of the available fuels at Attica region (d03) was achieved by reclassifying CORINE 2012 raster data (v18, 100 m x 100 m) into fuel models according to the Northern Forest Fire Laboratory (NFFL) classification (Anderson, 1982) and resampling them (nearest neighbor) into 30 m x 30 m spatial resolution (Fig. 4.1b). Lacking any finer resolution fuel dataset, publicly available for Greece and already converted into NFFL fuel models as well, the conversion matrix (Table 4.1) was based on literature regarding Mediterranean ecosystems (Benali et al., 2016; Duguay et al., 2007; Jordanov et al., 2012; Kalabokidis et al., 2012; Sá et al., 2017; Sebastián López et al., 2002). Each NFFL fuel category (13 in total) is associated with specific fuel properties, such as fuel density, depth and mass, surface to volume ratio, mineral content and moisture of extinction, which are provided externally to the fire module. Although these fuel properties were based on field work in the United States, no any adjustments were considered. In addition, in the area of the devastating fire at Kallitehnoupolis, the originally assigned NFFL fuel type 2 (Timber) was replaced by the NFFL fuel type 6 (Dormant brush), in order to represent in a more accurate way the actual fuel conditions.

The parameterization of microphysical processes was carried out by the Eta-Ferrier scheme (ETA; Rogers et al., 2001). The RRTMG scheme (Iacono et al., 2008) was used, at 5 minutes intervals, for the shortwave and longwave radiation, with the slope effects option active in order to modify the surface solar radiation flux according to terrain slope. Boundary layer processes were represented by the Mellor-Yamada-Janjic scheme (MYJ; Janjić, 2002, 1994), surface layer by the Eta similarity scheme (Monin and Obukhov, 1954; Janjić, 2002, 1996, 1994), based on Monin-Obukhov with Zilitinkevich thermal roughness length, while the soil properties and land-atmosphere interactions were described by the Unified Noah Land Surface Model (NOAH; Chen and Dudhia, 2001; Tewari et al., 2004). The Betts–Miller–Janjic scheme (BMJ; Janjić, 2002, 1994) was responsible for the parameterization of sub-grid convection. The convection scheme was activated only in the outer nest (d01), following other numerical studies in the wider Mediterranean region (Karacostas et al., 2018; Kotroni and Lagouvardos, 2004; Lagouvardos et al., 2013; Pytharoulis et al., 2016; Sindosi et al., 2012). The model physics configuration was consistent in all three domains, while it has been used during the operational

period (2013-2015) of Wave4Us (Wave climate and coastal circulation Forecasts for public Use; <http://wave4us.web.auth.gr>) project. Although the domain configuration was different in the operational model, this physics suite has been verified and found to be in good agreement with the observations (Pytharoulis et al., 2015; Krestenitis et al., 2017)

The NCAR Command Language (v.6.4.0) and its special routines were used for the analysis of the numerical experiments and the production of the graphics in this study, while the GNU Fortran Compiler was also utilized in various source codes. The numerical experiments performed in the National HPC facility – ARIS, by computational time granted from the Greek Research & Technology Network (GRNET), under project ID-PR005025_thin.

Table 4.1. Conversion matrix of CLC 2012 land uses to NFFL fuel models (Anderson, 1982).

GRID_CODE	CLC_CODE	CLC_Description	NFFL	NFFL_Description
1	111	Continuous urban fabric	14	No fuel
2	112	Discontinuous urban fabric	14	No fuel
3	121	Industrial or commercial units	14	No fuel
4	122	Road and rail networks and associated land	14	No fuel
5	123	Port areas	14	No fuel
6	124	Airports	14	No fuel
7	131	Mineral extraction sites	14	No fuel
8	132	Dump sites	14	No fuel
9	133	Construction sites	14	No fuel
10	141	Green urban areas	2	Timber (grass and understory)
11	142	Sport and leisure facilities	1	Short grasses (30 cm)
12	211	Non-irrigated arable land	1	Short grasses (30 cm)
13	212	Permanently irrigated land	1	Short grasses (30 cm)
14	213	Rice fields	14	No fuel
15	221	Vineyards	5	Brush (61 cm)
16	222	Fruit trees and berry plantations	2	Timber (grass and understory)
17	223	Olive groves	8	Closed timber litter
18	231	Pastures	1	Short grasses (30 cm)
19	241	Annual crops associated with permanent crops	3	Tall grass (76 cm)
20	242	Complex cultivation patterns	1	Short grasses (30 cm)
21	243	Land principally occupied by agriculture, with significant areas of natural vegetation	7	Southern rough
22	244	Agro-forestry areas	2	Timber (grass and understory)
23	311	Broad-leaved forest	9	Hardwood litter
24	312	Coniferous forest	10	Timber (litter and understory)
25	313	Mixed forest	8	Closed timber litter
26	321	Natural grasslands	1	Short grasses (30 cm)
27	322	Moors and heathland	6	Dormantbrush, hardwood slash
28	323	Sclerophyllous vegetation	4	Chaparral (183 cm)
29	324	Transitional woodland-shrub	7	Southern rough
30	331	Beaches, dunes, sands	1	Short grasses (30 cm)
31	332	Bare rocks	14	No fuel

32	333	Sparsely vegetated areas	2	Timber (grass and understory)
33	334	Burnt areas	8	Closed timber litter
34	335	Glaciers and perpetual snow	14	No fuel
35	411	Inland marshes	1	Short grasses (30 cm)
36	412	Peat bogs	5	Brush (61 cm)
37	421	Salt marshes	14	No fuel
38	422	Salines	14	No fuel
39	423	Intertidal flats	14	No fuel
40	511	Water courses	14	No fuel
41	512	Water bodies	14	No fuel
42	521	Coastal lagoons	14	No fuel
43	522	Estuaries	14	No fuel
44	523	Sea and ocean	14	No fuel

4.4 Synoptic Analysis and Observational Data

The prevailed synoptic conditions, which greatly influenced the behavior and evolution of the two extreme fire events in the Attica region on 23rd of July 2018, are presented below along with the available surface observations.

According to the ECMWF operational analyses on 23/07 00Z, at 500 hPa, a low upper air system was dominating north and east of Greek region, while a southwest-northeast oriented short wave trough was developed west of North Italy, over Sardinia. Moreover, a high upper air system was located over Atlas Mountains in North Africa, at 500 hPa, with its eastern flank elongating southwest of Greece. As a result, a west-northwest flow was prevailing over the area of interest (Fig. 4.2a). This synoptic pattern was coherent in vertical, resembling the zonal flow circulation type, according to Karacostas et al. (1992) and Karacostas (2003) synoptic classification. Also, the position of the subtropical jet stream coincided with the mid-tropospheric baroclinic zone, where wind speeds of above 55 m s^{-1} were presented into its core (Fig. 4.2a). The area of interest was located at the right flank of the jet stream exit, which is associated with subsidence. In the following hours, the short wave trough moved eastwards and merged with the low upper air system resulting in a closed long wave trough with no significant deepening on the isoheights, while the position of the upper air ridge remained almost unchanged (Fig. 4.2b, c, d). In addition, the 500 hPa geostrophic wind (Holton and Hakim, 2012) on 23/07 at 12Z was calculated over Greece and found equal to approximately 20.5 m s^{-1} .

Examination of potential temperature field at 850 hPa (Fig. 4.3a) reveals an eastwards cold air advection (CAA) over the Greek area (23/07, 12Z), which produced isentropic downglide and sinking as it will be described later. The west-northwest flow is also evident, while the wind speed at that level was above 20 m s^{-1} over the central and southern Greece. The Met Office surface analysis chart at 12Z on 23/07 depicts an upper troposphere cold front, moving southeastwards (Fig. 4.3c), which dissipated after a few hours and influenced the area of interest (Attica region). In addition, on 23/07 at 12Z, a relative weak south–east mean sea-level pressure (MSLP) gradient (Fig. 4.3b,c) is presented, while the calculated geostrophic wind (over Greece) of approximately 8 m s^{-1} is comparable with the wind speed field extracted from the ECMWF analyses (Fig. 4.3d). Also, the 2m air temperature gradient between western and eastern Greece is noticeable (23/07, 12Z), where the temperature lied above $36 \text{ }^\circ\text{C}$ over the eastern parts (Fig. 4.3b) and the 2m relative humidity dropped below 20% (not shown) according to analyses.

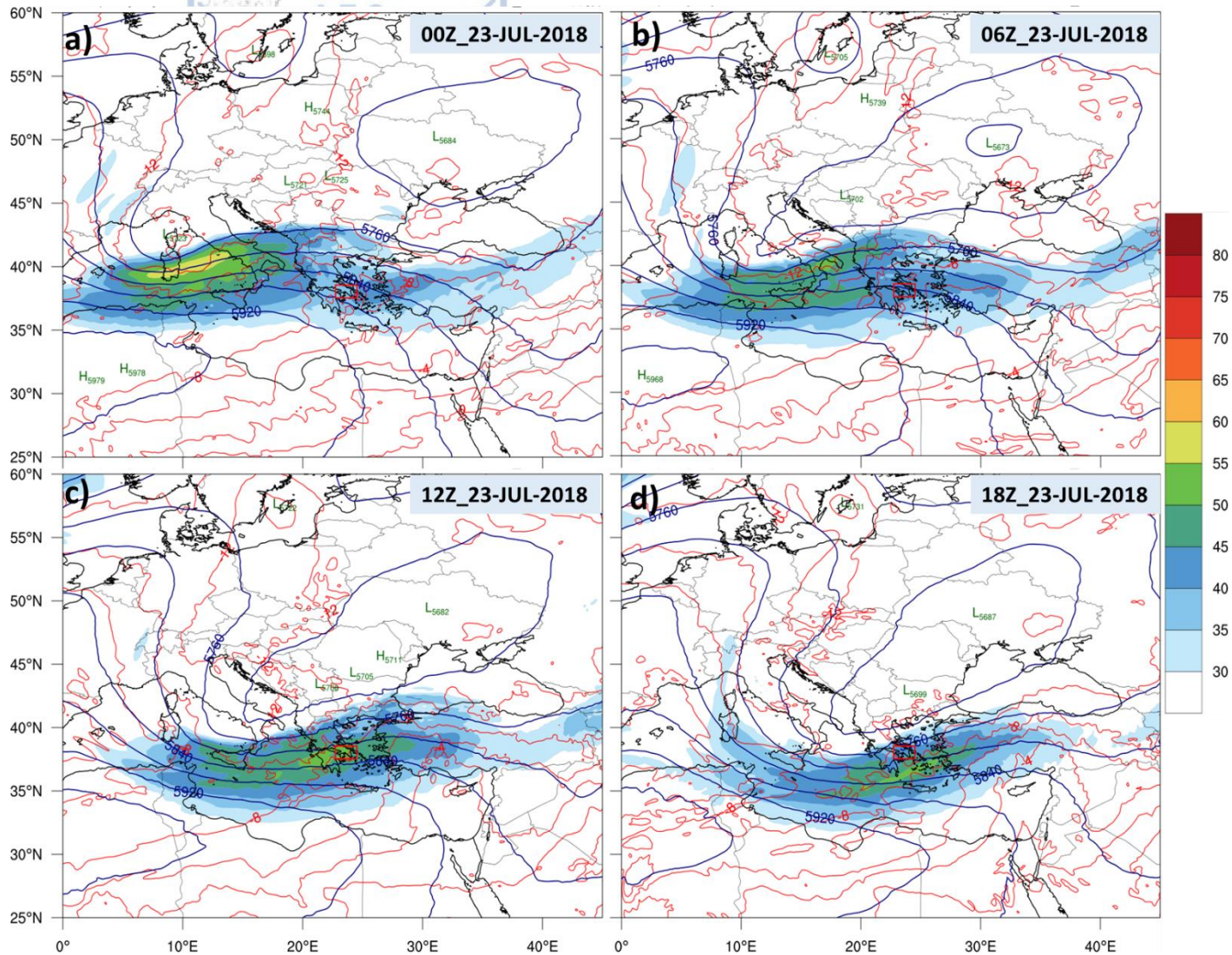


Fig. 4.2. Horizontal sections of geopotential height (gpm, blue contours) and temperature ($^{\circ}\text{C}$, red contours) at 500hPa and wind speed (m s^{-1} , shaded contours) at 250hPa on 23th July 2018 at a) 00Z, b) 06Z, c) 12Z and d) 18Z, according to operational ECMWF analyses. Red box covers the area of interest (Attica region).

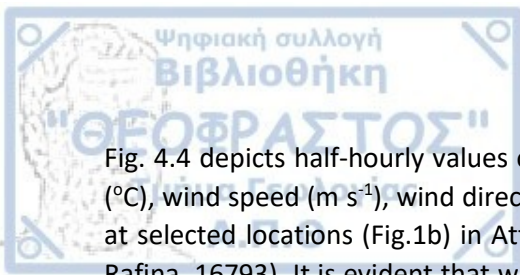


Fig. 4.4 depicts half-hourly values of 2m air temperature ($^{\circ}\text{C}$) and calculated dew-point temperature ($^{\circ}\text{C}$), wind speed (m s^{-1}), wind direction (degrees) and wind gusts (m s^{-1}) from 23/07 00Z to 24/07 00Z at selected locations (Fig.1b) in Attica region (Elefsina, 16718; Ellhniko airport, 16716; Tatoi, 16715; Rafina, 16793). It is evident that windy conditions persisted from 07Z until 22Z, where the maximum wind speed (gust) record at Elefsina was 16.6 (23.6) m s^{-1} , 8.4 (15.3) m s^{-1} at Ellhniko, 9.3 (15.9) m s^{-1} at Tatoi and 11.8 (25.2) m s^{-1} at Rafina station. For the same period, Elefsina, Ellhniko and Tatoi experienced lower maximum temperatures (37.4 $^{\circ}\text{C}$, 34.8 $^{\circ}\text{C}$, 36.0 $^{\circ}\text{C}$, respectively) than Rafina (39 $^{\circ}\text{C}$). Also, the maximum temperature at Ellhniko was 3°C higher than the climatological mean for July (31.8 $^{\circ}\text{C}$), while at Tatoi, the difference was 3.9 $^{\circ}\text{C}$ (max. 32.1 $^{\circ}\text{C}$) according to HNMS. Moreover, at Rafina station, a rapid increase on temperature values is observed between 09Z and 11Z with simultaneously decrease in relative humidity below 15%, resulting in increased potentiality for extreme fire behavior (Sharples, 2009; Sharples et al., 2010). At the same time, a nearly 180° change in wind direction is evident and was not related with the passage of the upper cold front that was depicted on Fig. 4.3c. According to analyses, the cold front influenced the area of interest a few hours later (between 12Z and 18Z). The increased wind speed and gust records along with the approximately westerly flow were observed at all available HNMS stations, due to the previously presented synoptic forcing. In Appendix III (Fig. C.1), time series of the recorded wind gusts from all available stations are provided.

In Fig. 4.5, time series of the calculated Fosberg Fire Weather Index (FFWI) (Fosberg, 1983) are presented for the available HNMS stations from 23/07 00Z to 24/07 00Z. The FFWI was calculated according to Eq. 1.11 by utilizing the equilibrium moisture content given by Eq. 1.13. According to Fig. 4.5, medium to high fire weather severity was presented nearly at all HNMS stations, while at Elefsina and Kotroni sites, the FFWI escalated rapidly to very high values, at specific time windows since 12Z (max. 74.15 and 74.13 , respectively). At Megara, which is the closest available observational HNMS station to KINETA event, fire risk was estimated as high from 13Z and afterwards (max. 52.4). Moreover, variations in FFWI level are observed at Rafina until 12:30 UTC, while at the time of the fire ignition at Kallitethnopolis settlement, the fire risk was high (max. 57.1).

FFWI presents stronger dependency on wind speed and relative humidity rather than temperature (Roads et al., 1991). Under windy, dry and relative warm conditions, higher FFWI values are expected. The latter could explain why at Rafina, lowest values of FFWI were presented despite the higher observed temperatures in comparison to other sites, such as Elefsina and Kotroni.

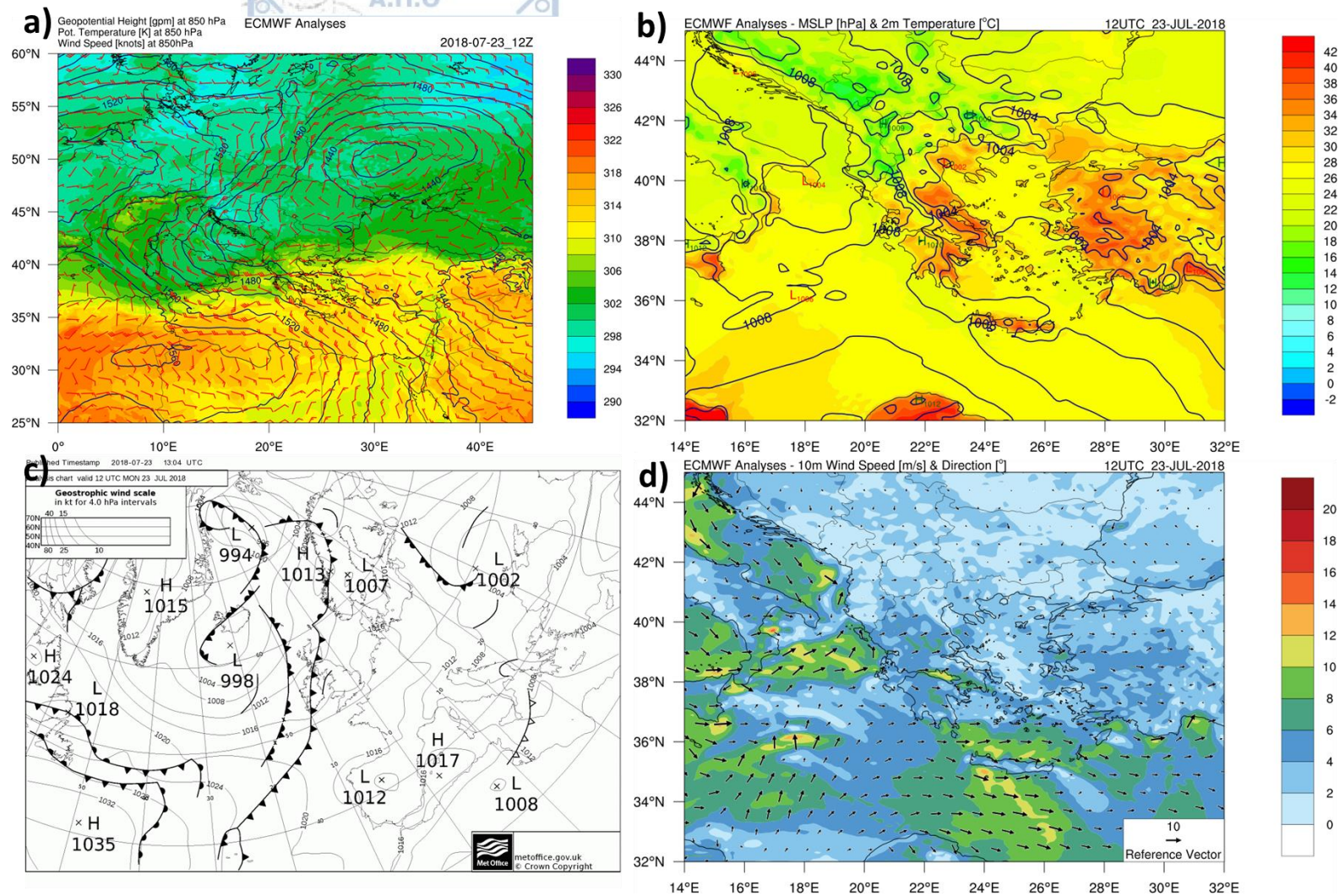


Fig. 4.3. a) ECMWF analysis of geopotential height (gpm, contours), potential temperature (K, shaded contours), wind speed and direction (knots, windbarbs) at 850 hPa, b) mean sea-level pressure (hPa, contours) and 2m air temperature (°C, shaded contours), c) Met Office surface analysis chart of mean sea-level pressure (hPa) and position of fronts and d) 10m wind speed ($m s^{-1}$, shaded contours) and direction ($^{\circ}$, arrows), on 23/07/2018 at 12Z.

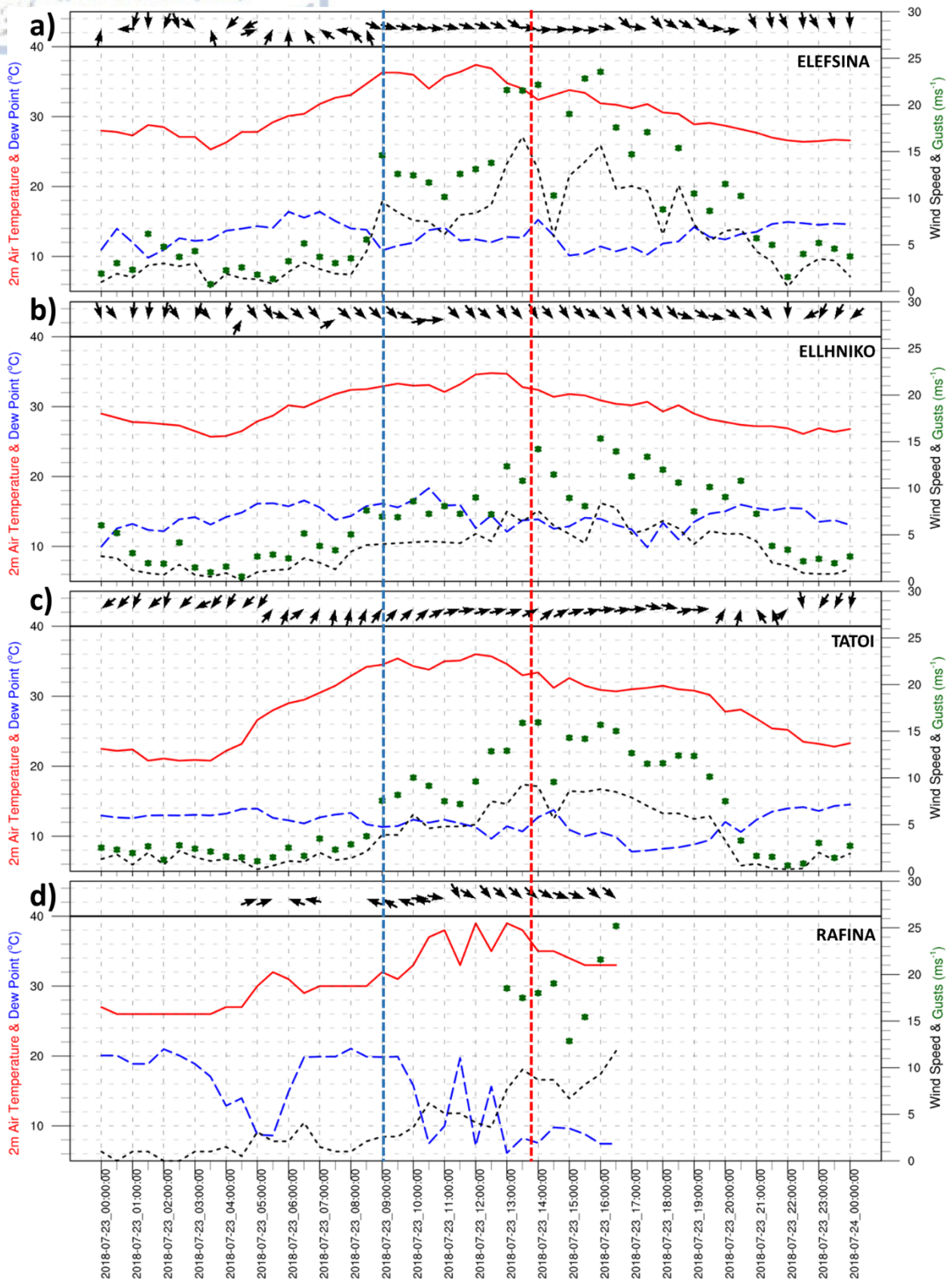


Fig. 4.4. Air temperature (red line) and dew point temperature (blue dashed line) at 2m ($^{\circ}\text{C}$), 10 m wind speed (black dashed line) and wind gusts (green asterisks) of the previous 10 minutes (m s^{-1}) and wind direction (arrows, degrees) at a) Elefsina(16718), b) Ellhniko (16716), c) Tatoi (16715) and d) Rafina (16793) HNMS stations, on 23rd of July 2018. Blue and red vertical dashed lines indicate the ignition time at KINETA and MATI fire events, respectively.

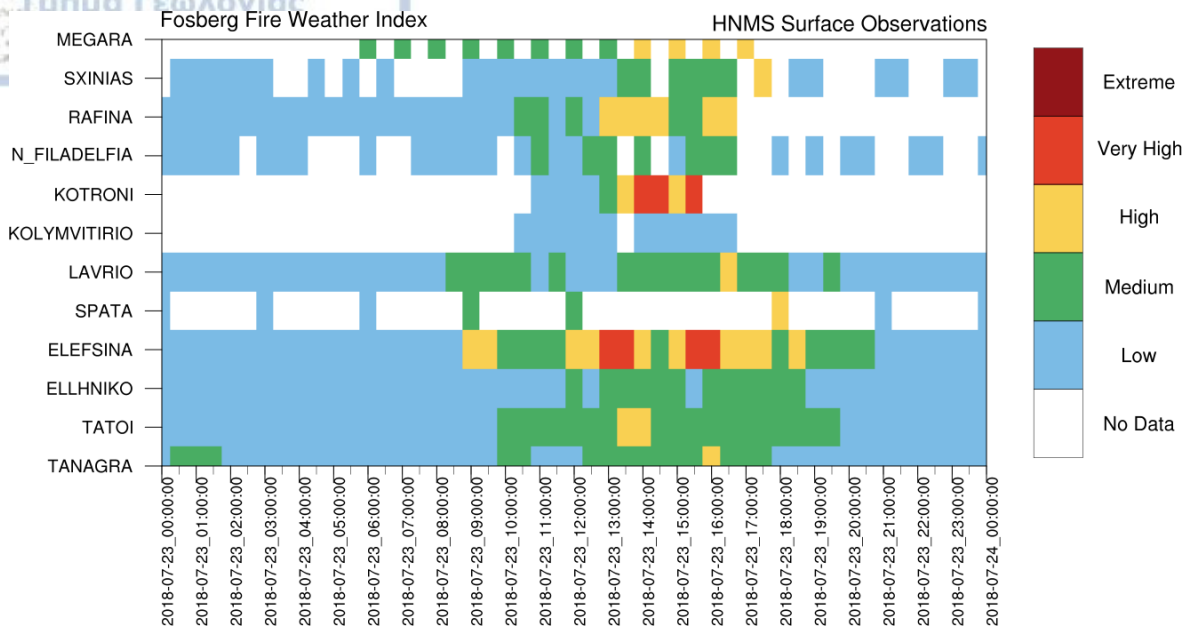


Fig. 4.5. Calculated Fosberg Fire Weather Index (FFWI) according to surface observations at available HNMS stations in the Attica region, from 23/07 00Z until 24/07 00Z. See Table 1.6 for details on classification values.

4.5 Airflow modification and mountain waves

The surface ECMWF analyses represent the magnitude of wind speed, temperature and relative humidity variations to some degree upon the area of interest but fail to capture the embedded variability mostly due to relatively coarse temporal and spatial resolution. In fact, the moderate background westerly flow led to local airflow modification (Barry, 1992; Whiteman, 2000) due to the presence of topographic barriers. Under certain conditions, the presence of mountain waves over the wider area of Attica resulted to the development of strong katabatic winds at the lee side of any barrier perpendicularly oriented to the flow in the region (Helmis et al., 2000).

In literature, mountain waves are recognized either as vertically propagating or trapped lee waves (Barry, 1992; Gill, 1982; Whiteman, 2000). The Scorer parameter (Scorer, 1949) is a stability factor that can determine the type of the wave and in a case of trapped lee waves what wavelengths will be trapped. It is defined as (Barry, 1992; Beer, 1974; Scorer and Klieforth, 1959):

$$l^2 = \frac{N^2}{U^2} - \frac{1}{U} \frac{\partial^2 U}{\partial z^2} \quad (4.1)$$

where $N(z)$ is the Brunt-Väisälä frequency and $U(z)$ is the vertical profile of the horizontal wind speed, perpendicular to the barrier. If l^2 (m^{-2}) is nearly constant with height, vertically propagating waves are expected, while if l^2 presents a rapid decrease with height, conditions are favorable for the formation of trapped lee waves (Sharples, 2009). The second term on the right-hand declaring the effects due to large shear of the vertical wind profile, usually is omitted, since Scorer (1949) assumes an undisturbed flow upstream of a mountain chain. Sawyer (1960) calculated streamlines showing wave development as a function of $l^2(z)$, which presented general agreement with the available observations. Also, if l_{low}^2 is calculated for a lower layer of thickness H and l_{up}^2 is for the upper layer, then the condition,



determines if waves are formed.

$$l_{low}^2 - l_{up}^2 > \frac{\pi^2}{4H^2} \quad (4.2)$$

Formation of mountain waves premises that a flow is capable of overcoming the barrier. Froude number (Smolarkiewicz and Rotunno, 1989; Stull, 1994), defined as:

$$Fr = \frac{U}{Nh} \quad (4.3)$$

where U is the normal wind component to the barrier, h is the height of the mountain and N the Brunt-Väisälä frequency, provides information whether the flow will be blocked ($Fr \ll 1$), will flow over the barrier without significant oscillations ($Fr \gg 1$), or there is a chance for orographic waves ($Fr \approx 1$).

Fig. 4.6a depicts longitude – pressure section of potential temperature (K) and u-wind component ($m s^{-1}$) at 38°N on 23/07 at 06Z, prior to the KINETA fire ignition. Locations of the KINETA and MATI fire events leeward of Gerania Mts. and Penteli Mt. are marked with black and red short lines, respectively. The fast isentropic lifting windward and descent downwind of Gerania Mts. (black line mark), along with the upwind deceleration of the flow and the rapid increase of the u-wind speed at the lee side (downwind jump), declares the presence of induced orographic waves (Fudeyasu et al., 2008). As a result, warm air advection from lower to higher layers is occurring while at the same time dry and cold air descends lower. Due to lifting of moist layers (Theta-E), clouds are expected, which is in agreement with the observed cloud formations from the satellite images (Fig. 4.8).

From 22°E to 24°E, the theta contours are nearly vertical at specific regions near the surface implying near-adiabatic conditions and almost neutral static stability (Bluestein, 1992; Young, 2003), which ranges from 0.02 to 0.06 K hPa⁻¹ (Fig. 4.6b). Moreover, two regions of increased stability (Fig. 4.6b) are observed west of 22°E (black line). A wide area from 18°E to 22°E, with maximum values at 900 hPa and aloft of Gerania Mts. at the same isobaric level (0.13 K hPa⁻¹), implying faster oscillations (e.g. larger Brunt-Väisälä frequencies), maximum displacements of the air parcels and fast horizontal wave speeds (Young, 2003). The former area covers the northern part of Peloponnese, where complex terrain is present across the section. Downwind of the Penteli Mt. (red line mark) and eastwards, the lower troposphere is also subjected to vertical displacements, however to a lesser degree, mostly due to the presence of the southern part of Euboea. In addition, calculated wavelengths (λ), $2\pi/l(z)$, of the potential formed waves are presented in Fig. 4.6b, where between Gerania Mts. and Penteli Mt., wavelength values below 2km are shown.

By applying the threshold criterion of Eq. 4.5 on 23/07 at 06Z, formation of waves was possible at the lower troposphere as it is depicted in Fig. 4.7a. In addition, examination of Scorer's parameter, $l(z)$, with height (Fig. 4.7b) revealed a strong decrease with height above certain longitudes (specifically in the region where the isentropic lifting occurs west of Gerania Mts.). The latter, in conjunction with the vertical decrease in static stability (Fig. 4.7c) and the sharp increase of wind speed, favored the development of trapped lee waves (Barry, 1992; Sharples 2009). Although the aforementioned is valid for the majority of the longitudes across the section, there are regions such as aloft Gerania Mts. or from 21°E and westwards where $l(z)$ presents near or moderate decrease with height and increased stability. Hence, the presence of vertically propagated waves cannot be excluded. In fact, the backwards tilting with height (Fig. 4.6a) of the isotachs at the location of Gerania Mts. (black line mark), resembles the pattern of vertically propagating waves (Durrant, 1986; Houze, Robert A., 1993; Young, 2003).

In addition, the formation of waves is supported by the values of Froude number (Fig. 4.7c, contours), which are below but close to unity up to 850 hPa. For the calculation of Froude number by Eq. 4.6, h was considered equal to 1300 m as the maximum height of Gerania Mts. The vertical tilting of the 0.5 contour line between Gerania Mts. and Penteli Mt., is also worth noticing, since the formulation of the Froude number is a function of wind speed across the mountain. Richardson number, Ri , (Fig. 4.7c, shaded contours) lies between 0.3 to 1, along the solid contour line (value equal to unity) of Froude's number and in a limited area around Gerania Mts., closed to the surface. This implies that possibly the flow was dynamically unstable and turbulent at these regions, although Richardson number never gets values below critical ($Ri_c = 0.25$). However, in the following hours Ri was smaller than 0.25 close to the surface and in the area of interest (Gerania Mts – Penteli Mts) with the Froude number equals to unity at the same time.

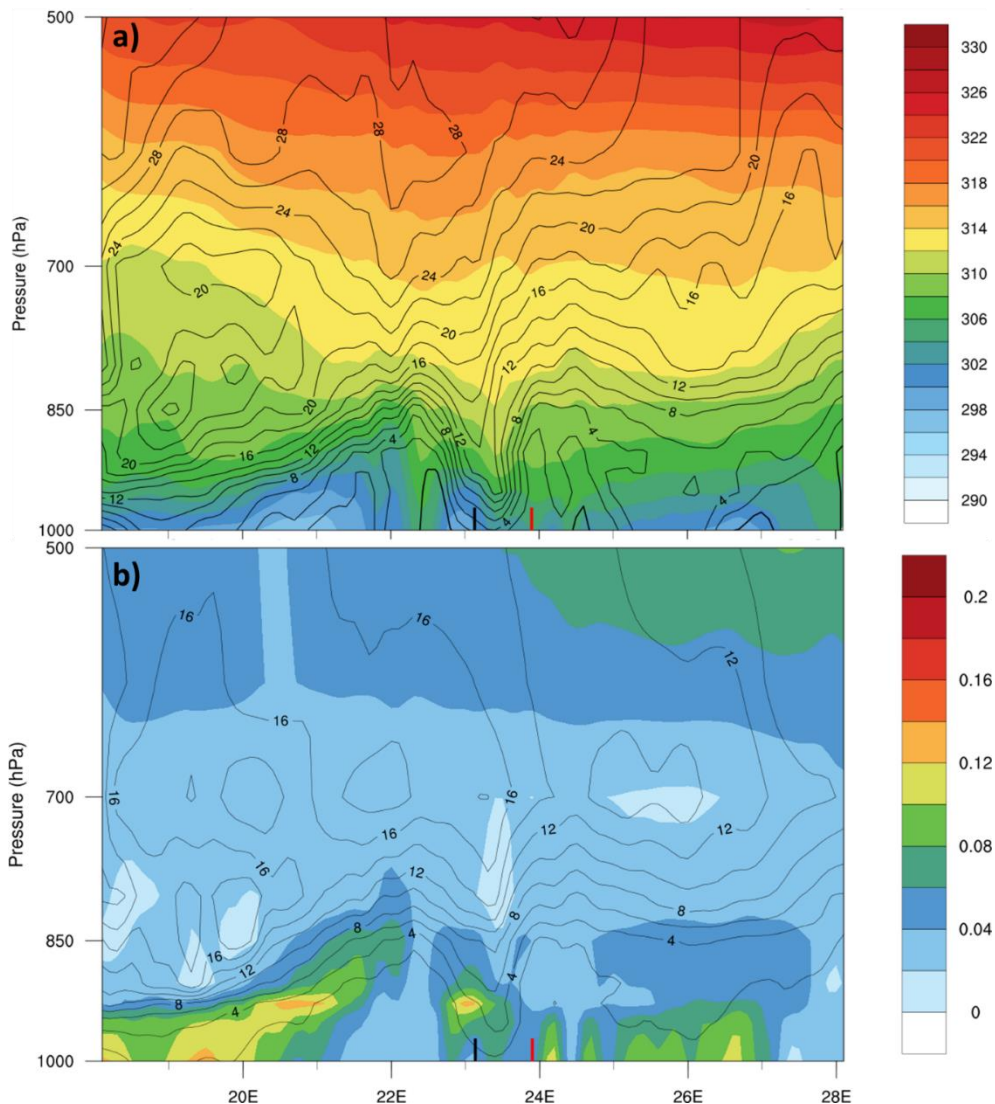


Fig. 4.6. Longitude – pressure section of a) potential temperature (K, shaded contours) and u -wind component ($m s^{-1}$, contours) and b) static stability ($K hPa^{-1}$, shaded contours) and wavelengths (km, contours), at $38^{\circ}N$ on 23/07 at 06Z (ECMWF operational analyses). Black and red line marks indicate the locations of Gerania Mts. and Penteli Mt., respectively.

Moreover, examination of satellite images (MeteoSat SEVIRI $0^{\circ}E$), at hourly basis from 06Z to 17Z on 23rd of July 2018, revealed areas with distinctive cloud formations which were related with the

presence of trapped lee waves west of Greece and also above west and north Peloponnese (Fig. 4.8a). However, as the upper cold front moved southeastwards and affected the wider area of Central Greece, rotor clouds begun to develop over Attica region, associated with turbulence and strong, localized and transient surface winds (Doyle and Durran, 2004; Sharples, 2009). This could also explain the observed wind gusts at the HNMS stations (Fig. 4.4). The lifting of the flow due to the presence of the Pindus mountain range resulted to condensation and cloud formation to its west (Fig. 4.8b), while bands of free cloud areas are observed downwind and possibly are related with the descending parts of the formed waves.

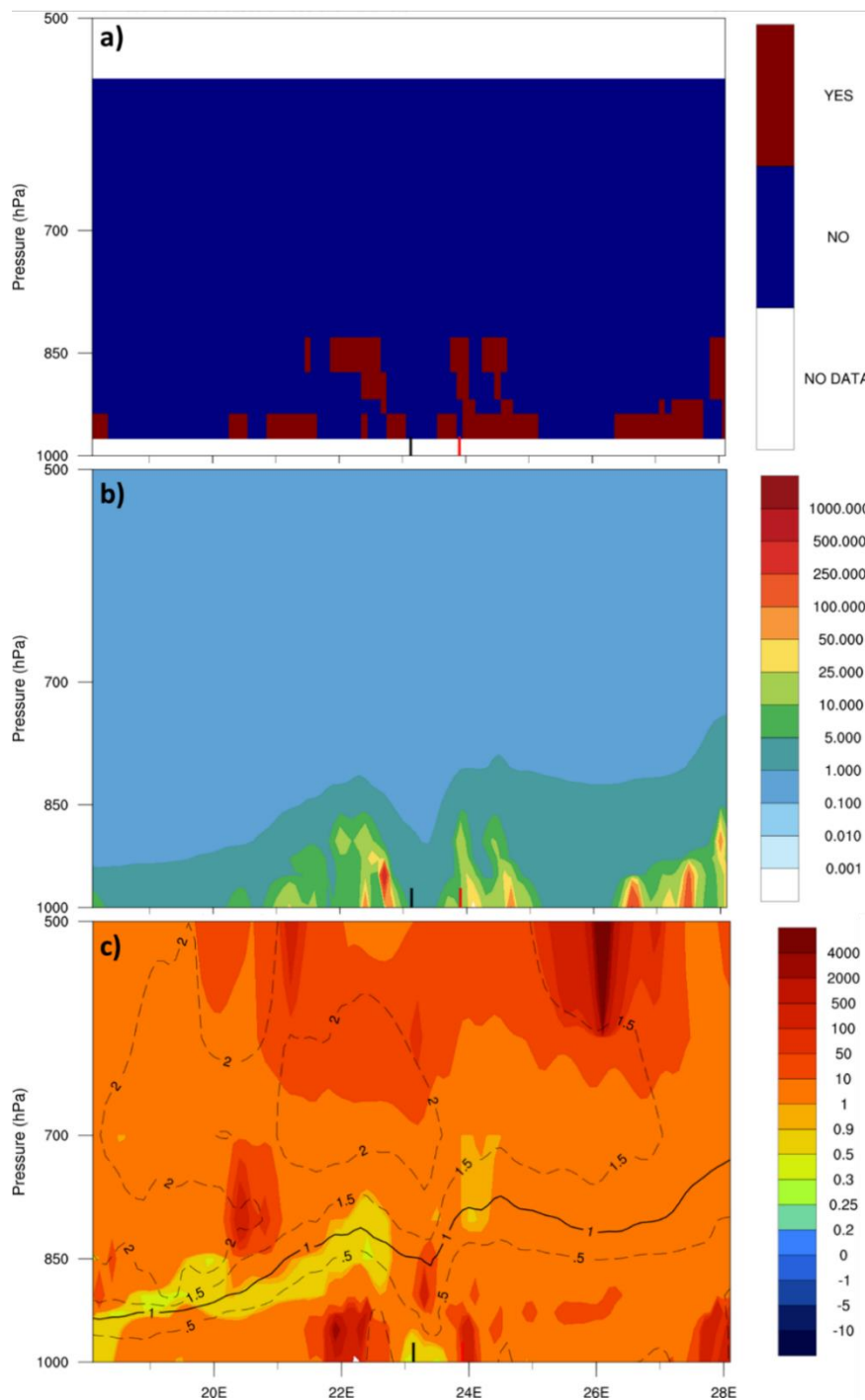


Fig. 4.7. Longitude – pressure section of a) condition threshold for wave formation, b) Scorer's parameter (km^{-1}) and c) Richardson (shaded contours) and Froude (contours) numbers, at 38°N on 23/07 at 06Z (ECMWF analyses). Black and red line marks indicate the locations of Gerania Mts. and Penteli Mt., respectively.

Lacking any upper air observations (sounding) in the wider area on 23rd of July 2008, vertical profiles of temperature, dew point and wind speed and direction were extracted from the WRF-D03 initial conditions (interpolated ECMWF analyses) at a location (37.9510N, 23.148°E) downwind of Gerania Mts. at 06Z. The analysis (Fig. C.2, Appendix III) revealed the presence of a very shallow inversion closed to the surface, nearly neutral conditions up to 900 hPa and stable layers aloft. Absence of any inversion at higher levels, the mechanism proposed by (Klemp and Lilly, 1975) which associates downslope windstorms with partial reflection or breaking of a vertical propagating mountain wave cannot be supported. In addition, ECMWF analyses data did not show any significant vertically change in wind direction above the mountain chains of Peloponnese and Attica region, and consequently the presence of, either a mean-state critical layer, in which there is a totally reverse of the flow (Doyle and Jiang, 2006), or a self-induced critical layer, where wave-overturning occurs in a region of locally reversed flow (Clark and Farley, 1984; Clark and Peltier, 1984, 1977). If such critical layers exist, then the wave energy may be reflected under certain conditions back to the surface, resulting in strong downslope winds (Durrant, 1990; Durrant and Klemp, 1987; Smith, 1985; Weisman and Klemp, 1986).

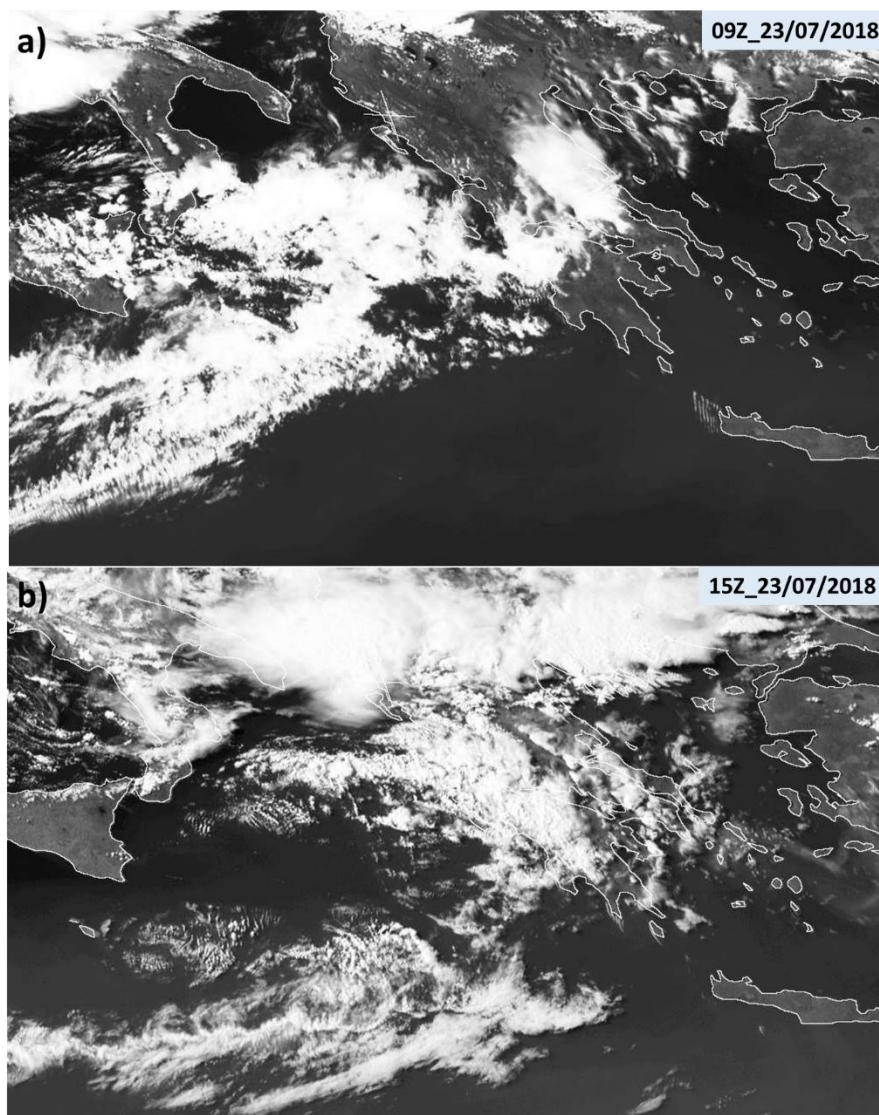
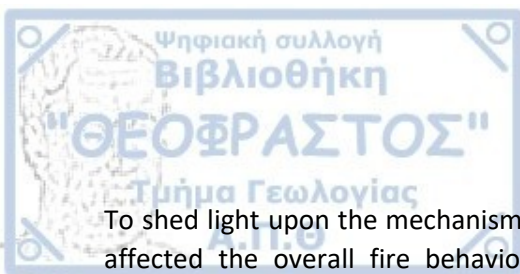


Fig. 4.8. Panchromatic Meteosat images (SEVIRI, 0°E) of 0.4 to 1.1 μm of the central Mediterranean Sea at a) 09Z and b) 15Z on 23rd of July 2018. Source: NERC Satellite Receiving Station, Dundee University, Scotland (<http://www.sat.dundee.ac.uk>).



To shed light upon the mechanisms that produced such windy conditions over the Attica region and affected the overall fire behavior at KINETA and MATI events, high spatiotemporal resolution numerical simulations were utilized. In the next section, an analysis of the prevailing weather conditions on 23rd of July 2018, along with the simulated fire behavior in both events is presented. The hindcasts were performed with the WRF-ARW numerical model, as it was described in Section 4.3.

4.6 Numerical simulations

The meteorological conditions along with the two extreme fire events on 23rd of July 2018 were simulated by utilizing the WRF-SFIRE modelling system. In total, four (4) experiments, with very high spatial and temporal resolution were performed in order to address the role of topography into the development of mountain waves and the associated fire behavior in each event. The control experiment (CNTRL) was based on the model configuration described in Section 4.3. In TOPOG and TOPOP experiments, the topography of Gerania Mts. and Penteli Mt. was removed, by setting the corresponding grid points equal to zero in all domains, respectively. Also, a 3 grid point smoothing was applied at the borders of each area, in order to avoid numerical instabilities due to the produced steep slopes. In NTOPO experiment, the topography of the innermost domain (d03) was completely removed in all nests, following the methodology in Pytharoulis et al. (2016). At all sensitivity experiments (TOPOG, TOPOP, NTOPO) the model configuration remained the same as in CNTRL experiment.

4.6.1 Model verification

Statistical evaluation was carried out in the CNTRL experiment at innermost (d03) domain, using all the available HNMS surface observations (12 stations). The first six (6) hours were not accounted in the results (spin-up) and the model verification was performed from 06:00 UTC on 23 July 2018 to 12:00 UTC, on 24th of July 2018. Each forecast value was obtained by first finding the four (4) grid points closest to the location of the observation and then applying the Inverse Distance Weighting (IDW) interpolation method (Isaaks and Srivastava, 1989; Li and Heap, 2014).

Also, the Cressman (Colle et al., 1999; Cressman, 1959; Sindosi et al., 2015) and the 4 grid point (Sindosi et al., 2012) methods were employed in order to investigate the sensitivity of the model performance to interpolation method. In Cressman method, an inverse distance formula was used but the calculation of the weights at the four surrounding grid points was slightly different from the classic IDW method. It is noted that if the distance of a grid point from the observation was higher than the spatial resolution of the model, that grid point was omitted and its weight was considered equal to zero. In the 4 grid point method, the grid point with the smallest absolute difference from the observation was picked as the forecast value. If the previous criterion was met more than once, then the closest grid point from the sample to the observation was considered. At all interpolation methods, the model grid points over the sea were filtered from the calculations.

The model was verified in terms of 2m air temperature (T_{mp}), 2m relative humidity (Rh) and 10m wind speed (W_{spd}) for all the pairs of forecast versus observed values. The errors (model – observation) with their corresponding confidence intervals at 95% significance level are illustrated in Table 4.2. According to IDW method, the model overestimated T_{mp} and W_{spd} by 1.4±0.2 K and 1.9±0.3 m s⁻¹, while the ME in Rh is underestimated (-3.7±1.0 %). The MAE (RMSE) of T_{mp}, Rh and W_{spd} were found equal to 1.8±0.1 (2.2±0.8) K, 8.7±0.7 (11.6±5.0) % and 2.8±0.2 (3.6±1.3) m s⁻¹, respectively. Moreover, the forecast and observed temperature values were highly correlated (Pearson, 0.92), while for the

relative humidity and wind speed, the Pearson correlation coefficients were found equal to 0.75 and 0.56. Also, the standard deviation (STDEV) for the Tmp, Rh and Wspd MAEs were 1.3 K, 7.7 % and 2.2 m s⁻¹, respectively. The above scores align with previous studies in the wider area of Mediterranean and Greece (Koletsis et al., 2016; Kotroni et al., 2014; Krestenitis et al., 2017; Matsangouras et al., 2014, 2016; Papadopoulos and Katsafados, 2009; Pytharoulis et al., 2016, 2015), revealing an overall satisfactory model performance.

The Cressman method produced same results as the IDW method for Tmp and Wspd variables, while slightly affected the scores of Rh. The applied distance criterion excluded Lavrio station from the statistical evaluation, as the only valid grid point lied beyond the horizontal resolution of the model at d03 (0.555 km). In addition, differences on skill scores appeared for Rafina site, where the underestimation of Rh was decreased from -4.6 % to -3.8 % in comparison to the ME from the IDW method, while the MAE (RMSE) decreased by 0.3 % (0.4 %). Rafina station was the only available HNMS station closed to the MATI fire event, thus the released sensible and latent heat fluxes from the fire model might have affected the predicted values at the vicinity of this station, in a non-homogenized way. Moreover, at Rafina site, all the valid grid points were closer than 0.555 km, contributing to the predicted value, while for the remaining stations, Cressman method excluded up to two (2) grid points from the calculations. In general, the Rh errors at Rafina station were affected the most by the change of the interpolation method. By applying the 4 grid point method to the verification procedure, the model errors (MAE, RMSE) are reduced in all variables under examination. The model underestimates Rh (-3.5±1.0 %), while Tmp and Wspd are overestimated (1.3±0.2 K, 1.7±0.3 m s⁻¹) as in the previous two methods. It is evident that due to the very fine resolution, the spatial variability of the temperature, relative humidity and wind fields contribute the most to model errors.

Table 4.2. The Mean Error (ME), Mean Absolute Error (MAE) and Root Mean Squared Error (RMSE) of the 2m air temperature, 2m relative humidity and 10m wind speed at the locations of the 12 HNMS surface observations from 06Z 23/07/2018 to 12Z 24/07/2018 in CNTRL innermost (d03) domain, regarding the 3 different verification methods. Also, the confidence intervals at the 95% significance level are shown.

	IDW method			Cressman method			4 grid point method		
	ME	MAE	RMSE	ME	MAE	RMSE	ME	MAE	RMSE
Tmp	1.4±0.2	1.9±0.1	2.4±0.9	1.5±0.2	1.9±0.1	2.3±0.8	1.3±0.2	1.6±0.1	2.1±0.7
Rh	-3.7±1.0	8.7±0.7	11.6±5.0	-4.1±1.1	8.7±0.8	11.8±5.4	-3.5±1.0	8.1±0.7	11.1±4.9
Wspd	1.9±0.3	2.8±0.2	3.6±1.3	1.9±0.3	2.8±0.2	3.6±1.4	1.7±0.3	2.5±0.2	3.2±1.2

In Fig. 4.9, the temporal evolution of the ME and MAE of Tmp, Rh and Wspd is depicted along with the 95% confidence intervals, where the predicted values were extracted by the IDW method. Confidence intervals at the 95% significance level were calculated using tabulated values of the t-distribution specified probabilities for a maximum of eleven (11) degrees of freedom. Due to the relative small sample (maximum of 12 forecast versus observed values for each forecast hour), the intervals on the t distribution are wider than the corresponding based on the normal distribution. Regarding the Tmp variable, the model presented the largest absolute errors during the warm hours (T+10 – T+16 h, T+30 – T+34 h), where clearly Tmp is overestimated. The overestimation in Tmp from T+10 to T+16 coincides with the largest errors in Wspd and the onset of the fire events at KINETA and MATI areas. The MAE of Rh is nearly constant during the simulation, while a clearly underestimation is shown from T+23 h and onwards, which is associated with a gradual 180 degrees change in wind direction and moisture advection in the model.

D03, 06Z_23 to 12Z_24 July 2018

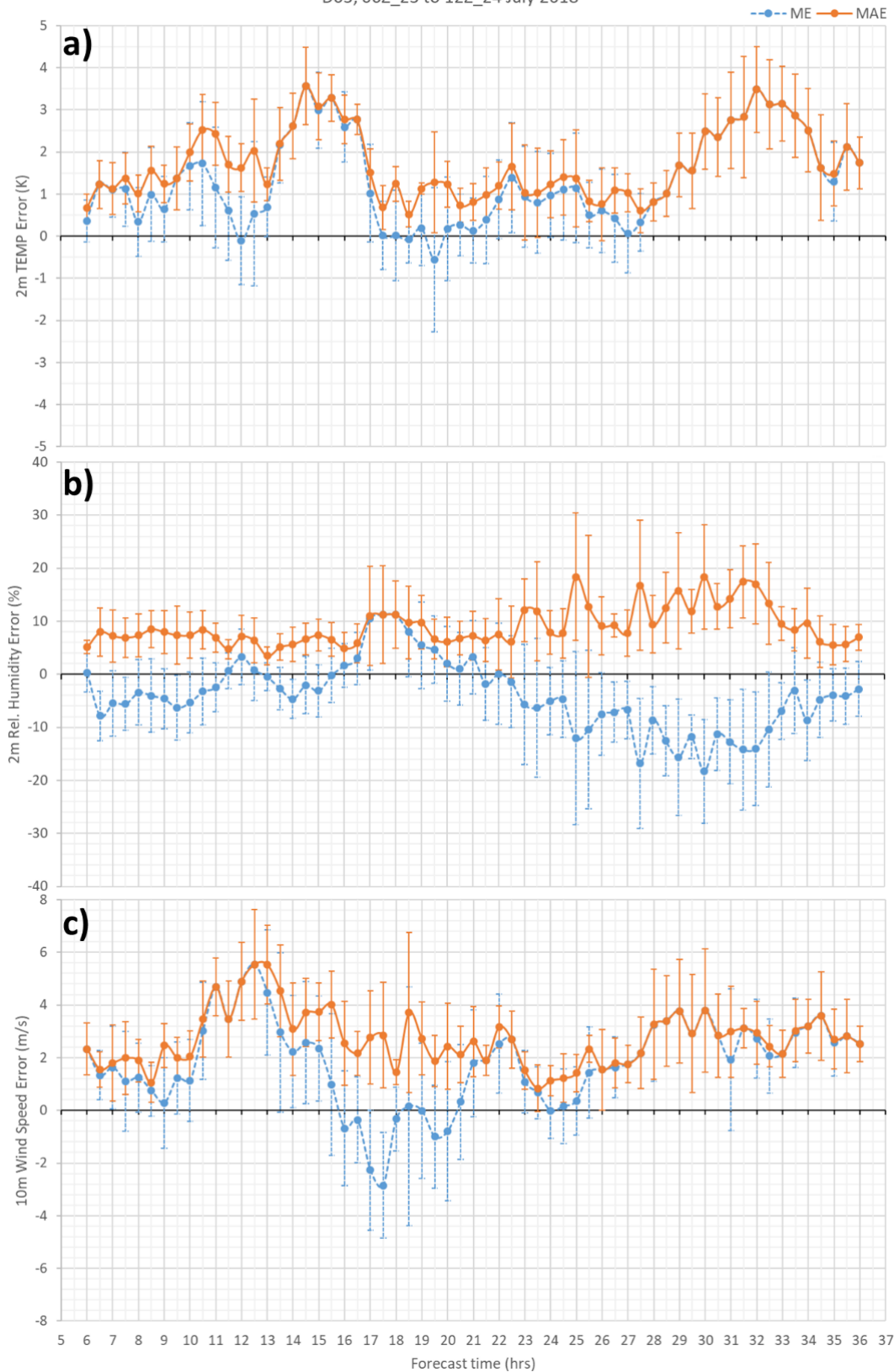


Fig. 4.9. Temporal evolution of the Mean Error (ME; blue dashed line) and the Mean Absolute Error (MAE; orange solid line) of a) 2m air temperature ($^{\circ}\text{C}$), b) 2m relative humidity (%) and c) 10m wind speed (m s^{-1}) at the locations of all HNMS stations. Also, the 95% confidence intervals are indicated.

Fig. 4.10 depicts timeseries of 2m air temperature ($^{\circ}\text{C}$), 2m relative humidity (%) and 10m wind speed (m s^{-1}) at Elefsina (Fig. 4.10a), Ellhniko (Fig. 4.10b), Tatoi (Fig. 4.10c) and Rafina (Fig. 4.10d) sites both from WRF and HNMS data. In general, there is a good agreement between predicted and observed values. The model was able to capture the temporal evolution of the presented meteorological variables at surface and the onset of the windy conditions to a certain degree, but showed discrepancies in temperature and wind speed maximum values (both in time and magnitude) in comparison to the observational data. However, regarding the wind speed field, recorded wind gusts from the HNMS stations are on the same magnitude as the simulated wind speed (e.g. Tatoi: obs = 15.9 m s^{-1} , model = 15.0 m s^{-1}). It must be considered that the output of the model was every five (5) minutes, while the observational records were available every thirty (30) minutes, which may justify the aforementioned differences. Moreover, the extraction method of the forecast values affects the results as it was shown in sub-section 4.6.1. Also, it must not be neglected the uncertainty on the observational data (Haylock et al., 2008; Klein Tank et al., 2002; Prein and Gobiet, 2017; Rauthe et al., 2013).

At Rafina site, WRF simulated a rapidly increase of 2m air temperature and 10m wind speed at 12Z on 23 July 2018 (Fig. 4.10d) with a simultaneously decrease in relative humidity. In the model, the 2m air temperature rose approximately 8°C in twenty (20) minutes (from 11:45 UTC to 12:05 UTC), while according to the observational data an increase of 4°C was recorded initially between 10:00 UTC and 10:30 UTC and during 11:30 UTC to 12:00 UTC afterwards (6°C). The maximum simulated (observed) air temperature at 2m was 40.1°C (39°C) at 12:10 UTC (12:00 UTC). The observed maximum 10 min wind gust was 25.2 m s^{-1} against the modeled maximum wind speed of 17.5 m s^{-1} . Although the model underestimates the wind speed at output intervals, its examination at time step intervals (wrfxtrm generated files) revealed values greater than 20 m s^{-1} .

In addition, the analysis on the simulated temperature field in vertical showed that the aforementioned changes at Rafina site occurred close to the surface and up to $\sim 800 \text{ m agl}$. The model results showed warming rates of 1 K min^{-1} (at $\sim 800 \text{ m agl}$, 9th theta model level) to 4.3 K min^{-1} (at $\sim 10 \text{ m agl}$, 1st theta model level), while the temperature begun to rise first aloft (11:35 UTC) and then at the lower levels (11:45 UTC). The wind speed followed the same temporal and vertical pattern but the onset of this increase was placed earlier (11:30 UTC), almost 10 minutes prior to temperature changes, implying vertical transport of energy and momentum from higher levels to the surface. Moreover, a decrease in wind speed magnitude was observed at all vertical levels close to the surface, prior to its intensification which is related with the gradually change in wind speed direction. The maximum rate of the wind speed change was found equal to 10.7 m s^{-1} , at nearly 45 m agl .

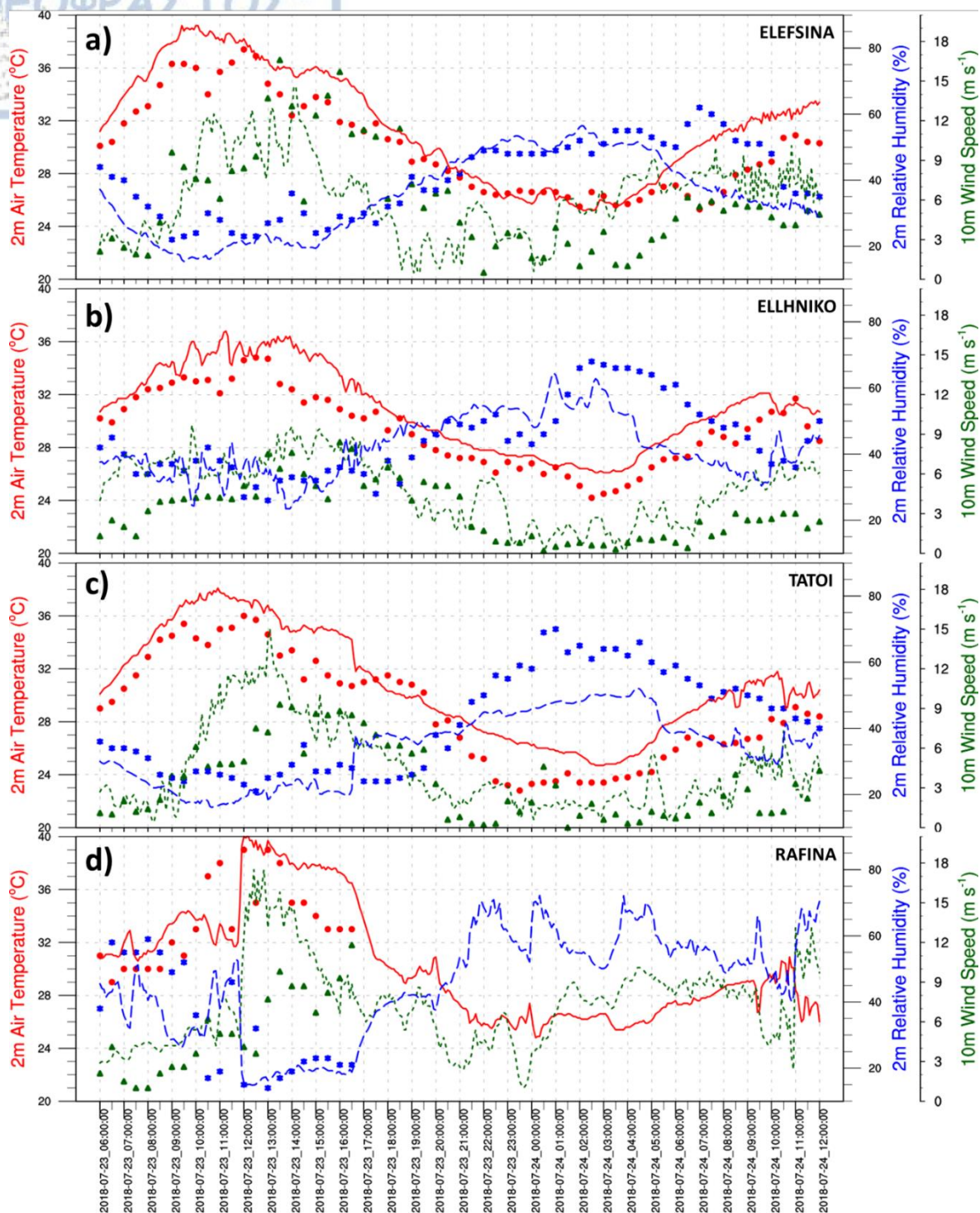


Fig. 4.10. Timeseries of 2m air temperature ($^{\circ}\text{C}$, red), 2m relative humidity (% , blue) and 10m wind speed (m s^{-1} , green) in CNTRL simulation (solid, dashed lines) and according to HNMS stations (dots, asterisks, triangles) at a) Elefsina(16718), b) Ellhniko (16716), c) Tatoi (16715) and d) Rafina (16793) sites. The WRF values were extracted by utilizing the IDW method.

The spatial analysis of the model results at surface (Fig. 4.11a) reveals that at 09:00 UTC, a pressure difference of ~ 3 hPa is established between northwest (higher pressures) and south east (lower pressures) of Gerania Mts (KINETA) and remains almost unchanged until the early evening hours on 23/07. At the time of fire ignition at KINETA ($\sim 09:00$ UTC), the simulated maximum wind speed is

approximately 15 m s^{-1} , peaking its highest values ($\sim 18 \text{ m s}^{-1}$) at 12:45 UTC. Koletsis et al. (2009) noted also the existence of a pressure gradient during a downslope windstorm in Northwestern Greece, with maximum pressure difference of $\sim 6 \text{ hPa}$. Moreover, at the greater area of MATI, the wind is blowing from east to east-southeast directions, with wind speed values below 5 m s^{-1} and no any significant pressure gradient. At 11:30 UTC (Fig. 4.11b), the prevailing weather conditions are characterized by strong westerly winds over the Attica region and high temperatures downwind of any orographic barrier. Worth of noting is the front-like feature of high temperatures at the vicinity of MATI, accompanied by high wind speeds with maxima of $\sim 18 \text{ m s}^{-1}$, propagating eastwards towards the coast (red frame, Fig.11b). Analysis of the simulated wind field at 10 m (not shown), revealed paths of strong localized and transient winds between Hymettus Mt and Penteli Mt. Moreover, the aforementioned rapid increase of 2m air temperature at Rafina site (Fig. 4.10d) is clearly related with the passage of this feature. At the area of KINETA, the increase in temperature due to the wind field is also evident. The fire at Kalliternoupolis (MATI event) ($\sim 13:49 \text{ UTC}$) ignited under strong westerlies ($19 \text{ to } 20 \text{ m s}^{-1}$), with relative humidity values less than 20% and ambient temperatures greater than $39 \text{ }^\circ\text{C}$.

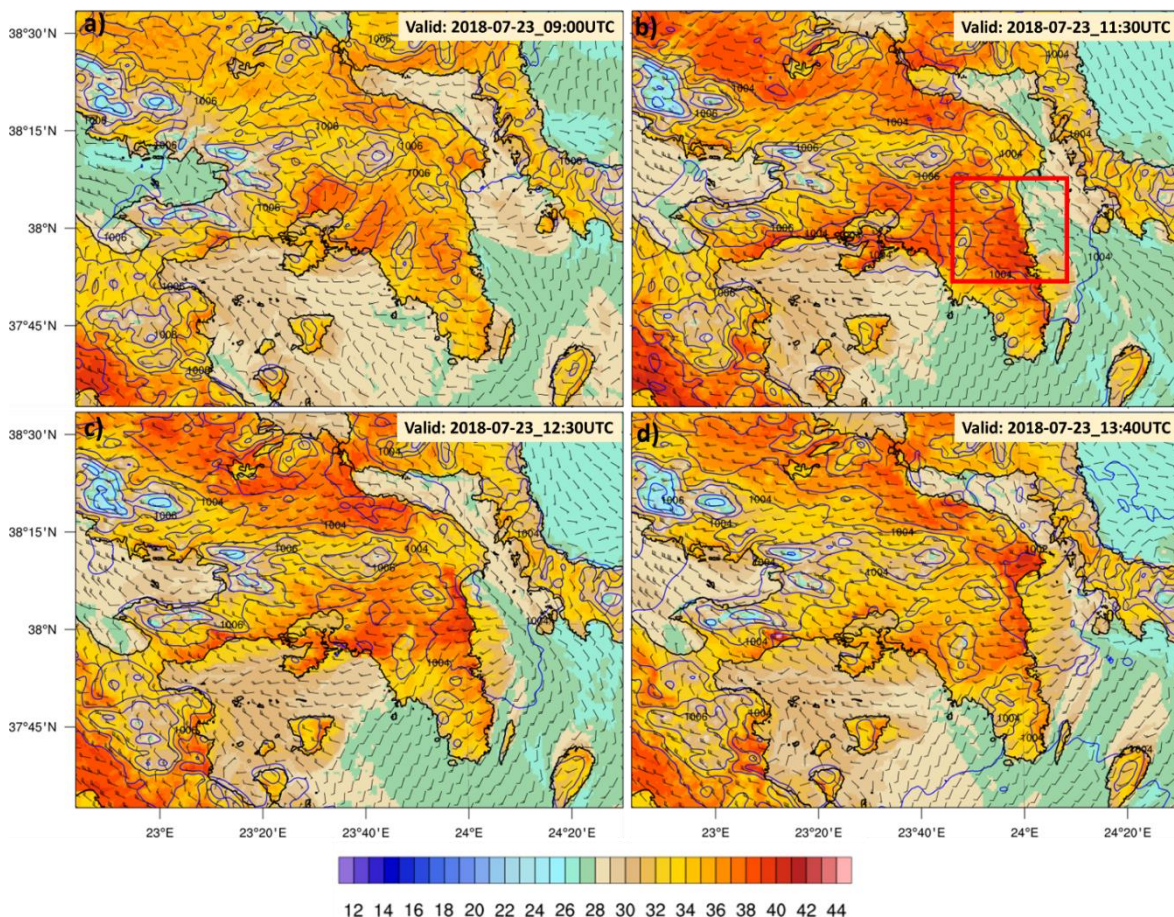


Fig. 4.11. Air temperature at 2m ($^\circ\text{C}$, shaded contours), mean sea-level pressure (hPa, blue contours) and 10m wind speed (knots, windbarbs) at a) 09:00 UTC, b) 11:30 UTC, c) 12:30 UTC and d) 13:40 UTC on 23/07/2018, based on WRF-d03 values. Full windbarb = 10 knots, half windbarb = 5 knots.

Fig. 4.12 displays the longitude – height section of potential temperature (K) and u-component of wind speed (m s^{-1}) from 06:00 UTC to 15:00 UTC at 3-hourly intervals, on 23/07. The aforementioned fields were extracted from the WRF-d02 intermediate nest (Fig. 4.1a) in order to highlight the effects of

mountain chains, west of the Attica region, on the flow. In general, stable conditions are observed allowing for the development of mountain waves (Simpson et al., 2013). The complex terrain at North Peloponnese (21.3°E to 22.7°E) interacts initially with the atmospheric flow, gradually enhancing the vertical displacement of the air parcels (Fig. 4.12a). As a result, orographic waves are formed leeward of Pindus mountain range (Fig. 4.12b) in a layer between 1 to 3 km above the surface, while close to the ground the flow is characterized by locally induced variations (e.g. the easterly wind component at MATI location). At 12:00 UTC (Fig. 4.12c), the increase in longitudinal wind speed is evident and strong downslope winds are dominating the lee-side of Gerania Mts (black short line), where the fire is active. Energy and momentum are propagating downwards into the lower troposphere, while a mid-level jet core lies from 3.5 to 5.5 km (not shown) and amplifying its strength from 13:00 UTC and onwards. Moreover, at the vicinity of MATI (red short line), a strong temperature and wind speed gradient is presented which coincides with the rapidly increase of 2m air temperature and 10m wind speed as it was described earlier (Fig. 4.10d, Fig. 4.11b). During the fire event at MATI (Fig. 4.12d), the isotachs tilt in vertical as they follow the descending part of the formed waves, resulting in strong katabatic winds and adiabatic heating of the lowest boundary layer in the region, as indicated by the isentropes.

The calculated omega (hPa hr^{-1}) values (Fig. 4.13) prior to the ignition times at both sites (09:00 UTC, KINETA; 13:40 UTC, MATI) declare strong downward motions (positive values) on the lee sides with a simultaneously decrease in water vapor mixing ratio, as drier air descends. This mechanism produces vertical mixing and thus the winds at lower levels inherit the characteristics of the wind field aloft, due to conservation of momentum (Sharples et al., 2012). At KINETA event, the model maintained these downward motions until the early night hours on 23/07, where the wind speed dropped significantly and turned into northerlies. Model results reveal also a minor directional wind shear from 06:00 UTC to 18:00 UTC, where at 500 hPa, the wind blows from the west and turns to north-west at lower levels (not shown). This shear is generated and it is driven by the presence of the mountain chains at Central Greece and North Peloponnese, along with the pressure gradient, which slightly divert the flow.

In addition, calculation of Richardson and Froude numbers (Fig. 4.14a,b) shows a transition from subcritical ($Fr < 1$) to supercritical ($Fr \sim 1$) flow on the lee slopes of Gerania Mts and Penteli Mt (Durran, 1990), while dynamically unstable and turbulent conditions ($Ri < 0.25$) are dominating at lower levels. At 09Z, the flow is subcritical ($Fr < 1$) over the area of interest (Attica region, 22.8°E – 24.1°E, Fig. 4.14a), with conversion of kinetic energy to potential energy (deceleration), as the air parcels ascent due to orography and vice-versa (acceleration) upon passing the crests. Upstream and aloft of Gerania Mts (Fig. 4.14c) static stability is positive, whereas negative values (instability) are shown downwind. Also, the predicted wavelengths (contour lines, Fig. 4.14c,d) are close to the leeward slope widths ($< 8\text{km}$) in the area, allowing for interaction between the mountain waves and the flow conditions downwind. At 12Z, the Froude number is approximately equal to unity over the crest of Gerania Mts and a supercritical regime eastwards is evident (23.1°E – 24.1°E, Fig. 4.14b), where the potential energy is converted into kinetic energy. This features is analogous to the hydraulic-like theory (Durran and Klemp, 1987; Smith, 1985), in which when the flow passes the top of the mountain, it accelerates further until the area referring as the hydraulic jump, where the flow turns back to the subcritical conditions ($Fr < 1$). In the case of 23rd of July 2018 at 12Z, this area is placed eastwards of Penteli Mt, as it can be shown in Fig. 4.14b.

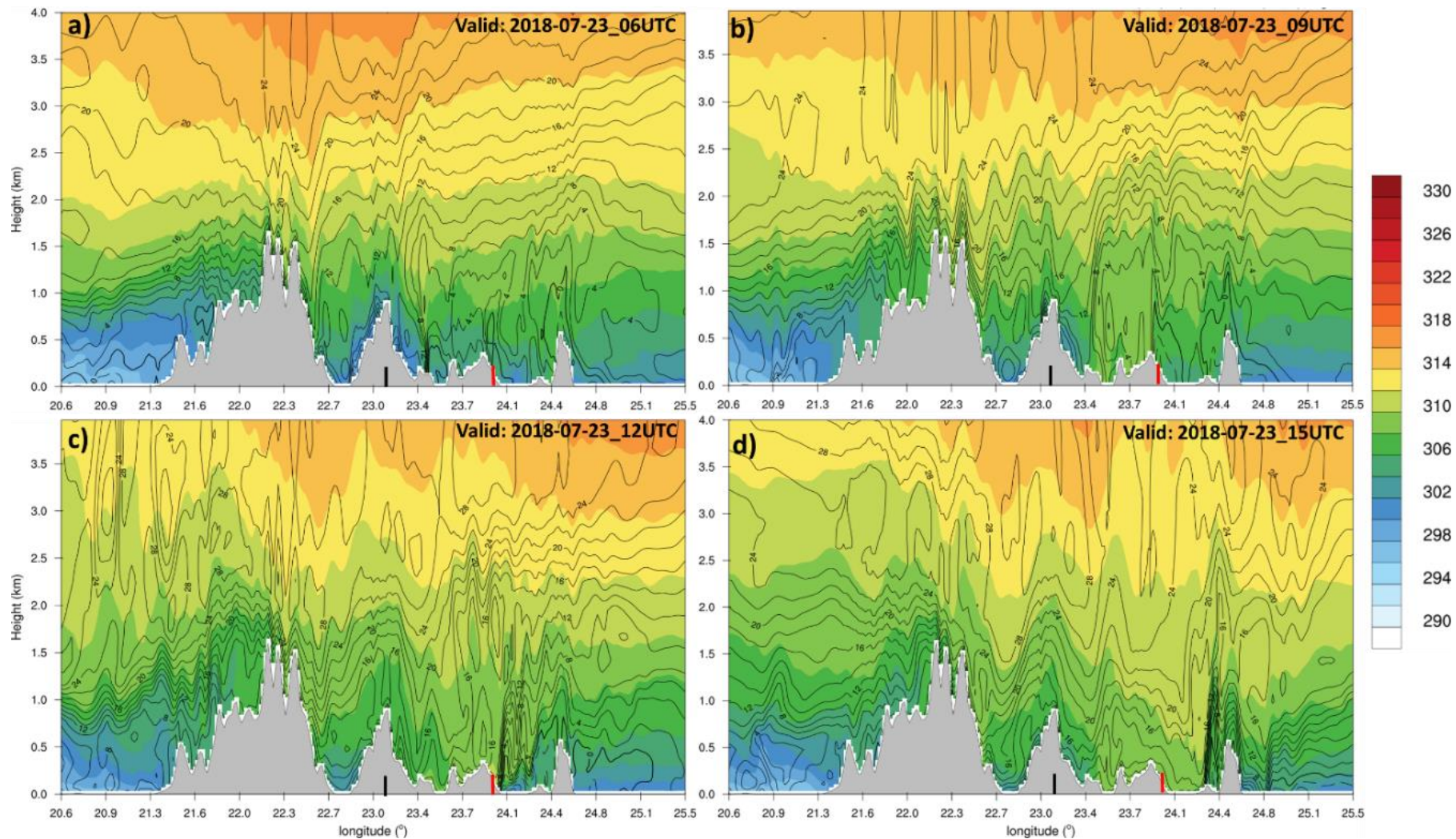


Fig. 4.12. Longitude - height sections along WRF-d02 of potential temperature (K, shaded contours) and u-component of wind speed ($m s^{-1}$, contours) at $38.035^{\circ}N$, on 23/07 at a) 06Z, b) 09Z, c) 12Z and d) 15Z. See text for further details. Black and red line marks indicate the locations of Gerania Mts. and Penteli Mt., respectively.

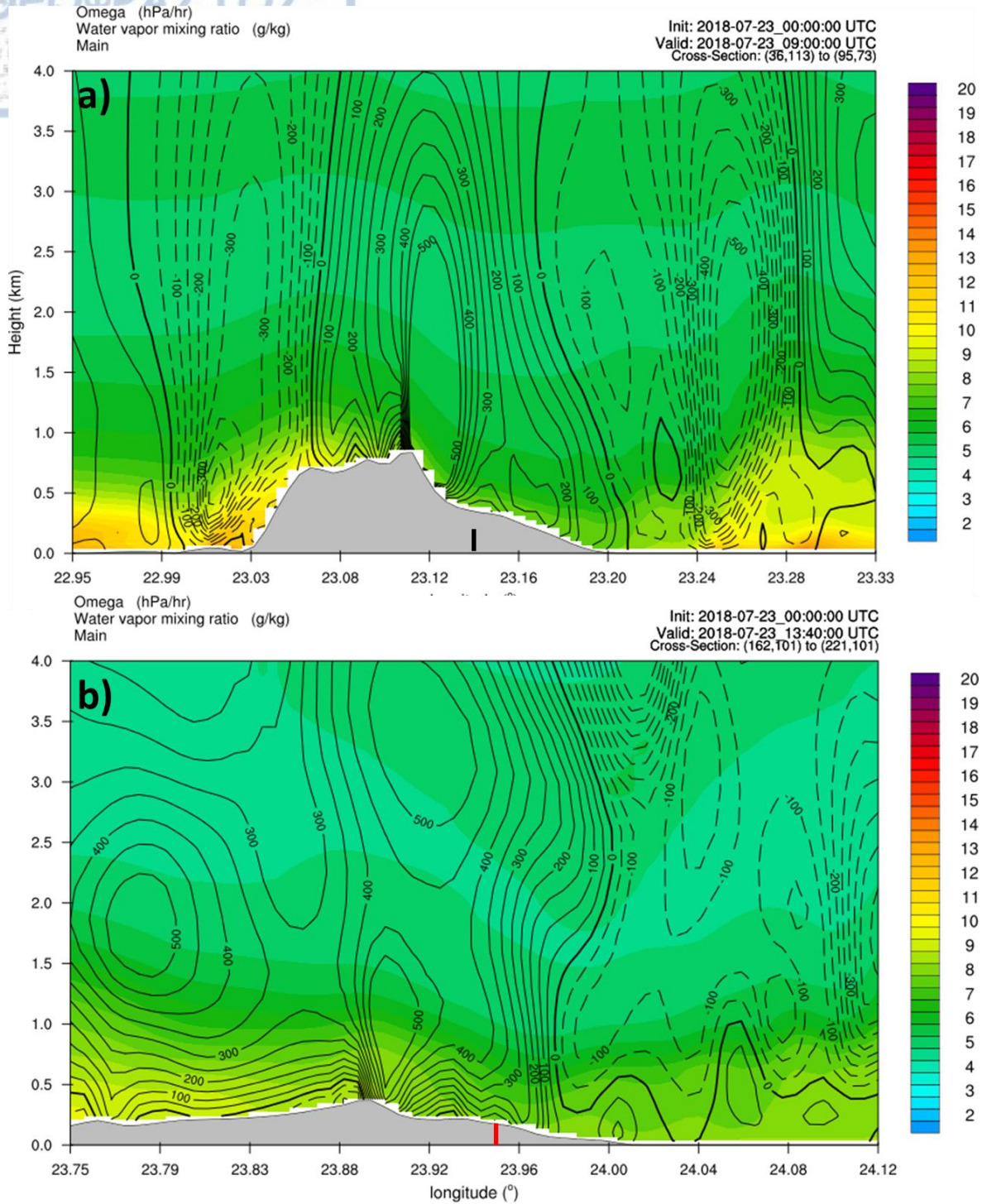


Fig. 4.13. a) Vertical cross-section through E-F dashed line (Fig. 4.1b) at 09:00 UTC and b) G-H dashed line at 13:40 UTC (Fig. 4.1b), of omega (hPa hr^{-1} , shaded contours, positive values declare downward motions) and water vapor mixing ratio (g/kg , contours) on 23rd of July 2018. Black and red line marks indicate the locations of fire ignition at KINETA and MATI, respectively.

It must be noted that, the hydraulic theory requires the determination of the top of the disturbed flow. According to Helmis et al. (2000) possible indicators can be the presence of a mean-state critical layer (Smith, 1985), a layer with decreased static stability with height or a temperature inversion (Durran, 1986; Klemp and Durran, 1987) or a wave-induced critical layer (wavebreaking, Klemp and Durran,

1987). Either a mean-state critical level or an inversion layer were not observed, which are important for the presence of vertical propagating mountain waves (Doyle and Jiang, 2006; Durran and Klemp, 1987; Fudeyasu et al., 2008; Klemp and Lilly, 1975; Koletsis et al., 2009; Peltier and Clark, 1979). Although the current analysis reveal a vertical variation on the static stability with height over the area of interest (Fig. 4.14c,d), the flow dynamics involved are much more complicated and the hydraulic model can be utilized only in a qualitative manner (Durran, 1990; Helmis et al., 2000).

The resolved turbulent kinetic energy (TKE), averaged horizontally and in vertical up to ~3600 m agl, from 23/07 at 06Z to 24/07 at 00Z over KINETA and MATI, was found equal to 0.31 and 0.37 m^2s^{-2} , respectively. The area under examination in both sites was defined downwind of Gerania Mts and Penteli Mt. The maximum averaged TKE at KINETA was 0.58 m^2s^{-2} (13:00 UTC) and 1.1 m^2s^{-2} at MATI (13:15 UTC), almost half an hour prior to the fire ignition at Kalliternoupolis. The temporal examination of the averaged TKE at MATI revealed that values greater than 0.6 m^2s^{-2} encountered from 11:20 UTC to 15:35 UTC, implying that the fire ignited under turbulent conditions, which affected the fire spread. Also, the higher values of TKE at MATI are in line with the calculated Richardson number values (Fig. 4.14a,b), which were below the critical value of 0.25. Moreover, the maximum TKE in vertical at KINETA (MATI) was 14.67 (10.79) m^2s^{-2} .

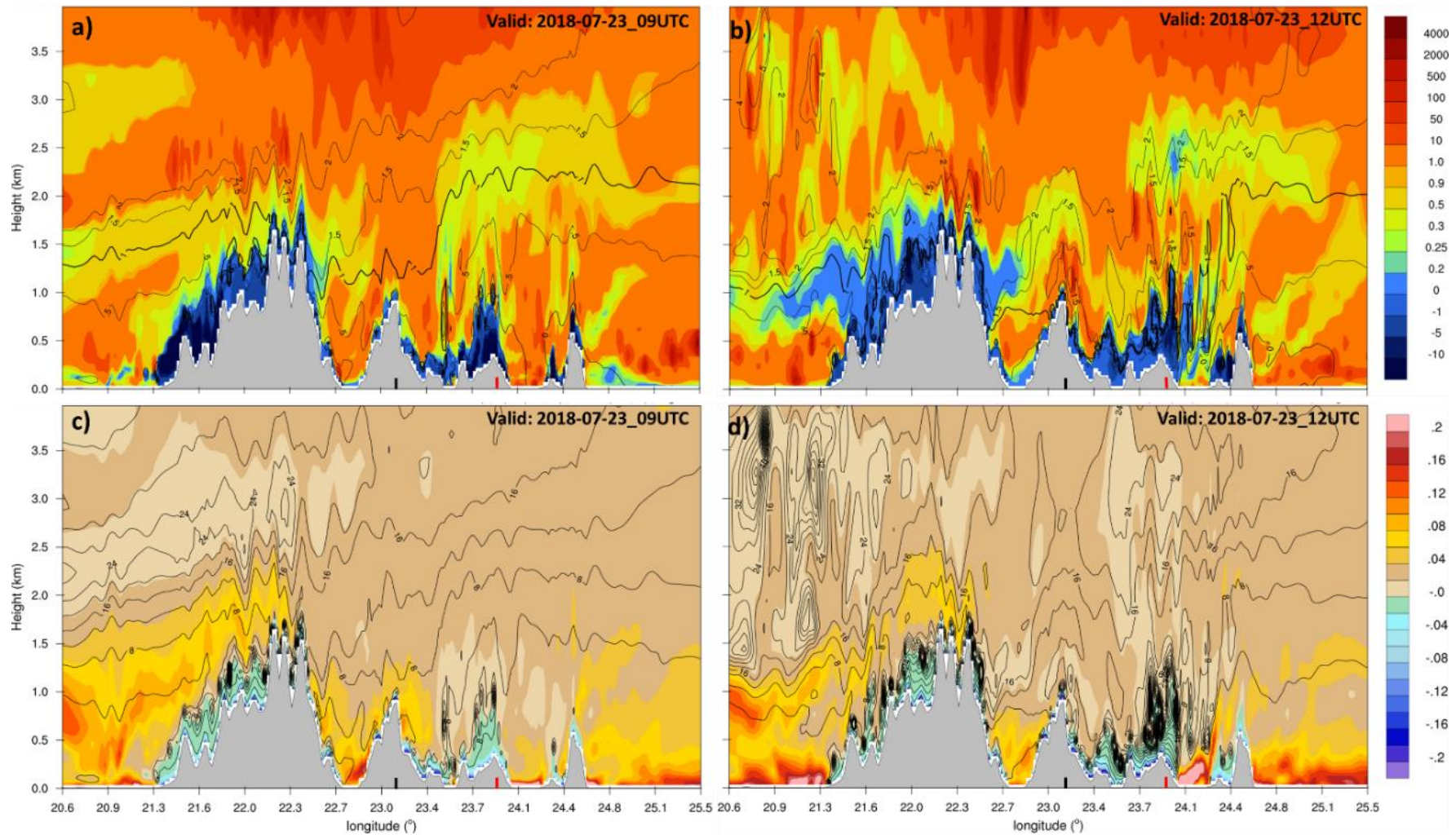


Fig. 4.14. Longitude - height sections along WRF-d02 of Richardson (shaded contours) and Froude (contours) numbers (top), static stability ($K hPa^{-1}$, shaded contours) and wavelengths (km, contours) (bottom) at $38.035^{\circ}N$, on 23/07 at a,c) 09Z, b,d) 12Z. Black and red line marks indicate the locations of Gerania Mts. and Penteli Mt., respectively.

4.6.2.2 Vorticity and horizontal roll vortices

Vorticity, the measure of the rotation in a fluid about some axis (Holton, 2004), is defined as the curl of the wind field, according to Eq. 2.8. Vorticity is associated with the formation of fire whirls and horizontal roll vortices (Forthofer and Goodrick, 2011), during a wildland fire or under certain conditions with lateral fire spread (Sharples et al., 2012; Simpson et al., 2013, 2014).

At KINETA event, the satellite image (Fig. 4.15a) from the Copernicus Sentinel-2A L1C (23/07, 09:28 UTC) depicts a distinct smoke plume, parallel to the mean flow, while photographs from the local news revealed its high proximity to the ground (not shown). The mechanism involved for the creation of this structure demands an imbalance between buoyance driven vorticity and shear driven vorticity (Etling and Brown, 1993; Forthofer and Goodrick, 2011), resulting to parallel orientation of the convective rolls to the mean wind, an analogous to the cloud streets which formed by the cumulus clouds (Etling and Brown, 1993). Also, the observed single longitudinal plume vortex (Haines and Smith, 1987) displayed a spiral and banding structure, at the time of satellite passing, but any information about its rotation was not available. On the contrary, lacking any high resolution satellite images from the deadly fire at MATI, it is hard to say anything about its observed plume characteristics.

The smoke plume at KINETA was resolved by the model, as emissions from the fire were activated in the SFIRE module and inserted into the WRF as passive tracers. Results showed high smoke concentrations simulated close to the ground at the vicinity of the fire, while a gradually ascent of the plume was observed eastwards. In Fig. 4.15b, a latitude-height cross section (south – north) of the calculated x component of vorticity vector (s^{-1} , shaded contours), ω_x in Eq. 2.8, wind barbs from the v and w wind components (knots), along with the resolved smoke plume (contours) are depicted at 09:30 UTC. The black line in Fig. 4.15a declares the location of the cross section. A region of negative (anticyclonic) vorticity values is located downwind of the land, suppressing the smoke emissions close to the surface, over the sea and southwards, where the smoke plume tends to rise, as positive (cyclonic) ω_x values dominate. Noticeable is also the pair of cyclonic and anticyclonic vortices upwind to the plume and over the land, evident of the turbulent conditions in the area. Moreover, a pattern of anticyclonic rolls in the layer between 500 to 1500 m over the sea is shown. Regarding the temporal evolution of the plume, at 11:45 UTC (Fig. 4.15c), fire emissions extent up to 1.5 km, while high concentrations are observed close to the ground. The anticyclonic vortex is still present but is reduced in magnitude, as embedded positive ω_x vorticity regions allow the vertical extension of the smoke over the sea. A cross-section eastwards (near the right boundary of Fig. 4.15a), also at 11:45 UTC (Fig. 4.15d), reveals a vortex pair, where in each core lie high smoke concentrations, while the plume has reached approximately at 2 km. This feature illustrates the impact of turbulence on plume dynamics and how topography plays an important factor to its development and characteristics, as vortex pairs are usually occurred over flat terrain (Haines and Smith, 1987).

During the event at KINETA, local news reported several line ignitions, which were not confirmed by the Hellenic Fire Service. In Fig. 4.15a, a lateral fire spread is also shown, indicating a possible vorticity-driven mechanism. Sharples et al. (2012) introduced a fire channeling mechanism based on the interaction between the fire and a lee rotor, which is associated with a flow separation on the leeward slope (their Fig. 4.12). Simpson et al. (2013, 2014, 2016) investigated this phenomenon through a series of very high-resolution sensitivity experiments, indicating several factors (e.g. stability conditions, leeward slope, fuel types), which affect its occurrence. However, a common feature was the existence of the flow separation, where on the lee slope, the wind direction changed 180° degrees relative to the mean flow, due to the rapidly decrease of the leeward wind speed. In the case of KINETA event, the model results did not reveal any flow separation, either at early hours since ignition or later on 23/07. Why this feature was not observed, requires further investigation, but an insight might be the

small wavelengths of the simulated mountain waves which were able to interact with the flow across the leeward slope or the relatively coarser resolution in order such features to be modelled (Simpson et al., 2014). However, the simulated fire showed lateral spread, mostly at first hours.

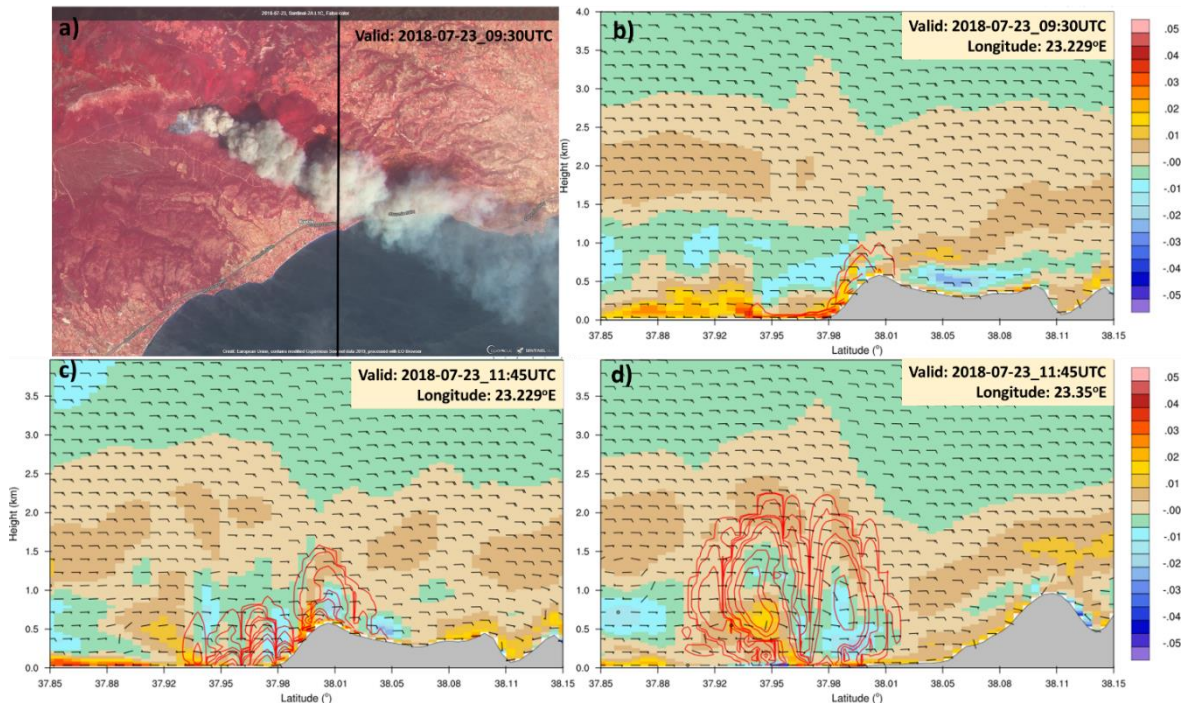


Fig. 4.15. a) False color (bands 8, 4, 3) Copernicus Sentinel-2A L1C satellite image over KINETA region and latitude-height cross sections of x component of vorticity vector (s^{-1} , shaded contours), wind bards based on v and w wind components (knots) and smoke plume from the modeled fire (contours) at b) $23.229^{\circ}E$, 09:30 UTC, c) at $23.229^{\circ}E$, 11:45 UTC and d) at $23.35^{\circ}E$, 11:45 UTC, on 23rd of July 2018.

At the wider area of MATI, analysis on the vorticity components in Eq. 2.8, corroborates that the fire ignited under favorable atmospheric conditions, which contributed to high spread rates and extreme fire behavior. Examination of the vertical profile of the y component of the vorticity vector (s^{-1}), ω_y in Eq. 2.8, shows an area of positive ω_y values ($\sim 0.02 s^{-1}$) close to the ground (Fig. 4.16a), resulting to vorticity driven flow prior to the fire ignition (13:30 UTC). A layer of negative ω_y values exists between 1.5 km to 2.5 km, while a core of wind speeds greater than $25 m s^{-1}$ (50 knots) is also shown in the layer between 1.0 km to 2.0 km. The cyclonic vortices were maintained until the late evening hours, providing additional forcing into the fire spread rates and the vertical mixing. In addition, at the same time, cyclonic vortices with their rotation axis parallel to the mean flow (ω_x vorticity) were resolved by the model, appearing upwind, over and downwind of Penteli Mt (Fig. 4.16b). Also, a well-organized cyclonic vortex is evident over the Messogia Plain (southwards of Kalliternoupolis), which it is assumed that it was generated due to the presence of Hymettus Mt. However, further investigation is required for the above statement.

The temporal evolution of the ω_z at surface showed that the z component of the vorticity vector, ζ , had a small impact on the lateral spread of the fire (not shown), due to the nearly uniform horizontal wind field and thus the absence of horizontal vorticity shear. Overall, the calculated magnitude of the 3D vorticity vector revealed high values (~ 0.1 to $0.18 s^{-1}$) in the area between 12:45 to 14:15 UTC.

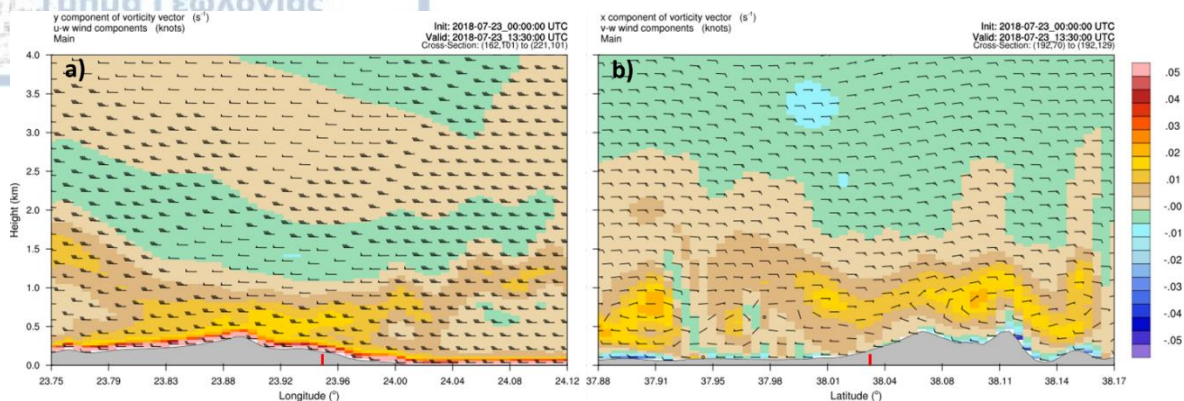


Fig. 4.16. a) Longitude-height cross section of y component of vorticity vector (s^{-1} , shaded contours) and wind bards based on u and w wind components (knots) at $38.035^{\circ}N$, b) latitude-height cross section of x component of vorticity vector (s^{-1} , shaded contours) and wind bards based on v and w wind components (knots) at $23.947^{\circ}E$, on 23^{rd} of July 2018, at 13:30 UTC.

4.6.2.3 Simulated fire behavior and evolution

The spatiotemporal evolution of the simulated fires at KINETA and MATI events was compared with fire data, derived from the 1-km spatial resolution MODIS Fire and Thermal Anomalies product (Giglio et al., 2003) and the corresponding Visible Infrared Imaging Radiometer Suite – VIIRS (Schroeder et al., 2014), at 375 m nominal resolution. At KINETA, the observed fire radiative power (FRP) on 23/07 lied between $5.7 W m^{-2}$ (~20:40 UTC, MOD14) to $2012.3 W m^{-2}$ (~09:35 UTC, MOD14), while at MATI, the FRP ranged from $6.9 W m^{-2}$ to $56.3 W m^{-2}$, during the Terra satellite passing (~20:40 UTC, MOD14). Also, the Suomi-National Polar-orbiting Partnership (S-NPP) satellite completed one pass on 23/07 (~11:40 UTC) and another one, on 24/07 (~00:00 UTC), over Attica region, with recorded VIIRS-FRP maxima equal to $187 W m^{-2}$ (~11:42 UTC, 23/07) and $17.1 W m^{-2}$ (~00:00 UTC, 24/07) at KINETA and MATI, respectively.

Fig. 4.17 depicts the temporal evolution (at 5-min intervals) of the simulated fire area (ha) at KINETA (red dashed line) and MATI (black solid line), along with the modeled total (sensible plus latent) heat fluxes ($MW m^{-2}$, red dotted line and black dashed line, respectively), derived as the sum of all WRF-d03 grid points at surface, in each history output. For KINETA, the total burnt area according to the WRF-SFIRE modelling system (from 23/07, 09Z until 24/07, 12Z) was 8336.82 ha, approximately 48% greater than the observed one (5613.3 ha, Copernicus EMS-event EMSR300). The mean rate of fire area growth was found equal to 0.04 ha/5min, while the maximum accumulated heat fluxes from the fire were $245.3 MW m^{-2}$, at 13:45 UTC. The rapid increase in the released heat fluxes since ignition, is placed at approximately at 11:15 UTC and is associated with the ignition of an additional fuel type (NFFL fuel type 7, Southern rough) with high moisture of extinction values (~40%) and live foliage flammability (Anderson, 1982). In the case of the deadly fire at MATI, the fire model produced higher burnt area growth rates (average equal to 0.09 ha/5min), representative of the actual fire propagation. The total modeled burnt area, at 00Z on 24/07, since ignition (23/07, ~13:49 UTC) was 1083.26 ha, against 1275.9 ha, as recorded in the EMSR300 data. Also, two distinctive peaks in the heat fluxes from the fire at MATI (black dashed line) are presented, which slightly affected the slope of the fire area line (black solid line). The local heat maxima are almost three times lower than the global maximum heat fluxes at KINETA, because of the different fuel types and most importantly the lower modeled wind field, at the time of occurrence.

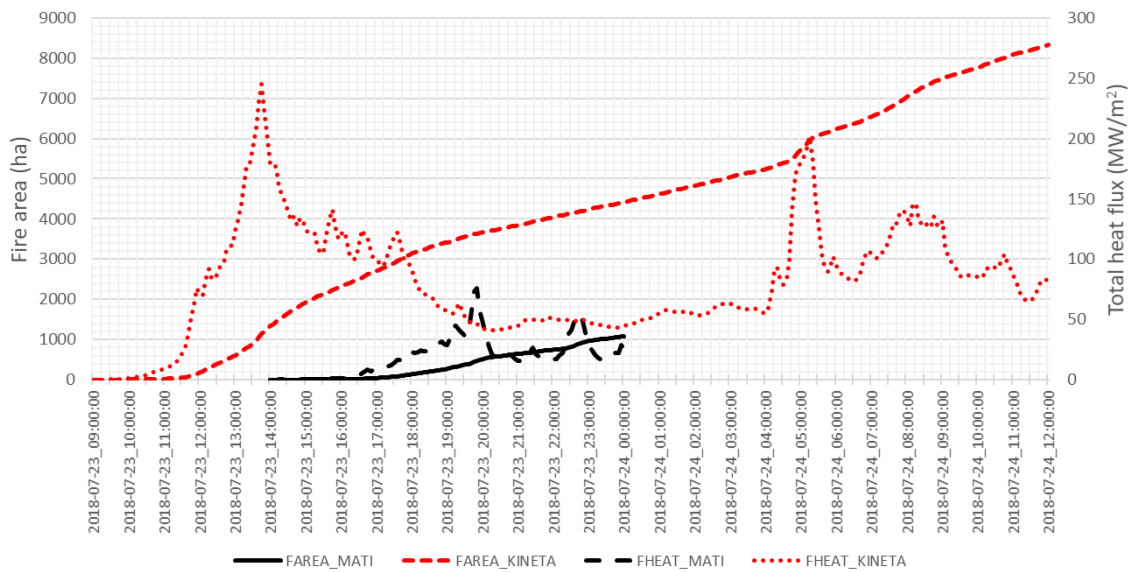


Fig. 4.17. Simulated burnt area (ha) at KINETA (red dashed line) and MATI (black solid line) and released sensible and latent heat flux (MW m^{-2}) at KINETA (red dotted line) and MATI (black dashed line) as a function of time (5-min intervals), in CNTRL experiment, according to the WRF-SFIRE modelling system.

In both events, the fire area overpassed 10 ha almost two hours since ignition, due to the required time in order the model to develop a quasi-steady state fire. The latter is clearly shown in Fig. 4.18, where the temporal evolution of the simulated burnt area (solid lines), along with the observed hot spots from MODIS (green asterisks) and VIIRS (dots) are depicted. At KINETA event (Fig. 4.18a), the modeled fire area (white solid line) is underestimated the most comparing to the VIIRS thermal anomalies (white dots), at 11:40 UTC, on 23/07. The satellite data suggest that the fire front had reached the coastal area at that time, which cannot be confirmed at this point. However, it is possible that the VIIRS assigned as potential hot spots, locations along the smoke plume, with brightness temperatures greater than the applied thresholds in the VIIRS algorithm (Schroeder et al., 2014). As a result, the actual burnt area at that time might be much smaller, while worth of noting is that the WRF-SFIRE produced the VIIRS burnt area approximately two hours afterwards (red solid line), at 13:55 UTC. Few hours later, at 20:40 UTC, the predicted fire area (green solid line) is close to the MODIS product, where active fire fronts were observed along the western and eastern flanks. Similar fire behavior was observed during the Suomi-NPP satellite passage over the area, at ~00:05 UTC on 24/07, with the modeled burnt area (orange solid line) in good agreement with the observed one (orange dots).

The fire ignition time at Kallitehnoupolis (MATI) along with the high propagation rates resulted to a limited number of satellite passes (only two), during this event. However, according to the MODIS Fire and Thermal Anomalies product (green asterisks, Fig. 4.18b), at 20:40 UTC, on 23/07, active fire fronts were spotted along the north and the southeast flanks, while the model produced an elongated towards east fire area (green solid line), which had arrived at the coastal area of Mati settlement. Despite the delay on the development of the fire momentum (dark blue solid line, Fig. 4.18b) and the late arrival time to the coast, the CNTRL simulation represented quite well the actual fire behavior, as the wind driven fire first reached to the sea and then started to spread laterally (orange dots and solid line, Fig. 4.18b). However, the WRF-SFIRE failed to represent the northward lateral propagation to Agia

Marina settlement, due to the change in the modeled wind direction (westerlies to north-westerlies, not shown).

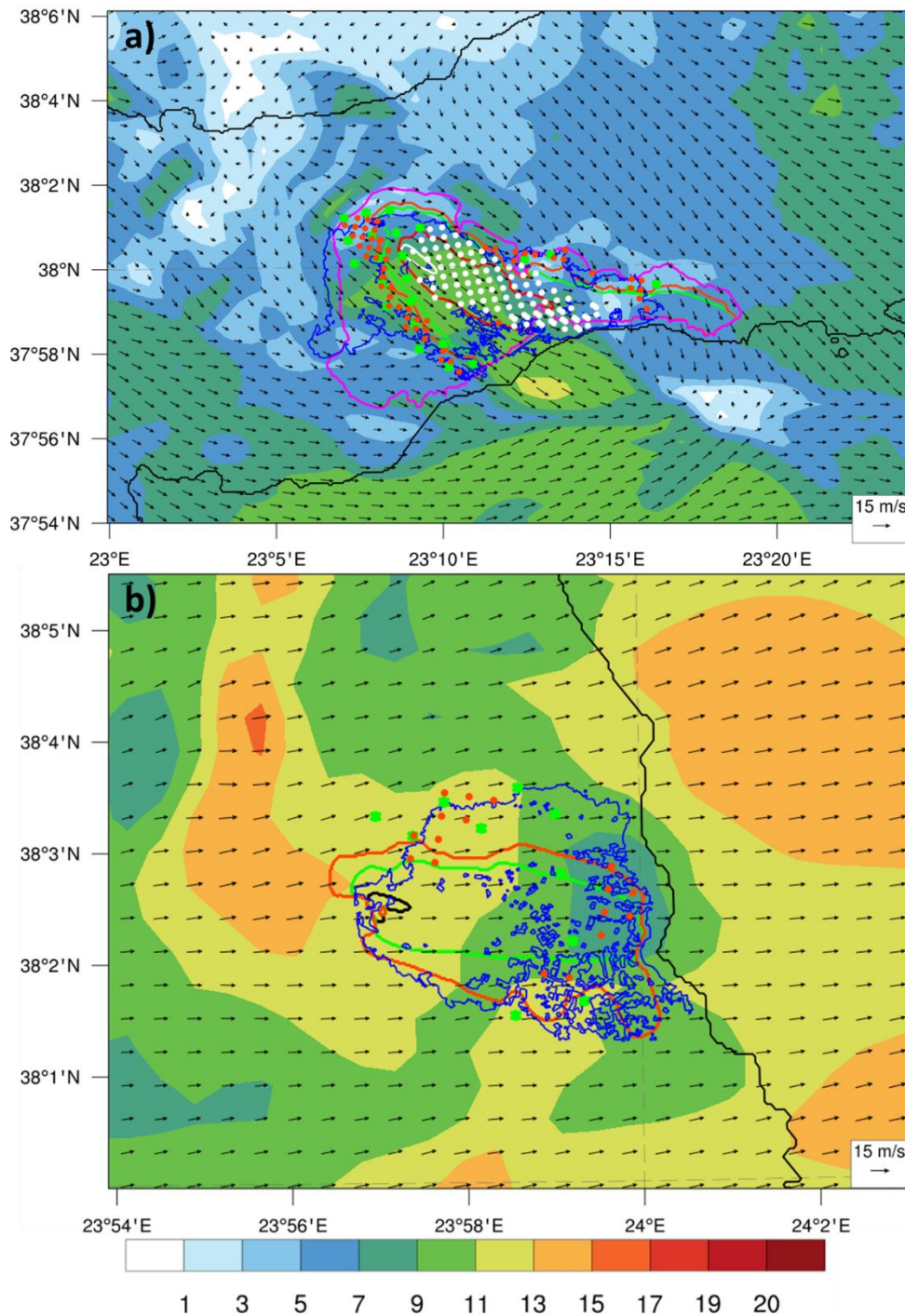


Fig. 4.18. Evolution of the simulated burnt area (solid lines), EMSR300 actual fire scar (blue solid line), observed hot spots from MODIS (green asterisks) and VIIRS (dots) and simulated wind speed (contours) and direction (arrows) upon ignition, at a) KINETA and b) MATI fire events. Different colors corresponds to different times. At KINETA (left), white, 11:40 UTC, red, 13:55 UTC, green, 20:40 UTC, on 23/07 and orange, 00:05 UTC, magenta, 12:00 UTC on 24/07. At MATI (right), dark blue, 16:30 UTC, green, 20:40 UTC, on 23/07 and orange, 00:00 UTC, on 24/07.

4.6.3 Sensitivity experiments

4.6.3.1 Effect of topography

In this sub-section, the effect of topography on the local atmospheric conditions and thus on the fire behavior in both events is investigated. The wider Attica region is dominated by complex topographical features, which interact with the mean flow, altering its kinematic and dynamic characteristics.

In Fig. 4.19, vertical cross-sections of 3-D wind speed (m s^{-1} , shaded contours) and potential temperature (K, contours) along the flow, in each site (columns; KINETA, left; MATI, right) and each experiment (rows; CNTRL, NTOPO, TOPOG and TOPOP) are shown. For the KINETA and MATI fire events, the cross-sections are along the E-F and G-H lines (Fig. 4.1b), respectively. According to the control simulation (CNTRL) and upon ignition time (23/07, 09Z) at KINETA (Fig. 4.19a), the flow decelerates upwind of Gerania Mts and accelerates on the lee of the mountain (values greater than 18 m s^{-1}), while a strong vertical wind shear is evident, with a local maximum greater than 36 m s^{-1} in the layer between 3.0 to 4.0 km. The isentropes rise and descent, following the terrain, where an unstable layer with near-adiabatic conditions (vertically tilted theta contours) close to the ground and upwind of the mountain is present but stable conditions are met downwind. The time evolution (not shown) revealed high wind peaks (greater than 16 m s^{-1}) and breaking offs downstream, until the late evening hours on 23rd of July 2018. By removing the topography in WRF-d03 (NTOPO), the isentropic lifting and descent weakens (Fig. 4.19c), the flow is more stratified in the lowest atmosphere, a very shallow deep layer with wind values between 14 m s^{-1} to 16 m s^{-1} lies above the ignition point, while the surface wind speed is less than 14 m s^{-1} . In addition, a region of strong static stability in the first 500 m above the surface is shown from 22.95°E to $\sim 23.08^\circ\text{E}$. In the TOPOG experiment (Fig. 4.19e), only the topography height of Gerania Mts was set equal to zero (dashed polygon line in Fig. 4.20e,f), in order to address the effects of the particular barrier to the flow over the fire regime. By comparing the model results between NTOPO and TOPOG experiments, similarities arise, in both potential temperature and wind field, but a closer examination reveals that in TOPOG sensitivity run, colder air is advected over the fire area and more neutral conditions reside. Moreover, wind speed values below 12 m s^{-1} are modeled and maintained throughout the 23rd of July 2018.

Approximately one hour before ignition time at Kalliternoupolis (MATI event), at 12:35 UTC (Fig. 4.19b), the flow in control (CNTRL) simulation is neutrally stratified over the area of interest (23.94°E – 24.01°E), where two layers of high wind speeds are modeled. The upper layer lies above 2 km with jet core maxima over 38 m s^{-1} , while the lower layer is placed from the surface up to $\sim 1 \text{ km}$, with local maximum above 32 m s^{-1} . The flow is accelerated over the crest and downstream of Penteli Mt. (the cross-section is slightly to the south, G-F line in Fig. 4.1b), where peaks of high speeds are encountered resembling a hydraulic jump, albeit this feature was transient and presented only in the time window between 12Z to 13Z. In this time slice, the highest modeled wind speeds at 10m were also recorded at Rafina site (Fig. 4.10d). In addition, the subsidence of the 310 K isentrope over the fire area ($\sim 1.5 \text{ km}$ at 12:30 UTC and $\sim 0.5 \text{ km}$ at 14:05 UTC, not shown) along with the simultaneously wind speed increase at lower levels, indicates downward transport of momentum. In NTOPO experiment (Fig. 4.19d), lacking any orography in the wider area of Attica resulted to increased stability followed by more neutral conditions at the time of the maximum wind speeds occurrence ($\sim 13:30 \text{ UTC}$ to $\sim 16:15 \text{ UTC}$). Although the two high wind speed regions are also resolved as in CNTRL, with nearly equal local maxima, the lower layer is located higher (1 km to 1.5 km agl.), due to the presence of the warm front at $\sim 23.81^\circ\text{E}$ (Fig. 4.19d). In addition, the absence of topography in WRF-d03 increased the magnitude of the simulated low-level jet (not shown), located at around 0.5 km agl, with higher peak values (above 24 m s^{-1}) than in CNTRL (18 - 20 m s^{-1}). The modeled low-level jet appeared from $\sim 17:00 \text{ UTC}$ to $\sim 19:00 \text{ UTC}$ in both experiments. According to Fig. 4.18f, Penteli Mt. (TOPOP) slightly modified the mean flow

over the area of MATI. The TOPOP sensitivity experiment produced similar results with the CNTRL simulation, but on average introduced higher low-level jet speed values than in control run. Moreover, any resemblance of a hydraulic jump was not observed in TOPOP experiment.

Fig. 4.20 displays the average (left column) and the maximum (right column) 10 m wind speed from the innermost domain (WRF-d03), between 06Z on 23rd of July 2018 and 00Z on 24th of July 2018, for the control (CNTRL) simulation (a,b), the NTOPO (c,d), the TOPOG (e,f) and the TOPOP (g,h) experiments. By eliminating the orographic features in WRF-d03, the model produced a west-east wind speed gradient field (Fig. 4.20c), with average values greater than 10 m s⁻¹ west of Gerania Mts. (Corinthian Bay), while along the east coast, the average wind speed lied between 6 to 8 m s⁻¹. In addition, the local maxima on the leeward slopes of Gerania Mts, as they appeared in the CNTRL experiment, were not observed in NTOPO and TOPOG simulations, demonstrating how the presence of the mountain affected the flow downwind of the mountain.

In the wider area of the MATI fire event (Kalliternoupolis, Neos Voutsas, Rafina, Mati), the surrounding topographical barriers (Penteli Mt., Hymettus Mt.) had a lesser impact on the average wind speed, as it is presented in Fig. 4.20b,d,f,h, but greatly affected the spatial distribution of its maxima, during the 23rd of July 2018. In NTOPO experiment (Fig. 4.20d), a core of maximum wind speed values greater than 20 m s⁻¹ is located slightly to the north of the area of interest. The Messogia Plains (red frame) experienced values below 16m s⁻¹ in compare to the CNTRL simulation, where strong downslope winds (greater than 20 m s⁻¹) were presented over the area of the deadly fire. Moreover, the removal of the Penteli Mt (TOPOP experiment, Fig. 4.19h), did not weaken the magnitude of the simulated wind speed, only changed its locality. A closer examination reveals that the only area that has been affected by the absence of the Penteli Mt. was a small portion downwind and to the north, in the area encompassed by the dashed line (Fig. 4.20h). The latter implies that Penteli Mt. might not acted as the major contributor to the enhanced surface flow. Under strong background westerly flow, Hymettus Mt. could also produce intense downslope winds downwind of the mountain (Helmis et al., 2000), affecting the vicinity of the fire. A possible explanation would be that the interference of the produced waves, both from Hymettus and Penteli Mts, led to the local extrema in terms of the wind speed. If these assumptions were robust then the resolved wind speed maxima at NTOPO experiment would not be observed. On the contrary, the NTOPO simulation delivered wind speed values of the same magnitude as in the CNTRL. This suggests that, in general, the kinetic and dynamic characteristics of the mean flow over the Attica region were driven by the upper levels of the atmosphere, while the presence of the complex topography induced only spatiotemporal variations.

In order to evaluate how these topography induced variations affected the surface meteorological conditions in the vicinity of the MATI fire event, the 2m air temperature, T2, (°C, Fig. 4.21a), the 10m wind speed, SPD, (m s⁻¹) and direction, DIR, (degrees, Fig. 4.21b), in a WRF-d03 grid point with longitude-latitude values of 24.01633°E, 38.00906°N, from the control (CNTRL) simulation, the NTOPO and TOPOP experiments, were extracted. The specific point was selected as the closest to the sea grid point, in order to minimize the altitude effect on temperature between the three experiments. According to Fig. 4.21a, the temporal evolution (23/07_06Z to 24/07_00Z) of T2 in CNTRL and TOPOP was approximately the same. For the NTOPO simulation, the T2 presented higher values at morning hours (06:00 UTC to 08:30 UTC), due to the prevailing westerlies (Fig. 4.21b, orange diamonds) which were advecting warm air from the inland, while the rapid rise in temperature (dashed orange line, Fig. 4.21a) resulted almost one hour prior to corresponding one in the control (CNTRL) simulation. The latter shows that topography did not contribute to the mechanism behind this increase, rather it delayed its occurrence. From 06:00 UTC to ~11:30 UTC, on 23rd of July 2018, the NTOPO wind speed (dashed orange line, Fig. 4.21b) was higher than in CNTRL and TOPOP (except at some instances where

the change in wind direction occurred), but lower in the time window between 11:50 UTC to 14:05 UTC, in which the CNTRL and TOPOP SPD maxima were presented. Moreover, the lack of Penteli Mt. (red dotted line, Fig. 4.21b) allowed the south-easterlies to maintain their strength until ~11:45 UTC, as they were penetrating towards the inland.

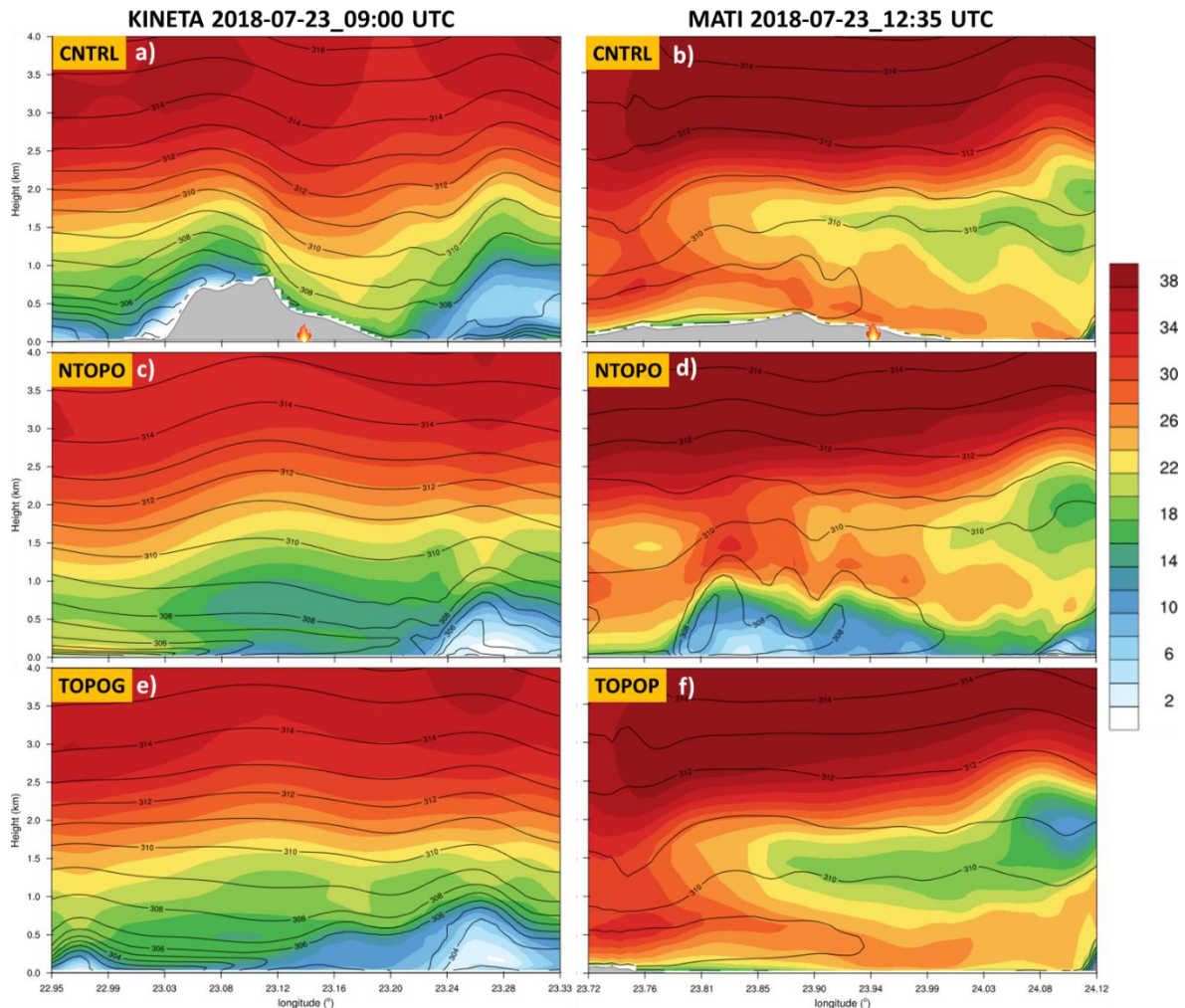


Fig. 4.19. Vertical cross-sections along E-F (left column) and G-H (right column) lines (Fig. 4.1b) of the 3-D wind magnitude (shaded contours) at 2 m s^{-1} intervals and potential temperature (contours) at 1 K interval, at KINETA (left) and MATI (right) fire events, for control (CNTRL) simulation (a,b), NTOPO (c,d), TOPOG (e) and TOPOP (f) sensitivity experiments. The fire symbols in (a) and (b) denote the location of fire ignition in each event.

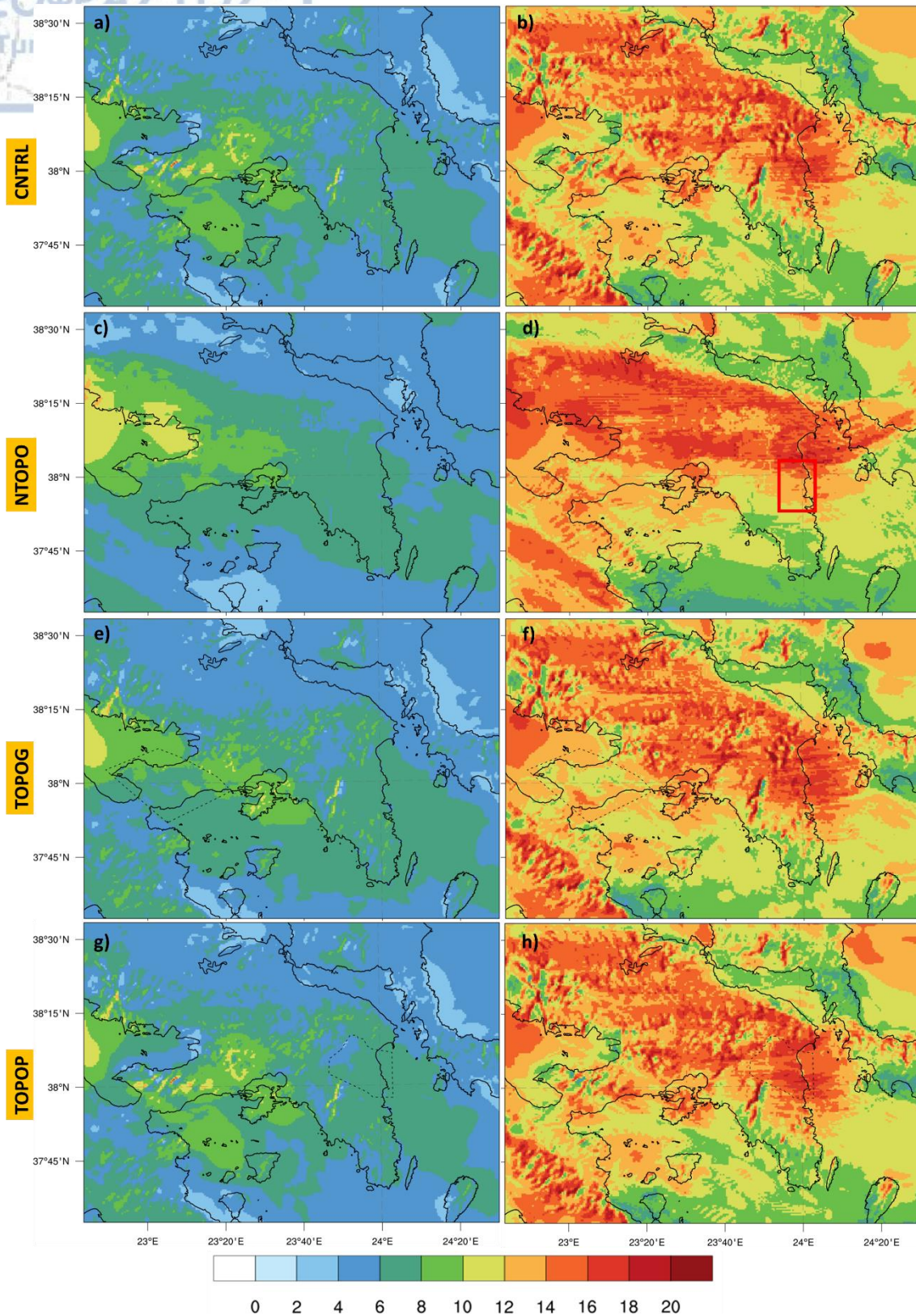


Fig. 4.20. WRF-d03 average (left column) and maximum (right column) 10m wind speed at $2 m s^{-1}$ intervals, from 23/07 at 06Z to 24/07/2018 at 00Z for control (CNTRL, a, b) and the three sensitivity experiments (NTOPO, c, d; TOPOG, e, f; TOPOP, g, h). The dashed lines in TOPOG (e, f) and TOPOP (g, h) images encompass the area where the topography was removed, while the red frame in NTOPO (d) dictates the Messogia Plains.

The mean turbulent kinetic energy ($\text{m}^2 \text{s}^{-2}$), TKE, from the lowest level ($\sim 10 \text{ m}$) up to $\sim 3600 \text{ m}$ agl, downwind of each topographic barrier and over the fire area (KINETA, MATI) was calculated, in the same manner as in section 6.2.2 (Fig. 4.22). According to Fig. 4.22a, Gerania Mts. (KINETA) influenced the mean turbulent flow downstream of the mountain by inducing higher perturbations in the wind components and thus affecting the ambient environment in which the fire ignited and propagated. In the CNTRL run (black line), the temporally averaged TKE, during the entire simulation (23-07-2018 06Z to 24-07-2018 12Z) was found equal to $0.32 \text{ m}^2 \text{ s}^{-2}$, against $0.26 \text{ m}^2 \text{ s}^{-2}$ and $0.27 \text{ m}^2 \text{ s}^{-2}$ in the NTOPO and TOPOG experiments, respectively. The impact of the mountain on TKE is evident from approximately 11Z to 18Z on 23/07, where the modeled NTOPO and TOPOG TKE is $\sim 24\%$ lower than in the CNTRL simulation. Worth of noticing is that during the warm hours on 24th of July 2018, the values of the TOPOG TKE (red dotted line) were close to the corresponding ones in the CNTRL experiment, which is attributed to the change in wind direction (from north-westerlies to northerlies) on the second day (24/07). As a result, the surrounding to the KINETA area topography (at north) produced turbulence, which affected the area of interest. On the contrary, the temporal evolution of the calculated TKE at MATI event (Fig. 4.22b) did not reveal significant differences between the CNTRL simulation (black line) and the other two sensitivity experiments (NTOPO, orange dashed line; TOPOP, red dotted line). In fact, the CNTRL TKE and TOPOP TKE presented very similar values, while the lack of topography in entire WRF-d03 resulted in a local minimum at 12:30 UTC ($0.56 \text{ m}^2 \text{ s}^{-2}$), nearly equal global maximum as in CNTRL and NTOPO and larger TKE values between 13:40 UTC and 15:00 UTC.

Fig. 4.23 presents the predicted fire perimeter as obtained from the control simulation (black solid line), the NTOPO (orange solid line), the TOPOG and TOPOP (red solid line) experiments, along with the observed EMSR300 burnt area (black dashed line) and the SRTM topography height (m; v_3 ; $30 \text{ m} \times 30 \text{ m}$; shaded contours), for a) KINETA (12Z, 24/07) and b) MATI fire events (00Z, 24/07). The previously presented analysis, in terms of vertical cross sections of potential temperature and 3-dimensional wind speed over the areas of interest, WRF-d03 mean wind speed (between 06Z on 23rd of July 2018 and 00Z on 24th of July 2018), 2m air temperature and 10m wind grid point values and averaged TKE timeseries, is reflected to the predicted fire area at KINETA (Fig. 4.23a), in both sensitivity experiments (NTOPO, TOPOG). Gerania Mts. contributed positively to warmer and drier surface conditions, enhanced the flow downstream, while the barrier produced and transported turbulence over the vicinity of the fire. As a result, the largest predicted fire area was presented in the CNTRL simulation (8336.82 ha). The lack of any topographical feature in the innermost domain (NTOPO) led to smaller fire area (5265.29 ha) than in control simulation, which justifies the aforementioned. Moreover, the removal of Gerania Mts. (TOPOG) resulted in the smallest burnt area (4327.94 ha) in total, which is about half of the predicted fire perimeter in the CNTRL experiment. The larger fire area in NTOPO compared to TOPOG sensitivity run is attributed to a) warmer and drier conditions overall in NTOPO and b) to the difference in wind direction (NTOPO, north-northwest; TOPOG northwest) during the morning hours of 24th of July 2018 and until the end of the simulation (12Z, 24/07). The latter allowed faster lateral fire spread on the southwest flank (orange line, Fig. 4.23a) against the TOPOG run. In addition, the NTOPO northeast flank experienced faster spread rates since ignition, due to the west-northwest wind direction, whereas in the TOPOG experiment the wind blew mostly from northwest directions.

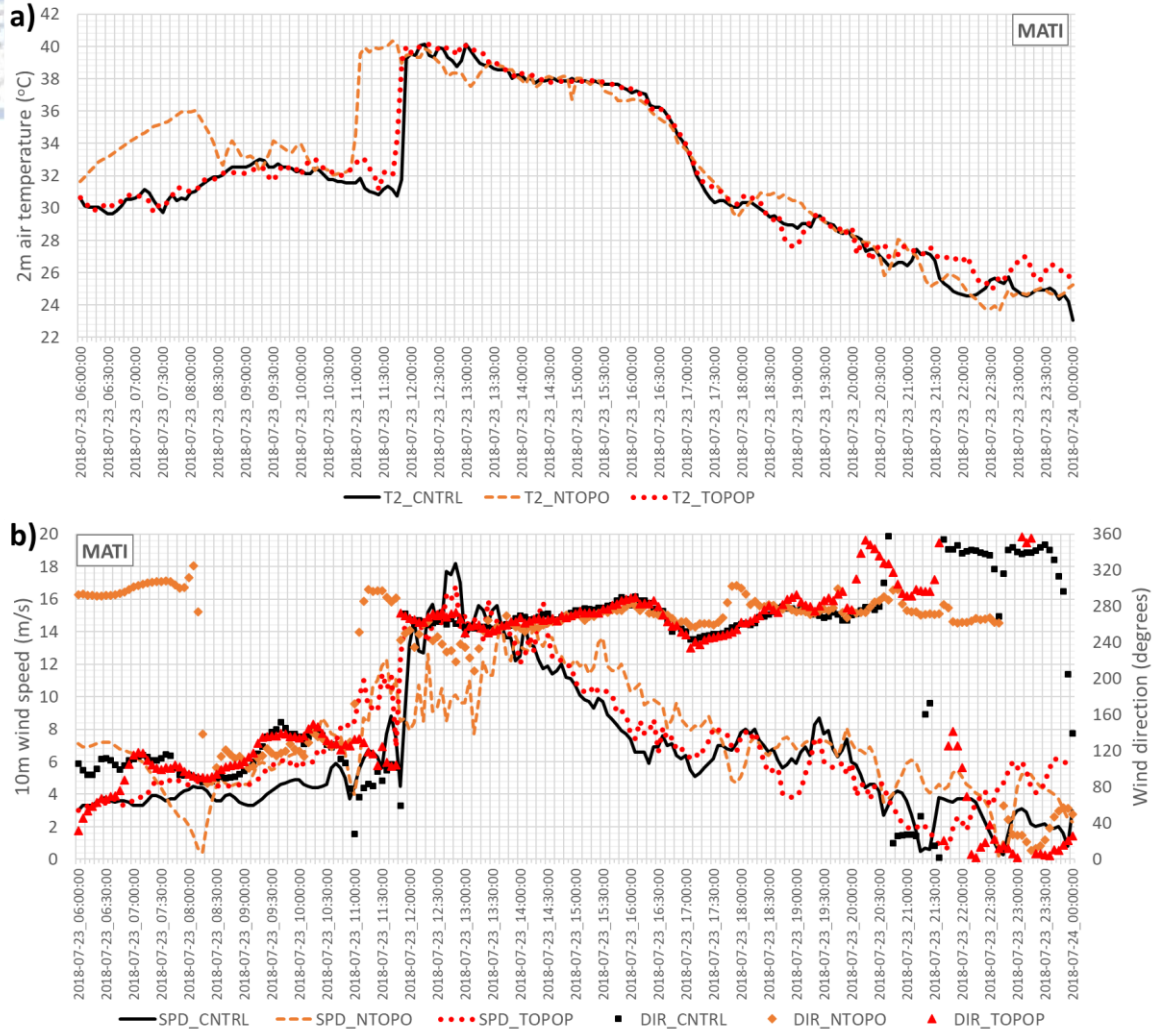


Fig. 4.21. Timeseries of a) air temperature at 2m ($^{\circ}\text{C}$), b) wind speed (m s^{-1}) and direction (degrees) at 10m, at the WRF-d03 grid point with longitude-latitude values of 24.01633°E , 38.00906°N , from CNTRL (black solid lines, black squares), NTOPO (orange dashed lines, orange diamonds) and TOPOP (red dotted lines, red triangles) experiments.

On the contrary, the topography at MATI event negatively affected the evolution of the fire, where the absence of either entire WRF-d03 orography (NTOPO) or only Penteli Mt. (TOPOP) led to larger burnt areas against the CNTRL run (Fig. 4.23b). In each experiment, the fire propagation was driven by the mean flow, which was affected by the morphological characteristics of the surroundings. In CNTRL simulation, the fire initially spread towards east (approximately until 19Z on 23/07), while it developed an east-northeast (east-southeast) direction in NTOPO (TOPOP). At 20Z, on 23/07, the CNTRL fire perimeter matched with the NTOPO burnt area (not shown), due to the presence of a north-westerly flow descending from Penteli Mt, but overall, the higher NTOPO wind speed values since ignition (orange dashed line, Fig. 4.23b), emanating from the lack of topography, contributed to faster burning rates ($2.0 \text{ ha}/5\text{min}$ against $1.8 \text{ ha}/5\text{min}$ on average). At the same time, in TOPOP experiment, a convergence region (with local maximum of $\sim 15 \text{ m s}^{-1}$) over the fire area (not shown) led to an escalating fire behavior ($2.8 \text{ ha}/5\text{min}$ on average), albeit it moved southwards and dissipated in the following hours. As a result, the TOPOP burnt area presented an extended south flank (red line, Fig. 4.23b) at 00Z, on 24th of July 2018 in contrast to the CNTRL fire area.

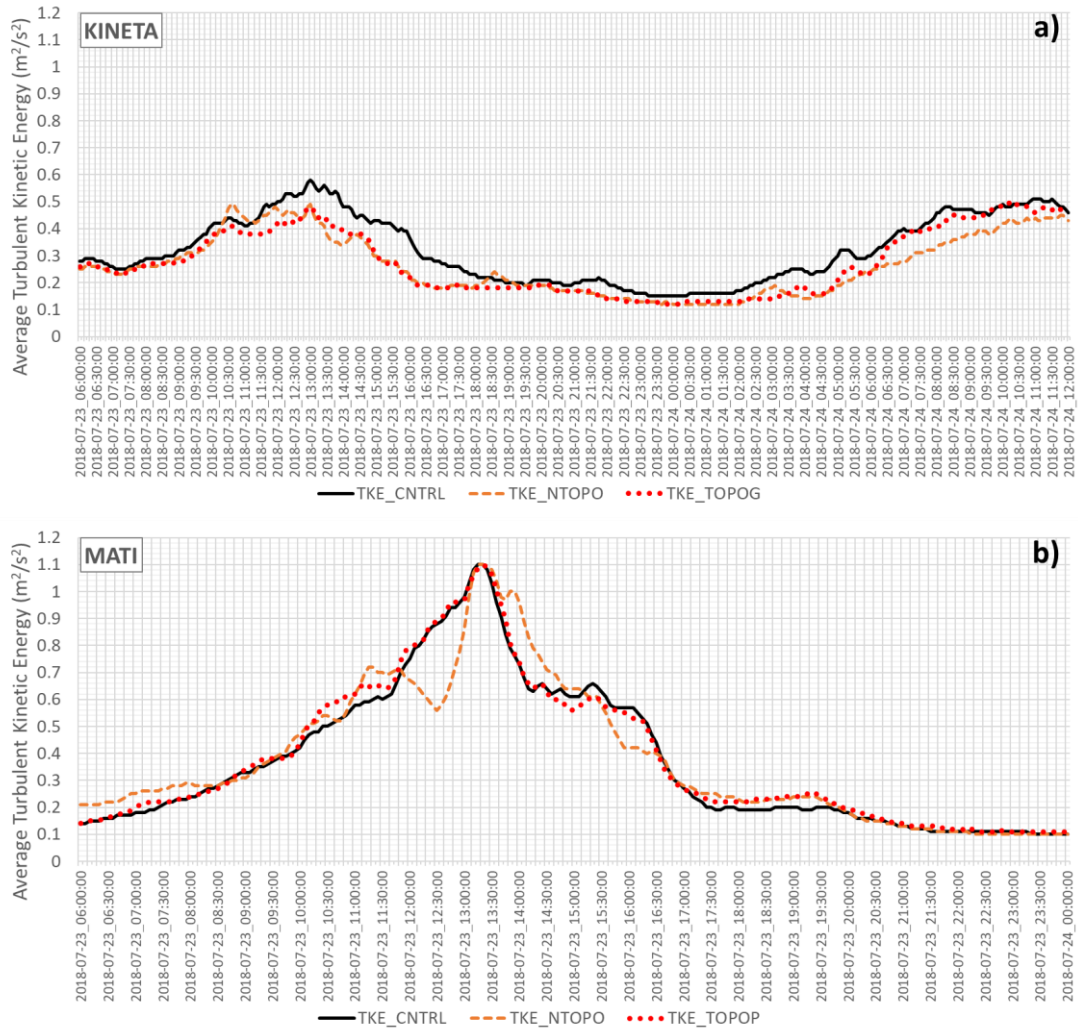


Fig. 4.22. Average turbulent kinetic energy ($m^2 s^{-2}$) up to ~ 3600 m agl over the area of a) KINETA and b) MATI fire event, as a function of time. Note the different time scales.

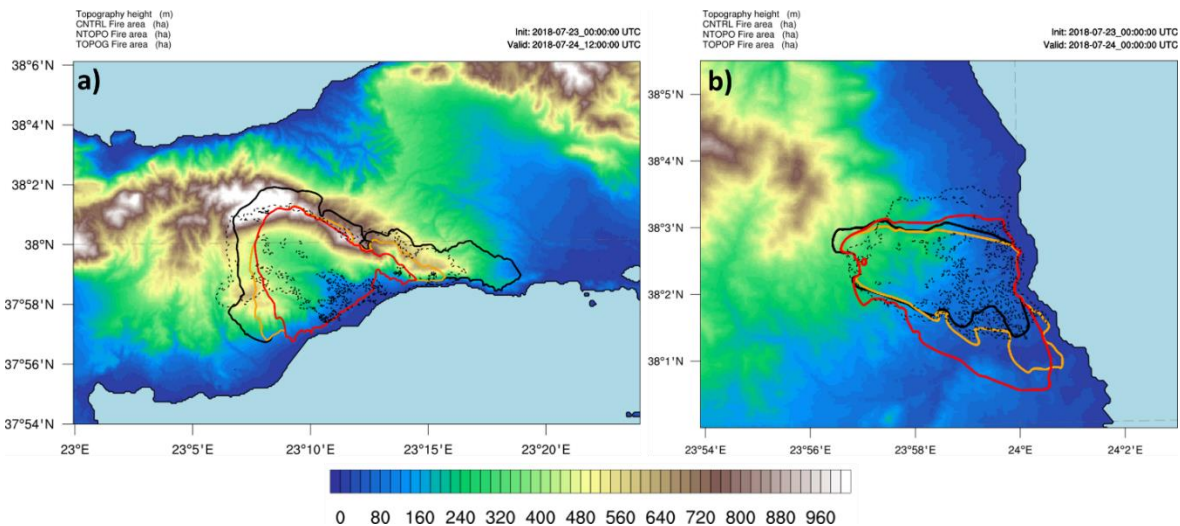


Fig. 4.23. Topography height (shaded contours), EMSR300 fire perimeter (black dashed line) and predicted burnt area in control (black solid line), NTOPO (orange solid line), TOPOG and TOPOP (red solid line) experiments for the a) KINETA and b) MATI fire events, respectively.

4.6.3.2 Impact of ignition parameters to fire evolution

Minor choices on the model setup and configuration may influence the results and the accuracy of the simulation overall. In this sub-section, the sensitivity of the user defined ignition parameters (time, location, type and initial rate of spread during ignition) and fuel information in the WRF-SFIRE modeling system is investigated, through a number of numerical experiments.

Seven experiments were performed in order to investigate how different choices regarding the time and the location of ignition, the type of ignition (point or line), the radius and the ignition rate of spread (ROS, rate of spread during ignition until the specified radius is reached) and the fuel model influence the simulated burnt area. From the aforementioned, the ignition's spatiotemporal input is crucial for the properly response of the WRF-SFIRE model and it is usually the least available information during the first stages of a fire. Table # summarizes the experimental setup of each simulation.

Table 4. 3. Experimental setup of each simulation

Experiment Name	Ignition type		Initial radius (fdx = 27.7 m)		Initial ROS (ms ⁻¹)		Time of ignition (UTC)		Fuel type	
	Point	Line	1 fdx	2 fdx	0.1	6	13:47	13:57	2	6
Exp00 (CTRL)	X		X		X			X	X	
Exp01	X			X	X			X	X	
Exp02	X			X	X			X		X
Exp03		X		X	X		X			X
Exp04				X	X		X			X
Exp05				X		X	X			X
Exp06				X		X	X		X	

Fig. 4.24 presents the time evolution of the simulated burnt area in each experiment. In general, in experiments with point ignition (Exp00, Exp01, Exp02 and Exp04), the fire front advances slower than in the experiments with line ignition (Exp04, Exp05 and Exp06). Approximately one hour since ignition (Fig. 4.24a), only the simulated fires in Exp05 and Exp06 sensitivities have built up their momentum and advance rapidly towards the coast (at this point these two experiments do not present any differences in the input data). Moreover, the fire in the experiment with line ignition and initial ROS equal to 0.1 m s⁻¹ (Exp04) has started to develop, showing how the initial ROS during ignition affect the resulting fire area. In the rest of the experiments, the corresponding fire areas are less than 10 ha.

At 1800 UTC (Fig. 4.24b), the fire front in Exp05 has reached the coastal area, while Exp04 and Exp06 present similar behavior but lower spread rates. It seems that the initial ROS of 6 m s⁻¹ and the NFFL fuel type 6 affected the most the spread rates at the first hours of the fire, as the maxima of the simulated wind were observed in that time period. Moreover, point ignition (the most accurate type of physical represented mechanism) failed to reproduce the fast moving fire front, in all corresponding experiments at the early stages of the fire, as it took long time for the fire to reach on the fire mesh nodes (not shown). At 2100 UTC (Fig. 4.24c), only the fire fronts of Exp00 and Exp01 sensitivities do not reach the coast, as the fire burns on NFFL fuel type 2 (timber grass and understory), which presents lower fuel load and burning time than the NFFL fuel type 6. The latter in conjunction with the weakened simulated wind field and its deviation from the westerly flow justifies the shape of the simulated fire areas compare to the other experiments. Moreover, Exp04 and Exp05 produces similar burnt areas, albeit in Exp05 the fire propagated along the flanks at the past 3 hours, with lower spread rates. The southwards expansion of the burnt area at 00 UTC on 24th of July 2018 (Fig. 4.24d), in all sensitivity runs is due to changes in the simulated wind field, which gradually turned from west to northwest directions.

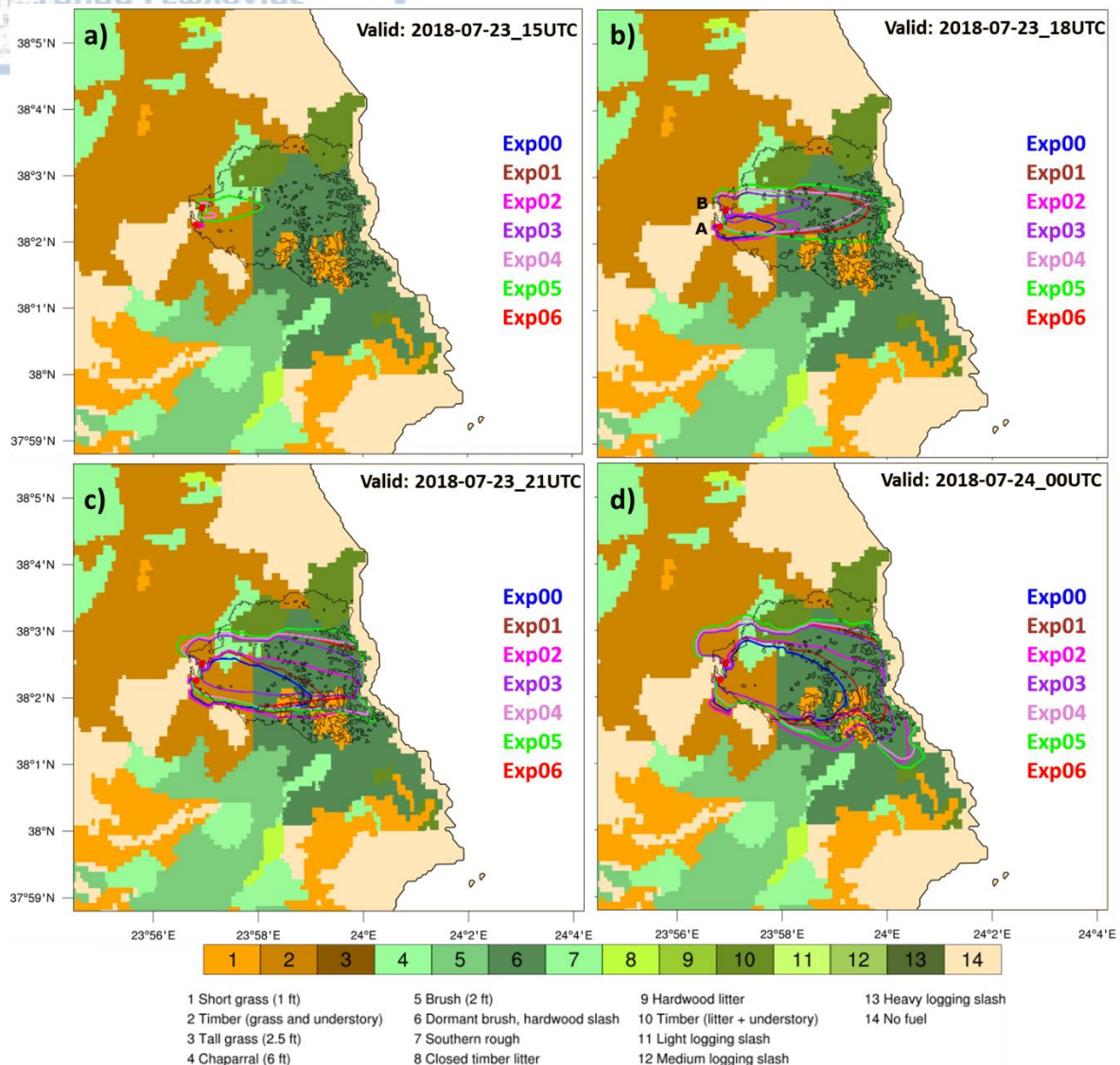


Fig. 4. 24. Simulated burnt area (contour) and NFFL fuel models (shaded contours) at a) 15 UTC, b) 18 UTC, c) 21 UTC on 23rd of July 2018 and d) at 00 UTC on 24th of July 2018, in each experiment. Black line represents the actual burnt area. A and B are the locations of the point ignition in Exp00, Exp01, Exp02 and Exp03, respectively. Pixels with NFFL fuel type 6 were assigned as NFFL fuel type 2 in Exp00, Exp01 and Exp06 experiments (horizontal stripes in b).

4.7 Discussion

This chapter presented the prevailing synoptic and surface weather conditions on 23rd of July 2018, in which two devastating fires ignited at Attica region, with 101 fatalities during the deadly fire at the area of Kallitethnoupolis, Neos Voutzas and Rafina settlements (MATI event) and over 8000 ha burned at KINETA event. It also examined the role of topography on the modification of the mean flow and its impact on the fire behavior in each event, through a number of high resolution numerical experiments.

The too complex morphological features in the wider area of Attica region did not allow for highly idealized numerical simulations at very fine resolutions (< 100 m), while the unavailability of radiosonde data and surface observations from a denser weather station network set some limitations to the analysis of the meteorological conditions that affected the fire propagation. Although the model

errors align with the bibliography for the wider area of Mediterranean region, they can be attributed to several factors. Karacostas et al. (2018) showed that the upper-air synoptic circulation type plays an important role in the performance of the WRF model. In addition, initialization errors due to the low density of surface and upper-air observations in the wider area, deficiencies in the representation of the physical mechanisms and in morphological features (e.g. topography, land uses) are some possible reasons contributing to the above discrepancies. In addition, the numerical experiments performed at high horizontal resolution (WRF-d03: $dx = dy = 0.555$ km), where predictability decreases as approaching the boundary layer processes deterministically (Mukherjee et al., 2016).

The examination of the physical processes that produced such windy conditions on the leeward slopes of Gerania Mts. and Penteli Mt., on 23rd of July 2018, did not reveal any distinctive mechanism involved. However, the lower atmosphere was subjected to vertical oscillations, where the complex terrain modified the mean airflow by inducing orographic waves, with wavelengths below 2 km. The presence of vertically propagating mountain waves requires specific criteria to be met, as described in Section 4.5. The control simulation (sub-section 4.6.2.1) did not resolve, either a mean-state critical level (reversed flow or mean flow equal to zero) or an inversion layer, albeit a vertical variation on the static stability with height was observed. The altered airflow showed also a transient resemblance of a hydraulic jump downstream of Penteli Mt., while on the lee-slopes of Gerania Mts. a strong vertical wind shear was evident. Moreover, the numerical simulations presented a sinking on the isotachs over the Attica region, where the highest wind speeds simulated. Although this feature needs further investigation, it is associated with downward transport of energy and momentum, as the subtropical jet passed over Central Greece. As a result, the question whether the hydraulic or vertically propagating wave theory applies in this case can be answered only in a qualitatively manner.

The effect of topography to fire behavior found to be different in the two cases. The isolated Gerania Mts. (KINETA event) influenced the lee-slope surface winds in a more linear way, where the presence of the particular barrier clearly enhanced the katabatic flow, which led to warmer and drier conditions at surface and thus affected the predicted total burnt area. On the other hand, Penteli Mt. (MATI event) contributed to the modification of the flow in the vicinity of the fire non-linearly, due to the surrounding complex terrain. The analysis indicated possible interferences on the flow by Hymettus Mt., which either amplified or diminished the surface winds in the sensitivity experiment (TOPOP).

The different fire ignition times resulted to different burnt areas as the temporal variation of simulated wind affected the fire spread rates, while the location of ignition point slightly improved the simulated burnt area. The most positively contributing factor was the initial rate of spread during ignition in the line ignition mechanism, where the model was able to capture the fast fire front propagation of the simulated event at the early stages of the fire.

The coupled model was able to reproduce the total burnt area in each event in a satisfactory way, taking advantage of the wind-driven propagation, where the fire behavior is mainly controlled by the mean flow (Morvan, 2011). In both fire events, the modeled fire required a "spin-up" time in order to develop a quasi-steady state, therefore discrepancies occurred in the temporal evolution of the predicted fire mostly at MATI event, as the fire module failed to represent the aggressive fire propagation. Given that the highest surface winds simulated during this "spin-up" period, the mismatch in fire spread rates is reasonable. Although, the same "delay" presented also in the fire at Gerania Mts., it had a lesser impact on its temporal evolution as the sustained windy conditions affected the propagation rates longer due to its earlier ignition time.

Another factor that adds limitations and inherits errors to the predicted fire is that the fire model (SFIRE) represents fire propagation only as surface fire (Mandel et al., 2011). In fact, the deadly fire at

East Attica (MATI) was characterized as canopy fire, at least upon arrival at the wildland urban interface of Neos Voutzas, Rafina, Mati and Kokkino Limaki settlements, which contributed to extreme spread rates and fire spotting (Egorova et al., 2019; Fernandez-Pello, 2017). In addition, the empirical fire spread formula (Rothermel, 1972) have not been validated at high wind speeds (Coen et al., 2018), while there is a hardcoded upper limit (6 m s^{-1}) in the predicted rate of spread (ROS) inside the fire module.

It is evident that the representation of the fuel conditions greatly affected the modeled fire behavior, where additional sensitivity experiments revealed the need for the applied fuel model reclassification in the area of MATI event (described in Section 3). Recently, two studies (Giannaros et al., 2019; Lagouvardos et al., 2019) investigated the performance of WRF-SFIRE modelling system in the case of MATI event. As they were closely related to each other, both studies utilized a fuel representation dataset, based on Scott and Burgan (2005) fuel models and additional custom fuels, albeit this dataset was constructed on relatively coarse resolution ($100 \text{ m} \times 100 \text{ m}$).

Moreover, the conversion and resampling of the relatively coarse resolution CORINE land use data ($100 \text{ m} \times 100 \text{ m}$) into NFFL fuel models ($30 \text{ m} \times 30 \text{ m}$) introduced errors, as the sub-grid variability in the fuel composition was not reflected inside the model, while the fuel moisture was tuned through the activation of the embedded fuel moisture model (Mandel et al., 2014), with no further adjusting. Even though the aforementioned conversion was based on literature, it stresses out the need for a common strategy regarding the mapping and representation of fuels at national level. Finally, the fire model did not account for fire-fighting operations, which play an important role in the shape of the final burnt area, albeit in the case of the MATI fire event, the response time was very limited.

4.8 Summary and conclusions

Two extreme fire events took place on 23rd of July 2018 at Attica region, Central Greece under favorable atmospheric conditions (high surface temperatures and wind speeds, low relative humidity values). The fire at East Attica (Kalliternoupolis, Neos Voutzas, Rafina, Mati and Kokkino Limanaki settlements) was the deadliest fire in Greek history, with 103 fatalities. The extreme windy conditions in conjunction with the morphological features of the area (wildland urban interface) resulted in aggressive spread rates and fire behavior, burning 1275.9 ha in total, until the early hours on 24th of July 2018. According to HNMS weather station data at Rafina site, which destroyed by the fire, the maximum recorded temperature was $39 \text{ }^\circ\text{C}$, wind speed reached 11.8 m s^{-1} , with maximum gustiness of 25.2 m s^{-1} . The fire at Gerania Mts. (West Attica) maintained until the late hours on 25th of July 2018, where the fire area was 5613.3 ha, as obtained from the Copernicus EMS – Mapping platform.

The online coupled WRF-SFIRE modelling system was utilized in order to simulate these two extreme fire events, analyze the prevailing synoptic and local atmospheric conditions and examine the impact of complex terrain to the mean flow and fire behavior. The model validated in terms of temperature, relative humidity and wind speed against the available HNMS surface observations and found to be consistent with the literature. The very high resolution ($0.555 \text{ km} \times 0.555 \text{ km}$) simulations revealed the presence of induced orographic waves, paths of high winds on the lee-slopes, transient resemblance of a hydraulic jump downstream of Penteli Mt., while indicated a downward transport of energy and momentum during the maximum wind speed occurrences. The turbulent and dynamically unstable conditions on the lee-slopes of Gerania Mts. and Penteli Mt. contributed to the flow kinetic energy, while vorticity provided additional forcing into the fire spread rates. Although the predicted fire perimeters were in agreement with the observed ones, there was a time-lag in the development of the fire momentum and thus discrepancies on the temporal evolution of the modeled fires.

Sensitivity experiments indicated quite different influences of topography in each fire event, where the isolated Gerania Mts contributed to warmer, drier and windier conditions leeward, while Penteli Mt. had a lesser impact on atmospheric variables downstream. The warm front feature and the increase on surface wind all along the Messogia Plains and east coastal area of Attica were common in all sensitivity experiments, supporting further the aforementioned downward transport of momentum. Nevertheless, variations in local maxima (e.g. temperature, wind speed) were observed and their spatial distribution affected the fire behavior non-linearly.

The choice of the user defined ignition parameters affected also the evolution of the simulated fire at MATI event. These choices rise in the framework of an emergency response system, where the ignition time and location are not always accurately available during the early hours of a wildfire. The type of ignition along with the rate of spread during ignition influenced the most the fire propagation at the early stages of the fire. The experiment with line ignition, high initial ROS and more representative fuel model in the area of interest reproduced the fast advancing fire front the most, while the most evident discrepancies were presented in the experiment with point ignition, low initial ROS and false information about the fuel conditions in the area. Fuel description had a lesser impact on the simulated rate of spreads during the early stages of the fire but influenced its behavior later. In addition, the period of the simulated wind maxima coincided with the early hours of the fire, acting synergetic to its evolution in the experiments where the fire had already built up its momentum.

The 1 to 20 ratio between atmospheric and fire mesh, led to a horizontal discretization of approximately 30 m x 30 m for the fire model, which is close to the available topographical SRTM data. Despite the very fine resolution, certain physical processes regarding the atmosphere-fire interactions were not resolved, such as the observed (Sentinel 2A) lateral fire spread at KINETA event, revealing potential limitations due to relative coarse resolution for these processes. Also, the potential contributions of Parnitha and Hymettus Mts. to the mean flow over the wider area has not been addressed, paving the way for further investigation. Finally, additional studies would be useful in order to understand the limitations that arise due to the simplified physical approach of numerical solving mixed complex problems at different scales.





Chapter 5 Conclusions and key remarks

This PhD dissertation investigates atmosphere –fire interactions by utilizing an online coupled atmosphere – fire numerical model (WRF-SFIRE) which is a combination of a numerical weather prediction (NWP) model with a semi-empirical numerical fire spread model. It consists of five distinct chapters, which introduce, present, investigate, evaluate and discuss several aspects on atmosphere interactions with wildland fires. It also addresses the performance of the coupled model by utilizing a number of surface observational data from the Hellenic National Meteorological Service (HNMS) and several EO data, which are provided by the Meteosat SEVIRI, SENTINEL-2, Aqua and Terra (MODIS) and Suomi-NPP (VIIRS) satellites, respectively. Moreover, the present PhD dissertation exploits the capabilities of WRF-SFIRE across several spatial scales, from mesoscale analysis on fire weather conditions during high-impact fire events to microscale analysis on highly idealized experiments, in Large Eddy Simulation (LES) mode. Next, the conclusions of this work are elaborated, following by the concluding key remarks.

5.1 Conclusions

5.1.1 The heat extinction depth concept: An application to the WRF-SFIRE modelling system

Eight highly idealized simulations were performed in order to investigate how the e-folding depth of the released sensible and latent heat fluxes from a surface fire into the lowest atmospheric computational domain of the WRF-SFIRE modelling system are affecting the evolution of the modelled fire. Since the vertical distribution of the fire's energy is not resolved explicitly in the coupled model but is parametrized by assuming an exponential decay with height, an assessment of the aforementioned formulation is necessary.

The analysis revealed that the choice of the z_{ext} parameter not only affects the vertical distribution of the fluxes but also the amount of the released energy from the surface fire. The higher the z_{ext} value, the higher the percentage of the released energy that resides on the first theta model level. For z_{ext} equal to 5 m it was found that only ~31.4% of the heat fluxes from the surface fire was entering into WRF (at 1st theta level), while for $z_{\text{ext}} = 200$ m, approximately 97% of the ground heat fluxes were inserted into the 1st theta level. Moreover, the results indicate that the height of the sigma levels can lead to further underestimation of the amount of the fire's energy that enters into the WRF domain, in the case where the z_{ext} value is lower than the first theta (mass) level. Since in real simulations the 1st theta level is usually much higher than in the experiments of this study, the latter must be taken into consideration upon configuration of the fire model. In addition, a linear behavior regarding the maximum injection height as a function of z_{ext} parameter was found.

In the surface, the ext15m sensitivity run produced the fastest advancing fire fronts, as rates of spread (ROS) equal to 5.97 m s^{-1} were simulated only in this experiment. The average ROS was 1.54 m s^{-1} , while in the rest experiments, the corresponding values were not greater than 0.5 m s^{-1} . The temporal evolution of the predicted fire area was in line with the temporal ROS peaks and found different in each experiment. The calculated burn probabilities revealed that under identical initial atmospheric conditions but different e-folding depths discrepancies may occur in the resulted fire area.

The so called “power of the fire” was also examined, revealing differences in the released energy from the surface fire both in time and magnitude between experiments. The ext015m presented the highest temporal heat output peak ($\sim 41,000$ MW), which led to erratic fire behavior and “blow-up” conditions at the end of the analyzed period. At the same time window, the maximum heat output in the ext005m run was found equal to $\sim 33,000$ MW, causing CFL violations and early termination of the simulation. In ext200m model run, heat release rates higher than 8,000 MW (max. $\sim 13,100$ MW) are produced in the middle of the analysis, resulting to high fire area growth rates.

The coupled WRF-SFIRE model was able to reproduce certain flow characteristics such as the convergence region ahead of the fire front and the descending rear inflow to the updraft’s base. The interactions between the ambient environment and the surface plume resulted into the formation of two main longitudinal horizontal vortices, which acted as inflow to the front of the half-upper part of the fire plume or interacted mostly with the surface. A possible mechanism is the reorientation of the shear-generated horizontal components of vorticity (ω_x, ω_y) in the ambient atmosphere due to the presence of fire plume and the convergence that occurs in vertical, while the stability profile of the atmosphere or even the presence of the inversion layer aloft could also contributed to their formation.

The highest vertical velocities were simulated in the ext015m experiment (max. 34.3 m s^{-1}) as a response to the high amount of released energy from the ground, but one should keep in mind the relatively small frequency of the model outputs (every 5 minutes). Thus, higher values could be encountered. The strongest downdrafts were also met in the ext015m sensitivity (max. 11.4 m s^{-1}), at ~ 43 m agl. Both maximums (upward and downward velocities) were encountered during the blow up conditions, at 60 min since ignition. In addition, the vertical distribution of upward velocities in almost all experiments (except in ext025m) was similar, where higher velocities were presented around 2 km agl and were decreasing up to the plume top.

In general, an increase of the z_{ext} parameter leads to weaker time-averaged potential temperature anomalies both close to the ground and in the top of the convective plume. However, the temporal peaks in theta anomalies do not follow any linearity and their occurrence varies both in time and space. In all experiments, the absolute minimum potential temperature anomaly occurred at 1st theta level (~ 5.8 m), while the maximum theta anomaly is met at 1st theta model level only in the CNTRL, ext005m, ext010m, ext015 and ext025m experiments. For the ext075m, ext100m and ext200m sensitivity runs, the maximum theta anomaly is located at 6th (~ 71.5 m), 11th (~ 155.7 m) and 9th (~ 119.5 m) mass level, respectively. Strong negative potential temperature anomalies were observed in ext015m (max. 207.3 K) and less intense minima in the rest experiments.

The time-mean plume-averaged properties indicated negative differences in plume vertical velocities, in ext075m, ext100m and ext200m up to ~ 1 km agl and positive aloft, while positive differences were observed in ext005m, ext010m, ext015m and ext025m experiments up to 2 km agl. In the layer between ~ 1200 m and ~ 1300 m agl, all experiments presented thinner plumes than in CNTRL, which coincided with the regime of higher vertical velocities in this layer. The vertical profiles of mass flux presented mostly negative discrepancies up to ~ 1200 m agl (except in ext200m sensitivity) compare to CNTRL’s one and positive differences aloft. Close to the ground and specifically up to ~ 18 m agl, all simulations but two (ext100m and ext200m) produced higher water vapor plume excesses than CNTRL, while discrepancies on plume temperature excesses occurred up to ~ 600 m agl. Aloft the differences became essentially zero against to CNTRL’s vertical profile.

The analysis on near surface dynamics revealed discrepancies in the patterns and the magnitude of vertical vorticity and divergence fields, in the shape of the fire perimeter and the location of the fire head. Low e-folding depth values produced more organized and intense counter-rotating vertical

vorticity pairs and regions along the fire flanks and in front of the active fire head, whilst in the sensitivities with z_{ext} greater than 50 m, this vorticity was less organized and more transient.

The vorticity equation budget analysis showed that the solenoidal term, which generates vorticity, was up to twelve orders of magnitude less than the other terms. During the "blow-up" conditions in ext015m sensitivity run, the latter amplified its strength up to four orders, where the vertical advection term presented the highest maximum among the other terms. In CNTRL experiment and at 50 m agl, the horizontal advection of vertical vorticity contributed the most to the increase of vorticity, while the tilting/twisting term was dominant at the early stages of the fire, where the ambient shear-generated horizontal vorticity, ω_y , was oriented into vertical due to buoyant gradients from the surface fire.

5.1.2 Numerical investigation of atmosphere-fire interactions during extreme fire events in Attica region

Two extreme fire events took place on 23rd of July 2018 at Attica region, Central Greece under favorable atmospheric conditions (high surface temperatures and wind speeds, low relative humidity values). The online coupled WRF-SFIRE modelling system was utilized in order to simulate these two extreme fire events, analyze the prevailing synoptic and local atmospheric conditions and examine the impact of complex terrain to the mean flow and fire behavior.

The model was validated in terms of temperature, relative humidity and wind speed against the available HNMS surface observations by applying the Inverse Distance Weighting (IDW) method, the Cressman method and a 4-grid point method. According to IDW method, the model overestimated Tmp and Wspd by 1.4 ± 0.2 K and 1.9 ± 0.3 m s⁻¹, while the ME in Rh is underestimated (-3.7 ± 1.0 %). The MAE (RMSE) of Tmp, Rh and Wspd were found equal to 1.8 ± 0.1 (2.2 ± 0.8) K, 8.7 ± 0.7 (11.6 ± 5.0) % and 2.8 ± 0.2 (3.6 ± 1.3) m s⁻¹, respectively. The forecast and observed temperature values were highly correlated (Pearson, 0.92), while for the relative humidity and wind speed, the Pearson correlation coefficients were found equal to 0.75 and 0.56. Also, the standard deviation (STDEV) for the Tmp, Rh and Wspd MAEs were 1.3 K, 7.7 % and 2.2 m s⁻¹, respectively. The Cressman method produced same results as the IDW method for Tmp and Wspd variables, while slightly affected the scores of Rh. Differences on skill scores appeared for Rafina site, where the underestimation of Rh was decreased from -4.6 % to -3.8 % in comparison to the ME from the IDW method, while the MAE (RMSE) decreased by 0.3 % (0.4 %). By applying the 4 grid point method to the verification procedure, the model errors (MAE, RMSE) are reduced in all variables under examination. The model underestimates Rh (-3.5 ± 1.0 %), while Tmp and Wspd are overestimated (1.3 ± 0.2 K, 1.7 ± 0.3 m s⁻¹) as in the previous two methods.

The very high resolution (0.555 km x 0.555 km) simulations revealed the presence of induced orographic waves, paths of high winds on the lee-slopes, transient resemblance of a hydraulic jump downstream of Penteli Mt., while indicated a downward transport of energy and momentum during the maximum wind speed occurrences. Worth of noting is the front-like feature of high temperatures at the vicinity of MATI, accompanied by high wind speeds with maxima of ~ 18 m s⁻¹, propagating eastwards towards the coast.

The turbulent and dynamically unstable conditions on the lee-slopes of Gerania Mts. and Penteli Mt. contributed to the flow kinetic energy, while vorticity provided additional forcing into the fire spread rates. At KINETA event, regions of negative (anticyclonic) vorticity values were located downwind of the land, suppressing the smoke emissions close to the surface, over the sea and southwards, where the smoke plume tended to rise, as positive (cyclonic) ω_x values dominated. Noticeable was also the

pair of cyclonic and anticyclonic vortices upwind to the plume and over the land, evident of the turbulent conditions in the area. Moreover, a pattern of anticyclonic rolls in the layer between 500 to 1500 m over the sea was shown. Regarding the temporal evolution of the plume, at 11:45 UTC, fire emissions extent up to 1.5 km, while high concentrations are observed close to the ground. The anticyclonic vortex was still present but was reduced in magnitude, as embedded positive ω_x vorticity regions allowed the vertical extension of the smoke over the sea. A cross-section, also at 11:45 UTC revealed a vortex pair, where in each core lied high smoke concentrations, while the plume had reached approximately at 2 km.

At MATI event, examination of the vertical profile of the y component of the vorticity vector (s^{-1}), ω_y , showed an area of positive ω_y values ($\sim 0.02 s^{-1}$) close to the ground, resulting to vorticity driven flow prior to the fire ignition (13:30 UTC). A layer of negative ω_y values existed between 1.5 km to 2.5 km, while a core of wind speeds greater than $25 m s^{-1}$ (50 knots) was also shown in the layer between 1.0 km to 2.0 km. The cyclonic vortices were maintained until the late evening hours, providing additional forcing into the fire spread rates and the vertical mixing. In addition, at the same time, cyclonic vortices with their rotation axis parallel to the mean flow (ω_x vorticity) were resolved by the model, appearing upwind, over and downwind of Penteli Mt. Also, a well-organized cyclonic vortex was evident over the Messogia Plain, which it is assumed that it was generated due to the presence of Hymettus Mt.

At KINETA, the observed fire radiative power (FRP) on 23/07 lied between $5.7 W m^{-2}$ ($\sim 20:40$ UTC) to $2012.3 W m^{-2}$ ($\sim 09:35$ UTC), while at MATI, the FRP ranged from $6.9 W m^{-2}$ to $56.3 W m^{-2}$, during the Terra satellite passing ($\sim 20:40$ UTC). Also, the Suomi-National Polar-orbiting Partnership (S-NPP) satellite completed one pass on 23/07 ($\sim 11:40$ UTC) and another one, on 24/07 ($\sim 00:00$ UTC), over Attica region, with recorded VIIRS-FRP maxima equal to $187 W m^{-2}$ ($\sim 11:42$ UTC, 23/07) and $17.1 W m^{-2}$ ($\sim 00:00$ UTC, 24/07) at KINETA and MATI, respectively.

Although the predicted fire perimeters were in agreement with the observed ones, there was a time-lag in the development of the fire momentum and thus discrepancies on the temporal evolution of the modeled fires. For KINETA, the total burnt area according to the WRF-SFIRE modelling system (from 23/07, 09Z until 24/07, 12Z) was 8336.82 ha, approximately 48% greater than the observed one (5613.3 ha, Copernicus EMS-event EMSR300). The mean rate of fire area growth was found equal to $0.04 ha/5min$, while the maximum accumulated heat fluxes from the fire were $245.3 MW m^{-2}$, at 13:45 UTC. The rapid increase in the released heat fluxes since ignition, is placed at approximately at 11:15 UTC and is associated with the ignition of an additional fuel type (NFFL fuel type 7, Southern rough) with high moisture of extinction values ($\sim 40\%$) and live foliage flammability. In the case of the deadly fire at MATI, the fire model produced higher burnt area growth rates (average equal to $0.09 ha/5min$), representative of the actual fire propagation. The total modeled burnt area, at 00Z on 24/07, since ignition (23/07, $\sim 13:49$ UTC) was 1083.26 ha, against 1275.9 ha, as recorded in the EMSR300 data. Also, two distinctive peaks in the heat fluxes from the fire at MATI (black dashed line) are presented, which slightly affected the slope of the fire area line (black solid line). The local heat maxima are almost three times lower than the global maximum heat fluxes at KINETA, because of the different fuel types and most importantly the lower modeled wind field, at the time of occurrence.

Sensitivity experiments indicated quite different influences of topography in each fire event, where the isolated Gerania Mts contributed to warmer, drier and windier conditions leeward, while Penteli Mt. had a lesser impact on atmospheric variables downstream. The warm front feature and the increase on surface wind all along the Messogia Plains and east coastal area of Attica were common in all sensitivity experiments, supporting further the aforementioned downward transport of momentum. Nevertheless, variations in local maxima (e.g. temperature, wind speed) were observed and their spatial distribution affected the fire behavior non-linearly.

The type of ignition along with the rate of spread during ignition influenced the most the fire propagation at the early stages of the fire. The experiment with line ignition, high initial ROS and more representative fuel model in the area of interest reproduced the fast advancing fire front the most, while the most evident discrepancies were presented in the experiment with point ignition, low initial ROS and false information about the fuel conditions in the area. Fuel description had a lesser impact on the simulated rate of spreads during the early stages of the fire but influenced its behavior later. In addition, the period of the simulated wind maxima coincided with the early hours of the fire, acting synergetical to its evolution in the experiments where the fire had already built up its momentum.

5.2 Key remarks

- The WRF-SFIRE modelling system was able to reproduce several observed flow characteristics during a wildland fire, in Large Eddy Simulation (LES) mode.
- The user-defined extinction depth parameter (z_{ext}) not only affected the vertical distribution of the released fire fluxes into the lower atmospheric layer but also controlled the amount of the energy that resides on the first model level.
- Under identical initial condition but different extinction depths discrepancies occurred in the simulated fire area, due to different responses between the fire heat output and flow dynamics.
- Maximum updraft velocities up to 34 m s^{-1} were observed, as a response to the high amount of released energy and the resulted convection. The higher upward velocities were presented around 2km above ground level .The strongest downdrafts were equal to 11.4 m s^{-1} and simulated at $\sim 43 \text{ m}$ above ground level.
- By increasing the z_{ext} parameter, the time-averaged potential temperature anomalies weakened close to the ground and at the top of the convective column. The temporal peaks of the anomalies did not follow any linearity and their occurrence varied both in time and space.
- The different values of the z_{ext} parameter affected the time-mean plume-averaged properties, where lower (higher) plume vertical velocities were encountered in the sensitivities with high (low) z_{ext} values close to the ground. Moreover, the absolute maximum plume temperature excesses were equal to $373 \text{ }^{\circ}\text{C}$ against the control simulation.
- Low e-folding depth values produced more organized and intense counter-rotating vertical vorticity pairs and regions along the fire flanks and in front of the active fire head, whilst in the sensitivities with higher z_{ext} , this vorticity was less organized and more transient.
- The solenoidal term was up to twelve orders of magnitude less than the other vorticity equation terms. Close to the ground, the horizontal advection of vertical vorticity (ζ) contributed the most to the increase of ζ , while the tilting/twisting term was dominant at the early stages of the fire.
- The synoptic analysis during the extreme fire weather conditions on 23rd of July 2018 revealed the presence of a positively tilted trough over the Central Mediterranean, moving eastwards and interacting with the subtropical jet, resulting in a strong westerly flow over Greece. The AWS in Penteli Mt recorded gusts reaching 25 m s^{-1} between 1230 and 1430 UTC, while several



HNMS surface stations in the wider area recorded wind gusts exceeding 20 m s^{-1} between 1200 and 1730 UTC.

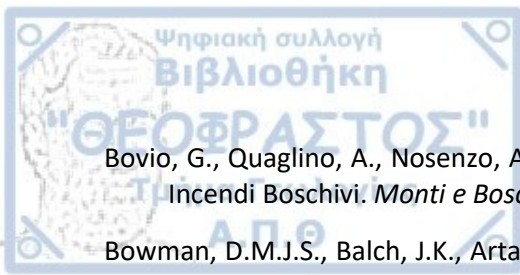
- The evaluation of the WRF-SFIRE revealed good performance in terms of temperature, relative humidity and wind speed in all verification methods that were employed. In general, the model overestimated the air temperature and wind speed, while underestimated the relative humidity.
- The predicted fire perimeters (burnt areas) in both events were in satisfactory agreement with the observed ones, but there were time lags in the initial development of the fires' momentum and subsequently, discrepancies on the temporal evolution of the modeled fires occurred.
- The simulations revealed the presence of induced orographic waves, paths of high winds on the lee-slopes, transient resemblance of a hydraulic jump downstream of Penteli Mt., while indicated a downward transport of energy and momentum during the maximum wind speed occurrences.
- The turbulent and dynamically unstable conditions on the lee-slopes of Gerania Mts. (KINETA) and Penteli Mt. (MATI) contributed to the flow kinetic energy, while vorticity provided additional forcing into the fire spread rates.
- Quite different influences of topography in each fire event were found, where the isolated Gerania Mts contributed to warmer, drier and windier conditions leeward, while Penteli Mt. had a lesser impact on atmospheric variables downstream.
- The type of ignition along with the rate of spread during ignition influenced the most the fire propagation at the early stages of the fire. Fuel description had a lesser impact on the simulated rate of spreads during the early stages of the fire but influenced its behavior later.

- Achtemeier, G.L., 2003. "Rabit Rules" - an application of Stephen Wolfram's "New Kind of Science" to fire spread modelling, in: *Fifth Symposium on Fire and Forest Meteorology. American Meteorological Society: Boston, MA, 16-20 November, Orlando, FL.*
- Adelabu, S.A., Adepoju, K.A., Mofokeng, O.D., 2020. Estimation of fire potential index in mountainous protected region using remote sensing. *Geocarto Int.* 35, 29–46. <https://doi.org/10.1080/10106049.2018.1499818>
- Albini, F.A., 1982. Response of Free-Burning Fires to Nonsteady Wind. *Combust. Sci. Technol.* 29, 225–241. <https://doi.org/10.1080/00102208208923599>
- Amraoui, M., Liberato, M.L.R., Calado, T.J., DaCamara, C.C., Coelho, L.P., Trigo, R.M., Gouveia, C.M., 2013. Fire activity over Mediterranean Europe based on information from Meteosat-8. *For. Ecol. Manage.* 294, 62–75. <https://doi.org/10.1016/J.FORECO.2012.08.032>
- Amraoui, M., Pereira, M.G., DaCamara, C.C., Calado, T.J., 2015. Atmospheric conditions associated with extreme fire activity in the Western Mediterranean region. *Sci. Total Environ.* 524–525, 32–39. <https://doi.org/10.1016/j.scitotenv.2015.04.032>
- Anderson, H.E., 1982. Aids to determining fuel models for estimating fire behavior. *Bark Beetles, Fuels, Fire Bibliogr.* 1–22. <https://doi.org/citeulike-article-id:12114185>
- Anderson, H.E., 1970. Forest fuel ignitibility. *Fire Technol.* 6, 312–319. <https://doi.org/10.1007/BF02588932>
- Anderson, H.E., 1969. Heat transfer and fire spread, Res. Pap. INT-RP-69. Ogden, Utah. <https://doi.org/10.5962/bhl.title.69024>
- Andrews, P.L., 2014. Current status and future needs of the BehavePlus Fire Modeling System. *Int. J. Wildl. Fire* 23. <https://doi.org/10.1071/WF12167>
- Andrews, P.L., 2007. BehavePlus fire modeling system: past, present, and future, in: *7th Symposium on Fire and Forest Meteorological Society.*, 13.
- Ångström, A., 1949. Swedish meteorological research 1939–1948. *Tellus* 1, 60–64.
- Ångström, A., 1942. The risks for forest fires and their relation to weather and climate [Riskerna för Skogsbrand och deras beroende av väder och klimat]. *Svenska skogårdsföreningens Tidskr.* 4, 18.
- Arnold, R.K., Buck, C.C., 1954. Blow-up fires - silviculture or weather problems? *J. For.* 52, 408–411.
- Arpaci, A., Eastaugh, C.S., Vacik, H., 2013. Selecting the best performing fire weather indices for Austrian ecoregions. *Theor. Appl. Climatol.* 114, 393–406. <https://doi.org/10.1007/s00704-013-0839-7>
- Bak, P., Chen, K., Tang, C., 1990. A forest-fire model and some thoughts on turbulence. *Phys. Lett. A* 147, 297–300. [https://doi.org/10.1016/0375-9601\(90\)90451-S](https://doi.org/10.1016/0375-9601(90)90451-S)
- Bakhshaii, A., Johnson, E.A., 2019. A review of a new generation of wildfire–atmosphere modeling. *Can. J. For. Res.* 565–574. <https://doi.org/10.1139/cjfr-2018-0138>
- Balbi, J.H., Morandini, F., Silvani, X., Filippi, J.B., Rinieri, F., 2009. A physical model for wildland fires. *Combust. Flame* 156, 2217–2230. <https://doi.org/10.1016/j.combustflame.2009.07.010>
- Bampzelis, D., Spiridonov, V., Kartsios, S., Pytharoulis, I., Tegoulis, I., Karacostas, T., 2015. Numerical

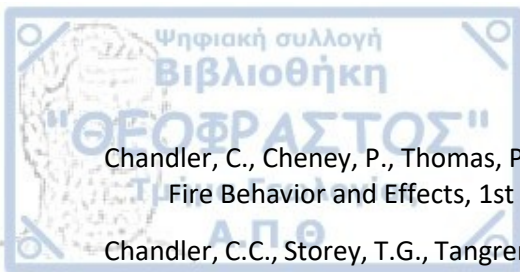


Simulation of Airborne Cloud Seeding for the DAPHNE Precipitation Enhancement Project in Central Greece, in: *95th AMS Annual Meeting, 20th Conference on Planned and Inadvertent Weather*. Phoenix, Arizona, USA.

- Banta, R.M., Olivier, L.D., Holloway, E.T., Kropfli, R.A., Bartram, B.W., Cupp, R.E., Post, M.J., 1992. Smoke-Column Observations from Two Forest Fires Using Doppler Lidar and Doppler Radar. *J. Appl. Meteorol.* 31, 1328–1349. [https://doi.org/10.1175/1520-0450\(1992\)031<1328:SCOTF>2.0.CO;2](https://doi.org/10.1175/1520-0450(1992)031<1328:SCOTF>2.0.CO;2)
- Barbero, R., Curt, T., Ganteaume, A., Maillé, E., Jappiot, M., Bellet, A., 2019. Simulating the effects of weather and climate on large wildfires in France. *Nat. Hazards Earth Syst. Sci.* 19, 441–454. <https://doi.org/10.5194/nhess-19-441-2019>
- Barry, R.G., 1992. *Mountain Weather and Climate*, 2nd ed. Routledge, New York.
- Batchelor, G.K., 1954. Heat convection and buoyancy effects in fluids. *Q. J. R. Meteorol. Soc.* 80, 339–358. <https://doi.org/10.1002/qj.49708034504>
- Bates, C.G., 1923. Evaporation as a simple index to weather conditions. *Mon. Weather Rev.* 51, 570–571. [https://doi.org/10.1175/1520-0493\(1923\)51<570:EAASIT>2.0.CO;2](https://doi.org/10.1175/1520-0493(1923)51<570:EAASIT>2.0.CO;2)
- Baughman, R.G., Albini, F.A., 1980. Estimating Midflame Windspeeds, in: *Sixth Conference on Fire and Forest Meteorology*. Seattle, WA, pp. 88–92.
- Bechtold, P., Köhler, M., Jung, T., Doblas-Reyes, F., Leutbecher, M., Rodwell, M.J., Vitart, F., Balsamo, G., 2008. Advances in simulating atmospheric variability with the ECMWF model: From synoptic to decadal time-scales. *Q. J. R. Meteorol. Soc.* 134, 1337–1351. <https://doi.org/10.1002/qj.289>
- Bedia, J., Golding, N., Casanueva, A., Iturbide, M., Buontempo, C., Gutiérrez, J.M., 2018. Seasonal predictions of Fire Weather Index: Paving the way for their operational applicability in Mediterranean Europe. *Clim. Serv.* 9, 101–110. <https://doi.org/10.1016/j.cliser.2017.04.001>
- Bedia, J., Herrera, S., Gutiérrez, J.M., Benali, A., Brands, S., Mota, B., Moreno, J.M., 2015. Global patterns in the sensitivity of burned area to fire-weather: Implications for climate change. *Agric. For. Meteorol.* 214–215, 369–379. <https://doi.org/10.1016/j.agrformet.2015.09.002>
- Beer, T., 1990. Percolation Theory and Fire Spread. *Combust. Sci. Technol.* 72, 297–304. <https://doi.org/10.1080/00102209008951653>
- Beer, T., 1974. *Atmospheric Waves*. Wiley, New York.
- Benali, A., Ervilha, A.R., Sá, A.C.L., Fernandes, P.M., Pinto, R.M.S., Trigo, R.M., Pereira, J.M.C., 2016. Deciphering the impact of uncertainty on the accuracy of large wildfire spread simulations. *Sci. Total Environ.* 569–570, 73–85. <https://doi.org/10.1016/j.scitotenv.2016.06.112>
- Benech, B., 1976. Experimental Study of an Artificial Convective Plume Initiated from the Ground. *J. Appl. Meteorol.* 15, 127–137. [https://doi.org/10.1175/1520-0450\(1976\)015<0127:ESOAAC>2.0.CO;2](https://doi.org/10.1175/1520-0450(1976)015<0127:ESOAAC>2.0.CO;2)
- Benedetti, A., Morcrette, J.-J., Boucher, O., Dethof, A., Engelen, R.J., Fisher, M., Flentje, H., Huneeus, N., Jones, L., Kaiser, J.W., Kinne, S., Mangold, A., Razingger, M., Simmons, A.J., Suttie, M., 2009. Aerosol analysis and forecast in the European Centre for Medium-Range Weather Forecasts Integrated Forecast System: 2. Data assimilation. *J. Geophys. Res.* 114, D13205. <https://doi.org/10.1029/2008JD011115>
- Bluestein, H.B., 1992. *Synoptic-dynamic Meteorology in Midlatitudes: Principles of kinematics and dynamics*. Oxford University Press, New York.



- Bovio, G., Quaglino, A., Nosenzo, A., 1984. Individuazione di un indice di previsione per il Pericolo di Incendi Boschivi. *Monti e Boschi Anno 35*, 39–44.
- Bowman, D.M.J.S., Balch, J.K., Artaxo, P., Bond, W.J., Carlson, J.M., Cochrane, M.A., D'Antonio, C.M., DeFries, R.S., Doyle, J.C., Harrison, S.P., Johnston, F.H., Keeley, J.E., Krawchuk, M.A., Kull, C.A., Marston, J.B., Moritz, M.A., Prentice, I.C., Roos, C.I., Scott, A.C., Swetnam, T.W., van der Werf, G.R., Pyne, S.J., 2009. Fire in the Earth System. *Science (80-)*. 324, 481–484. <https://doi.org/10.1126/science.1163886>
- Bromwich, D.H., Hines, K.M., Bai, L., 2009. Development and testing of Polar Weather Research and Forecasting model: 2. *Arctic Ocean. J. Geophys. Res.* 114, D08122. <https://doi.org/10.1029/2008JD010300>
- Bromwich, D.H., Otieno, F.O., Hines, K.M., Manning, K.W., Shilo, E., 2013. Comprehensive evaluation of polar weather research and forecasting model performance in the Antarctic. *J. Geophys. Res. Atmos.* 118, 274–292. <https://doi.org/10.1029/2012JD018139>
- Brown, J.K., 1974. Handbook for Inventorying Downed Woody Material. Gen. Tech. Rep. INT-16.
- Brown, J.K., 1970. Ratios of Surface Area to Volume for Common Fine Fuels. *For. Sci.* 16, 101–105. <https://doi.org/10.1093/FORRESTSCIENCE/16.1.101>
- Buizza, R., Milleer, M., Palmer, T.N., 2007. Stochastic representation of model uncertainties in the ECMWF ensemble prediction system. *Q. J. R. Meteorol. Soc.* 125, 2887–2908. <https://doi.org/10.1002/qj.49712556006>
- Burgan, R.E., 1988. 1988 Revisions to the 1978 National Fire-Danger Rating System. <https://doi.org/10.2737/SE-RP-273>
- Burgan, R.E., Hartford, R.A., 1993. Monitoring vegetation greenness with satellite data. Ogden, UT.
- Burgan, R.E., Klaver, R.W., Klarer, J.M., 1998. Fuel models and fire potential from satellite and surface observations. *Int. J. Wildl. Fire* 8, 159–170. <https://doi.org/10.1071/WF9980159>
- Bush, A.F., Leonard, J.J., Yundt, W.H., 1969. Gas analysis in large fire experiments. In “Project Flambeau: an Investigation of Mass Fire (1964-1967): Final Report - Volume III”. Berkeley, CA.
- Butler, B.W., Bartlette, R.A., Bradshaw, L.S., Cohen, J.D., Andrews, P.L., Putnam, T., Mangan, R.J., 1998. Fire behavior associated with the 1994 South Canyon fire on Storm King Mountain, Colorado. Ogden, UT. <https://doi.org/10.2737/RMRS-RP-9>
- Byram, G.M., 1959. Combustion of forest fuels, in: Davis, K.P., McGraw-Hill (Eds.), *Forest Fires: Control and Use*. New York, pp. 61–89.
- Byram, G.M., 1954. Atmospheric conditions related to blowup fires.
- Byram, G.M., Nelson, R.M., 1951. The possible relation of air turbulence to erratic fire behavior in the Southeast. *Fire Contol Notes* 12, 1–8.
- Caldarelli, G., Frondoni, R., Gabrielli, A., Montuori, M., Retzlaff, R., Ricotta, C., 2001. Percolation in real wildfires. *Europhys. Lett.* 56, 510–516. <https://doi.org/10.1209/epl/i2001-00549-4>
- Carrega, P., 1991. A Meteorological Index of Forest Fire Hazard in Mediterranean France. *Int. J. Wildl. Fire* 1, 79–86.
- Catchpole, E.A., Hatton, T.J., Catchpole, W.R., 1989. Fire spread through nonhomogeneous fuel modelled as a Markov process. *Ecol. Modell.* 48, 101–112. [https://doi.org/10.1016/0304-3800\(89\)90062-8](https://doi.org/10.1016/0304-3800(89)90062-8)



Chandler, C., Cheney, P., Thomas, P., Trabaud, L., Williams, D., 1983. Fire in Forestry, Volume 1: Forest Fire Behavior and Effects, 1st ed. John Wiley & Sons, Inc., New York, NY.

Chandler, C.C., Storey, T.G., Tangren, C.D., 1963. Prediction of fire spread following nuclear explosions. Berkeley, CA.

Chen, F., Dudhia, J., 2002. Coupling an Advanced Land Surface–Hydrology Model with the Penn State–NCAR MM5 Modeling System. Part II: Preliminary Model Validation. *Mon. Weather Rev.* 129, 587–604. [https://doi.org/10.1175/1520-0493\(2001\)129<0587:caalsh>2.0.co;2](https://doi.org/10.1175/1520-0493(2001)129<0587:caalsh>2.0.co;2)

Cheney, N., Gould, J., Catchpole, W., 1998. Prediction of Fire Spread in Grasslands. *Int. J. Wildl. Fire* 8, 1. <https://doi.org/10.1071/WF9980001>

Church, C.R., Snow, J.T., Dessens, J., 1980. Intense Atmospheric Vortices Associated with a 1000 MW Fire. *Bull. Am. Meteorol. Soc.* 61, 682–694. [https://doi.org/10.1175/1520-0477\(1980\)061<0682:iavawa>2.0.co;2](https://doi.org/10.1175/1520-0477(1980)061<0682:iavawa>2.0.co;2)

Clark, T., Jenkins, M., Coen, J., Packham, D., 1996a. A Coupled Atmosphere-Fire Model: Role of the Convective Froude Number and Dynamic Fingering at the Fireline. *Int. J. Wildl. Fire* 6, 177. <https://doi.org/10.1071/WF9960177>

Clark, T., Jenkins, M., Coen, J., Packham, D., 1996b. A Coupled Atmosphere-Fire Model: Convective Feedback on Fire-Line Dynamics. *J. Appl. Meteorol.* 35, 875–901. [https://doi.org/10.1175/1520-0450\(1996\)035<0875:ACAMCF>2.0.CO;2](https://doi.org/10.1175/1520-0450(1996)035<0875:ACAMCF>2.0.CO;2)

Clark, T.L., Coen, J., Latham, D., 2004. Description of a coupled atmosphere - fire model. *Int. J. Wildl. Fire* 13, 49. <https://doi.org/10.1071/WF03043>

Clark, T.L., Farley, R.D., 1984. Severe Downslope Windstorm Calculations in Two and Three Spatial Dimensions Using Anelastic Interactive Grid Nesting: A Possible Mechanism for Gustiness. *J. Atmos. Sci.* 41, 329–350. [https://doi.org/10.1175/1520-0469\(1984\)041<0329:SDWCIT>2.0.CO;2](https://doi.org/10.1175/1520-0469(1984)041<0329:SDWCIT>2.0.CO;2)

Clark, T.L., Peltier, W.R., 1984. Critical Level Reflection and the Resonant Growth of Nonlinear Mountain Waves. *J. Atmos. Sci.* 41, 3122–3134. [https://doi.org/10.1175/1520-0469\(1984\)041<3122:CLRATR>2.0.CO;2](https://doi.org/10.1175/1520-0469(1984)041<3122:CLRATR>2.0.CO;2)

Clark, T.L., Peltier, W.R., 1977. On the Evolution and Stability of Finite-Amplitude Mountain Waves. *J. Atmos. Sci.* 34, 1715–1730. [https://doi.org/10.1175/1520-0469\(1977\)034<1715:OTEASO>2.0.CO;2](https://doi.org/10.1175/1520-0469(1977)034<1715:OTEASO>2.0.CO;2)

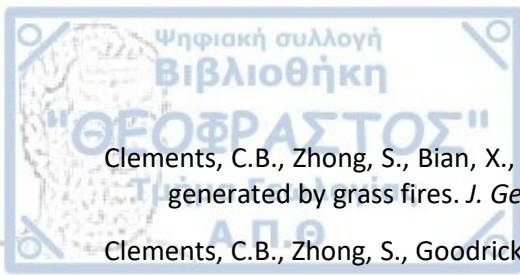
Clarke, K.C., Brass, J.A., Riggan, P.J., 1994. A cellular automaton model of wildfire propagation and extinction. *Photogramm. Eng. Remote Sensing* 60, 1355–1367.

Clements, C.B., 2010. Thermodynamic structure of a grass fire plume. *Int. J. Wildl. Fire* 19, 895. <https://doi.org/10.1071/WF09009>

Clements, C.B., Kochanski, A.K., Seto, D., Davis, B., Camacho, C., Lareau, N.P., Contezac, J., Restaino, J., Heilman, W.E., Krueger, S.K., Butler, B., Ottmar, R.D., Vihnanek, R., Flynn, J., Filippi, J.-B., Barboni, T., Hall, D.E., Mandel, J., Jenkins, M.A., O'Brien, J., Hornsby, B., Teske, C., 2019. The FireFlux II experiment: a model-guided field experiment to improve understanding of fire–atmosphere interactions and fire spread. *Int. J. Wildl. Fire* 28, 308–326. <https://doi.org/10.1071/WF18089>

Clements, C.B., Lareau, N.P., Kingsmill, D.E., Bowers, C.L., Camacho, C.P., Bagley, R., Davis, B., 2018. The Rapid Deployments to Wildfires Experiment (RaDFIRE): Observations from the Fire Zone. *Bull. Am. Meteorol. Soc.* 99, 2539–2559. <https://doi.org/10.1175/BAMS-D-17-0230.1>

Clements, C.B., Potter, B.E., Zhong, S., 2006. In situ measurements of water vapor, heat, and CO₂ fluxes within a prescribed grass fire. *Int. J. Wildl. Fire* 15, 299. <https://doi.org/10.1071/WF05101>



- Clements, C.B., Zhong, S., Bian, X., Heilman, W.E., Byun, D.W., 2008. First observations of turbulence generated by grass fires. *J. Geophys. Res.* 113, D22102. <https://doi.org/10.1029/2008JD010014>
- Clements, C.B., Zhong, S., Goodrick, S., Li, J., Potter, B.E., Bian, X., Heilman, W.E., Charney, J.J., Perna, R., Jang, M., Lee, D., Patel, M., Street, S., Aumann, G., 2007. Observing the dynamics of wildland grass fires: FireFlux - A field validation experiment. *Bull. Am. Meteorol. Soc.* 88, 1369–1382. <https://doi.org/10.1175/BAMS-88-9-1369>
- Clyne, D.J., Mininni, P., Norton, A., Rast, M., 2007. Interactive desktop analysis of high resolution simulations: Application to turbulent plume dynamics and current sheet formation. *New J. Phys.* 9. <https://doi.org/10.1088/1367-2630/9/8/301>
- Coen, J., 2018. Some Requirements for Simulating Wildland Fire Behavior Using Insight from Coupled Weather—Wildland Fire Models. *Fire* 1, 6. <https://doi.org/10.3390/fire1010006>
- Coen, J., Mahalingam, S., Daily, J., Coen, J., Mahalingam, S., Daily, J., 2004. Infrared Imagery of Crown-Fire Dynamics during FROSTFIRE. *J. Appl. Meteorol.* 43, 1241–1259. [https://doi.org/10.1175/1520-0450\(2004\)043<1241:IIOCDD>2.0.CO;2](https://doi.org/10.1175/1520-0450(2004)043<1241:IIOCDD>2.0.CO;2)
- Coen, J., Schroeder, W., Quayle, B., Coen, J.L., Schroeder, W., Quayle, B., 2018. The Generation and Forecast of Extreme Winds during the Origin and Progression of the 2017 Tubbs Fire. *Atmosphere (Basel)*. 9, 462. <https://doi.org/10.3390/atmos9120462>
- Coen, J.L., 2013. Modeling Wildland Fires : of the Coupled Atmosphere- Wildland Fire Environment Model (CAWFE). NCAR Tech. Note NCAR/TN-500+STR 38. <https://doi.org/10.5065/D6K64G2G>
- Coen, J.L., Cameron, M., Michalakes, J., Patton, E.G., Riggan, P.J., Yedinak, K.M., 2013. Wrf-fire: Coupled weather-wildland fire modeling with the weather research and forecasting model. *J. Appl. Meteorol. Climatol.* <https://doi.org/10.1175/JAMC-D-12-023.1>
- Colle, B.A., Westrick, K.J., Mass, C.F., Colle, B.A., Westrick, K.J., Mass, C.F., 1999. Evaluation of MM5 and Eta-10 Precipitation Forecasts over the Pacific Northwest during the Cool Season. *Weather Forecast.* 14, 137–154. [https://doi.org/10.1175/1520-0434\(1999\)014<0137:EOMAEP>2.0.CO;2](https://doi.org/10.1175/1520-0434(1999)014<0137:EOMAEP>2.0.CO;2)
- Conedera, M., Marxer, P., Ambrosetti, P., Della Bruna, G., Spinedi, F., 1998. The 1997 forest fire season in Switzerland. *Int. For. Fires News* 18, 85–88.
- Coppola, E., Sobolowski, S., Pichelli, E., Raffaele, F., Ahrens, B., Anders, I., Ban, N., Bastin, S., Belda, M., Belusic, D., Caldas-Alvarez, A., Cardoso, R.M., Davolio, S., Dobler, A., Fernandez, J., Fita, L., Fumiere, Q., Giorgi, F., Goergen, K., Güttler, I., Halenka, T., Heinzeller, D., Hodnebrog, Ø., Jacob, D., Kartsios, S., Katragkou, E., Kendon, E., Khodayar, S., Kunstmann, H., Knist, S., Lavín-Gullón, A., Lind, P., Lorenz, T., Maraun, D., Marelle, L., van Meijgaard, E., Milovac, J., Myhre, G., Panitz, H.-J., Piazza, M., Raffa, M., Raub, T., Rockel, B., Schär, C., Sieck, K., Soares, P.M.M., Somot, S., Srnec, L., Stocchi, P., Tölle, M.H., Truhetz, H., Vautard, R., de Vries, H., Warrach-Sagi, K., 2018. A first-of-its-kind multi-model convection permitting ensemble for investigating convective phenomena over Europe and the Mediterranean. *Clim. Dyn.* 27. <https://doi.org/10.1007/s00382-018-4521-8>
- Countryman, C.M., 1969. Project Flambeau: an investigation of mass fire (1964-1967): final report - Volume I. Berkeley, CA.
- Countryman, C.M., 1964. Mass fires and fire behavior.
- Cressman, G.P., 1959. An Operational Objective Analysis System. *Mon. Weather Rev.* 87, 367–374. [https://doi.org/10.1175/1520-0493\(1959\)087<0367:AOOAS>2.0.CO;2](https://doi.org/10.1175/1520-0493(1959)087<0367:AOOAS>2.0.CO;2)
- Cunningham, P., Goodrick, S.L., Hussaini, M.Y., Linn, R.R., 2005. Coherent vortical structures in numerical simulations of buoyant plumes from wildland fires. *Int. J. Wildl. Fire* 14, 61.



<https://doi.org/10.1071/WF04044>

Cunningham, P., Linn, R.R., 2007. Numerical simulations of grass fires using a coupled atmosphere-fire model: Dynamics of fire spread. *J. Geophys. Res.* 112, D05108. <https://doi.org/10.1029/2006JD007638>

Curry, J.R., Fons, W.L., 1940. Forest-fire behavior studies. *Mech. Eng.* 62, 219–225.

Curry, J.R., Fons, W.L., 1938. Rate of spread of surface fires in the Ponderosa pine type of California. *J. Agric. Res.* 57, 239–267.

Dahl, N., Xue, H., Hu, X., Xue, M., 2015. Coupled fire–atmosphere modeling of wildland fire spread using DEVS-FIRE and ARPS. *Nat. Hazards* 77. <https://doi.org/10.1007/s11069-015-1640-y>

Davin, E.L., Rechid, D., Breil, M., Cardoso, R.M., Coppola, E., Hoffmann, P., Jach, L.L., Katragkou, E., de Noblet-Ducoudré, N., Radtke, K., Raffa, M., Soares, P.M.M., Sofiadis, G., Strada, S., Strandberg, G., Tölle, M.H., Warrach-Sagi, K., Wulfmeyer, V., 2019. Biogeophysical impacts of forestation in Europe: First results from the LUCAS Regional Climate Model intercomparison. *Earth Syst. Dyn. Discuss.* 1–31. <https://doi.org/10.5194/esd-2019-4>

Deeming, J.E., Burgan, R.E., Cohen, J.D., 1977. The National Fire-danger Rating System-1978.

Dimitrakopoulos, A.P., 2009. Forest Fires. University Publications, AUTH, Thessaloniki, Greece (In Greek).

Dimitrakopoulos, A.P., 2002. Mediterranean fuel models and potential fire behaviour in Greece. *Int. J. Wildl. Fire* 11, 127. <https://doi.org/10.1071/WF02018>

Dimitrakopoulos, A.P., Bemmerzouk, A.M., 2003. Predicting live herbaceous moisture content from a seasonal drought index. *Int. J. Biometeorol.* 47, 73–79. <https://doi.org/10.1007/s00484-002-0151-1>

Dimitrakopoulos, A.P., Bemmerzouk, A.M., Mitsopoulos, I.D., 2011a. Evaluation of the Canadian fire weather index system in an eastern Mediterranean environment. *Meteorol. Appl.* 18, 83–93. <https://doi.org/10.1002/met.214>

Dimitrakopoulos, A.P., Gogi, C., Stamatelos, G., Mitsopoulos, I., 2011b. Statistical Analysis of the Fire Environment of Large Forest Fires (>1000 ha) in Greece. *Polish J. Environ. Stud.* 20, 327–332.

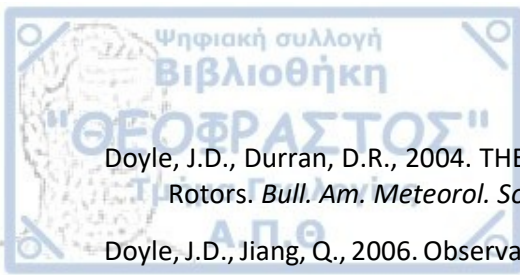
Dimitrakopoulos, A.P., Panov, P.I., 2001. Pyric properties of some dominant Mediterranean vegetation species. *Int. J. Wildl. Fire* 10, 23. <https://doi.org/10.1071/WF01003>

Dimitrakopoulos, A.P., Vlahou, M., Anagnostopoulou, C.G., Mitsopoulos, I.D., 2011c. Impact of drought on wildland fires in Greece: Implications of climatic change? *Clim. Change* 109, 331–347. <https://doi.org/10.1007/s10584-011-0026-8>

Dobrinkova, N., Jordanov, G., Mandel, J., 2011. WRF-fire applied in Bulgaria, in: *Lecture Notes in Computer Science* (Including Subseries Lecture Notes in Artificial Intelligence and Lecture Notes in Bioinformatics). https://doi.org/10.1007/978-3-642-18466-6_15

Dolling, K., Chu, P.S., Fujioka, F., 2005. A climatological study of the Keetch/Byram drought index and fire activity in the Hawaiian Islands, in: *Agricultural and Forest Meteorology*. pp. 17–27. <https://doi.org/10.1016/j.agrformet.2005.07.016>

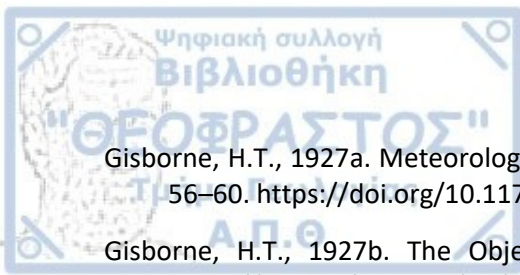
Dowdy, A.J., Mills, G. a, Finkele, K., Groot, W. De, 2009. Australian fire weather as represented by the McArthur Forest Fire Danger Index and the Canadian Forest Fire Weather Index Australian fire weather as represented by the McArthur Forest Fire Danger Index and the Canadian Forest Fire Weather Index, CAWCR technical report. Victoria.



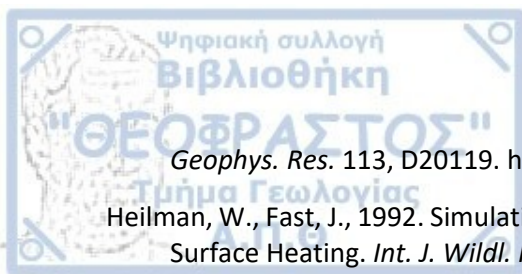
- Doyle, J.D., Durran, D.R., 2004. THE MAP ROOM: Recent Developments in the Theory of Atmospheric Rotors. *Bull. Am. Meteorol. Soc.* 85, 337–342. <https://doi.org/10.1175/BAMS-85-3-337>
- Doyle, J.D., Jiang, Q., 2006. Observations and numerical simulations of mountain waves in the presence of directional wind shear. *Q. J. R. Meteorol. Soc.* 132, 1877–1905. <https://doi.org/10.1256/qj.05.140>
- Drakou, E.G., Kallimanis, A.S., Mazaris, A.D., Apostolopoulou, E., Pantis, J.D., 2011. Habitat type richness associations with environmental variables: a case study in the Greek Natura 2000 aquatic ecosystems. *Biodivers. Conserv.* 20, 929–943. <https://doi.org/10.1007/s10531-011-0005-4>
- Drouet, J.C., Sol, B., 1990. Mise au point d'un Indice numérique de risque météorologique d'incendie. *Rev. Générale Secur.* 92.
- Drusch, M., Scipal, K., de Rosnay, P., Balsamo, G., Andersson, E., Bougeault, P., Viterbo, P., 2009. Towards a Kalman Filter based soil moisture analysis system for the operational ECMWF Integrated Forecast System. *Geophys. Res. Lett.* 36, L10401. <https://doi.org/10.1029/2009GL037716>
- Duane, A., Brotons, L., 2018. Synoptic weather conditions and changing fire regimes in a Mediterranean environment. *Agric. For. Meteorol.* 253–254, 190–202. <https://doi.org/10.1016/j.agrformet.2018.02.014>
- Duane, A., Piqué, M., Castellnou, M., Brotons, L., 2015. Predictive modelling of fire occurrences from different fire spread patterns in Mediterranean landscapes. *Int. J. Wildl. Fire* 24, 407. <https://doi.org/10.1071/WF14040>
- Duarte, J.A.M.S., 1997. Bushfire Automata and Their Phase Transitions. *Int. J. Mod. Phys. C* 08, 171–189. <https://doi.org/10.1142/S0129183197000175>
- Dudhia, J., 1996. A multi-layer soil temperature model for MM5, in: 6th PSU/NCAR Mesoscale Model Users' Workshop. NCAR, Boulder, CO, USA.
- Duguay, B., Alloza, J.A., Röder, A., Vallejo, R., Pastor, F., 2007. Modelling the effects of landscape fuel treatments on fire growth and behaviour in a Mediterranean landscape (eastern Spain). *Int. J. Wildl. Fire* 16, 619. <https://doi.org/10.1071/WF06101>
- Dunn, A., Milne, G., 2004. Modelling wildfire dynamics via interacting automata, in: Sloot, P.M.A., Chopard, B., Hoekstra, A.G. (Eds.), *Cellular Automata, 6th International Conference on Cellular Automata for Research and Industry*. Springer-Verlag, Berlin, Germany, Amsterdam, The Netherlands, October 25-28, pp. 395–404.
- Durran, D.R., 1990. Mountain Waves and Downslope Winds, in: *Atmospheric Processes over Complex Terrain*. American Meteorological Society, Boston, MA, pp. 59–81. https://doi.org/10.1007/978-1-935704-25-6_4
- Durran, D.R., 1986. Another Look at Downslope Windstorms. Part I: The Development of Analogs to Supercritical Flow in an Infinitely Deep, Continuously Stratified Fluid. *J. Atmos. Sci.* 43, 2527–2543. [https://doi.org/10.1175/1520-0469\(1986\)043<2527:ALADWP>2.0.CO;2](https://doi.org/10.1175/1520-0469(1986)043<2527:ALADWP>2.0.CO;2)
- Durran, D.R., Klemp, J.B., 1987. Another Look at Downslope Winds. Part II: Nonlinear Amplification beneath Wave-Overtaking Layers. *J. Atmos. Sci.* 44, 3402–3412. [https://doi.org/10.1175/1520-0469\(1987\)044<3402:ALADWP>2.0.CO;2](https://doi.org/10.1175/1520-0469(1987)044<3402:ALADWP>2.0.CO;2)
- Eastaugh, C.S., Hasenauer, H., 2014. Deriving forest fire ignition risk with biogeochemical process modelling. *Environ. Model. Softw.* 55, 132–142. <https://doi.org/10.1016/j.envsoft.2014.01.018>
- Edgar, R.A., Sharples, J.J., Sidhu, H.S., 2015. Revisiting the King's Cross underground disaster with

- implications for modelling wildfire eruption, in: Weber, T., McPhee, M.J., Anderssen, R.S. (Eds.), MODSIM2015, 21st International Congress on Modelling and Simulation. Modelling and Simulation Society of Australia and New Zealand, Broadbeach, Qld., pp. 215–221.
- Egorova, V.N., Trucchia, A., Pagnini, G., 2019. Fire-spotting generated fires. Part I: The role of atmospheric stability. *Appl. Math. Model.* <https://doi.org/10.1016/J.APM.2019.02.010>
- Elhag, M., Boteva, S., 2017. Assessment of Forest Fire Rating Systems in Typical Mediterranean Forest, Crete, Greece. *Nat. Hazards Earth Syst. Sci. Discuss.* 1–27. <https://doi.org/10.5194/nhess-2017-318>
- Etling, D., Brown, R.A., 1993. Roll vortices in the planetary boundary layer: A review. *Boundary-Layer Meteorol.* 65, 215–248. <https://doi.org/10.1007/BF00705527>
- Falk, D.A., Miller, C., McKenzie, D., Black, A.E., 2007. Cross-Scale Analysis of Fire Regimes. *Ecosystems* 10, 809–823. <https://doi.org/10.1007/s10021-007-9070-7>
- Farguella, À., Cortés, A., Margalef, T., Miro, J.R., Mercader, J., 2017. Data resolution effects on a coupled data driven system for forest fire propagation prediction. *Procedia Comput. Sci.* 108, 1562–1571.
- Farr, T.G., Rosen, P.A., Caro, E., Crippen, R., Duren, R., Hensley, S., Kobrick, M., Paller, M., Rodriguez, E., Roth, L., Seal, D., Shaffer, S., Shimada, J., Umland, J., Werner, M., Oskin, M., Burbank, D., Alsdorf, D., 2007. The Shuttle Radar Topography Mission. *Rev. Geophys.* 45, RG2004. <https://doi.org/10.1029/2005RG000183>
- Fast, J.D., Gustafson, W.I., Easter, R.C., Zaveri, R.A., Barnard, J.C., Chapman, E.G., Grell, G.A., Peckham, S.E., 2006. Evolution of ozone, particulates, and aerosol direct radiative forcing in the vicinity of Houston using a fully coupled meteorology-chemistry-aerosol model. *J. Geophys. Res.* 111, D21305. <https://doi.org/10.1029/2005JD006721>
- Fastie, C.L., Lloyd, A.H., Doak, P., 2002. Fire history and postfire forest development in an upland watershed of interior Alaska. *J. Geophys. Res.* 108, 8150. <https://doi.org/10.1029/2001JD000570>
- Favier, C., 2004. Percolation model of fire dynamic. *Phys. Lett. A* 330, 396–401. <https://doi.org/10.1016/j.physleta.2004.07.053>
- Fernandes, P.M., 2009. Combining forest structure data and fuel modelling to classify fire hazard in Portugal. *Ann. For. Sci.* 66, 415–415. <https://doi.org/10.1051/forest/2009013>
- Fernandez-Pello, A.C., 2017. Wildland fire spot ignition by sparks and firebrands. *Fire Saf. J.* 91, 2–10. <https://doi.org/10.1016/J.FIRESAF.2017.04.040>
- Filippi, J.-B., Bosseur, F., Mari, C., Lac, C., 2018. Simulation of a Large Wildfire in a Coupled Fire-Atmosphere Model. *Atmosphere (Basel)*. 9, 218. <https://doi.org/10.3390/atmos9060218>
- Filippi, J.-B., Bosseur, F., Pialat, X., Santoni, P.-A., Strada, S., Mari, C., 2011. Simulation of Coupled Fire/Atmosphere Interaction with the MesoNH-ForeFire Models. *J. Combust.* 2011, 1–13. <https://doi.org/10.1155/2011/540390>
- Filippi, J.-B., Pialat, X., Clements, C.B., 2013. Assessment of ForeFire/Meso-NH for wildland fire/atmosphere coupled simulation of the FireFlux experiment. *Proc. Combust. Inst.* 34, 2633–2640. <https://doi.org/10.1016/J.PROCI.2012.07.022>
- Filippi, J.B., Bosseur, F., Mari, C., Lac, C., Le Moigne, P., Cuenot, B., Veynante, D., Cariolle, D., Balbi, J.-H., 2009. Coupled atmosphere–wildland fire modelling. *J. Adv. Model. Earth Syst.* 2, 11. <https://doi.org/10.3894/JAMES.2009.1.11>
- Filippopoulos, I., 2012. Managing forest fires with i-protect fire simulation module. *PhD Thesis*.

- University of Thessaly, School of Engineering (in Greek). <https://doi.org/10.12681/eadd/29344>
- Finney, M.A., 1998. FARSITE: Fire Area Simulator-model development and evaluation.
- Foley, J.C., 1947. A study of meteorological conditions associated with bush and grass fires and fire protection strategy in Australia.
- Fons, W.L., 1946. Analysis of Fire Spread in Light Forest Fuels. *J. Agric. Res.* 72, 92–121.
- Forestry Canada Fire Danger Group, 1992. Development and structure of the Canadian Forest Fire Behavior Prediction System.
- Forthofer, J.M., Goodrick, S.L., 2011. Review of Vortices in Wildland Fire. *J. Combust.* 2011, 1–14. <https://doi.org/10.1155/2011/984363>
- Fosberg, M.A., 1983. Weather in wildland fire management: the Fire Weather Index, in: *Conference on Sierra Nevada Meteorology. Lake Tahoe, CA, USA.*
- Fosberg, M.A., Deeming, J.E., 1971. Derivation of the 1- and 10-hour timelag fuel moisture calculations of fire-danger.
- Founda, D., Giannakopoulos, C., 2009. The exceptionally hot summer of 2007 in Athens, Greece — A typical summer in the future climate? *Glob. Planet. Change* 67, 227–236. <https://doi.org/10.1016/j.gloplacha.2009.03.013>
- Freeborn, P.H., Wooster, M.J., Roy, D.P., Cochrane, M.A., 2014. Quantification of MODIS fire radiative power (FRP) measurement uncertainty for use in satellite-based active fire characterization and biomass burning estimation. *Geophys. Res. Lett.* 41, 1988–1994. <https://doi.org/10.1002/2013GL059086>
- Fudeyasu, H., Kuwagata, T., Ohashi, Y., Suzuki, S., Kiyohara, Y., Hozumi, Y., 2008. Numerical Study of the Local Downslope Wind “Hirodo-Kaze” in Japan. *Mon. Weather Rev.* 136, 27–40. <https://doi.org/10.1175/2007MWR2049.1>
- Ganteaume, A., Jappiot, M., 2013. What causes large fires in Southern France. *For. Ecol. Manage.* 294, 76–85. <https://doi.org/10.1016/j.foreco.2012.06.055>
- Giannaros, T.M., Kotroni, V., Lagouvardos, K., 2019. IRIS – Rapid response fire spread forecasting system: Development, calibration and evaluation. *Agric. For. Meteorol.* 279, 107745. <https://doi.org/10.1016/J.AGRFORMET.2019.107745>
- Gibbs, J.A., Fedorovich, E., Gibbs, J.A., Fedorovich, E., 2014. Comparison of Convective Boundary Layer Velocity Spectra Retrieved from Large- Eddy-Simulation and Weather Research and Forecasting Model Data. *J. Appl. Meteorol. Climatol.* 53, 377–394. <https://doi.org/10.1175/JAMC-D-13-033.1>
- Giglio, L., Descloitres, J., Justice, C.O., Kaufman, Y.J., 2003. An Enhanced Contextual Fire Detection Algorithm for MODIS. *Remote Sens. Environ.* 87, 273–282. [https://doi.org/10.1016/S0034-4257\(03\)00184-6](https://doi.org/10.1016/S0034-4257(03)00184-6)
- Gill, A.E., 1982. Atmosphere-ocean dynamics, International Geophysics Series, Vol. 30. Academic Press, New York.
- Girardin, M.P., Wotton, B.M., 2009. Summer Moisture and Wildfire Risks across Canada. *J. Appl. Meteorol. Climatol.* 48, 517–533. <https://doi.org/10.1175/2008JAMC1996.1>
- Gisborne, H.T., 1929. The Complicated Controls of Fire Behaviour. *J. For.* 27, 311–312.
- Gisborne, H.T., 1928. Measuring forest fire danger in northern Idaho. Washington, DC.



- Gisborne, H.T., 1927a. Meteorological factors in the Quartz Creek forest fire. *Mon. Weather Rev.* 55, 56–60. [https://doi.org/10.1175/1520-0493\(1927\)55<56:MFITQC>2.0.CO;2](https://doi.org/10.1175/1520-0493(1927)55<56:MFITQC>2.0.CO;2)
- Gisborne, H.T., 1927b. The Objectives of Forest Fire-Weather Research. *J. For.* 25, 452–456. <https://doi.org/10.1093/jof/25.4.452>
- Gitelson, A.A., Stark, R., Grits, U., Rundquist, D., Kaufman, Y., Derry, D., 2002. Vegetation and soil lines in visible spectral space: A concept and technique for remote estimation of vegetation fraction. *Int. J. Remote Sens.* 23, 2537–2562. <https://doi.org/10.1080/01431160110107806>
- Gochis, D.J., Yu, W., Yates, D.N., 2015. The WRF- Hydro Model technical description and user's guide, version 3.0. NCAR Tech. Doc 123.
- Good, P., Moriondo, M., Giannakopoulos, C., Bindi, M., 2008. The meteorological conditions associated with extreme fire risk in Italy and Greece: relevance to climate model studies. *Int. J. Wildl. Fire* 17, 155. <https://doi.org/10.1071/WF07001>
- Goodrick, S.L., 2002. Modification of the Fosberg fire weather index to include drought. *Int. J. Wildl. Fire* 11, 205. <https://doi.org/10.1071/WF02005>
- Grell, G.A., Peckham, S.E., Schmitz, R., McKeen, S.A., Frost, G., Skamarock, W.C., Eder, B., 2005. Fully coupled “online” chemistry within the WRF model. *Atmos. Environ.* 39, 6957–6975. <https://doi.org/10.1016/j.atmosenv.2005.04.027>
- Griffiths, D., 1999. Improved Formula for the Drought Factor in McArthur's Forest Fire Danger Meter. *Aust. For.* 62, 202–206. <https://doi.org/10.1080/00049158.1999.10674783>
- Groisman, P.Y., Sherstyukov, B.G., Razuvaev, V.N., Knight, R.W., Enloe, J.G., Stroumentova, N.S., Whitfield, P.H., Førland, E., Hannsen-Bauer, I., Tuomenvirta, H., Aleksandersson, H., Mescherskaya, A. V., Karl, T.R., 2007. Potential forest fire danger over Northern Eurasia: Changes during the 20th century. *Glob. Planet. Change* 56, 371–386. <https://doi.org/10.1016/j.gloplacha.2006.07.029>
- Haines, D.A., 1988. A lower atmosphere severity index for wildlife fires. *Natl. Weather Dig.* 13, 23–27.
- Haines, D.A., Lyon, L.J., 1990. Horizontal roll vortices in complex terrain. *Fire Manag. notes U.S. Dep. Agric. For. Serv.*
- Haines, D.A., Main, W.A., Frost, J.S., Simard, A.J., 1983. Fire-danger rating and wildfire occurrence in the northeastern United States. *For. Sci.* 29, 679–696. <https://doi.org/10.1093/forestscience/29.4.679>
- Haines, D.A., Smith, M.C., 1987. Three Types of Horizontal Vortices Observed in Wildland Mass and Crown Fires. *J. Clim. Appl. Meteorol.* 26, 1624–1637. [https://doi.org/10.1175/1520-0450\(1987\)026<1624:TTOHVO>2.0.CO;2](https://doi.org/10.1175/1520-0450(1987)026<1624:TTOHVO>2.0.CO;2)
- Hardy, C.C., 2005. Wildland fire hazard and risk: Problems, definitions, and context, in: *Forest Ecology and Management*. pp. 73–82. <https://doi.org/10.1016/j.foreco.2005.01.029>
- Hargrove, W., Gardner, R., Turner, M., Romme, W., Despain, D., 2000. Simulating fire patterns in heterogeneous landscapes. *Ecol. Modell.* 135, 243–263. [https://doi.org/10.1016/S0304-3800\(00\)00368-9](https://doi.org/10.1016/S0304-3800(00)00368-9)
- Hawley, L., 1926. Theoretical Considerations Regarding Factors which Influence Forest Fires. *J. For.* 24, 756–763. <https://doi.org/10.1093/jof/24.7.756>
- Haylock, M.R., Hofstra, N., Klein Tank, A.M.G., Klok, E.J., Jones, P.D., New, M., 2008. A European daily high-resolution gridded data set of surface temperature and precipitation for 1950–2006. *J.*



- Geophys. Res.* 113, D20119. <https://doi.org/10.1029/2008JD010201>
- Heilman, W., Fast, J., 1992. Simulations of Horizontal Roll Vortex Development Above Lines of Extreme Surface Heating. *Int. J. Wildl. Fire* 2, 55. <https://doi.org/10.1071/WF9920055>
- Helmis, C.G., Flocas, H.A., Kalogiros, J.A., Asimakopoulos, D.N., 2000. Strong downslope winds and application of hydraulic-like theory. *J. Geophys. Res. Atmos.* 105, 18039–18051. <https://doi.org/10.1029/2000JD900246>
- Hines, K.M., Bromwich, D.H., 2008. Development and Testing of Polar Weather Research and Forecasting (WRF) Model. Part I: Greenland Ice Sheet Meteorology. *Mon. Weather Rev.* 136, 1971–1989. <https://doi.org/10.1175/2007MWR2112.1>
- Hinzman, L.D., 2003. FROSTFIRE: An experimental approach to predicting the climate feedbacks from the changing boreal fire regime. *J. Geophys. Res.* 108, 8153. <https://doi.org/10.1029/2001JD000415>
- Holton, J.R., 2004. An introduction to dynamic meteorology. Elsevier Academic Press.
- Holton, J.R., Hakim, G.J., 2012. Geostrophic Approximation and Geostrophic Wind, in: *An Introduction to Dynamic Meteorology*. Academic Press, pp. 42–43.
- Houze, Robert A., J., 1993. Cloud Dynamics. Academic Press, San Diego.
- Hu, X., Sun, Y., Ntairo, L., 2012. DEVS-FIRE: design and application of formal discrete event wildfire spread and suppression models. *Simulation* 88, 259–279. <https://doi.org/10.1177/0037549711414592>
- Hunt, G.R., van den Bremer, T.S., 2011. Classical plume theory: 1937-2010 and beyond. *IMA J. Appl. Math.* 76, 424–448. <https://doi.org/10.1093/imamat/hxq056>
- Iacono, M.J., Delamere, J.S., Mlawer, E.J., Shephard, M.W., Clough, S.A., Collins, W.D., 2008. Radiative forcing by long-lived greenhouse gases: Calculations with the AER radiative transfer models. *J. Geophys. Res.* 113, D13103. <https://doi.org/10.1029/2008JD009944>
- ICONA, 1988. Experimentation de un nuevo sistema para determinacion del peligro de incendios forestales derivado de los combustibles: instrucciones de calculo. Madrid, Spain.
- Iliopoulos, N., 2013. Fire-weather, wildfires and climate change. *PhD Thesis. University of Aegean* (in Greek).
- INMG, 1988. Nota explicativa sobre o Índice de Risco Meteorológico de Incêndios Rurais. Lisbon, Portugal.
- Isaaks, E.H., Srivastava, R.M., 1989. An Introduction to Applied Geostatistics.
- Janis, M.J., Johnson, M.B., Forthun, G., 2002. Near-real time mapping of Keetch-Byram drought index in the south-eastern United States. *Int. J. Wildl. Fire* 11, 281. <https://doi.org/10.1071/wf02013>
- Janjić, Z.I., 2002. Nonsingular implementation of the Mellor-Yamada Level 2.5 Scheme in the NCEP Meso model.
- Janjić, Z.I., 1996. The surface layer in the NCEP Eta Model, in: *11th Conference on Numerical Weather Prediction. Amer Meteor Soc, Boston, MA, Norfolk, VA*, pp. 354–355.
- Janjić, Z.I., 1994. The Step-Mountain Eta Coordinate Model: Further Developments of the Convection, Viscous Sublayer, and Turbulence Closure Schemes. *Mon. Weather Rev.* 122, 927–945. [https://doi.org/10.1175/1520-0493\(1994\)122<0927:TSMECM>2.0.CO;2](https://doi.org/10.1175/1520-0493(1994)122<0927:TSMECM>2.0.CO;2)



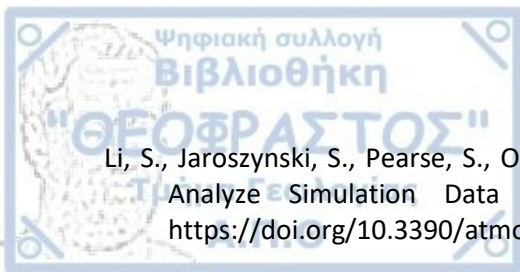
- Jenkins, M.A., 2004. Investigating the Haines Index using parcel model theory. *Int. J. Wildl. Fire* 13, 297. <https://doi.org/10.1071/WF03055>
- Jenkins, M.A., Kochanski, A.K., Krueger, S.K., 2011. The fluid dynamics of steady-state fireline propagation, in: *Ninth Symposium on Fire and Forest Meteorology. Palm Springs, CA, October 18-20*.
- Jiménez, P.A., Dudhia, J., González-Rouco, J.F., Navarro, J., Montávez, J.P., García-Bustamante, E., 2012. A Revised Scheme for the WRF Surface Layer Formulation. *Mon. Weather Rev.* 140, 898–918. <https://doi.org/10.1175/MWR-D-11-00056.1>
- Jimenez, P.A., Hacker, J.P., Dudhia, J., Haupt, S.E., Ruiz-Arias, J.A., Gueymard, C.A., Thompson, G., Eidhammer, T., Deng, A., 2016. WRF-Solar: Description and Clear-Sky Assessment of an Augmented NWP Model for Solar Power Prediction. *Bull. Am. Meteorol. Soc.* 97, 1249–1264. <https://doi.org/10.1175/BAMS-D-14-00279.1>
- Jordanov, G., Beezley, J.D., Dobrinkova, N., Kochanski, A.K., Mandel, J., Sousedík, B., 2012. Simulation of the 2009 Harmanli Fire (Bulgaria), in: *Lecture Notes in Computer Science (Including Subseries Lecture Notes in Artificial Intelligence and Lecture Notes in Bioinformatics)*. pp. 291–298. https://doi.org/10.1007/978-3-642-29843-1_33
- Josipa, M., Joachim, I., Kirsten, W.-S., 2014. Soil texture forcing data for the whole world for the Weather Research and Forecasting (WRF) Model of the University of Hohenheim (UHOH) based on the Harmonized World Soil Database (HWSD) at 30 arc-second horizontal resolution. World Data Center for Climate.
- Kalabokidis, K., Iliopoulos, N., Gliginos, D., 2012. Pyro-Meteorology and wildfires behavior in an environment under change. IWN, Athens (In Greek).
- Kambezidis, H.D., Kalliampakos, G.K., 2016. Fire-Risk Assessment in Northern Greece Using a Modified Fosberg Fire-Weather Index That Includes Forest Coverage. *Int. J. Atmos. Sci.* 2016, 1–8. <https://doi.org/10.1155/2016/8108691>
- Karacostas, T., 2008. Notes on dynamic meteorology. University Publications, AUTH, Thessaloniki, Greece (In Greek).
- Karacostas, T., 2003. Synoptic, dynamic and cloud microphysical characteristics related to precipitation enhancement projects, in: *Regional Seminar on Cloud Physics and Weather Modification. World Meteorological Organization, WMP No. 42, WMO-TD*, pp. 194–200.
- Karacostas, T., Flocas, A.A., Flocas, H.A., Kakaliagou, O., Rizou, C., 1992. A study of the synoptic situations over the area of Eastern Mediterranean, in: *1st Greek Conference On Meteorology-Climatology-Physics of the Atmosphere. Thessaloniki, Greece*.
- Karacostas, T., Kartsios, S., Pytharoulis, I., Tegoulis, I., Bampzelis, D., 2018. Observations and modelling of the characteristics of convective activity related to a potential rain enhancement program in central Greece. *Atmos. Res.* 208, 218–228. <https://doi.org/10.1016/j.atmosres.2017.08.014>
- Karafyllidis, I., 1999. Acceleration of cellular automata algorithms using genetic algorithms. *Adv. Eng. Softw.* 30, 419–437. [https://doi.org/10.1016/S0965-9978\(98\)00091-X](https://doi.org/10.1016/S0965-9978(98)00091-X)
- Karali, A., Hatzaki, M., Giannakopoulos, C., Roussos, A., Xanthopoulos, G., Tenentes, V., 2014. Sensitivity and evaluation of current fire risk and future projections due to climate change: the case study of Greece. *Nat. Hazards Earth Syst. Sci.* 14, 143–153. <https://doi.org/10.5194/nhess-14-143-2014>

- Kartsios, S., 2013. Online coupling between Atmosphere – Fire Models for investigation of Wildland Fires. *MSc Thesis. Faculty of Sciences, School of Geology, Aristotle University of Thessaloniki* (in Greek).
- Kartsios, S., Karacostas, T., Pytharoulis, I., Dimitrakopoulos, A.P., 2014a. Coupled Weather – Wildland Fire Model for fire behaviour interpretation, in: *12th International Conference on Meteorology, Climatology and Atmospheric Physics (COMECAP 2014). Herakleion, Greece.*
- Kartsios, S., Karacostas, T., Pytharoulis, I., Dimitrakopoulos, A.P., 2014b. Simulating Atmosphere-Fire Interactions using a Coupled Weather – Wildland Fire Model, in: *10th Congress of the Hellenic Geographical Society. Thessaloniki, Greece.*
- Kartsios, S., Karacostas, T.S., Pytharoulis, I., Dimitrakopoulos, A.P., 2017. The Role of Heat Extinction Depth Concept to Fire Behavior: An Application to WRF-SFIRE Model, in: Karacostas, T., Bais, A., Nastos, P.T. (Eds.), *Perspectives on Atmospheric Sciences*. Springer International Publishing, Cham, pp. 137–142. https://doi.org/10.1007/978-3-319-35095-0_20
- Kartsios, S., Kotsopoulos, S., Karacostas, T.S., Tegoulis, I., Pytharoulis, I., Bampzelis, D., 2015. Statistical evaluation of the simulated convective activity over Central Greece, in: *Geophysical Research Abstracts EGU General Assembly*. pp. 2015–8418.
- Katragkou, E., Garcíá-Diéz, M., Vautard, R., Sobolowski, S., Zanis, P., Alexandri, G., Cardoso, R.M., Colette, A., Fernandez, J., Gobiet, A., Goergen, K., Karacostas, T., Knist, S., Mayer, S., Soares, P.M.M., Pytharoulis, I., Tegoulis, I., Tsikerdekis, A., Jacob, D., 2015. Regional climate hindcast simulations within EURO-CORDEX: Evaluation of a WRF multi-physics ensemble. *Geosci. Model Dev.* 8, 603–618. <https://doi.org/10.5194/gmd-8-603-2015>
- Katragkou, E., Gkotovou, I., Kartsios, S., Pavlidis, V., Tsigaridis, K., Trail, M., Nazarenko, L., Karacostas, T.S., 2017. AUTH Regional Climate Model Contributions to EURO-CORDEX, in: Karacostas, T., Bais, A., Nastos, P. (Eds.), *Springer Atmospheric Sciences*. Springer, Cham, pp. 741–746. https://doi.org/10.1007/978-3-319-35095-0_106
- Kaufman, Y.J., Justice, C.O., Flynn, L.P., Kendall, J.D., Prins, E.M., Giglio, L., Ward, D.E., Menzel, W.P., Setzer, A.W., 1998. Potential global fire monitoring from EOS-MODIS. *J. Geophys. Res. Atmos.* 103, 32215–32238. [https://doi.org/10.1029/98JD01644@10.1002/\(ISSN\)2169-8996.EOSAM1](https://doi.org/10.1029/98JD01644@10.1002/(ISSN)2169-8996.EOSAM1)
- Keeley, J.E., Fotheringham, C.J., 2001. History and Management of Crown-Fire Ecosystems: a Summary and Response, *Conservation Biology* 15, 1561-1567. <https://doi.org/10.1046/j.1523-1739.2001.t01-1-00186.x>
- Keetch, J., Byram, B., 1968. A Drought Index for Forest Fire Control. <https://doi.org/10.1016/j.accpm.2015.04.007>
- Kiefer, M.T., Heilman, W.E., Zhong, S., Charney, J.J., Bian, X., 2015. Mean and Turbulent Flow Downstream of a Low-Intensity Fire: Influence of Canopy and Background Atmospheric Conditions. *J. Appl. Meteorol. Climatol.* 54, 42–57. <https://doi.org/10.1175/JAMC-D-14-0058.1>
- Kiefer, M.T., Lin, Y.-L., Charney, J.J., 2008. A Study of Two-Dimensional Dry Convective Plume Modes with Variable Critical Level Height. *J. Atmos. Sci.* 65, 448–469. <https://doi.org/10.1175/2007JAS2301.1>
- Kiefer, M.T., Parker, M.D., Charney, J.J., 2009. Regimes of Dry Convection above Wildfires: Idealized Numerical Simulations and Dimensional Analysis. *J. Atmos. Sci.* 66, 806–836. <https://doi.org/10.1175/2008JAS2896.1>
- Klein Tank, A.M.G., Wijngaard, J.B., Können, G.P., Böhm, R., Demarée, G., Gocheva, A., Mileta, M., Pashiardis, S., Hejkrlik, L., Kern-Hansen, C., Heino, R., Bessemoulin, P., Müller-Westermeier, G.,

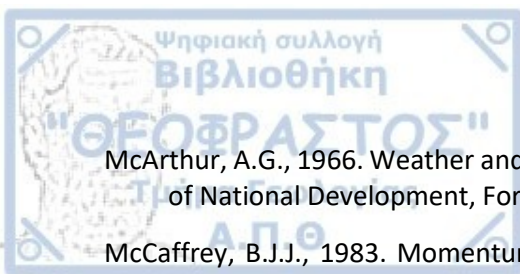
- Tzanakou, M., Szalai, S., Pálsdóttir, T., Fitzgerald, D., Rubin, S., Capaldo, M., Maugeri, M., Leitass, A., Bukantis, A., Aberfeld, R., van Engelen, A.F. V., Forland, E., Mietus, M., Coelho, F., Mares, C., Razuvaev, V., Nieplova, E., Cegnar, T., Antonio López, J., Dahlström, B., Moberg, A., Kirchhofer, W., Ceylan, A., Pachaliuk, O., Alexander, L. V., Petrovic, P., 2002. Daily dataset of 20th-century surface air temperature and precipitation series for the European Climate Assessment. *Int. J. Climatol.* 22, 1441–1453. <https://doi.org/10.1002/joc.773>
- Klemp, J.B., Dudhia, J., Hassiotis, A.D., 2008. An Upper Gravity-Wave Absorbing Layer for NWP Applications. *Mon. Weather Rev.* 136, 3987–4004. <https://doi.org/10.1175/2008MWR2596.1>
- Klemp, J.B., Durran, D.R., 1987. Numerical modelling of Bora winds. *Meteorol. Atmos. Phys.* 36, 215–227. <https://doi.org/10.1007/BF01045150>
- Klemp, J.B., Lilly, D.R., 1975. The Dynamics of Wave-Induced Downslope Winds. *J. Atmos. Sci.* 32, 320–339. [https://doi.org/10.1175/1520-0469\(1975\)032<0320:TADOWID>2.0.CO;2](https://doi.org/10.1175/1520-0469(1975)032<0320:TADOWID>2.0.CO;2)
- Knierel, J.C., Bryan, G.H., Hacker, J.P., 2007. Explicit Numerical Diffusion in the WRF Model. <https://doi.org/10.1175/2007MWR2100.1>
- Knist, S., Goergen, K., Buonomo, E., Christensen, O.B., Colette, A., Cardoso, R.M., Fealy, R., Fernández, J., García-Díez, M., Jacob, D., Kartsios, S., Katragkou, E., Keuler, K., Mayer, S., Van Meijgaard, E., Nikulin, G., Soares, P.M.M., Sobolowski, S., Szepszo, G., Teichmann, C., Vautard, R., Warrach-Sagi, K., Wulfmeyer, V., Simmer, C., 2017. Land-atmosphere coupling in EURO-CORDEX evaluation experiments. *J. Geophys. Res.* 122, 79–103. <https://doi.org/10.1002/2016JD025476>
- Knist, S., Goergen, K., Simmer, C., 2018. Effects of land surface inhomogeneity on convection-permitting WRF simulations over Central Europe. *Meteorol. Atmos. Phys.* 0, 2. <https://doi.org/10.1007/s00382-018-4147-x>
- Knorr, W., Pytharoulis, I., Petropoulos, G.P., Gobron, N., 2011. Combined use of weather forecasting and satellite remote sensing information for fire risk, fire and fire impact monitoring. *Comput. Ecol. Softw.* 1, 112–120.
- Kochanski, A.K., Jenkins, M.A., Mandel, J., Beezley, J.D., Clements, C.B., Krueger, S., 2013a. Evaluation of WRF-SFIRE performance with field observations from the FireFlux experiment. *Geosci. Model Dev.* 6, 1109–1126. <https://doi.org/10.5194/gmd-6-1109-2013>
- Kochanski, A.K., Jenkins, M.A., Mandel, J., Beezley, J.D., Krueger, S.K., 2013b. Real time simulation of 2007 Santa Ana fires. *For. Ecol. Manage.* 294, 136–149. <https://doi.org/10.1016/j.foreco.2012.12.014>
- Kochanski, A.K., Jenkins, M.A., Sun, R., Krueger, S., Abedi, S., Charney, J., 2013c. The importance of low-level environmental vertical wind shear to wildfire propagation: Proof of concept. *J. Geophys. Res. Atmos.* 118, 8238–8252. <https://doi.org/10.1002/jgrd.50436>
- Kochanski, A.K., Jenkins, M.A., Yedinak, K., Mandel, J., Beezley, J., Lamb, B., 2016. Toward an integrated system for fire, smoke and air quality simulations. *Int. J. Wildl. Fire* 25, 534. <https://doi.org/10.1071/WF14074>
- Kochanski, A.K., Mallia, D. V., Fearon, M.G., Mandel, J., Sourì, A.H., Brown, T., 2019. Modeling wildfire smoke feedback mechanisms using a coupled fire-atmosphere model with a radiatively active aerosol scheme. *J. Geophys. Res. Atmos.* 2019JD030558. <https://doi.org/10.1029/2019JD030558>
- Koletsis, I., Giannaros, T.M., Lagouvardos, K., Kotroni, V., 2016. Observational and numerical study of the Vardaris wind regime in northern Greece. *Atmos. Res.* 171, 107–120. <https://doi.org/10.1016/j.atmosres.2015.12.011>



- Koletsis, I., Lagouvardos, K., Kotroni, V., Bartzokas, A., 2009. Numerical study of a downslope windstorm in Northwestern Greece. *Atmos. Res.* 94, 178–193. <https://doi.org/10.1016/j.atmosres.2009.05.012>
- Kontoes, C., Papoutsis, I., Herekakis, T., Sifakis, N., 2013. Wildfire Rapid Detection and Mapping and Post-fire Damage Assessment in Greece. *Earthzine*.
- Kotroni, V., Lagouvardos, K., 2004. Evaluation of MM5 High-Resolution Real-Time Forecasts over the Urban Area of Athens, Greece. *J. Appl. Meteorol.* 43, 1666–1678. <https://doi.org/10.1175/jam2170.1>
- Kotroni, V., Lagouvardos, K., Lykoudis, S., 2014. High-resolution model-based wind atlas for Greece. *Renew. Sustain. Energy Rev.* 30, 479–489. <https://doi.org/10.1016/J.RSER.2013.10.016>
- Koutsias, N., Arianoutsou, M., Kallimanis, A.S., Mallinis, G., Halley, J.M., Dimopoulos, P., 2012. Where did the fires burn in Peloponnisos, Greece the summer of 2007? Evidence for a synergy of fuel and weather. *Agric. For. Meteorol.* 156, 41–53. <https://doi.org/10.1016/j.agrformet.2011.12.006>
- Kraaij, T., Cowling, R.M., van Wilgen, B.W., 2013. Lightning and fire weather in eastern coastal fynbos shrublands: seasonality and long-term trends. *Int. J. Wildl. Fire* 22, 288. <https://doi.org/10.1071/WF11167>
- Krestenitis, Y., Pytharoulis, I., Karacostas, T.S., Androulidakis, Y., Makris, C., Kombiadou, K., Tegoulas, I., Baltikas, V., Kotsopoulos, S., Kartsios, S., 2017. Severe Weather Events and Sea Level Variability Over the Mediterranean Sea: The WaveForUs Operational Platform, in: Karacostas, T., Bais, A., Nastos, P.T. (Eds.), *Perspectives on Atmospheric Sciences*. Springer International Publishing, Cham, pp. 63–68. https://doi.org/10.1007/978-3-319-35095-0_9
- Lafore, J.P., Stein, J., Asencio, N., Bougeault, P., Ducrocq, V., Duron, J., Fischer, C., Hérelil, P., Mascart, P., Masson, V., Pinty, J.P., Redelsperger, J.L., Richard, E., Vilà-Guerau de Arellano, J., 1998. The Meso-NH Atmospheric Simulation System. Part I: adiabatic formulation and control simulations. *Ann. Geophys.* 16, 90–109. <https://doi.org/10.1007/s00585-997-0090-6>
- Lagouvardos, K., Kotroni, V., Defer, E., Bousquet, O., 2013. Study of a heavy precipitation event over southern france, in the frame of HYMEX project: Observational analysis and model results using assimilation of lightning. *Atmos. Res.* 134, 45–55. <https://doi.org/10.1016/j.atmosres.2013.07.003>
- Lagouvardos, K., Kotroni, V., Giannaros, T.M., Dafis, S., 2019. Meteorological Conditions Conducive to the Rapid Spread of the Deadly Wildfire in Eastern Attica, Greece. *Bull. Am. Meteorol. Soc.* 100, 2137–2145. <https://doi.org/10.1175/BAMS-D-18-0231.1>
- Laprise, R., 1992. The Euler Equations of Motion with Hydrostatic Pressure as an Independent Variable. *Mon. Weather Rev.* 120, 197–207. [https://doi.org/10.1175/1520-0493\(1992\)120<0197:TEEOMW>2.0.CO;2](https://doi.org/10.1175/1520-0493(1992)120<0197:TEEOMW>2.0.CO;2)
- Lareau, N.P., Clements, C.B., 2016. Environmental controls on pyrocumulus and pyrocumulonimbus initiation and development. *Atmos. Chem. Phys.* 16, 4005–4022. <https://doi.org/10.5194/acp-16-4005-2016>
- Le Page, Y., Oom, D., Silva, J.M.N., Jönsson, P., Pereira, J.M.C., 2010. Seasonality of vegetation fires as modified by human action: observing the deviation from eco-climatic fire regimes. *Glob. Ecol. Biogeogr.* <https://doi.org/10.1111/j.1466-8238.2010.00525.x>
- Li, J., Heap, A.D., 2014. Spatial interpolation methods applied in the environmental sciences: A review. *Environ. Model. Softw.* 53, 173–189. <https://doi.org/10.1016/j.envsoft.2013.12.008>

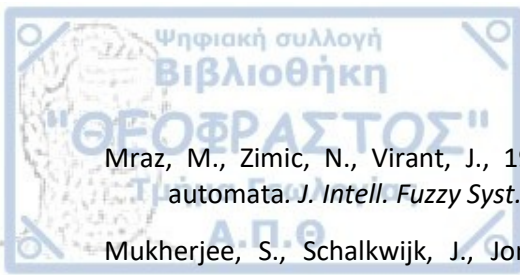


- Li, S., Jaroszynski, S., Pearse, S., Orf, L., Clyne, J., 2019. VAPOR: A Visualization Package Tailored to Analyze Simulation Data in Earth System Science. *Atmosphere (Basel)*. 10, 488. <https://doi.org/10.3390/atmos10090488>
- Li, X., Magill, W., 2000. Modeling fire spread under environmental influence using a cellular automaton approach. *Complex. Int.* 08.
- Linn, R., Reisner, J., Colman, J.J., Winterkamp, J., 2002. Studying wildfire behavior using FIRETEC. *Int. J. Wildl. Fire* 11, 233. <https://doi.org/10.1071/WF02007>
- Linn, R., Winterkamp, J., Edminster, C., Colman, J.J., Smith, W.S., 2007. Coupled influences of topography and wind on wildland fire behaviour. *Int. J. Wildl. Fire* 16, 183. <https://doi.org/10.1071/WF06078>
- Linn, R.R., Cunningham, P., 2005. Numerical simulations of grass fires using a coupled atmosphere–fire model: Basic fire behavior and dependence on wind speed. *J. Geophys. Res.* 110, D13107. <https://doi.org/10.1029/2004JD005597>
- Long, R.R., 1955. Some Aspects of the Flow of Stratified Fluids: III. Continuous Density Gradients. *Tellus* 7, 341–357. <https://doi.org/10.1111/j.2153-3490.1955.tb01171.x>
- Long, R.R., 1953. Some Aspects of the Flow of Stratified Fluids: I. A Theoretical Investigation. *Tellus* 5, 42–58. <https://doi.org/10.3402/tellusa.v5i1.8563>
- Mallia, D., Kochanski, A., Urbanski, S., Lin, J., 2018. Optimizing Smoke and Plume Rise Modeling Approaches at Local Scales. *Atmosphere (Basel)*. 9, 166. <https://doi.org/10.3390/atmos9050166>
- Mandel, J., Amram, S., Beezley, J.D., Kelman, G., Kochanski, A.K., Kondratenko, V.Y., Lynn, B.H., Regev, B., Vejmelka, M., 2014. Recent advances and applications of WRF-SFIRE. *Nat. Hazards Earth Syst. Sci.* 14, 2829–2845. <https://doi.org/10.5194/nhess-14-2829-2014>
- Mandel, J., Beezley, J.D., Kochanski, A.K., 2011. Coupled atmosphere-wildland fire modeling with WRF 3.3 and SFIRE 2011. *Geosci. Model Dev.* 4, 591–610. <https://doi.org/10.5194/gmd-4-591-2011>
- Mandel, J., Beezley, J.D., Kochanski, A.K., Kondratenko, V.Y., Kim, M., 2012. Assimilation of perimeter data and coupling with fuel moisture in a wildland fire - Atmosphere DDDAS, in: *Procedia Computer Science*. pp. 1100–1109. <https://doi.org/10.1016/j.procs.2012.04.119>
- Margerit, J., Sero-Guillaume, O., 1998. Richards' model, Hamilton-Jacobi equations and temperature field equations of forest fires, in: Viegas, D.X. (Ed.), *III International Conference on Forest Fire Research and 14th Conference on Fire and Forest Meteorology*. Viegas DX, Coimbra, Portugal, 16-20 November, Luso, Portugal, pp. 281–294.
- Matsangouras, I.T., Nastos, P.T., Pytharoulis, I., 2016. Study of the tornado event in Greece on March 25, 2009: Synoptic analysis and numerical modeling using modified topography. *Atmos. Res.* 169, 566–583. <https://doi.org/10.1016/j.atmosres.2015.08.010>
- Matsangouras, I.T., Pytharoulis, I., Nastos, P.T., 2014. Numerical modeling and analysis of the effect of complex Greek topography on tornadogenesis. *Hazards Earth Syst. Sci.* 14, 1905–1919. <https://doi.org/10.5194/nhess-14-1905-2014>
- Matthews, S., 2006. A process-based model of fine fuel moisture. *Int. J. Wildl. Fire* 15, 155. <https://doi.org/10.1071/WF05063>
- McArthur, A.G., 1977. Grassland Fire Danger Meter, Mk 5. Melbourne, Australia.
- McArthur, A.G., 1967. Fire behaviour in eucalypt forests.

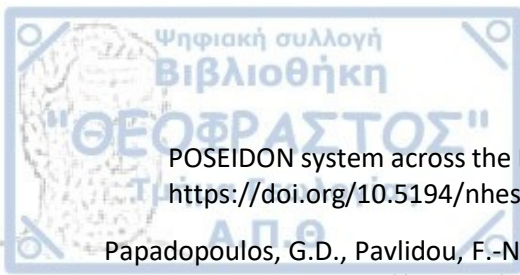


- McArthur, A.G., 1966. Weather and grassland fire behaviour. Commonwealth of Australia Department of National Development, Forestry and Timber Bureau, Canberra, Australia.
- McCaffrey, B.J.J., 1983. Momentum implications for buoyant diffusion flames. *Combust. Flame* 52, 149–167. [https://doi.org/10.1016/0010-2180\(83\)90129-3](https://doi.org/10.1016/0010-2180(83)90129-3)
- McCarthy, E.F., 1923. Forest fire weather in the southern Appalachians. *Mon. Weather Rev.* 51, 182–185. [https://doi.org/10.1175/1520-0493\(1923\)51<182:FFWITS>2.0.CO;2](https://doi.org/10.1175/1520-0493(1923)51<182:FFWITS>2.0.CO;2)
- McCaw, L., Marchetti, P., Elliott, G., Reader, G., 2007. Bushfire weather climatology of the Haines Index in southwestern Australia. *Aust. Meteorol. Mag.* 56, 75–80.
- McCormick, R.J., Brandner, T.A., Allen, T.F.H., 1999. Towards a theory of meso-scale wildfire modeling -- a complex systems approach using artificial neural networks, in: Neuenschwander, L., Ryan, K. (Eds.), *Proceedings of the Joint Fire Science Conference and Workshop. University of Idaho and International Association of Wildland Fire, Moscow, ID, 15-17 June, Boise, ID.*
- McCutchan, M.H., Fox, D.G., 1986. Effect of Elevation and Aspect on Wind, Temperature and Humidity. *J. Clim. Appl. Meteorol.* 25, 1996–2013. [https://doi.org/10.1175/1520-0450\(1986\)025<1996:EOEAAO>2.0.CO;2](https://doi.org/10.1175/1520-0450(1986)025<1996:EOEAAO>2.0.CO;2)
- McCutchan, M.H., Main, W.A., 1989. The relationship between mean monthly fire potential indices and monthly fire severity, in: Maiver, D.C., Auld, H., Whitewood, R. (Eds.), *Proceedings of the 10th Conference on Fire and Forest Meteorology. Ottawa, Ontario, Canada*, pp. 430–435.
- McGrattan, K.B., 2004. Fire Dynamics Simulator Version 4: Technical Reference Guide.
- McRae, D.J., Conard, S.G., Ivanova, G.A., Sukhinin, A.I., Baker, S.P., Samsonov, Y.N., Blake, T.W., Ivanov, V.A., Ivanov, A. V., Churkina, T. V., Hao, W.M., Koutzenogij, K.P., Kovaleva, N., 2006. Variability of fire behavior, fire effects, and emissions in Scotch pine forests of central Siberia. *Mitig. Adapt. Strateg. Glob. Chang.* 11, 45–74. <https://doi.org/10.1007/s11027-006-1008-4>
- Mell, W., Jenkins, M.A., Gould, J., Cheney, P., 2007. A physics-based approach to modelling grassland fires. *Int. J. Wildl. Fire* 16, 1. <https://doi.org/10.1071/WF06002>
- Méndez, V., Llebot, J., 1997. Hyperbolic reaction-diffusion equations for a forest fire model. *Phys. Rev. E* 56, 6557–6563. <https://doi.org/10.1103/PhysRevE.56.6557>
- Mestre, M., Allue, M., Peral, C., Santamaría, R., Lazcan, M., 2009. Operational Fire Danger Rating System in Spain, in: *International Workshop on Advances in Operational Weather Systems for Fire Danger Rating. Edmonton, Canada.*
- Millán, M.M., Estrela, M.J., Badenas, C., 1998. Meteorological Processes Relevant to Forest Fire Dynamics on the Spanish Mediterranean Coast. *J. Appl. Meteorol.* 37, 83–100. [https://doi.org/10.1175/1520-0450\(1998\)037<0083:MPRTFF>2.0.CO;2](https://doi.org/10.1175/1520-0450(1998)037<0083:MPRTFF>2.0.CO;2)
- Miller, N.L., Schlegel, N.J., 2006. Climate change projected fire weather sensitivity: California Santa Ana wind occurrence. *Geophys. Res. Lett.* 33, L15711. <https://doi.org/10.1029/2006GL025808>
- Minnich, R.A., 2001. An Integrated Model of Two Fire Regimes. *Conserv. Biol.* 15, 1549–1553. <https://doi.org/10.1046/j.1523-1739.2001.01067.x>
- Mirocha, J.D., Lundquist, J.K., Kosović, B., 2010. Implementation of a Nonlinear Subfilter Turbulence Stress Model for Large-Eddy Simulation in the Advanced Research WRF Model. *Mon. Weather Rev.* 138, 4212–4228. <https://doi.org/10.1175/2010MWR3286.1>
- Moeng, C.-H., Dudhia, J., Klemp, J., Sullivan, P., Moeng, C.-H., Dudhia, J., Klemp, J., Sullivan, P., 2007. Examining Two-Way Grid Nesting for Large Eddy Simulation of the PBL Using the WRF Model.

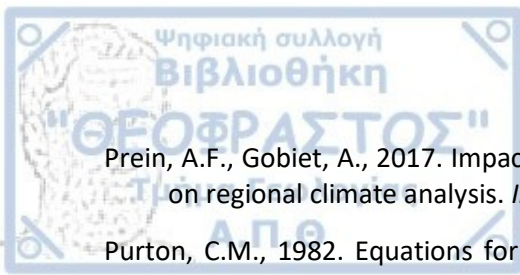
- Mon. *Weather Rev.* 135, 2295–2311. <https://doi.org/10.1175/MWR3406.1>
- Moisseeva, N., Stull, R., 2019. Capturing Plume Rise and Dispersion with a Coupled Large-Eddy Simulation: Case Study of a Prescribed Burn. *Atmosphere (Basel)*. 10, 579. <https://doi.org/10.3390/atmos10100579>
- Monin, A.S., Obukhov, A.M., 1954. Basic laws of turbulent mixing in the atmosphere near the ground. *Tr. Akad. Nauk SSSR Geofiz. Inst* 24, 163–187.
- Morcrette, J.-J., Beljaars, A., Benedetti, A., Jones, L., Boucher, O., 2008. Sea-salt and dust aerosols in the ECMWF IFS model. *Geophys. Res. Lett.* 35, L24813. <https://doi.org/10.1029/2008GL036041>
- Morcrette, J.-J., Boucher, O., Jones, L., Salmond, D., Bechtold, P., Beljaars, A., Benedetti, A., Bonet, A., Kaiser, J.W., Razinger, M., Schulz, M., Serrar, S., Simmons, A.J., Sofiev, M., Suttie, M., Tompkins, A.M., Untch, A., 2009. Aerosol analysis and forecast in the European Centre for Medium-Range Weather Forecasts Integrated Forecast System: Forward modeling. *J. Geophys. Res.* 114, D06206. <https://doi.org/10.1029/2008JD011235>
- Moreira, F., Russo, D., 2007. Modelling the impact of agricultural abandonment and wildfires on vertebrate diversity in Mediterranean Europe. *Landsc. Ecol.* 22, 1461–1476. <https://doi.org/10.1007/s10980-007-9125-3>
- Mori, A.S., Johnson, E.A., 2013. Assessing possible shifts in wildfire regimes under a changing climate in mountainous landscapes. *For. Ecol. Manage.* 310, 875–886. <https://doi.org/10.1016/j.foreco.2013.09.036>
- Moriondo, M., Good, P., Durao, R., Bindi, M., Giannakopoulos, C., Corte-Real, J., 2006. Potential impact of climate change on fire risk in the Mediterranean area. *Clim. Res.* 31, 85–95. <https://doi.org/10.3354/cr031085>
- Moritz, M.A., 1997. Analyzing extreme disturbance events: Fire in Los Padres National Forest. *Ecol. Appl.* 7, 1252–1262. [https://doi.org/10.1890/1051-0761\(1997\)007\[1252:AEDEFI\]2.0.CO;2](https://doi.org/10.1890/1051-0761(1997)007[1252:AEDEFI]2.0.CO;2)
- Moritz, M.A., Moody, T.J., Krawchuk, M.A., Hughes, M., Hall, A., 2010. Spatial variation in extreme winds predicts large wildfire locations in chaparral ecosystems. *Geophys. Res. Lett.* 37. <https://doi.org/10.1029/2009GL041735>
- Morton, B.R., Taylor, G., Turner, J.S., 1956. Turbulent gravitational convection from maintained and instantaneous sources. *Proc. R. Soc. London. Ser. A. Math. Phys. Sci.* 234, 1–23. <https://doi.org/10.1098/rspa.1956.0011>
- Morvan, D., 2011. Physical Phenomena and Length Scales Governing the Behaviour of Wildfires: A Case for Physical Modelling. *Fire Technol.* 47, 437–460. <https://doi.org/10.1007/s10694-010-0160-2>
- Morvan, D., Dupuy, J.L., 2004. Modeling the propagation of a wildfire through a Mediterranean shrub using a multiphase formulation. *Combust. Flame* 138, 199–210. <https://doi.org/10.1016/J.COMBUSTFLAME.2004.05.001>
- Morvan, D., Dupuy, J.L., 2001. Modeling of fire spread through a forest fuel bed using a multiphase formulation. *Combust. Flame* 127, 1981–1994. [https://doi.org/10.1016/S0010-2180\(01\)00302-9](https://doi.org/10.1016/S0010-2180(01)00302-9)
- Morvan, D., Meradji, S., Accary, G., 2008. Wildfire Behavior Study in a Mediterranean Pine Stand Using a Physically Based Model. *Combust. Sci. Technol.* 180, 230–248. <https://doi.org/10.1080/00102200701600978>
- Morvan, D., Méradji, S., Accary, G., 2009. Physical modelling of fire spread in Grasslands. *Fire Saf. J.* 44, 50–61. <https://doi.org/10.1016/j.firesaf.2008.03.004>



- Mraz, M., Zimic, N., Virant, J., 1999. Intelligent bush fire spread prediction using fuzzy cellular automata. *J. Intell. Fuzzy Syst.* 7, 203–207.
- Mukherjee, S., Schalkwijk, J., Jonker, H.J.J., Mukherjee, S., Schalkwijk, J., Jonker, H.J.J., 2016. Predictability of Dry Convective Boundary Layers: An LES Study. *J. Atmos. Sci.* 73, 2715–2727. <https://doi.org/10.1175/JAS-D-15-0206.1>
- Munger, T.T., 1916. Graphic method of representing and comparing drought intensities. *Mon. Weather Rev.* 44, 642–643. [https://doi.org/10.1175/1520-0493\(1916\)44<642:gmorac>2.0.co;2](https://doi.org/10.1175/1520-0493(1916)44<642:gmorac>2.0.co;2)
- Munns, E.N., 1921. Evaporation and forest fires. *Mon. Weather Rev.* 49, 149–152. [https://doi.org/10.1175/1520-0493\(1921\)49<149:EAFF>2.0.CO;2](https://doi.org/10.1175/1520-0493(1921)49<149:EAFF>2.0.CO;2)
- Muzy, A., Innocenti, E., Aiello, A., Santucci, J.-F., Wainer, G., 2002. Methods for Special Applications: Cell-DEVS Quantization Techniques in a Fire Spreading Application, in: Snowdon, J., Charnes, J. (Eds.), *Proceedings of the 34th Conference on Winter Simulation: Exploring New Frontiers, WSC '02. Winter Simulation Conference, December 8-11, San Diego, CA, USA*, pp. 542–549.
- Nahmias, J., Téphany, H., Duarte, J., Letaconnoux, S., 2000. Fire spreading experiments on heterogeneous fuel beds. Applications of percolation theory. *Can. J. For. Res.* 30, 1318–1328. <https://doi.org/10.1139/cjfr-30-8-1318>
- NASA, J., 2013. NASA Shuttle Radar Topography Mission Global 1 arc second. <https://doi.org/https://doi.org/10.5067/MEaSUREs/SRTM/SRTMGL1.003>
- Nauslar, N., Abatzoglou, J., Marsh, P., 2018. The 2017 North Bay and Southern California Fires: A Case Study. *Fire* 1, 18. <https://doi.org/10.3390/fire1010018>
- Nelson Jr, R.M., 2000. Prediction of diurnal change in 10-h fuel stick moisture content. *Can. J. For. Res.* 30, 1071–1087. <https://doi.org/10.1139/x00-032>
- Nesterov, V.G., 1949. Flammability of the Forest and Methods of its Determination, USSR State Industry Press. Moscow.
- Noble, I.R., Gill, A.M., Bary, G.A.V., 1980. McArthur's fire-danger meters expressed as equations. *Aust. J. Ecol.* 5, 201–203. <https://doi.org/10.1111/j.1442-9993.1980.tb01243.x>
- Ntaimo, L., Zeigler, B.P., Vasconcelos, M.J., Khargharia, B., 2004. Forest Fire Spread and Suppression in DEVS. *Simulation* 80, 479–500. <https://doi.org/10.1177/0037549704050918>
- Nunes, S.A., DaCamara, C.C., Turkman, K.F., Calado, T.J., Trigo, R.M., Turkman, M.A.A., 2019. Wildland fire potential outlooks for Portugal using meteorological indices of fire danger. *Nat. Hazards Earth Syst. Sci.* 19, 1459–1470. <https://doi.org/10.5194/nhess-19-1459-2019>
- Ogura, Y., Phillips, N.A., 1962. Scale Analysis of Deep and Shallow Convection in the Atmosphere. *J. Atmos. Sci.* 19, 173–179. [https://doi.org/10.1175/1520-0469\(1962\)019<0173:saodas>2.0.co;2](https://doi.org/10.1175/1520-0469(1962)019<0173:saodas>2.0.co;2)
- Onderka, M., Melicherčik, I., 2010. Fire-prone areas delineated from a combination of the Nesterov fire-risk rating Index with multispectral satellite data. *Appl. Geomatics* 2, 1–7. <https://doi.org/10.1007/s12518-009-0014-0>
- Osher, S., Fedkiw, R., 2003. Level Set Methods and Dynamic Implicit Surfaces, Applied Mathematical Sciences. Springer New York, New York, NY. <https://doi.org/10.1007/b98879>
- Palmer, T.Y., 1981. Large fire winds, gases and smoke. *Atmos. Environ.* 15, 2079–2090. [https://doi.org/10.1016/0004-6981\(81\)90241-9](https://doi.org/10.1016/0004-6981(81)90241-9)
- Papadopoulos, A., Katsafados, P., 2009. Verification of operational weather forecasts from the



- POSEIDON system across the Eastern Mediterranean. *Nat. Hazards Earth Syst. Sci.* 9, 1299–1306. <https://doi.org/10.5194/nhess-9-1299-2009>
- Papadopoulos, G.D., Pavlidou, F.-N., 2011. A Comparative Review on Wildfire Simulators. *IEEE Syst. J.* 5, 233–243. <https://doi.org/10.1109/JSYST.2011.2125230>
- Paschalidou, A.K., Kassomenos, P.A., 2016. What are the most fire-dangerous atmospheric circulations in the Eastern-Mediterranean? Analysis of the synoptic wildfire climatology. *Sci. Total Environ.* 539, 536–545. <https://doi.org/10.1016/J.SCITOTENV.2015.09.039>
- Patton, E.G., Coen, J.L., 2004. WRF-Fire: A Coupled Atmosphere-Fire Module for WRF, in: Joint MM5/Weather Research and Forecasting Model Users' Workshop. NCAR, Boulder, CO, USA.
- Pausas, J.G., Llovet, J., Rodrigo, A., Vallejo, R., 2008. Are wildfires a disaster in the Mediterranean basin? - A review. *Int. J. Wildl. Fire* 17, 713. <https://doi.org/10.1071/WF07151>
- Pavlidis, V., Katragkou, E., Prein, A., Georgoulas, A.K., Kartsios, S., Zanis, P., Karacostas, T., 2019. Investigating the sensitivity to resolving aerosol interactions in downscaling regional model experiments with WRFv3.8.1 over Europe. *Geosci. Model Dev. Discuss.* 1–34. <https://doi.org/10.5194/gmd-2019-161>
- Peace, M., Mattner, T., Mills, G., 2011. The Kangaroo Island bushfires of 2007. A meteorological case study and WRF-fire simulation, in: *9th Symposium on Fire and Forest Meteorology, American Meteorological Society, October 17-21, USA*, pp 228-234.
- Peltier, W.R., Clark, T.L., 1979. The Evolution and Stability of Finite-Amplitude Mountain Waves. Part II: Surface Wave Drag and Severe Downslope Windstorms. *J. Atmos. Sci.* 36, 1498–1529. [https://doi.org/10.1175/1520-0469\(1979\)036<1498:TEASOF>2.0.CO;2](https://doi.org/10.1175/1520-0469(1979)036<1498:TEASOF>2.0.CO;2)
- Pereira, M.G., Trigo, R.M., da Camara, C.C., Pereira, J.M.C., Leite, S.M., 2005. Synoptic patterns associated with large summer forest fires in Portugal. *Agric. For. Meteorol.* 129, 11–25. <https://doi.org/10.1016/J.AGRFORMET.2004.12.007>
- Petritsch, R., Hasenauer, H., 2014. Climate input parameters for real-time online risk assessment. *Nat. Hazards* 70, 1749–1762. <https://doi.org/10.1007/s11069-011-9880-y>
- Potter, B., 2018. The Haines Index – it's time to revise it or replace it. *Int. J. Wildl. Fire* 27, 437. <https://doi.org/10.1071/WF18015>
- Potter, B., 1996. Atmospheric Properties Associated With Large Wildfires. *Int. J. Wildl. Fire* 6, 71. <https://doi.org/10.1071/WF9960071>
- Potter, B.E., 2012a. Atmospheric interactions with wildland fire behaviour - I. Basic surface interactions, vertical profiles and synoptic structures. *Int. J. Wildl. Fire* 21, 779. <https://doi.org/10.1071/WF11128>
- Potter, B.E., 2012b. Atmospheric interactions with wildland fire behaviour - II. Plume and vortex dynamics. *Int. J. Wildl. Fire* 21, 802. <https://doi.org/10.1071/WF11129>
- Potter, B.E., 2005. The role of released moisture in the atmospheric dynamics associated with wildland fires. *Int. J. Wildl. Fire* 14, 77. <https://doi.org/10.1071/WF04045>
- Powers, J.G., Klemp, J.B., Skamarock, W.C., Davis, C.A., Dudhia, J., Gill, D.O., Coen, J.L., Gochis, D.J., Ahmadov, R., Peckham, S.E., Grell, G.A., Michalakes, J., Trahan, S., Benjamin, S.G., Alexander, C.R., Dimego, G.J., Wang, W., Schwartz, C.S., Romine, G.S., Liu, Z., Snyder, C., Chen, F., Barlage, M.J., Yu, W., Duda, M.G., 2017. The weather research and forecasting model: Overview, system efforts, and future directions. *Bull. Am. Meteorol. Soc.* 98, 1717–1737. <https://doi.org/10.1175/BAMS-D-15-00308.1>



- Prein, A.F., Gobiet, A., 2017. Impacts of uncertainties in European gridded precipitation observations on regional climate analysis. *Int. J. Climatol.* 37, 305–327. <https://doi.org/10.1002/joc.4706>
- Purton, C.M., 1982. Equations for the McArthur mark 4 grassland fire danger meters. Melbourne, Australia.
- Pytharoulis, I., 2018. Analysis of a Mediterranean tropical-like cyclone and its sensitivity to the sea surface temperatures. *Atmos. Res.* 208, 167–179. <https://doi.org/10.1016/j.atmosres.2017.08.009>
- Pytharoulis, I., Kartsios, S., Tegoulas, I., Feidas, H., Miglietta, M., Matsangouras, I., Karacostas, T., 2018. Sensitivity of a Mediterranean Tropical-Like Cyclone to Physical Parameterizations. *Atmosphere (Basel)*. 9, 436. <https://doi.org/10.3390/atmos9110436>
- Pytharoulis, I., Kotsopoulos, S., Tegoulas, I., Kartsios, S., Bampzelis, D., Karacostas, T., 2016. Numerical modeling of an intense precipitation event and its associated lightning activity over northern Greece. *Atmos. Res.* 169, 523–538. <https://doi.org/10.1016/j.atmosres.2015.06.019>
- Pytharoulis, I., Tegoulas, I., Kotsopoulos, S., Bampzelis, D., Karacostas, T., Katragkou, E., 2015. Verification of the operational high-resolution WRF forecasts produced by WaveForUs project, in: *16th Annual WRF Users' Workshop. Boulder, CO, USA.*
- Rabier, F., Järvinen, H., Klinker, E., Mahfouf, J.-F., Simmons, A., 2007. The ECMWF operational implementation of four-dimensional variational assimilation. I: Experimental results with simplified physics. *Q. J. R. Meteorol. Soc.* 126, 1143–1170. <https://doi.org/10.1002/qj.49712656415>
- Rauthe, M., Steiner, H., Riediger, U., Mazurkiewicz, A., Gratzki, A., 2013. A Central European precipitation climatology; Part I: Generation and validation of a high-resolution gridded daily data set (HYRAS). *Meteorol. Zeitschrift* 22, 235–256. <https://doi.org/10.1127/0941-2948/2013/0436>
- Reid, D.G., Vines, R.G., 1972. Radar study of the smoke plume from a forest fire.
- Reinhard, M., Rebetez, M., Schlaepfer, R., 2005. Recent climate change: Rethinking drought in the context of Forest Fire Research in Ticino, South of Switzerland. *Theor. Appl. Climatol.* 82, 17–25. <https://doi.org/10.1007/s00704-005-0123-6>
- Reisner, J., Linn, R., Bossert, J., 1998. Comparison of a diagnostic wildfire modeling system (HIGRAD/BEHAVE) with a self-determining wildfire modeling system (HIGRAD/FIRETEC). Los Alamos, NM. <https://doi.org/10.2172/314170>
- Reisner, J., Wynne, S., Margolin, L., Linn, R., 2000. Coupled Atmospheric–Fire Modeling Employing the Method of Averages. *Mon. Weather Rev.* 128, 3683–3691. [https://doi.org/10.1175/1520-0493\(2001\)129<3683:CAFMET>2.0.CO;2](https://doi.org/10.1175/1520-0493(2001)129<3683:CAFMET>2.0.CO;2)
- Ricotta, C., Retzlaff, R., 2000. Self-similar spatial clustering of wildland fires: The example of a large wildfire in Spain. *Int. J. Remote Sens.* 21, 2113–2118. <https://doi.org/10.1080/01431160050021330>
- Roads, J., Tripp, P., Juang, H., Wang, J., Chen, S., Fujioka, F., 2008. ECPC/NCEP March 2008 seasonal fire danger forecasts, *Experimental Long-Lead Forecasts Bulletin.*
- Roads, J.O., Ueyoshi, K., Chen, S.C., Alpert, J., Fujioka, F., 1991. Medium-range fire weather forecasts. *Int. J. Wildl. Fire* 1, 159–176. <https://doi.org/10.1071/WF9910159>
- Rogers, E., Black, T., Ferrier, B., Lin, Y., Parrish, D., DiMego, G., 2001. Changes to the NCEP Meso Eta Analysis and Forecast System: Increase in Resolution, New Cloud Microphysics, Modified Precipitation Assimilation, Modified 3DVAR Analysis, NOAA/NWS Technical Procedures Bulletin

488; Washington, DC, USA. Washington, DC, USA.

- Rolinski, T., Capps, S.B., Fovell, R.G., Cao, Y., D'Agostino, B.J., Vanderburg, S., Rolinski, T., Capps, S.B., Fovell, R.G., Cao, Y., D'Agostino, B.J., Vanderburg, S., 2016. The Santa Ana Wildfire Threat Index: Methodology and Operational Implementation. *Weather Forecast.* 31, 1881–1897. <https://doi.org/10.1175/WAF-D-15-0141.1>
- Rothermel, R.C., 1993. Mann Gulch Fire: A Race That Couldn't Be Won.
- Rothermel, R.C., 1972. A mathematical model for predicting fire spread in wildland fuels, USDA Forest Service Research Paper INT-116 USA.
- Rouse, J., Haas, R., Schell, J., Deering, D., 1973. Monitoring vegetation systems in the great plains with ERTS. *Third ERTS Symp.*
- Sá, A.C.L., Benali, A., Fernandes, P.M., Pinto, R.M.S., Trigo, R.M., Salis, M., Russo, A., Jerez, S., Soares, P.M.M., Schroeder, W., Pereira, J.M.C., 2017. Evaluating fire growth simulations using satellite active fire data. *Remote Sens. Environ.* 190, 302–317. <https://doi.org/10.1016/j.rse.2016.12.023>
- Saltenberger, J., Barker, T., 1993. Weather related unusual fire behavior in the Awbrey Hall fire. *Natl. Weather Dig.* 18, 20–29.
- San-Miguel-Ayanz, J., Carlson, J.D., Alexander, M., Tolhurst, K., Morgan, G., Sneeuwjagt, R., Dudley, M., 2003. Current Methods to Assess Fire Danger Potential, in: Chuvieco, E. (Ed.), *Wildland Fire Danger Estimation and Mapping - The Role of Remote Sensing Data*. World Scientific Publishing Co. Pte. Ltd., pp. 21–61. https://doi.org/10.1142/9789812791177_0002
- San-Miguel-Ayanz, J., Durrant, T., Boca, R., Libertà, G., Branco, A., De Rigo, D., Ferrari, D., Maianti, P., Artés Vivancos, T., Pfeiffer, H., Nuijten, D., 2019. Advance EFFIS Report on Forest Fires in Europe, Middle East and North Africa 2018. Ispra. <https://doi.org/10.2760/262459>
- San Jose, R., Luis Perez, J., Perez, L., Maria Gonzalez, R., Pecci, J., Palacios, M., 2015. Forest fire forecasting tool for air quality modelling systems. *Fis. La Tierra* 27, 69–90. https://doi.org/http://dx.doi.org/10.5209/rev_FITE.2015.v27.51194
- Sawyer, J.S., 1960. Numerical calculation of the displacements of a stratified airstream crossing a ridge of small height. *Q. J. R. Meteorol. Soc.* 86, 326–345. <https://doi.org/10.1002/qj.49708636905>
- Schneider, P., Roberts, D.A., Kyriakidis, P.C., 2008. A VARI-based relative greenness from MODIS data for computing the Fire Potential Index. *Remote Sens. Environ.* 112, 1151–1167. <https://doi.org/10.1016/j.rse.2007.07.010>
- Schroeder, W., Oliva, P., Giglio, L., Csizsar, I.A., 2014. The New VIIRS 375m active fire detection data product: Algorithm description and initial assessment. *Remote Sens. Environ.* 143, 85–96. <https://doi.org/10.1016/j.rse.2013.12.008>
- Scorer, R.S., 1949. Theory of waves in the lee of mountains. *Q. J. R. Meteorol. Soc.* 75, 41–56. <https://doi.org/10.1002/qj.49707532308>
- Scorer, R.S., Klieforth, H., 1959. Theory of mountain waves of large amplitude. *Q. J. R. Meteorol. Soc.* 85, 131–143. <https://doi.org/10.1002/qj.49708536406>
- Scott, J.H., Burgan, R.E., 2005. Standard fire behavior fuel models: A comprehensive set for use with Rothermel's surface fire spread model. USDA For. Serv. - Gen. Tech. Rep. RMRS-GTR. <https://doi.org/10.2737/RMRS-GTR-153>
- Sebastián López, A., San-Miguel-Ayanz, J., Burgan, R.E., 2002. Integration of satellite sensor data, fuel type maps and meteorological observations for evaluation of forest fire risk at the pan-European



- scale. *Int. J. Remote Sens.* 23, 2713–2719. <https://doi.org/10.1080/01431160110107761>
- Shabbar, A., Skinner, W., Flannigan, M.D., 2011. Prediction of Seasonal Forest Fire Severity in Canada from Large-Scale Climate Patterns. *J. Appl. Meteorol. Climatol.* 50, 785–799. <https://doi.org/10.1175/2010JAMC2547.1>
- Sharples, J.J., 2009. An overview of mountain meteorological effects relevant to fire behaviour and bushfire risk. *Int. J. Wildl. Fire* 18, 737. <https://doi.org/10.1071/WF08041>
- Sharples, J.J., Kiss, A.E., Raposo, J., Viegas, D.X., Simpson, C.C., 2015. Pyrogenic vorticity from windward and lee slope fires. *MODSIM2015, 21st International Congress of Modelling and Simulation*.
- Sharples, J.J., McRae, R.H.D., Weber, R.O., Gill, A.M., 2009a. A simple index for assessing fire danger rating. *Environ. Model. Softw.* 24, 764–774. <https://doi.org/10.1016/j.envsoft.2008.11.004>
- Sharples, J.J., McRae, R.H.D., Weber, R.O., Gill, A.M., 2009b. A simple index for assessing fuel moisture content. *Environ. Model. Softw.* 24, 637–646. <https://doi.org/10.1016/j.envsoft.2008.10.012>
- Sharples, J.J., McRae, R.H.D., Wilkes, S.R., 2012. Wind - terrain effects on the propagation of wildfires in rugged terrain: fire channelling. *Int. J. Wildl. Fire* 21, 282. <https://doi.org/10.1071/WF10055>
- Sharples, J.J., Mills, G.A., McRae, R.H.D., Weber, R.O., 2010. Foehn-Like Winds and Elevated Fire Danger Conditions in Southeastern Australia. *J. Appl. Meteorol. Climatol.* 49, 1067–1095. <https://doi.org/10.1175/2010JAMC2219.1>
- Sharples, J.J., Simpson, C.C., Evans, J.P., 2013. Examination of wind speed thresholds of vorticity-driven lateral fire spread, in: Piantadosi, J., Anderssen, R., Boland, J. (Eds.), *20th International Congress of Modelling and Simulation*.
- Simard, A.J., 1968. The moisture content of forest fuels – 1. A review of the basic concepts. Ottawa, Ontario, Canada.
- Simpson, C.C., Sharples, J.J., Evans, J.P., 2016. Sensitivity of atypical lateral fire spread to wind and slope. *Geophys. Res. Lett.* 43, 1744–1751. <https://doi.org/10.1002/2015GL067343>
- Simpson, C.C., Sharples, J.J., Evans, J.P., 2014. Resolving vorticity-driven lateral fire spread using the WRF-Fire coupled atmosphere–fire numerical model. *Nat. Hazards Earth Syst. Sci.* 14, 2359–2371. <https://doi.org/10.5194/nhess-14-2359-2014>
- Simpson, C.C., Sharples, J.J., Evans, J.P., McCabe, M.F., 2013a. Large eddy simulation of atypical wildland fire spread on leeward slopes. *Int. J. Wildl. Fire* 22, 599. <https://doi.org/10.1071/WF12072>
- Simpson, C.C., Sturman, A., Zawar-Reza, P., Pearce, G., 2013b. Assessment of fire weather during a Foehn event in South Island, New Zealand.
- Sindosi, O.A., Bartzokas, A., Kotroni, V., Lagouvardos, K., 2015. Influence of orography on precipitation amount and distribution in NW Greece; A case study. *Atmos. Res.* 152, 105–122. <https://doi.org/10.1016/j.atmosres.2014.06.013>
- Sindosi, O.A., Bartzokas, A., Kotroni, V., Lagouvardos, K., 2012. Verification of precipitation forecasts of MM5 model over Epirus, NW Greece, for various convective parameterization schemes. *Nat. Hazards Earth Syst. Sci.* 12, 1393–1405. <https://doi.org/10.5194/nhess-12-1393-2012>
- Skamarock, W.C., 2004. Evaluating Mesoscale NWP Models Using Kinetic Energy Spectra. *Mon. Weather Rev.* 132, 3019–3032. <https://doi.org/10.1175/MWR2830.1>
- Skamarock, W.C., Klemp, J.B., Dudhia, J., Gill, D.O., Barker, D.M., Duda, M.G., Huang, X.-Y., Wang, W.,



- Powers, J.G., 2008. A Description of the Advanced Research WRF Version 3. <https://doi.org/10.5065/D68S4MVH>
- Skamarock, W.C., Klemp, J.B., Dudhia, J., Gill, D.O., Zhiquan, L., Berner, J., Wang, W., Powers, J.G., Duda, M.G., Barker, D.M., Huang, X.-Y., 2019. A Description of the Advanced Research WRF Model Version 4 NCAR Technical Note. *Natl. Cent. Atmos. Res.* 145. <https://doi.org/10.5065/1dfh-6p97>
- Škvarenina, J., Mindáš, J., Holécy, J., Tuček, J., 2004. An analysis of the meteorological conditions during two largest forest fire events in the Slovak Paradise National Park. *Meteorol. J.* 7, 167–171.
- Smith, R.B., 1985. On Severe Downslope Winds. *J. Atmos. Sci.* 42, 2597–2603. [https://doi.org/10.1175/1520-0469\(1985\)042<2597:OSDW>2.0.CO;2](https://doi.org/10.1175/1520-0469(1985)042<2597:OSDW>2.0.CO;2)
- Smolarkiewicz, P.K., Rotunno, R., 1989. Low Froude Number Flow Past Three-Dimensional Obstacles. Part I: Baroclinically Generated Lee Vortices. *J. Atmos. Sci.* 46, 1154–1164. [https://doi.org/10.1175/1520-0469\(1989\)046<1154:LFNFPT>2.0.CO;2](https://doi.org/10.1175/1520-0469(1989)046<1154:LFNFPT>2.0.CO;2)
- Sneeuwjagt, R.J., Peet, G.B., 1985. Forest fire behaviour tables for western Australia. Perth.
- Sol, B., 1989. Risque numérique météorologique d'incendies de forêt en Région Méditerranéenne: dépouillement du test de l'été 1988 et propositions d'améliorations.
- Srock, A., Charney, J., Potter, B., Goodrick, S., 2018. The Hot-Dry-Windy Index: A New Fire Weather Index. *Atmosphere (Basel)*. 9, 279. <https://doi.org/10.3390/atmos9070279>
- Steiner, J.T., 1976. Blowup fires - the Byram wind profile. *Aust. Meteorol. Mag.* 24, 139–142.
- Stolaki, S., Pytharoulis, I., Karacostas, T., 2012. A study of fog characteristics using a coupled WRF-COBEL model over Thessaloniki Airport, Greece. *Pure Appl. Geophys.* 169, 961–981. <https://doi.org/10.1007/s00024-011-0393-0>
- Stull, R., 1994. An Introduction to Boundary Layer Meteorology. Kluwer Academic Publishers, Dordrecht. <https://doi.org/10.1007/978-94-009-3027-8>
- Sullivan, A.L., 2009a. Wildland surface fire spread modelling, 1990 - 2007. 1: Physical and quasi-physical models. *Int. J. Wildl. Fire* 18, 349. <https://doi.org/10.1071/WF06143>
- Sullivan, A.L., 2009b. Wildland surface fire spread modelling, 1990 - 2007. 2: Empirical and quasi-empirical models. *Int. J. Wildl. Fire* 18, 369. <https://doi.org/10.1071/wf06142>
- Sullivan, A.L., 2009c. Wildland surface fire spread modelling, 1990 - 2007. 3: Simulation and mathematical analogue models. *Int. J. Wildl. Fire* 18, 387. <https://doi.org/10.1071/WF06144>
- Sullivan, P.P., Patton, E.G., Sullivan, P.P., Patton, E.G., 2011. The Effect of Mesh Resolution on Convective Boundary Layer Statistics and Structures Generated by Large-Eddy Simulation. *J. Atmos. Sci.* 68, 2395–2415. <https://doi.org/10.1175/JAS-D-10-05010.1>
- Sun, R., Jenkins, M.A., Krueger, S.K., Mell, W., Charney, J.J., 2006. An evaluation of fire-plume properties simulated with the Fire Dynamics Simulator (FDS) and the Clark coupled wildfire model. *Can. J. For. Res.* 36, 2894–2908. <https://doi.org/10.1139/x06-138>
- Sun, R., Krueger, S.K., Jenkins, M.A., Zulauf, M.A., Charney, J.J., 2009. The importance of fire - atmosphere coupling and boundary-layer turbulence to wildfire spread. *Int. J. Wildl. Fire* 18, 50. <https://doi.org/10.1071/WF07072>
- Sun, W.-Y., 2013. Numerical study of severe downslope windstorm. *Weather Clim. Extrem.* 2, 22–30. <https://doi.org/10.1016/j.wace.2013.10.002>
- Tallapragada, V., Coauthors, 2014. Hurricane Weather Research and Forecasting (HWRF) Model.



- Tatli, H., Türkeş, M., 2014. Climatological evaluation of haines forest fire weather index over the Mediterranean Basin. *Meteorol. Appl.* 21, 545–552. <https://doi.org/10.1002/met.1367>
- Taylor, R.J., Bethwaite, F.D., Packham, D.R., Vines, R.G., 1968. A meso- meteorological investigation of five forest fires.
- Taylor, R.J., Corke, D.G., King, N.K., MacArthur, D.A., Packham, D.R., Vines, R.G., 1971. Some meteorological aspects of three intense forest fires.
- Tegoulis, I., Kartsios, S., Pytharoulis, I., Kotsopoulos, S., Karacostas, T.S., 2017. The Influence of WRF Parameterisation Schemes on High Resolution Simulations Over Greece, in: Karacostas, T., Bais, A., Nastos, P. (Eds.), *Perspectives on Atmospheric Sciences*. Springer International Publishing, Cham, pp. 3–8. https://doi.org/10.1007/978-3-319-35095-0_1
- Tegoulis, I., Pytharoulis, I., Kotsopoulos, S., Bampzelis, D., Kartsios, S., Karacostas, T., 2014a. The influence of WRF parameterisation schemes on high resolution simulations over Central Greece, in: *15th Annual WRF Users' Workshop*. Boulder, CO, USA.
- Tegoulis, I., Pytharoulis, I., Kotsopoulos, S., Karacostas, T., 2014b. Numerical weather prediction sensitivity to sea-surface temperatures, in: *12th International Conference on Meteorology, Climatology and Atmospheric Physics (COMECAP2014)*. Herakleion, Crete, Greece, pp. 203–208.
- Tewari, M., Chen, F., Wang, W., Dudhia, J., Lemone, M.A., Mitchell, K., Ek, M., Gayno, G., Wegiel, J., Cuenca, R.H., 2004. Implementation and verification of the unified NOAA land surface model in the WRF model, in: *20th Conference on Weather Analysis and Forecasting/16th Conference on Numerical Weather Prediction*. pp. 11–15.
- The NCAR Command Language (Version 6.4.0) [Software]. (2016). Boulder, Colorado: UCAR/NCAR/CISL/TDD. <http://dx.doi.org/10.5065/D6WD3XH5>
- The NCAR Command Language (Version 6.6.2) [Software]. (2019). Boulder, Colorado: UCAR/NCAR/CISL/TDD. <http://dx.doi.org/10.5065/D6WD3XH5>
- Thomas, C.M., Sharples, J.J., Evans, J.P., 2017. Modelling the dynamic behaviour of junction fires with a coupled atmosphere–fire model. *Int. J. Wildl. Fire* 26, 331. <https://doi.org/10.1071/WF16079>
- Tian, X., McRae, D.J., Jin, J., Shu, L., Zhao, F., Wang, M., 2011. Wildfires and the Canadian Forest Fire Weather Index system for the Daxing'anling region of China. *Int. J. Wildl. Fire* 20, 963. <https://doi.org/10.1071/WF09120>
- Tohidi, A., Gollner, M.J., Xiao, H., 2018. Fire Whirls. *Annu. Rev. Fluid Mech.* 50, 187–213. <https://doi.org/10.1146/annurev-fluid-122316-045209>
- Tolika, K., Maheras, P., Tegoulis, I., 2009. Extreme temperatures in Greece during 2007: Could this be a “return to the future”? *Geophys. Res. Lett.* 36, L10813. <https://doi.org/10.1029/2009GL038538>
- Trouet, V., Taylor, A.H., Carleton, A.M., Skinner, C.N., 2009. Interannual variations in fire weather, fire extent, and synoptic-scale circulation patterns in northern California and Oregon. *Theor. Appl. Climatol.* 95, 349–360. <https://doi.org/10.1007/s00704-008-0012-x>
- Tsagari, K., Karetos, G., Prokopos, N., 2011. Forest Fires of Greece, 1983-2008. WWF Hellas and NAGREG-IMDO & TDP.
- Tsinko, Y., Bakhshaii, A., Johnson, E.A., Martin, Y.E., 2018. Comparisons of fire weather indices using Canadian raw and homogenized weather data. *Agric. For. Meteorol.* 262, 110–119. <https://doi.org/10.1016/j.agrformet.2018.07.005>
- Ulmer, F.-G., Bals, U., 2016. Spin-up time research on the weather research and forecasting model for



- atmospheric delay mitigations of electromagnetic waves. *J. Appl. Remote Sens.* 10, 016027. <https://doi.org/10.1117/1.JRS.10.016027>
- Vakalis, D., Sarimveis, H., Kiranoudis, C., Alexandridis, A., Bafas, G., 2004. A GIS based operational system for wildland fire crisis management I. Mathematical modelling and simulation. *Appl. Math. Model.* 28, 389–410. <https://doi.org/10.1016/j.apm.2003.10.005>
- Van Wagner, C.E., 1987. Development and structure of the Canadian Forest Fire Weather Index System. Canadian Forestry Service.
- Van Wagner, C.E., 1979. A laboratory study of weather effects on the drying rate of jack pine litter. *Can. J. For. Res.* 9, 267–275. <https://doi.org/10.1139/x79-044>
- Van Wagner, C.E., 1967. Calculations of Forest Fire Spread by Flame Radiation.
- Van Wagner, C.E., Pickett, T.L., 1985. Equations and FORTRAN program for the Canadian Forest Fire Weather Index System, Forestry Technical Report. Canadian Forestry Service, Ottawa, Ontario, Canada.
- Vázquez, A., Pérez, B., Fernández-González, F., Moreno, J.M., 2002. Recent fire regime characteristics and potential natural vegetation relationships in Spain. *J. Veg. Sci.* 13, 663–676. <https://doi.org/10.1111/j.1654-1103.2002.tb02094.x>
- Vejmelka, M., Kochanski, A.K., Mandel, J., 2016. Data assimilation of dead fuel moisture observations from remote automated weather stations. *Int. J. Wildl. Fire* 25. <https://doi.org/10.1071/WF14085>
- Viegas, D., Neto, L., 1991. Wall Shear-Stress as a Parameter to Correlate the Rate of Spread of a Wind Induced Forest Fire. *Int. J. Wildl. Fire* 1, 177. <https://doi.org/10.1071/WF9910177>
- Viegas, D.X., 2009. Recent Forest Fire Related Accidents in Europe. Ispra. <https://doi.org/10.2788/50781>
- Viegas, D.X., Bovio, G., Ferreira, A., Nosenzo, A., Sol, B., 1999. Comparative study of various methods of fire danger evaluation in southern Europe. *Int. J. Wildl. Fire* 9, 235. <https://doi.org/10.1071/WF00015>
- Viney, N., 1991. A Review of Fine Fuel Moisture Modelling. *Int. J. Wildl. Fire* 1, 215. <https://doi.org/10.1071/WF9910215>
- Wallenius, T.H., Pennanen, J., Burton, P.J., 2011. Long-term decreasing trend in forest fires in northwestern Canada. *Ecosphere* 2, art53. <https://doi.org/10.1890/ES11-00055.1>
- Wang, W., Bruyère, C., Duda, M.G., Dudhia, J., Gill, D.O., Hin, H.C., Michalakes, J., Rizvi, S., Zhang, X., Beezley, J.D., Coen, J.L., Mandel, J., Chuang, H.-Y., Mckee, N., Slovacek, T., Wolff, J., 2012. ARW version 3 modeling system user's guide.
- Watt, S.D., Roberts, A.J., Weber, R.O., 1995. Dimensional reduction of a bushfire model. *Math. Comput. Model.* 21, 79–83. [https://doi.org/10.1016/0895-7177\(95\)00055-7](https://doi.org/10.1016/0895-7177(95)00055-7)
- Weber, R.O., 1991. Modelling fire spread through fuel beds. *Prog. Energy Combust. Sci.* 17, 67–82. [https://doi.org/10.1016/0360-1285\(91\)90003-6](https://doi.org/10.1016/0360-1285(91)90003-6)
- Weisman, M.L., Klemp, J.B., 1986. Characteristics of Isolated Convective Storms, in: *Mesoscale Meteorology and Forecasting*. American Meteorological Society, Boston, MA, pp. 331–358. https://doi.org/10.1007/978-1-935704-20-1_15
- Weiss, S.J., Pyle, M.E., Janjic, Z., Bright, D.R., Kain, J.S., Dimego, G.J., 2008. Runs At Ncep : Advantages

- of Multiple Model Runs, in: *24th Conference on Severe Local Storms*. pp. 1–11.
- Werth, P., Ochoa, R., 1993. The Evaluation of Idaho Wildfire Growth Using the Haines Index. *Weather Forecast.* 8, 223–234. [https://doi.org/10.1175/1520-0434\(1993\)008<0223:TEOIWG>2.0.CO;2](https://doi.org/10.1175/1520-0434(1993)008<0223:TEOIWG>2.0.CO;2)
- Whiteman, C.D., 2000. *Mountain Meteorology: Fundamentals and Applications*. Oxford University Press, New York.
- Whitman, E., Sherren, K., Rapaport, E., 2015. Increasing daily wildfire risk in the Acadian Forest Region of Nova Scotia, Canada, under future climate change. *Reg. Environ. Chang.* 15, 1447–1459. <https://doi.org/10.1007/s10113-014-0698-5>
- Wilson, G.U., 1969. Meteorological aspects of the Tumut fire experiment. *Aust. Meteorol. Mag.* 17, 25–47.
- Wolfram, S., 1983. Statistical mechanics of cellular automata. *Rev. Mod. Phys.* 55, 601–644. <https://doi.org/10.1103/RevModPhys.55.601>
- Xue, H., Gu, F., Hu, X., 2012a. Data assimilation using sequential monte carlo methods in wildfire spread simulation. *ACM Trans. Model. Comput. Simul.* 22, 1–25. <https://doi.org/10.1145/2379810.2379816>
- Xue, H., Hu, X., Dahl, N., Xue, M., 2012b. Post-frontal Combustion Heat Modeling in DEVS-fire for Coupled Atmosphere-fire Simulation. *Procedia Comput. Sci.* 9, 302–311. <https://doi.org/10.1016/j.procs.2012.04.032>
- Xue, M., 2000. High-order monotonic numerical diffusion and smoothing. *Mon. Weather Rev.* 128, 2853–2864. [https://doi.org/10.1175/1520-0493\(2000\)128<2853:homnda>2.0.co;2](https://doi.org/10.1175/1520-0493(2000)128<2853:homnda>2.0.co;2)
- Xue, M., Droegemeier, K.K., Wong, V., 2000. The Advanced Regional Prediction System (ARPS) - A multi-scale nonhydrostatic atmospheric simulation and prediction model. Part I: Model dynamics and verification. *Meteorol. Atmos. Phys.* 75, 161–193. <https://doi.org/10.1007/s007030070003>
- Xue, M., Droegemeier, K.K., Wong, V., Shapiro, A., Brewster, K., Carr, F., Weber, D., Liu, Y., Wang, D., 2001. The Advanced Regional Prediction System (ARPS) - A multi-scale nonhydrostatic atmospheric simulation and prediction tool. Part II: Model physics and applications. *Meteorol. Atmos. Phys.* 76, 143–165. <https://doi.org/10.1007/s007030170027>
- Xystrakis, F., Kallimanis, A.S., Dimopoulos, P., Halley, J.M., Koutsias, N., 2014. Precipitation dominates fire occurrence in Greece (1900–2010): its dual role in fuel build-up and dryness. *Nat. Hazards Earth Syst. Sci.* 14, 21–32. <https://doi.org/10.5194/nhess-14-21-2014>
- Yair, Y., Lynn, B., Price, C., Kotroni, V., Lagouvardos, K., Morin, E., Mugnai, A., Llasat, M. del C., 2010. Predicting the potential for lightning activity in Mediterranean storms based on the Weather Research and Forecasting (WRF) model dynamic and microphysical fields. *J. Geophys. Res.* 115, D04205. <https://doi.org/10.1029/2008JD010868>
- Yamaguchi, T., Feingold, G., 2012. Technical note: Large-eddy simulation of cloudy boundary layer with the Advanced Research WRF model. *J. Adv. Model. Earth Syst.* 4, n/a-n/a. <https://doi.org/10.1029/2012MS000164>
- Young, J.A., 2003. Static Stability, in: North, G.R., Pyle, J.A., Zhang, F. (Eds.), *Encyclopedia of Atmospheric Sciences*, Vol. 1-6. Elsevier, p. 2998.
- Zeldovich, Y.B., 1937. The Asymptotic Laws of Freely-Ascending Convective Flows. *Zh. Eksp. Teor. Fiz., Chemical Physics and Hydrodynamics* 7, 1463– 1465.





Acknowledgements

This work has been supported by computational time granted from the Greek Research & Technology Network (GRNET) in the National High Performance Computing facility ARIS under the projects “Large Eddy Simulations in wildland FIRES (LESinFIRE)”, “CLOud Resolving climate and FIRE Simulations (COrFIRE)” and “Impact of Land Use Changes on regional and local climate in Europe (LUCe)”. I would like to acknowledge the AUTH Scientific Computing Centre Infrastructure and technical support and the computing infrastructure at the Department of Meteorology and Climatology, AUTH for the support and the exploitation of their resources. Special thanks to the Open Wildland Fire Modeling Community (www.openwfm.org) for providing the WRF-SFIRE modelling system. I thank NCAR, ECMWF, EUMETSAT and NCEP for providing the WRF-ARW numerical weather prediction model, the operational gridded analyses, the satellite images and the sea-surface temperature data, respectively. I would like also to thank the Hellenic National Meteorological Service (<http://www.hnms.gr/>) for providing the surface observations. I acknowledge the use of the Copernicus Emergency Management Service (<https://emergency.copernicus.eu/>), the Copernicus CORINE land cover data (<https://land.copernicus.eu/pan-european/corine-land-cover>) and the NASA products regarding the Fire Thermal Anomalies dataset (<https://modis.gsfc.nasa.gov/data/dataproduct/mod14.php>) and the Shuttle Radar Topography Mission dataset (<https://www2.jpl.nasa.gov/srtm/>). Finally, I acknowledge the Earth Science Data and Information System (ESDIS) Project (<https://earthdata.nasa.gov/esdis>) and the Visible Infrared Imaging Radiometer Suite (VIIRS). For analysis and visualization purposes, the NCAR Command Language (NCL; v.6.4.0 and v.6.6.2) was utilized. 3-D visualization was carried out with the Visualization and Analysis Platform for Research (VAPOR; v.2.6.0). The resampling of land use data to fuel models was performed in Quantum GIS (v.2.18.16).





Appendix I
Statistical formulas
Mean Error (ME):

$$ME = \frac{1}{n} \sum_{i=1}^n (\text{forecast} - \text{observation})$$

Mean Absolute Error (MAE):

$$MAE = \frac{1}{n} \sum_{i=1}^n |\text{forecast} - \text{observation}|$$

Root Mean Square Error (RMSE):

$$RMSE = \sqrt{\frac{1}{n} \sum_{i=1}^n (\text{forecast} - \text{observation})^2}$$

95% confidence interval (normal distribution):

$$\bar{x} \pm 1.96 \frac{\text{sample's standard deviation}}{\sqrt{n}}$$

Spatial interpolation formulas

Inverse distance weighting (IDW):

$$Z_p = \frac{\sum_{i=1}^n \left(\frac{z_i}{\text{dist}_i^2} \right)}{\sum_{i=1}^n \left(\frac{1}{\text{dist}_i^2} \right)}$$

Gressman Method:

$$Z = \frac{\sum_{i=1}^4 \left[\left(\frac{dx^2 - \text{dist}_n^2}{dx^2 + \text{dist}_n^2} \right) Z_n \right]}{\sum_{i=1}^4 \left(\frac{dx^2 - \text{dist}_n^2}{dx^2 + \text{dist}_n^2} \right)}$$

Meteorological variables

Vapor pressure:

$$e(\text{hPa}) = \frac{p(\text{hPa}) \cdot r \left(\frac{\text{gr}}{\text{kgr}} \right) \cdot 10^{-3}}{0.622 + r \left(\frac{\text{gr}}{\text{kgr}} \right) \cdot 10^{-3}}$$

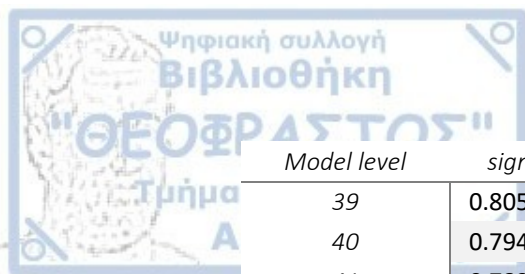


Saturation vapor pressure:

$$e_{max}(hPa) = 6.11 \cdot e^{\frac{17.38 \cdot T(K)}{239 + T(K)}}$$

Table B.1: Sigma model coordinate, mass-theta height (m) and Δz between mass levels, during the first time-step of the WRF-SFIRE.

Model level	sigma	Mass level	Mass height (m)	Δz (m)
0	1	0	5.78972	
1	0.998205	1	17.6633	11.87358
2	0.99632	2	30.141	12.4777
3	0.994341	3	43.2546	13.1136
4	0.992263	4	57.0366	13.782
5	0.990081	5	71.5201	14.4835
6	0.987791	6	86.7399	15.2198
7	0.985387	7	102.733	15.9931
8	0.982864	8	119.537	16.804
9	0.980216	9	137.193	17.656
10	0.977438	10	155.742	18.549
11	0.974524	11	175.229	19.487
12	0.971467	12	195.698	20.469
13	0.968261	13	217.198	21.5
14	0.9649	14	239.779	22.581
15	0.961375	15	263.492	23.713
16	0.95768	16	288.392	24.9
17	0.953808	17	314.538	26.146
18	0.94975	18	341.988	27.45
19	0.945499	19	370.806	28.818
20	0.941046	20	401.057	30.251
21	0.936383	21	432.81	31.753
22	0.931501	22	466.134	33.324
23	0.926391	23	501.104	34.97
24	0.921043	24	537.797	36.693
25	0.915448	25	576.292	38.495
26	0.909596	26	616.671	40.379
27	0.903478	27	659.017	42.346
28	0.897082	28	703.42	44.403
29	0.890399	29	749.972	46.552
30	0.883418	30	798.771	48.799
31	0.876128	31	849.919	51.148
32	0.868517	32	903.521	53.602
33	0.860576	33	959.683	56.162
34	0.852292	34	1018.52	58.837
35	0.843655	35	1080.13	61.61
36	0.834654	36	1144.65	64.52
37	0.825276	37	1212.2	67.55
38	0.815511	38	1282.92	70.72



<i>Model level</i>	<i>sigma</i>	<i>Mass level</i>	<i>Mass height (m)</i>	<i>Δz (m)</i>
39	0.805348	39	1356.93	74.01
40	0.794775	40	1434.38	77.45
41	0.783783	41	1515.5	81.12
42	0.77236	42	1600.67	85.17
43	0.760496	43	1690.18	89.51
44	0.748181	44	1784.14	93.96
45	0.735406	45	1882.57	98.43
46	0.722163	46	1985.61	103.04
47	0.708442	47	2093.42	107.81
48	0.694236	48	2206.21	112.79
49	0.679538	49	2324.21	118
50	0.664343	50	2447.62	123.41
51	0.648644	51	2576.64	129.02
52	0.632438	52	2711.53	134.89
53	0.615722	53	2852.53	141
54	0.598494	54	2999.88	147.35
55	0.580752	55	3153.84	153.96
56	0.562499	56	3314.68	160.84
57	0.543735	57	3482.68	168
58	0.524464	58	3658.13	175.45
59	0.504691	59	3841.32	183.19
60	0.484423	60	4032.58	191.26
61	0.463668	61	4232.24	199.66
62	0.442436	62	4440.64	208.4
63	0.420738	63	4658.16	217.52
64	0.398588	64	4885.19	227.03
65	0.376002	65	5122.13	236.94
66	0.352994	66	5369.35	247.22
67	0.329586	67	5627.27	257.92
68	0.305796	68	5896.39	269.12
69	0.281647	69	6177.23	280.84
70	0.257162	70	6470.37	293.14
71	0.232366	71	6776.43	306.06
72	0.207286	72	7096.1	319.67
73	0.181951	73	7430.16	334.06
74	0.156388	74	7779.44	349.28
75	0.130629	75	8144.99	365.55
76	0.104704	76	8528.01	383.02
77	0.078645	77	8929.81	401.8
78	0.052486	78	9351.87	422.06
79	0.02626	79	9795.89	444.02
80	0			



Table B.2: Anderson's thirteen (13) fuel categories as they are used by default in the WRF-SFIRE. Adopted from Anderson (1982), his Table 1.

Fuel model	Typical fuel complex	Fuel loading				Fuel bed depth	Moisture of extinction dead fuels	
		1 hour	10 hours	100 hours	Live		Feet	Percent
		-----Tons/acre-----				Feet	Percent	
Grass and grass-dominated								
1	Short grass (1 foot)	0.74	0.00	0.00	0.00	1.0	12	
2	Timber (grass and understory)	2.00	1.00	.50	.50	1.0	15	
3	Tall grass (2.5 feet)	3.01	.00	.00	.00	2.5	25	
Chaparral and shrub fields								
4	Chaparral (6 feet)	5.01	4.01	2.00	5.01	6.0	20	
5	Brush (2 feet)	1.00	.50	.00	2.00	2.0	20	
6	Dormant brush, hardwood slash	1.50	2.50	2.00	.00	2.5	25	
7	Southern rough	1.13	1.87	1.50	.37	2.5	40	
Timber litter								
8	Closed timber litter	1.50	1.00	2.50	0.00	0.2	30	
9	Hardwood litter	2.92	.41	.15	.00	.2	25	
10	Timber (litter and understory)	3.01	2.00	5.01	2.00	1.0	25	
Slash								
11	Light logging slash	1.50	4.51	5.51	0.00	1.0	15	
12	Medium logging slash	4.01	14.03	16.53	.00	2.3	20	
13	Heavy logging slash	7.01	23.04	28.05	.00	3.0	25	

Table B.3: Input sounding file for the construction of the ideal atmosphere in numerical experiments.

Height (m)	Temperature (K)	mixing ratio (g kg ⁻¹)	u (m s ⁻¹)	v (m s ⁻¹)
0	300	12		
25	300	11.95	2	0
75	300	11.9	2	0
125	300	11.85	2	0
175	300	11.8	2.1	0
225	300	11.75	2.1	0
275	300	11.58	2.1	0
325	300	11.41	2.1	0
375	300	11.24	2.1	0
425	300	11.07	2.2	0
475	300	10.9	2.2	0
525	300	10.73	2.2	0
575	300	10.56	2.2	0
625	300	10.39	2.2	0
675	300	10.22	2.3	0
725	300	10.05	2.3	0
775	300	9.88	2.3	0
825	300	9.71	2.3	0
875	300	9.54	2.3	0
925	300	9.37	2.4	0
975	300	9.2	2.4	0
1025	300	9.03	2.4	0
1075	300	8.86	2.4	0
1125	300	8.69	2.4	0
1175	300	8.52	2.5	0

Height (m)	Temperature (K)	mixing ratio (g kg ⁻¹)	u (m s ⁻¹)	v (m s ⁻¹)
1225	300	8.35	2.5	0
1275	300	8.18	2.5	0
1325	300	8.01	2.5	0
1375	300	7.84	2.5	0
1425	300	7.67	2.6	0
1475	300	7.5	2.6	0
1525	301	7.25	2.6	0
1575	302	7	2.6	0
1625	303	6.75	2.6	0
1675	304	6.5	2.7	0
1725	305	6.25	2.7	0
1775	305.2	6.2	2.7	0
1825	305.5	6.15	2.7	0
1875	305.7	6.1	2.7	0
1925	305.9	6.05	2.8	0
1975	306.2	6	2.8	0
2025	306.4	5.95	2.8	0
2075	306.6	5.9	2.8	0
2125	306.8	5.85	2.8	0
2175	307.1	5.8	2.9	0
2225	307.3	5.75	2.9	0
2275	307.5	5.7	2.9	0
2325	307.8	5.65	2.9	0
2375	308	5.6	2.9	0
2425	308.2	5.55	3	0
2475	308.5	5.5	3	0
2525	308.7	5.45	3	0
2575	308.9	5.4	3	0
2625	309.1	5.35	3	0
2675	309.4	5.3	3.1	0
2725	309.6	5.25	3.1	0
2775	309.8	5.2	3.1	0
2825	310.1	5.15	3.1	0
2875	310.3	5.1	3.1	0
2925	310.5	5.05	3.2	0
2975	310.8	5	3.2	0
3025	311	4.95	3.2	0
3075	311.2	4.9	3.2	0
3125	311.4	4.85	3.2	0
3175	311.7	4.8	3.3	0
3225	311.9	4.75	3.3	0
3275	312.1	4.7	3.3	0
3325	312.4	4.65	3.3	0
3375	312.6	4.6	3.3	0
3425	312.8	4.55	3.4	0

Height (m)	Temperature (K)	mixing ratio (g kg ⁻¹)	u (m s ⁻¹)	v (m s ⁻¹)
3475	313.1	4.5	3.4	0
3525	313.3	4.45	3.4	0
3575	313.5	4.4	3.4	0
3625	313.7	4.35	3.4	0
3675	314	4.3	3.5	0
3725	314.2	4.25	3.5	0
3775	314.4	4.2	3.5	0
3825	314.7	4.15	3.5	0
3875	314.9	4.1	3.5	0
3925	315.1	4.05	3.6	0
3975	315.4	4	3.6	0
4025	315.6	3.95	3.6	0
4075	315.8	3.9	3.6	0
4125	316	3.85	3.6	0
4175	316.3	3.8	3.7	0
4225	316.5	3.75	3.7	0
4275	316.7	3.7	3.7	0
4325	317	3.65	3.7	0
4375	317.2	3.6	3.7	0
4425	317.4	3.55	3.8	0
4475	317.7	3.5	3.8	0
4525	317.9	3.45	3.8	0
4575	318.1	3.4	3.8	0
4625	318.3	3.35	3.8	0
4675	318.6	3.3	3.9	0
4725	318.8	3.25	3.9	0
4775	319	3.2	3.9	0
4825	319.3	3.15	3.9	0
4875	319.5	3.1	3.9	0
4925	319.7	3.05	4	0
4975	320	3	4	0
5025	320.2	2.95	4	0
5075	320.4	2.9	4.1	0
5125	320.6	2.85	4.2	0
5175	320.8	2.8	4.3	0
5225	321	2.75	4.4	0
5275	321.2	2.7	4.5	0
5325	321.4	2.65	4.6	0
5375	321.6	2.6	4.7	0
5425	321.8	2.55	4.8	0
5475	322	2.5	4.9	0
5525	322.2	2.45	5	0
5575	322.4	2.4	5.1	0
5625	322.6	2.35	5.2	0
5675	322.8	2.3	5.3	0

Height (m)	Temperature (K)	mixing ratio (g kg ⁻¹)	u (m s ⁻¹)	v (m s ⁻¹)
5725	323	2.25	5.4	0
5775	323.2	2.2	5.5	0
5825	323.4	2.15	5.6	0
5875	323.6	2.1	5.7	0
5925	323.8	2.05	5.8	0
5975	324	2	5.9	0
6025	324.2	1.95	6	0
6075	324.4	1.9	6.1	0
6125	324.6	1.85	6.2	0
6175	324.8	1.8	6.3	0
6225	325	1.75	6.4	0
6275	325.2	1.7	6.5	0
6325	325.4	1.65	6.6	0
6375	325.6	1.6	6.7	0
6425	325.8	1.55	6.8	0
6475	326	1.5	6.9	0
6525	326.2	1.45	7	0
6575	326.4	1.4	7.1	0
6625	326.6	1.35	7.2	0
6675	326.8	1.3	7.3	0
6725	327	1.25	7.4	0
6775	327.2	1.2	7.5	0
6825	327.4	1.15	7.6	0
6875	327.6	1.1	7.7	0
6925	327.8	1.05	7.8	0
6975	328	1	7.9	0
7025	328.2	0.95	8	0
7075	328.4	0.9	8.1	0
7125	328.6	0.85	8.2	0
7175	328.8	0.8	8.3	0
7225	329	0.75	8.4	0
7275	329.2	0.7	8.5	0
7325	329.4	0.65	8.6	0
7375	329.6	0.6	8.7	0
7425	329.8	0.55	8.8	0
7475	330	0.5	8.9	0
7525	330.2	0.45	9	0
7575	330.4	0.4	9.1	0
7625	330.6	0.35	9.2	0
7675	330.8	0.3	9.3	0
7725	331	0.25	9.4	0
7775	331.2	0.2	9.5	0
7825	331.4	0.15	9.6	0
7875	331.6	0.1	9.7	0
7925	331.8	0.1	9.8	0

Height (m)	Temperature (K)	mixing ratio (g kg ⁻¹)	u (m s ⁻¹)	v (m s ⁻¹)
7975	332	0.1	9.9	0
8025	332.2	0.1	10	0
8075	332.4	0.1	10.1	0
8125	332.6	0.1	10.2	0
8175	332.8	0.1	10.3	0
8225	333	0.1	10.4	0
8275	333.2	0.1	10.5	0
8325	333.4	0.1	10.6	0
8375	333.6	0.1	10.7	0
8425	333.8	0.09	10.8	0
8475	334	0.09	10.9	0
8525	334.2	0.09	11	0
8575	334.4	0.09	11.1	0
8625	334.6	0.09	11.2	0
8675	334.8	0.09	11.3	0
8725	335	0.09	11.4	0
8775	335.2	0.09	11.5	0
8825	335.4	0.09	11.6	0
8875	335.6	0.09	11.7	0
8925	335.8	0.09	11.8	0
8975	336	0.09	11.9	0
9025	336.2	0.09	12	0
9075	336.4	0.09	12.1	0
9125	336.6	0.09	12.2	0
9175	336.8	0.09	12.3	0
9225	337	0.09	12.4	0
9275	337.2	0.09	12.5	0
9325	337.4	0.09	12.6	0
9375	337.6	0.09	12.7	0
9425	337.8	0.08	12.8	0
9475	338	0.08	12.9	0
9525	338.2	0.08	13	0
9575	338.4	0.08	13.1	0
9625	338.6	0.08	13.2	0
9675	338.8	0.08	13.3	0
9725	339	0.08	13.4	0
9775	339.2	0.08	13.5	0
9825	339.4	0.08	13.6	0
9875	339.6	0.08	13.7	0
9925	339.8	0.08	13.8	0
9975	340	0.08	13.9	0
10025	340.2	0.08	14	0

Table B.4: Portion of heat flux (%) from the surface fire that resides on every theta level, in all experiments.

CNTRL	ext005m	ext010m	ext015m	ext025m	ext075m	ext100m	ext200m
89.06583	31.41314	56.04742	67.97832	79.32722	92.57082	94.3747	97.14664
70.23903	2.922707	17.09593	30.80315	49.33522	79.01672	83.80873	91.54711
54.72662	0.240983	4.909	13.40691	29.95003	66.9061	73.97744	86.01014
42.10128	0.017497	1.322746	5.59308	17.72518	56.17334	64.8855	80.55154
31.9585	0.001111	0.333374	2.231625	10.21346	46.74383	56.53185	75.18766
23.92127	6.14E-05	0.078329	0.84973	5.722273	38.53507	48.90938	69.93524
17.64358	2.92E-06	0.017098	0.308051	3.11296	31.45752	42.00427	64.8107
12.81364	1.19E-07	0.003454	0.106066	1.641894	25.41646	35.79614	59.82988
9.15619	4.14E-09	0.000644	0.034598	0.838358	20.31467	30.2592	55.00836
6.432159	1.21E-10	0.00011	0.010662	0.413727	16.05355	25.3617	50.3604
4.438561	2.97E-12	1.72E-05	0.003096	0.197008	12.53607	21.06789	45.89977
3.00594	6.02E-14	2.45E-06	0.000845	0.090357	9.667633	17.33765	41.6385
1.99613	1E-15	3.17E-07	0.000216	0.039845	7.358555	14.12845	37.58782
1.298501	1.36E-17	3.69E-08	5.15E-05	0.016861	5.524523	11.39518	33.75674
0.82662	1.49E-19	3.86E-09	1.14E-05	0.006833	4.088249	9.091866	30.15272
0.514443	1.3E-21	3.6E-10	2.35E-06	0.002647	2.98006	7.172471	26.78147
0.31265	8.92E-24	2.99E-11	4.47E-07	0.000978	2.138155	5.591515	23.64638
0.185335	4.78E-26	2.19E-12	7.82E-08	0.000343	1.508823	4.305056	20.74863
0.107036	1.97E-28	1.4E-13	1.25E-08	0.000115	1.046373	3.271636	18.08766
0.060148	6.2E-31	7.87E-15	1.84E-09	3.62E-05	0.712547	2.452506	15.66048
0.032845	1.46E-33	3.82E-16	2.44E-10	1.08E-05	0.476039	1.812306	13.46219
0.017404	2.55E-36	1.6E-17	2.94E-11	3.03E-06	0.311726	1.319259	11.4859
0.008937	3.25E-39	5.7E-19	3.19E-12	7.99E-07	0.199898	0.945379	9.723058
0.004441	2.98E-42	1.73E-20	3.1E-13	1.97E-07	0.125404	0.666397	8.163314
0.002132	1.94E-45	4.4E-22	2.69E-14	4.54E-08	0.076884	0.461719	6.794987
0.000987	8.79E-49	9.37E-24	2.06E-15	9.75E-09	0.046018	0.314192	5.605287
0.00044	2.73E-52	1.65E-25	1.4E-16	1.94E-09	0.02686	0.209813	4.580532
0.000189	5.73E-56	2.39E-27	8.31E-18	3.56E-10	0.015272	0.137381	3.706489
7.77E-05	7.97E-60	2.82E-29	4.3E-19	6.03E-11	0.008449	0.088122	2.96854
3.06E-05	7.22E-64	2.69E-31	1.93E-20	9.37E-12	0.004542	0.055324	2.352104
1.15E-05	4.17E-68	2.04E-33	7.47E-22	1.33E-12	0.002369	0.033961	1.842854
4.15E-06	1.5E-72	1.23E-35	2.47E-23	1.72E-13	0.001198	0.020363	1.427001
1.42E-06	3.32E-77	5.76E-38	6.92E-25	2.01E-14	0.000586	0.011914	1.091513
4.62E-07	4.4E-82	2.1E-40	1.64E-26	2.13E-15	0.000277	0.006794	0.82428
1.42E-07	3.41E-87	5.84E-43	3.24E-28	2.03E-16	0.000127	0.003772	0.614203
4.15E-08	1.52E-92	1.23E-45	5.33E-30	1.72E-17	5.56E-05	0.002037	0.451365
1.14E-08	3.78E-98	1.94E-48	7.23E-32	1.3E-18	2.35E-05	0.001069	0.326907
2.96E-09	5.1E-104	2.26E-51	8E-34	8.75E-20	9.56E-06	0.000544	0.233207
7.19E-10	3.7E-110	1.92E-54	7.17E-36	5.17E-21	3.73E-06	0.000268	0.163747
1.64E-10	1.4E-116	1.17E-57	5.16E-38	2.68E-22	1.39E-06	0.000128	0.1131
3.48E-11	2.6E-123	5.08E-61	2.95E-40	1.21E-23	4.94E-07	5.9E-05	0.076786
6.86E-12	2.3E-130	1.52E-64	1.32E-42	4.71E-25	1.68E-07	2.62E-05	0.051184
1.25E-12	9.3E-138	3.05E-68	4.53E-45	1.56E-26	5.38E-08	1.12E-05	0.033434
2.09E-13	1.6E-145	3.95E-72	1.16E-47	4.35E-28	1.63E-08	4.57E-06	0.021371

CNTRL	ext005m	ext010m	ext015m	ext025m	ext075m	ext100m	ext200m
3.19E-14	1.1E-153	3.28E-76	2.21E-50	1.01E-29	4.66E-09	1.78E-06	0.013359
4.45E-15	3E-162	1.74E-80	3.12E-53	1.98E-31	1.26E-09	6.67E-07	0.008167
5.67E-16	3.4E-171	5.84E-85	3.24E-56	3.21E-33	3.18E-10	2.38E-07	0.004879
6.56E-17	1.5E-180	1.21E-89	2.45E-59	4.3E-35	7.55E-11	8.1E-08	0.002846
6.87E-18	2.3E-190	1.53E-94	1.33E-62	4.72E-37	1.68E-11	2.62E-08	0.001619
6.49E-19	1.3E-200	1.2E-99	5.1E-66	4.21E-39	3.48E-12	8.06E-09	0.000898
5.5E-20	2.5E-211	5E-105	1.36E-69	3.02E-41	6.71E-13	2.34E-09	0.000484
4.16E-21	1.6E-222	1.3E-110	2.5E-73	1.73E-43	1.2E-13	6.45E-10	0.000254
2.81E-22	3E-234	1.7E-116	3.11E-77	7.87E-46	1.99E-14	1.67E-10	0.000129
1.67E-23	1.7E-246	1.3E-122	2.58E-81	2.8E-48	3.04E-15	4.09E-11	6.39E-05
8.78E-25	2.7E-259	5.2E-129	1.4E-85	7.7E-51	4.26E-16	9.37E-12	3.06E-05
4.04E-26	1.2E-272	1.1E-135	4.86E-90	1.63E-53	5.46E-17	2.01E-12	1.42E-05
1.62E-27	1.2E-286	1.1E-142	1.07E-94	2.62E-56	6.4E-18	4.02E-13	6.34E-06
5.62E-29	3.1E-301	5.6E-150	1.5E-99	3.16E-59	6.81E-19	7.5E-14	2.74E-06
1.68E-30	0	1.3E-157	1.2E-104	2.83E-62	6.57E-20	1.3E-14	1.14E-06
4.31E-32	0	1.5E-165	6.1E-110	1.86E-65	5.71E-21	2.08E-15	4.56E-07
9.41E-34	0	7.4E-174	1.8E-115	8.85E-69	4.46E-22	3.07E-16	1.75E-07
1.73E-35	0	1.6E-182	2.9E-121	3.01E-72	3.11E-23	4.17E-17	6.45E-08
2.69E-37	0	1.4E-191	2.7E-127	7.21E-76	1.93E-24	5.18E-18	2.28E-08
3.47E-39	0	5E-201	1.4E-133	1.2E-79	1.06E-25	5.89E-19	7.67E-09
3.7E-41	0	6.9E-211	3.6E-140	1.37E-83	5.15E-27	6.08E-20	2.47E-09
3.23E-43	0	3.5E-221	5E-147	1.05E-87	2.19E-28	5.69E-21	7.54E-10
2.3E-45	0	6.5E-232	3.5E-154	5.31E-92	8.1E-30	4.8E-22	2.19E-10
1.32E-47	0	4.1E-243	1.2E-161	1.76E-96	2.6E-31	3.64E-23	6.03E-11
6.09E-50	0	8.4E-255	1.9E-169	3.7E-101	7.18E-33	2.47E-24	1.57E-11
2.21E-52	0	5.3E-267	1.4E-177	4.9E-106	1.7E-34	1.49E-25	3.86E-12
6.3E-55	0	9.9E-280	4.6E-186	4E-111	3.41E-36	7.93E-27	8.91E-13
1.38E-57	0	5.1E-293	6.3E-195	1.9E-116	5.76E-38	3.72E-28	1.93E-13
2.31E-60	0	6.6E-307	3.5E-204	5.3E-122	8.12E-40	1.52E-29	3.9E-14
2.9E-63	0	0	7.5E-214	8.4E-128	9.44E-42	5.39E-31	7.34E-15
2.68E-66	0	0	5.8E-224	7.2E-134	8.96E-44	1.64E-32	1.28E-15
1.79E-69	0	0	1.5E-234	3.2E-140	6.85E-46	4.23E-34	2.06E-16
8.45E-73	0	0	1.2E-245	7.1E-147	4.15E-48	9.19E-36	3.03E-17
2.73E-76	0	0	2.9E-257	7.5E-154	1.95E-50	1.65E-37	4.07E-18
5.9E-80	0	0	1.7E-269	3.5E-161	7.03E-53	2.43E-39	4.93E-19
8.2E-84	0	0	2.4E-282	6.7E-169	1.89E-55	2.86E-41	5.35E-20

Table B.5: Descriptive statistics for each plume variable in each experiment.

Experiment	Metric	vertical velocity ($m s^{-1}$)	plume radius (m)	plume area (m)	mass flux ($10^3 m^3 s^{-1}$)	vapor excess ($g kg^{-1}$)	temp excess ($^{\circ}C$)	temp max excess ($^{\circ}C$)	temp absmx excess ($^{\circ}C$)
CNTRL	avg	8.3	86.7	2.8	235.3	0.4	5.4	10.9	16.4
	min	0.7	51.3	0.9	6.9	-0.1	-1.8	0.9	0.9
	max	11.8	136.4	7.0	509.8	2.3	13.0	22.4	53.1

Experiment	Metric	vertical velocity ($m s^{-1}$)	plume radius (m)	plume area (m^2)	mass flux ($10^3 m^3 s^{-1}$)	vapor excess ($g kg^{-1}$)	temp excess ($^{\circ}C$)	temp max excess ($^{\circ}C$)	temp absmx excess ($^{\circ}C$)
	st. Dev.	2.9	25.9	1.7	130.0	0.5	4.3	6.5	13.0
	Range	11.1	85.1	6.0	502.9	2.4	14.8	21.5	52.2
	st. Err.	0.4	3.8	0.3	19.0	0.1	0.6	1.0	1.9
	Conf.	0.9	7.6	0.5	38.2	0.158	1.3	1.9	3.8
ext005 m	avg	10.6	78.4	2.3	239.4	0.6	9.4	24.1	24.3
	min	1.2	48.9	0.8	11.5	0.0	-2.1	0.6	0.6
	max	13.7	138.7	6.5	563.9	2.4	47.0	143.3	143.3
	st. Dev.	3.2	26.2	1.6	154.7	0.6	10.3	27.6	27.4
	Range	12.6	89.8	5.7	552.4	2.4	49.1	142.7	142.7
	st. Err.	0.5	3.8	0.2	22.6	0.1	1.5	4.0	4.0
	Conf.	0.9	7.7	0.5	45.4	0.178	3.0	8.1	8.1
ext010 m	avg	10.5	75.0	2.1	219.8	0.6	8.9	13.6	15.7
	min	1.1	47.1	0.8	11.1	0.0	-2.1	0.1	0.1
	max	13.8	126.0	6.2	633.8	2.3	35.7	48.8	66.0
	st. Dev.	3.3	27.9	1.7	158.9	0.6	9.0	11.1	14.9
	Range	12.7	78.8	5.4	622.7	2.3	37.8	48.7	65.9
	st. Err.	0.5	4.1	0.2	23.2	0.1	1.3	1.6	2.2
	Conf.	1.0	8.2	0.5	46.7	0.180	2.6	3.3	4.4
ext015 m	avg	11.0	76.8	2.2	227.9	0.7	12.1	57.4	57.7
	min	1.5	48.2	0.8	12.6	0.0	-2.2	0.2	0.2
	max	14.3	138.5	6.7	482.1	2.3	53.7	373.0	373.0
	st. Dev.	3.2	26.6	1.7	139.0	0.7	13.3	87.3	87.2
	Range	12.8	90.3	5.9	469.5	2.4	55.9	372.9	372.9
	st. Err.	0.5	3.9	0.2	20.3	0.1	1.9	12.7	12.7
	Conf.	0.9	7.8	0.5	40.8	0.196	3.9	25.6	25.6
ext025 m	avg	9.6	78.9	2.3	217.0	0.6	8.3	21.7	22.3
	min	1.1	47.8	0.8	7.8	-0.1	-1.9	0.6	0.6
	max	12.7	128.2	6.1	416.3	2.2	29.3	129.3	129.3
	st. Dev.	2.8	23.0	1.4	119.7	0.6	8.4	29.1	28.9
	Range	11.6	80.3	5.3	408.5	2.4	31.1	128.7	128.7
	st. Err.	0.4	3.4	0.2	17.5	0.1	1.2	4.2	4.2
	Conf.	0.8	6.8	0.4	35.1	0.180	2.5	8.5	8.5
ext075 m	avg	8.4	84.9	2.7	232.4	0.5	5.2	12.9	17.7
	min	0.6	52.9	1.0	6.3	-0.2	-2.3	0.6	0.6
	max	11.4	124.2	6.0	549.6	2.7	11.0	37.2	66.5
	st. Dev.	3.0	22.5	1.5	139.4	0.6	4.0	10.6	18.2
	Range	10.8	71.3	5.0	543.4	2.9	13.3	36.6	66.0
	st. Err.	0.4	3.3	0.2	20.3	0.1	0.6	1.5	2.7
	Conf.	0.9	6.6	0.4	40.9	0.180	1.2	3.1	5.3
ext100 m	avg	8.1	86.0	2.8	241.7	0.5	4.6	11.2	12.7

Experiment	Metric	vertical velocity ($m s^{-1}$)	plume radius (m)	plume area (m)	mass flux ($10^3 m^3 s^{-1}$)	vapor excess ($g kg^{-1}$)	temp excess ($^{\circ}C$)	temp max excess ($^{\circ}C$)	temp absmx excess ($^{\circ}C$)
	min	0.6	52.0	1.0	5.9	-0.2	-2.6	0.3	0.3
	max	11.2	144.0	7.3	566.2	2.7	9.6	22.5	22.5
	st. Dev.	2.9	27.9	1.9	164.9	0.7	3.4	7.1	7.5
	Range	10.6	92.0	6.4	560.3	2.9	12.1	22.2	22.2
	st. Err.	0.4	4.1	0.3	24.0	0.1	0.5	1.0	1.1
	Conf.	0.9	8.2	0.6	48.4	0.194	1.0	2.1	2.2
ext200 m	avg	8.0	86.8	2.8	241.0	0.4	4.1	16.0	23.4
	min	0.5	51.2	0.9	4.9	0.0	-1.6	0.9	0.9
	max	11.7	138.8	6.5	494.1	2.4	7.4	42.3	48.6
	st. Dev.	3.1	20.9	1.3	134.3	0.5	2.5	13.2	15.8
	Range	11.2	87.6	5.6	489.1	2.4	9.0	41.4	47.7
	st. Err.	0.5	3.0	0.2	19.6	0.1	0.4	1.9	2.3
	Conf.	0.9	6.1	0.4	39.4	0.156	0.7	3.9	4.6

Table B.6: Absolute values of the time-mean plume-averaged vertical profiles in CNTRL experiment.

height (m)	vertical velocity ($m s^{-1}$)	plume radius (m)	plume area (m)	mass flux ($10^3 m^3 s^{-1}$)	vapor excess ($g kg^{-1}$)	temp excess ($^{\circ}C$)	temp max excess ($^{\circ}C$)	temp absmx excess ($^{\circ}C$)
5.77	0.69	51.3	0.94	6.9	0.288	9.87	22.42	53.09
17.6	1.92	56.51	1.12	22.82	0.896	10.79	20.01	44.22
30.04	3.06	58.29	1.19	37.16	0.783	11.67	19.58	38.49
43.12	4	59.2	1.25	50.74	0.828	12.38	19.31	31.34
56.86	4.95	57.31	1.17	58.42	0.941	12.97	21.46	32.38
71.3	5.73	58.49	1.21	69.95	0.909	12.86	16.88	36.05
86.48	6.34	61.66	1.38	87.37	0.776	11.89	15.52	36.79
102.44	7.01	62.77	1.42	99.82	0.617	10.71	15.17	33.47
119.2	7.62	64.47	1.46	112.62	0.572	10.76	15.58	29.22
136.82	8.31	63.03	1.38	115.43	0.518	10.83	16.76	28.27
155.32	8.6	64.73	1.42	125.37	0.409	10.19	16.66	27.52
174.77	8.88	68.71	1.54	142.13	0.217	9.45	16.32	28.38
195.19	9.06	69.82	1.58	150.22	0.141	9.01	22.15	29.51
216.65	8.98	70.81	1.65	158.61	0.048	7.94	18.54	24.86
239.2	9.71	65.64	1.42	144.75	0.107	8.2	14.03	18.88
262.87	10.22	63.66	1.33	143.09	0.157	8.1	18.95	18.95
287.74	10.13	68.82	1.56	165.85	0.188	7.55	17.06	17.06
313.85	9.55	73.7	1.85	191.94	0.139	6.57	13.33	14.26
341.27	9.72	71.68	1.73	182.9	0.073	6.19	14.01	14.37
370.05	10.06	70.57	1.67	180.87	0.051	5.79	10.96	14.26
400.28	10.42	73.22	1.83	203.21	0.007	5.42	10.14	13.64
432	10.48	79.59	2.19	240.66	0.048	5.09	9.8	12.79
465.3	10.62	82.1	2.33	258.89	0.089	4.88	10.27	11.86

height (m)	vertical velocity(m s ⁻¹)	plume radius (m)	plume area (m)	mass flux (10 ³ m ³ s ⁻¹)	vapor excess (g kg ⁻¹)	temp excess (°C)	temp max excess (°C)	temp absmx excess (°C)
500.25	11.03	78.82	2.15	246.06	0.096	4.8	11	11.25
536.92	11.28	78.1	2.04	239.64	0.067	4.64	11.13	11.44
575.4	11.7	75.11	1.88	227.38	0.116	4.58	11.13	11.39
615.78	11.75	80.43	2.19	266.33	0.098	4.42	10.61	11.16
658.12	11.34	82.91	2.42	282.2	0.005	4.17	10.5	11.84
702.54	10.93	88.62	2.79	313.79	0.064	3.8	9.87	12.16
749.13	11.1	90.36	2.81	322.56	0.074	3.14	8.54	11.53
797.97	11.46	93.16	2.94	345.64	0.05	2.95	8.04	10.75
849.17	11.47	93.98	2.96	350.4	0.016	2.74	6.69	10.96
902.85	11.07	94.94	3.02	349.66	-0.081	2.3	5.46	9.75
959.09	10.81	95.04	3.08	344.13	0.124	2.13	5.43	7.28
1018.03	9.93	105.68	3.92	398.91	0.43	1.9	6.35	6.88
1079.77	9.23	107.39	4.19	395.05	0.394	1.73	6.63	6.63
1144.44	9.08	102.87	3.81	353.36	0.412	1.66	4.52	4.52
1212.16	8.46	128.12	5.6	488.62	0.388	1.41	3.04	3.7
1283.08	8.55	131.2	5.79	509.75	0.159	1.33	2.74	3.17
1357.31	8.62	122.09	4.96	443.73	0.165	1.27	2.61	3.03
1435.03	7.98	126.08	5.31	443.96	0.198	0.96	2.35	2.82
1516.41	7.88	123.38	5.02	400.67	0.479	0.64	2.53	2.53
1601.67	6.9	126.54	5.38	371.21	1.142	-0.19	1.12	1.29
1691.04	5.55	129.19	5.56	312.44	2.236	-1.38	0.89	0.89
1784.74	4.06	136.42	6.33	268.69	2.283	-1.84	1.68	1.68
1882.96	3.17	135.92	6.69	233.66	1.661	-1.56	1.63	1.63
1985.89	2.55	130.72	6.98	200.89	0.979	-0.99	1.35	1.54

Table B.7: Absolute values of the time-mean plume-averaged vertical profiles in ext005m experiment.

height (m)	vertical velocity(m s ⁻¹)	plume radius (m)	plume area (m)	mass flux (10 ³ m ³ s ⁻¹)	vapor excess (g kg ⁻¹)	temp excess (°C)	temp max excess (°C)	temp absmx excess (°C)
5.77	1.16	52.44	1	11.49	0.942	47.02	143.29	143.29
17.61	3.22	53.11	0.98	31.73	1.351	37.61	100.79	100.79
30.05	5.06	48.89	0.83	41.38	1.249	31.44	78.4	78.4
43.13	6.36	51.32	0.9	55.6	1.392	27.31	65.06	65.06
56.87	7.15	53.69	0.98	69.32	1.317	23.02	54.36	54.36
71.32	8.05	52.3	0.94	74.3	1.118	20.11	45.04	45.04
86.49	8.79	50.43	0.9	78.1	0.975	18.19	40.39	40.39
102.45	9.51	49.74	0.85	80.14	0.847	17.45	39.7	39.7
119.21	9.64	50.72	0.88	84.74	0.653	15.07	38.22	38.22
136.82	10.32	51.86	0.88	88.73	0.718	13.94	36.13	36.13
155.33	10.54	56.5	1.04	108.02	0.66	12.77	33.55	33.55
174.77	11.26	55.02	0.98	107.93	0.627	13.12	30.3	30.3
195.2	11.8	56.13	1.02	115.97	0.475	13.02	26.18	26.18

height (m)	vertical velocity(m s ⁻¹)	plume radius (m)	plume area (m)	mass flux (10 ³ m ³ s ⁻¹)	vapor excess (g kg ⁻¹)	temp excess (°C)	temp max excess (°C)	temp absmx excess (°C)
216.66	12.08	56.76	1.04	122.67	0.338	12.2	25.8	25.8
239.2	12.19	57.44	1.06	129.73	0.183	11.71	24.19	24.19
262.87	12.43	57.94	1.1	136.53	0.192	11	20.9	20.9
287.74	12.05	61.39	1.25	150.81	0.111	9.12	21.31	21.31
313.85	12.46	63.27	1.33	167.2	0.142	8.47	21.05	21.05
341.27	12.68	65.63	1.44	184.03	0.133	8.15	20.92	20.92
370.05	13.27	64.83	1.4	185.92	0.186	8.11	20.18	20.18
400.28	13.47	65	1.44	193.42	0.158	7.97	18.89	18.89
432	13.73	66.59	1.44	198.77	0.174	8.2	21.15	21.15
465.3	13.41	70.76	1.6	215.23	0.311	7.72	23.25	23.25
500.25	13.05	70.92	1.6	211.04	0.23	6.68	25.5	25.5
536.92	13.22	70.01	1.58	206.68	0.227	6.08	25.38	25.38
575.4	12.88	72.67	1.73	222.18	0.205	5.26	22.63	22.63
615.77	13.38	70.81	1.6	216.66	0.172	4.89	18.45	18.45
658.12	13.51	73.28	1.75	236.2	0.049	4.6	13.81	13.81
702.54	13.18	76.73	1.9	250.93	0.168	4.48	10.73	10.73
749.12	12.37	81.62	2.17	271.68	0.216	4.22	8.71	8.71
797.96	11.2	87.31	2.58	300.78	0.169	3.66	5.86	7.98
849.16	11.97	90.12	2.65	326.06	0.16	3.02	5.68	7.12
902.83	12.72	92.13	2.75	359.68	0.098	2.79	5.73	5.94
959.08	13.42	92.16	2.75	377.59	0.164	2.75	4.95	6.29
1018.01	13.48	90.47	2.69	371.97	0.484	2.96	6.49	6.66
1079.75	12.45	97.81	3.19	405.71	0.483	2.71	4.07	6.71
1144.42	11.96	100.01	3.33	402.74	0.442	2.36	3.68	4.22
1212.14	11.14	112.19	4.31	490.82	0.434	1.99	3.4	4.22
1283.05	11.76	114.5	4.54	540.74	0.261	1.86	3.23	4.19
1357.29	12.25	114.48	4.58	563.9	0.388	1.83	3.33	3.98
1435.01	12.27	112.75	4.35	532.02	0.479	1.68	3.24	3.63
1516.39	11.05	118.21	4.58	507.26	0.583	1.28	2.96	3.06
1601.66	10.04	120.45	4.81	485.81	1.236	0.38	1.44	1.95
1691.05	8.13	123.06	5.19	445.05	2.315	-1.04	0.88	0.89
1784.78	5.7	138.7	6.5	404.48	2.449	-1.96	0.62	0.62
1883.02	4.42	127.77	5.81	273.53	2.19	-2.12	0.72	0.72
1985.95	3.2	124.36	6.23	217.25	1.547	-1.63	1.58	1.58

Table B.8: Absolute values of the time-mean plume-averaged vertical profiles in ext010m experiment.

height (m)	vertical velocity(m s ⁻¹)	plume radius (m)	plume area (m)	mass flux (10 ³ m ³ s ⁻¹)	vapor excess (g kg ⁻¹)	temp excess (°C)	temp max excess (°C)	temp absmx excess (°C)
5.77	1.09	53.18	0.98	11.05	0.959	35.66	48.78	66.03
17.61	3.05	49.85	0.88	27.96	1.538	32.86	39.84	56.29
30.05	4.61	49.03	0.83	40.6	1.42	28.44	35.04	48.31

height (m)	vertical velocity(m s ⁻¹)	plume radius (m)	plume area (m)	mass flux (10 ³ m ³ s ⁻¹)	vapor excess (g kg ⁻¹)	temp excess (°C)	temp max excess (°C)	temp absmx excess (°C)
43.13	5.91	48.21	0.79	49	1.455	25.89	34.78	47.24
56.87	6.98	48.18	0.77	55.58	1.254	23.7	31.7	42.75
71.31	7.8	49.35	0.79	62.83	1.166	20.5	26.18	28.21
86.49	8.27	50.42	0.83	71	0.872	17.51	25.49	26.38
102.44	9.4	48.59	0.79	73.45	0.734	17.44	24.46	24.96
119.21	9.91	47.13	0.75	74.59	0.545	15.92	22.69	23.89
136.82	10.13	48.34	0.77	81.2	0.513	13.98	20.79	22.87
155.33	10.54	50.56	0.83	91.28	0.487	13.07	19.42	21.87
174.77	10.55	52.78	0.92	102.49	0.349	11.67	18.06	20.86
195.2	11.11	52.49	0.9	104.83	0.247	11.52	15.9	19.79
216.65	11.58	51.99	0.88	105.72	0.018	11.07	16.14	18.58
239.19	11.78	52.56	0.9	109.92	0.003	10.62	15.5	17.15
262.87	12.17	52.3	0.88	108.86	0.057	10.04	14.76	16.96
287.73	12.34	52.93	0.9	113.78	0.115	9.53	14.64	16.33
313.84	12.56	53.75	0.94	121.43	0.135	9.09	14.19	14.53
341.26	12.53	55.19	0.98	127.53	0.169	8.31	13.98	14.12
370.05	13.08	54.37	0.96	128.96	0.162	8.42	14.7	14.7
400.27	12.77	58.35	1.1	146.92	0.115	7.63	14.27	14.27
432	12.57	64.81	1.38	177.57	0.181	6.81	12.68	13.16
465.3	12.99	66.15	1.42	187.74	0.244	6.42	12.22	12.54
500.24	13.12	67.43	1.46	192.47	0.274	5.93	11.8	11.8
536.92	13.46	67.9	1.5	199.78	0.238	5.69	11.09	11.09
575.4	13.33	69.71	1.6	213.15	0.31	5.34	10.07	10.07
615.77	13.22	71.19	1.71	227.23	0.271	5.11	8.33	9.1
658.12	13.44	70.05	1.58	212.7	0.256	4.92	8.54	9.85
702.53	13.42	73.97	1.75	234.74	0.275	4.54	7.38	9.4
749.11	13.77	72.22	1.67	227.44	0.262	4.54	7.92	7.92
797.95	13.32	70.75	1.62	220.32	0.109	4.16	8.86	8.86
849.16	12.36	76.05	1.92	241.07	-0.003	3.71	8.13	8.13
902.83	11.86	84.15	2.29	278.98	0.103	3.04	6.34	6.86
959.07	11.91	91.3	2.73	327.57	0.218	2.64	4.92	5.42
1018.01	12.36	92.36	2.83	352.06	0.53	2.43	5.37	5.37
1079.75	12.61	96.55	3	376.77	0.519	2.45	4.88	5.11
1144.41	13.33	92.94	2.81	368	0.514	2.47	4.39	4.7
1212.13	12.74	109.76	3.98	504.23	0.449	2.29	4.14	4.14
1283.05	12.87	118.32	4.69	592.2	0.221	2.14	4.16	4.16
1357.29	12.56	123.01	5.08	633.75	0.306	2.21	4.14	4.14
1435.01	11.46	119.87	4.69	547.99	0.461	1.94	3.98	4.58
1516.39	9.78	121.8	4.83	491.55	0.517	1.41	2.59	3.09
1601.64	8.17	125.96	5.25	450.6	1.192	0.3	1.18	1.62
1691.03	7.09	124.6	5.31	390.88	2.272	-1.08	0.88	0.88
1784.75	5.45	125.18	5.65	346.52	2.139	-1.57	0.57	0.57
1882.99	4.71	123.11	5.65	294.14	2.262	-2.12	0.12	0.12

height (m)	vertical velocity(m s ⁻¹)	plume radius (m)	plume area (m)	mass flux (10 ³ m ³ s ⁻¹)	vapor excess (g kg ⁻¹)	temp excess (°C)	temp max excess (°C)	temp absmx excess (°C)
1985.92	3.2	125.48	6.17	231.77	1.639	-1.67	1.25	1.25

Table B.9: Absolute values of the time-mean plume-averaged vertical profiles in ext015m experiment.

height (m)	vertical velocity(m s ⁻¹)	plume radius (m)	plume area (m)	mass flux (10 ³ m ³ s ⁻¹)	vapor excess (g kg ⁻¹)	temp excess (°C)	temp max excess (°C)	temp absmx excess (°C)
5.77	1.5	56.25	1.06	12.56	1.301	53.71	373.01	373.01
17.6	3.94	54.22	1	33.55	1.887	45.14	305.58	305.58
30.05	5.3	52.74	0.98	47.34	1.603	34.73	253.31	253.31
43.13	6.78	53.92	1.02	63.29	1.696	31.79	219.23	219.23
56.87	8.02	51.9	0.94	69.52	1.6	28.77	189.42	189.42
71.32	10.24	52.06	0.92	82.79	1.735	32.35	171.84	171.84
86.5	11.73	50.57	0.88	90.47	1.678	32.46	155.62	155.62
102.45	12.17	49.7	0.83	90.21	1.424	29.36	133.54	133.54
119.21	11.14	48.19	0.81	85.75	0.973	21.5	115.88	115.88
136.83	13.24	50.06	0.83	97.94	1.341	29.45	101.23	101.23
155.33	12.26	52.26	0.9	102.45	1.002	22.53	90.15	90.15
174.78	12.03	55.8	1	114.22	0.871	20.69	73.21	73.21
195.2	11.91	56.74	1.04	120.31	0.652	18.61	63.06	63.06
216.66	12.04	51.59	0.88	103.16	0.387	14.42	48.72	48.72
239.2	12.21	56.81	1.04	124.6	0.319	13.3	45.62	45.62
262.88	12.72	58.1	1.08	135.51	0.384	13.12	42.64	42.64
287.74	13.66	57.07	1.06	139.34	0.372	13.21	36.06	36.06
313.85	13.39	56.65	1.06	139.65	0.29	11.28	32.32	32.32
341.27	12.9	59.43	1.17	151.16	0.177	9.57	29.73	29.73
370.06	13.56	55.71	1.04	142.24	0.17	9.13	25.69	25.69
400.28	13.72	60.43	1.21	167.93	0.182	8.38	22.32	22.32
432.01	14.18	60.83	1.25	179.37	0.253	8.14	19.69	19.69
465.31	14.27	60.05	1.23	177.43	0.37	8.41	19.74	19.74
500.25	13.24	64.09	1.38	186.63	0.391	7.57	16.58	16.58
536.93	12.1	68.4	1.56	198.53	0.205	5.81	10.01	10.12
575.4	11.62	74.22	1.83	221.13	0.194	5.15	9.14	9.45
615.77	12.14	73.57	1.77	224.1	0.151	4.95	9.29	10.74
658.12	12.47	79.84	2.06	260.73	0.116	4.51	10.09	10.09
702.54	12.9	81.07	2.15	280.39	0.169	4.44	8.43	8.43
749.11	12.63	83.46	2.31	301.45	0.141	3.84	6.65	6.88
797.95	12.45	85.61	2.42	309.05	0.164	3.58	6.2	7.13
849.16	12.99	82.93	2.21	292.5	0.22	3.43	6.16	7.43
902.83	12.13	91.71	2.85	362.13	-0.016	2.84	4.76	6.61
959.07	12.59	92.88	2.81	367.34	0.073	2.71	4.43	6.23
1018.01	13.12	95.71	2.98	401.53	0.444	2.78	5.41	5.51

height (m)	vertical velocity(m s ⁻¹)	plume radius (m)	plume area (m)	mass flux (10 ³ m ³ s ⁻¹)	vapor excess (g kg ⁻¹)	temp excess (°C)	temp max excess (°C)	temp absmx excess (°C)
1079.74	13.34	91.02	2.75	379.92	0.526	2.72	4.95	5.42
1144.41	13.22	98.71	3.17	423.93	0.48	2.6	3.83	4.93
1212.13	12.76	100.99	3.35	429.54	0.473	2.48	4.49	5.17
1283.04	12.86	95.83	3.04	395.2	0.237	2.48	4.56	4.98
1357.28	11.93	106.38	3.73	456.26	0.302	1.98	4.43	4.57
1435	10.37	118.32	4.58	482.09	0.37	1.63	4.41	4.46
1516.38	9.69	120.64	4.88	472.35	0.538	1.3	4.11	4.11
1601.64	8.45	124.51	5.23	434.56	1.169	0.14	1.21	1.95
1691.03	6.6	123.7	5.48	375.59	1.964	-0.91	0.96	0.96
1784.76	5.98	129.62	6.23	397.61	2.261	-1.66	0.63	0.63
1883	5.08	138.49	6.69	373.52	2.342	-2.21	0.16	0.16
1985.92	2.77	128.58	6.46	213.98	1.386	-1.44	1.1	1.1

Table B.10: Absolute values of the time-mean plume-averaged vertical profiles in ext025m experiment.

height (m)	vertical velocity(m s ⁻¹)	plume radius (m)	plume area (m)	mass flux (10 ³ m ³ s ⁻¹)	vapor excess (g kg ⁻¹)	temp excess (°C)	temp max excess (°C)	temp absmx excess (°C)
5.77	1.05	47.82	0.81	7.8	1.062	29.25	129.27	129.27
17.6	2.9	48.91	0.85	23.11	1.531	27.59	109.85	109.85
30.05	4.29	52.24	0.96	39.28	1.271	24.77	86.9	86.9
43.12	5.92	54.23	1	53.87	1.332	24.29	74.1	74.1
56.87	6.92	52.48	0.96	62.22	1.254	22.66	64.18	64.18
71.31	7.81	55.02	1.04	76.2	1.108	20.95	54.5	54.5
86.49	8.69	53.97	1	82.16	1.015	19.9	45.71	45.71
102.45	9.42	54.8	1.04	92.54	0.868	18.92	40.47	40.47
119.21	9.96	56.52	1.08	101.18	0.827	18.07	39.2	39.2
136.82	10.33	54.83	1.02	100.26	0.74	16.6	34.75	34.75
155.33	10.34	55.04	1.02	104.02	0.603	14.99	38.22	38.22
174.77	10.35	57.58	1.12	115.85	0.519	13.9	39.33	39.33
195.2	10.09	60.68	1.25	127.33	0.279	11.08	21.36	21.36
216.66	10.07	64.7	1.38	141.28	0.154	9.58	17.8	17.8
239.2	10.43	62.39	1.29	137.45	0.059	9.06	14.71	15.6
262.87	10.51	61.82	1.27	137.53	0.016	8.23	13.47	14.02
287.74	10.96	59.57	1.19	132.9	0.04	7.94	12.56	14.09
313.85	10.92	63.21	1.33	149.63	-0.079	7.2	11.62	14.09
341.26	10.82	66.58	1.48	164.28	-0.109	6.55	10.41	13.6
370.05	10.73	68.88	1.58	175.74	-0.122	6.19	9.72	12.79
400.27	10.66	70.82	1.69	186.47	0.006	5.89	9.84	11.86
432	10.57	75.91	1.98	214.91	0.111	5.66	9.4	11.12
465.3	10.97	78.39	2.04	229.88	0.178	5.34	8.38	10.83
500.24	11.69	77.13	1.96	231.42	0.218	5.08	9.64	10.78
536.91	12.1	77.72	1.98	241.83	0.168	4.87	9.81	10.56

height (m)	vertical velocity(m s ⁻¹)	plume radius (m)	plume area (m)	mass flux (10 ³ m ³ s ⁻¹)	vapor excess (g kg ⁻¹)	temp excess (°C)	temp max excess (°C)	temp absmx excess (°C)
575.39	12.27	76.12	1.94	243.21	0.113	4.57	9.44	9.91
615.76	12.45	73.32	1.81	230.23	0.138	4.35	8.24	9.79
658.11	12.67	72.5	1.73	222.12	0.116	4.55	8.61	9.71
702.53	12.1	76.74	1.94	235.07	0.237	4.13	7.93	8.31
749.11	11.72	81.28	2.21	255.83	0.252	3.83	7.03	8.23
797.95	11.43	89.87	2.62	296.59	0.131	3.29	6.77	7.46
849.15	11.87	90.41	2.67	312.95	0.058	3.12	6.73	6.89
902.82	11.27	94.17	2.92	330.42	-0.008	2.8	5.56	6.39
959.06	11.03	95.63	3.04	336.57	0.127	2.48	5.41	6.31
1018	11.27	98.74	3.21	363.44	0.455	2.33	5.65	5.78
1079.73	11.6	96.37	3.04	349.81	0.474	2.31	5.8	5.8
1144.4	11.68	98.05	3.1	350.09	0.505	2.39	4.97	4.97
1212.12	11.53	100.24	3.38	384.06	0.49	2.31	4.38	4.38
1283.03	11.75	103.15	3.48	407.68	0.314	2.24	4.13	4.13
1357.27	11.25	105.83	3.65	416.28	0.303	1.95	3.55	3.55
1434.99	9.48	111.5	4.12	411.66	0.368	1.43	3.24	3.29
1516.37	9.67	112.52	4.08	406.34	0.399	1.35	2.96	3.02
1601.62	9.34	111.95	4.25	380.08	1.076	0.57	1.84	1.95
1690.99	7.07	120.1	5.23	378.28	2.045	-0.76	0.93	0.93
1784.7	5.5	122.2	5.75	324	2.238	-1.64	0.6	0.6
1882.95	4.23	128.16	6.08	258.81	2.035	-1.86	1.3	1.3
1985.88	3.08	118.14	5.69	174.4	1.57	-1.62	0.84	0.84

Table B.11: Absolute values of the time-mean plume-averaged vertical profiles in ext075m experiment.

height (m)	vertical velocity(m s ⁻¹)	plume radius (m)	plume area (m)	mass flux (10 ³ m ³ s ⁻¹)	vapor excess (g kg ⁻¹)	temp excess (°C)	temp max excess (°C)	temp absmx excess (°C)
5.77	0.64	52.9	0.96	6.25	0.632	8.41	12.5	28.72
17.6	1.84	53.4	0.98	18.03	0.906	9.59	14.93	36.81
30.04	2.66	57.13	1.19	32	0.775	9.93	17.36	43.77
43.11	3.57	57.59	1.21	43.32	0.805	10.7	22.61	51.73
56.86	4.35	56.77	1.19	52.12	0.86	10.74	24.74	57.78
71.3	5.06	60.31	1.31	66.1	0.828	10.91	26.56	63.6
86.48	5.69	64.24	1.46	82.25	0.81	11.02	37.2	66.53
102.43	6.17	67.54	1.6	98.87	0.692	10.57	31.87	56.43
119.2	6.63	69.41	1.73	113.39	0.655	10.23	35.83	35.83
136.81	7.4	66.32	1.54	112.48	0.648	10.18	26.68	26.68
155.32	7.82	70.56	1.71	131.56	0.465	9.5	25.94	25.94
174.76	8.34	68.43	1.6	132.89	0.347	9.42	25.55	25.55
195.19	8.76	69.05	1.62	141.19	0.188	9.19	25.18	25.18
216.65	9.42	67.33	1.54	141.71	0.205	9.12	25.44	25.44
239.19	9.85	69.56	1.62	155.24	0.216	9.04	26.47	26.47

height (m)	vertical velocity(m s ⁻¹)	plume radius (m)	plume area (m)	mass flux (10 ³ m ³ s ⁻¹)	vapor excess (g kg ⁻¹)	temp excess (°C)	temp max excess (°C)	temp absmx excess (°C)
262.87	9.97	71.03	1.71	167.48	0.184	8.13	26.44	26.44
287.73	10.2	73.74	1.85	184.21	0.22	7.78	22.18	22.18
313.84	10.27	74.31	1.92	193.6	0.074	7.06	16.62	16.62
341.26	10.72	70.54	1.71	182.66	0.062	6.72	15.89	15.89
370.05	10.87	70.69	1.71	185.9	0.018	6.33	14.1	14.1
400.27	11.1	73.37	1.81	202.56	0.124	6.04	11.78	11.78
432	11.07	74.26	1.81	204.33	0.218	5.61	9.63	9.63
465.3	10.73	77.53	2.02	224.55	0.217	4.99	8.41	9.61
500.25	10.5	78.82	2.12	235.58	0.14	4.71	8.89	9.52
536.92	10.24	80.6	2.29	249.71	0.025	4.14	8.98	8.98
575.4	10.6	79.13	2.21	246.83	0	3.86	7.81	7.81
615.77	10.81	81.65	2.35	265.81	0.017	3.63	6.37	7.5
658.12	10.77	85.89	2.54	286.05	0.045	3.36	5.53	7.27
702.54	10.73	86.04	2.58	289.62	0.131	3.04	6.38	6.98
749.12	11.31	79.59	2.27	264.17	0.079	3.02	6.66	6.66
797.96	11.39	82.59	2.42	282.01	-0.047	2.89	7.03	7.03
849.16	11.3	89.23	2.62	304.31	-0.081	2.76	7.04	7.04
902.84	10.97	93.15	2.96	334.71	-0.159	2.3	5.68	5.68
959.08	10.8	96.9	3.1	350.14	0.019	2.17	5.55	5.55
1018.02	10.97	97.94	3.1	354.53	0.418	2.08	3.55	4.18
1079.76	10.67	99.91	3.27	365.72	0.435	1.98	3.27	3.81
1144.42	10.28	109.19	3.94	425.5	0.361	1.86	3.14	3.99
1212.15	9.9	123.3	5.35	549.64	0.371	1.61	2.76	3.11
1283.06	9.96	121.36	5.12	526.3	0.224	1.55	2.82	2.96
1357.3	9.69	120.65	5.12	512.47	0.221	1.44	2.59	2.85
1435.02	9.52	123.25	5.1	495.15	0.336	1.31	2.43	2.43
1516.4	8.77	124.16	5.1	452.84	0.667	0.97	1.9	1.9
1601.66	7.56	121.27	4.83	368.94	1.31	-0.05	0.95	0.95
1691.03	6.23	121.56	5.06	327.86	2.443	-1.56	0.93	0.93
1784.73	5.13	116.06	4.81	251.94	2.712	-2.3	0.58	0.58
1882.95	3.27	119.16	5.21	183.04	2.184	-2.19	1.84	1.84
1985.87	1.95	121.64	6	128.84	0.902	-0.9	1.54	1.54

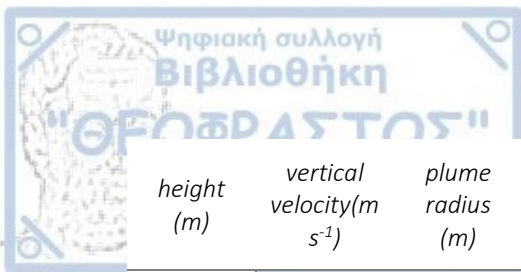
Table B.12: Absolute values of the time-mean plume-averaged vertical profiles in ext100m experiment.

height (m)	vertical velocity(m s ⁻¹)	plume radius (m)	plume area (m)	mass flux (10 ³ m ³ s ⁻¹)	vapor excess (g kg ⁻¹)	temp excess (°C)	temp max excess (°C)	temp absmx excess (°C)
5.77	0.6	53.18	1	5.88	0.257	6.38	20.31	20.31
17.6	1.68	51.96	0.96	15.87	0.789	7.67	21.61	21.61
30.04	2.59	54.13	1.04	26.04	0.768	9.48	21.63	21.63
43.11	3.3	54.72	1.06	34.46	0.798	9.57	14.82	20.48
56.86	3.92	54.26	1.06	41.7	0.835	9.45	16.6	20.27

height (m)	vertical velocity(m s ⁻¹)	plume radius (m)	plume area (m)	mass flux (10 ³ m ³ s ⁻¹)	vapor excess (g kg ⁻¹)	temp excess (°C)	temp max excess (°C)	temp absmx excess (°C)
71.3	4.59	58.18	1.21	55.18	0.801	9.51	17.53	19.69
86.48	5.28	58.88	1.23	64.09	0.711	9.5	18.06	18.86
102.43	5.93	60.45	1.27	74.5	0.73	9.45	18.42	18.42
119.2	6.43	60.96	1.31	84.45	0.594	8.89	20.12	20.12
136.81	6.92	60.9	1.31	91.54	0.547	8.78	21.74	21.74
155.32	7.47	61.65	1.31	98.19	0.518	8.33	22.5	22.5
174.76	7.72	64.35	1.42	110.96	0.387	8.11	22.24	22.24
195.19	8.16	63.18	1.38	113.22	0.243	7.76	20.92	20.92
216.65	8.51	63.61	1.35	116.61	0.152	7.79	18.67	18.67
239.19	8.73	62.54	1.31	118.1	0.104	7.3	15.72	16.38
262.87	8.94	68.56	1.56	143.85	0.04	6.78	17.75	17.75
287.73	9.22	73.25	1.75	167.04	0.089	6.51	18.72	18.72
313.84	9.2	75.57	1.9	184.28	0.03	5.94	11.06	18.47
341.26	9.45	76.27	1.92	192.41	0.022	5.78	11.19	17.16
370.05	9.72	74.36	1.81	187.58	-0.048	5.39	12.11	17.88
400.28	10.24	71.35	1.69	179.78	-0.015	5.36	12.9	17.91
432.01	10.26	72.51	1.79	191.75	0.066	4.85	11.68	17.23
465.31	10.16	76.1	2	213.97	0.107	4.52	11.1	16.86
500.26	10.41	77.01	2	218.9	0.074	4.27	10.18	16.36
536.93	10.53	74.9	1.9	212.38	-0.044	4.22	14.47	14.86
575.41	10.25	76.65	2.02	223.4	-0.054	3.82	11.1	12.49
615.78	10.07	78.99	2.17	235.54	-0.041	3.5	7.37	12.22
658.13	10.31	77.89	2.15	235.43	0.005	3.5	6.85	10.62
702.55	10.38	81.06	2.38	259.94	0.06	3.2	6.34	8.79
749.13	10.93	82.35	2.38	267.85	0.05	3.3	7.87	8.17
797.97	10.95	91.18	2.83	314.62	-0.063	3.05	8.65	8.65
849.17	11	97.4	3.17	352.46	-0.119	2.79	7.54	7.54
902.85	11.17	94.56	3.04	343.53	-0.172	2.65	7.07	7.07
959.09	11.2	100.6	3.42	383.87	0.034	2.53	5.79	5.79
1018.03	11.08	106.41	3.85	427.09	0.4	2.25	5.72	5.72
1079.77	10.95	112.84	4.4	476.75	0.465	2.09	5.83	5.83
1144.44	10.67	120.85	5.17	544.7	0.462	2	5.39	5.39
1212.17	10.58	123.6	5.38	566.18	0.447	1.83	4.15	5.21
1283.08	10.59	119.22	4.92	521.59	0.295	1.86	3.07	4.49
1357.33	9.83	112.99	4.48	443.49	0.326	1.83	3.24	3.76
1435.05	8.68	124.04	5.25	458.45	0.408	1.44	2.84	2.84
1516.43	7.65	138.69	7.04	558.01	0.709	0.73	1.74	1.91
1601.7	7.1	143.95	7.31	554.29	1.408	-0.34	0.89	0.89
1691.08	6.2	138.63	6.5	443.48	2.458	-1.73	0.82	0.82
1784.77	5.22	133.3	6.12	351.75	2.705	-2.38	0.54	0.54
1882.98	4.11	130.57	5.77	260.71	2.508	-2.57	0.28	0.28
1985.91	2.51	132.18	6.98	195.91	1.261	-1.32	1.53	1.53

Table B.13: Absolute values of the time-mean plume-averaged vertical profiles in ext200m experiment.

height (m)	vertical velocity(m s ⁻¹)	plume radius (m)	plume area (m ²)	mass flux (10 ³ m ³ s ⁻¹)	vapor excess (g kg ⁻¹)	temp excess (°C)	temp max excess (°C)	temp absmx excess (°C)
5.77	0.49	54.45	1.02	4.94	-0.021	4.28	17.39	29.26
17.6	1.4	51.69	0.92	12.85	0.386	5.62	23.65	33.91
30.04	2.17	51.17	0.9	19.5	0.374	6.73	28.12	37.83
43.11	2.67	54.95	1.1	29.54	0.581	7.05	30.96	41.19
56.85	3.18	58.91	1.29	40.75	0.579	7.18	33.22	44.01
71.29	3.75	58.26	1.31	48.98	0.606	7.36	35.32	46.22
86.47	4.32	58.99	1.33	56.97	0.593	7.26	37.39	47.79
102.42	4.74	65.44	1.56	73.05	0.543	7.17	39.41	48.51
119.18	5.17	68.44	1.71	87.57	0.411	7.04	41.32	48.61
136.8	5.69	70.56	1.75	99.17	0.414	7.11	42.29	48.3
155.3	6.22	70.39	1.73	106.48	0.406	7.19	42.1	48.13
174.74	6.68	73.52	1.94	128	0.335	7.19	41.83	47.61
195.17	6.94	75.42	2.06	143.65	0.216	6.82	39.13	45.22
216.63	7.17	77.78	2.17	158.17	0.118	6.26	27.16	48.13
239.17	7.43	78.23	2.17	164.12	0.019	5.89	24.85	43.37
262.84	7.73	78.66	2.17	172.43	0.041	5.5	12.35	32.22
287.71	8.12	82.76	2.33	196.18	0.075	5.65	13.59	27.41
313.82	8.67	83.19	2.35	207.78	0.084	5.62	12.74	24.42
341.24	9.09	81.43	2.29	211.89	0.102	5.54	10.4	21.78
370.03	9.43	81.6	2.31	221.78	0.113	5.3	10.37	20.03
400.25	9.73	83.32	2.4	236.52	0.135	5.06	9.58	19.15
431.98	9.94	85.34	2.52	254.99	0.204	4.87	9.17	18.73
465.28	10.11	86.67	2.62	270.29	0.255	4.71	8.89	18.49
500.23	10.3	86.57	2.62	277.43	0.25	4.52	8.88	18.18
536.9	10.49	85.45	2.6	281.39	0.194	4.39	7.97	17.69
575.39	10.63	87.24	2.67	291.01	0.217	4.19	8.73	16.94
615.76	11.05	83.75	2.42	272.39	0.131	4.13	9.43	16.04
658.11	11.23	86.35	2.5	285.22	0.103	4.11	9.94	15.77
702.53	11.21	87.85	2.62	301.34	0.066	3.87	10.45	15.47
749.11	11.21	90.09	2.81	326.01	-0.019	3.71	10.79	15.44
797.95	11.31	91.35	2.9	339.15	-0.03	3.49	8.48	15.69
849.16	11.17	91.18	2.81	326.84	-0.003	3.24	6.9	15.84
902.83	10.52	92.87	2.88	318.95	0.044	2.73	5.97	15.35
959.07	10.48	94.45	3	323.73	0.102	2.53	7.11	14.82
1018.01	8.64	105.16	4	379.32	0.546	1.67	8.93	14.57
1079.74	10.87	99.45	3.31	373.67	0.405	2.15	6.25	11.52
1144.41	11.68	98.76	3.21	382.45	0.542	2.32	7.89	10.04
1212.12	11.54	95.93	3.04	357.58	0.6	2.31	5.94	9.69
1283.03	9.67	104.71	3.67	379.02	0.324	1.75	8.26	8.26
1357.27	10.03	103.41	3.54	373.82	0.265	1.76	7.15	7.22
1434.97	9.43	112.55	4.19	419.9	0.288	1.47	5.72	6.1



<i>height (m)</i>	<i>vertical velocity(m s⁻¹)</i>	<i>plume radius (m)</i>	<i>plume area (m)</i>	<i>mass flux (10³ m³s⁻¹)</i>	<i>vapor excess (g kg⁻¹)</i>	<i>temp excess (°C)</i>	<i>temp max excess (°C)</i>	<i>temp absmx excess (°C)</i>
1516.33	9.48	119.28	4.79	465.39	0.629	1.12	5.74	5.74
1601.57	9.33	123.54	5.17	494.07	1.404	0.4	5.2	5.2
1690.94	8.45	121.09	5.02	432.07	2.355	-0.87	1.85	2.49
1784.68	6.03	138.79	6.5	428.33	1.997	-1.23	1.56	1.56
1882.94	5.31	125.69	5.56	327.4	1.945	-1.64	1.23	1.23
1985.87	3.13	121.12	6.4	226.16	1.291	-1.24	0.9	0.9

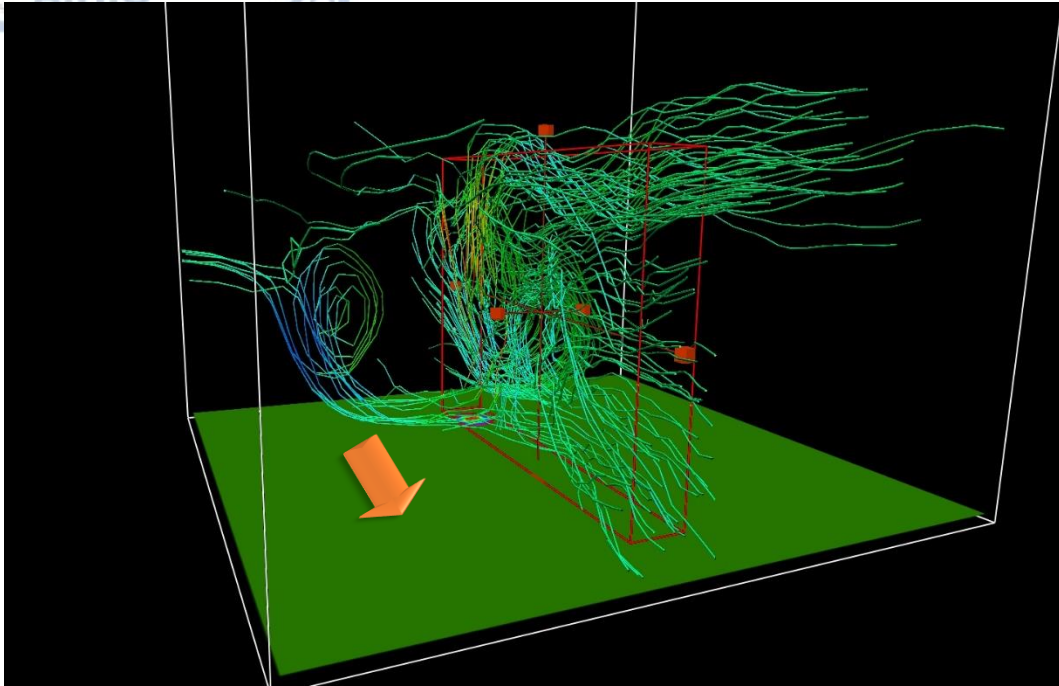


Fig. B.1: Streamlines at 60 min since ignition, for the CNTRL experiment. At surface, the fire area is shown with different colors according to the remaining fuel. The green color corresponds to unignited fuel. Red box indicates the volume of interaction. The orange arrow indicates the ambient wind (westerlies). Created in VAPOR using 60 random seeds (flow type steady).

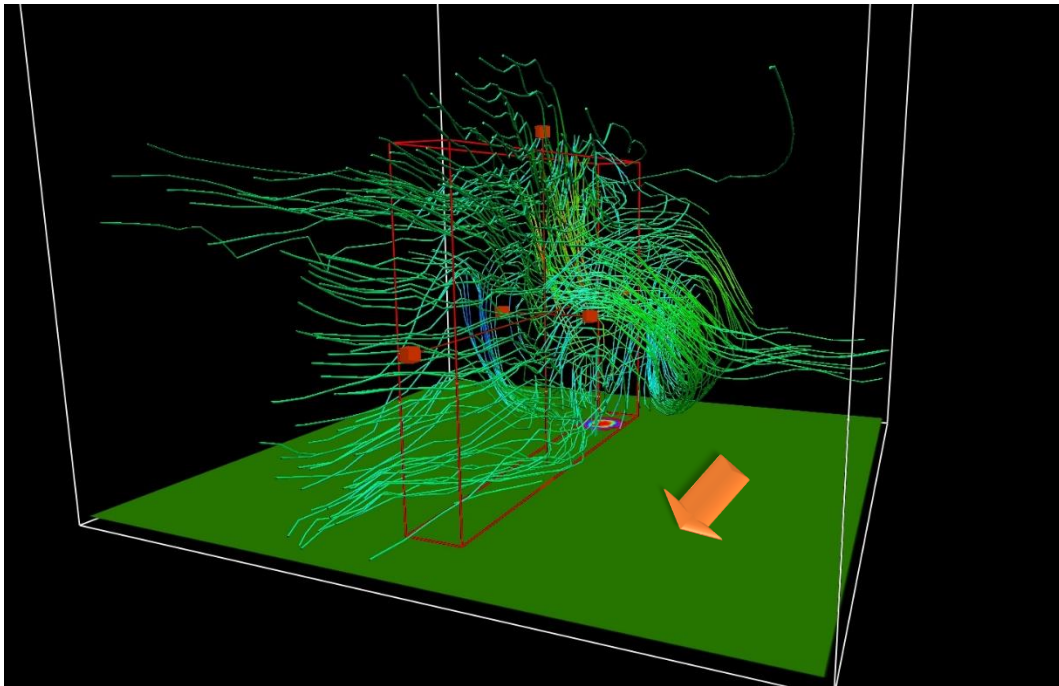


Fig. B.2: Streamlines at 60 min since ignition, for the CNTRL experiment. At surface, the fire area is shown with different colors according to the remaining fuel. The green color corresponds to unignited fuel. Red box indicates the volume of interaction. The orange arrow indicates the ambient wind (westerlies). Created in VAPOR using 60 random seeds (flow type steady).

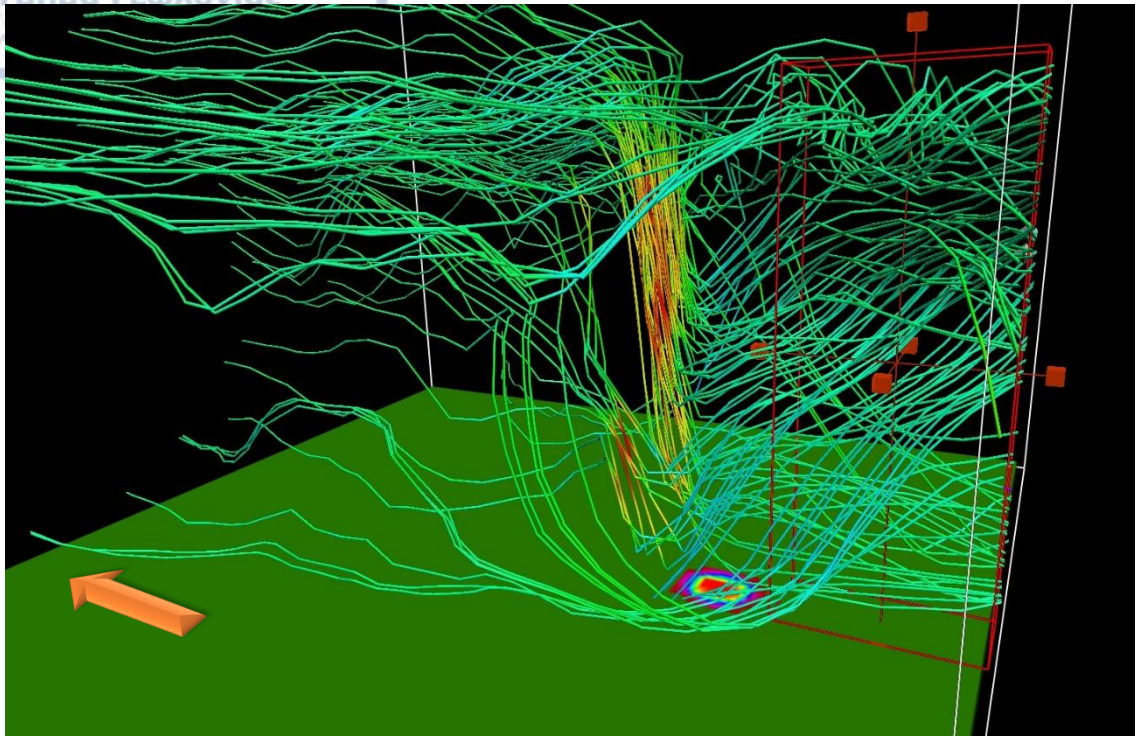


Fig. B.3: Streamlines at 60 min since ignition, for the CNTRL experiment. At surface, the fire area is shown with different colors according to the remaining fuel. The green color corresponds to unignited fuel. Red box indicates the volume of interaction. The orange arrow indicates the ambient wind (westerlies). Created in VAPOR using 60 random seeds (flow type steady).

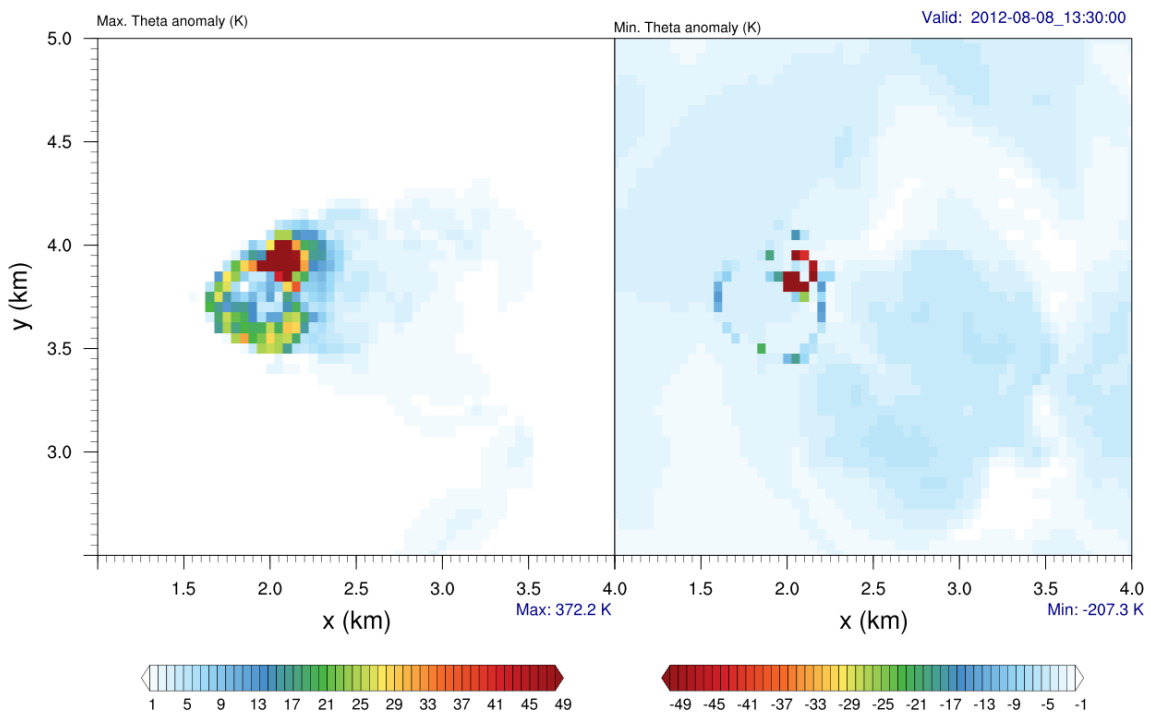


Fig. B.4: Maximum (left) and minimum (right) potential temperature anomaly (K, shaded contours) in every grid cell column, at 60 min since ignition, in ext015m experiment. The panel plot depicts only a subarea of the original domain.

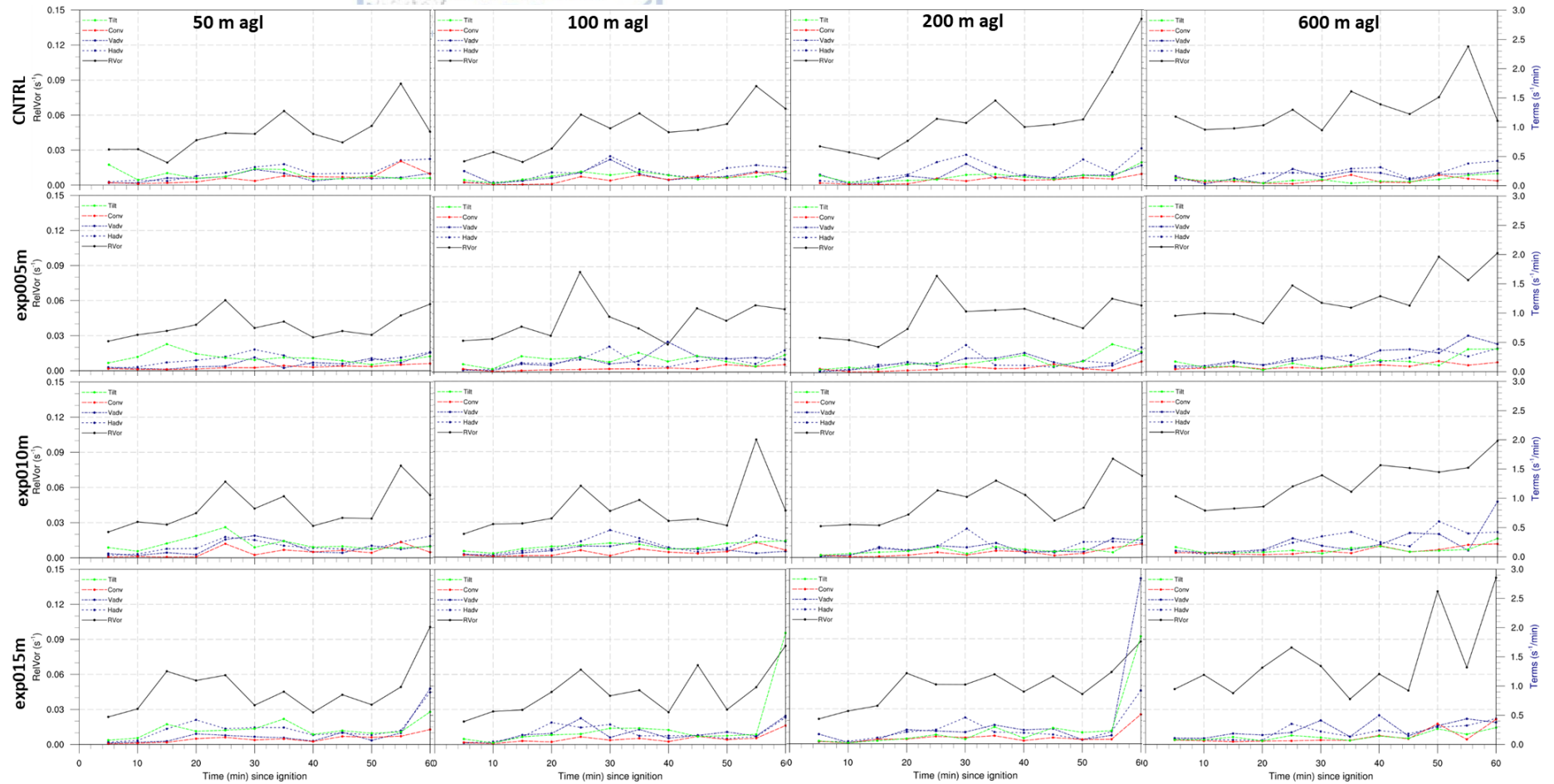


Fig. B.5: Maximum relative vorticity (s^{-1}) and vorticity equation terms ($s^{-1} m^{-1}$) of horizontal (Hadv) and vertical (Vadv) advection, convergence (Conv) and tilting/twisting (Tilt) as a function of time since fire flaming, for CNTRL, exp005m, exp010m and exp015m experiments, in a box of 1.5 km x 1.5 km over the fire area (1.5 km to 3 km west-east, 3 km to 4.5 km south-north), at 50, 100, 200 and 600 m agl, respectively.

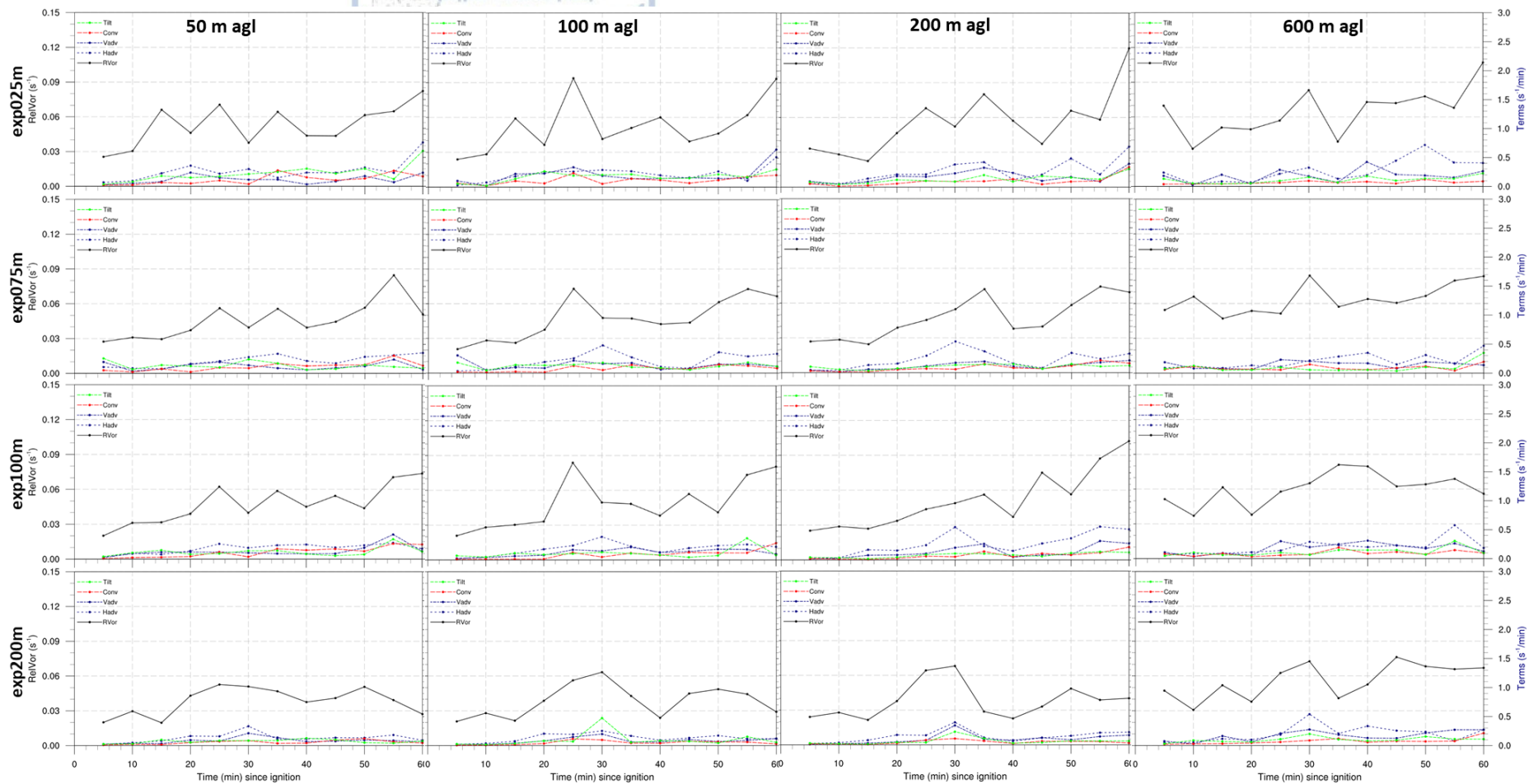


Fig. B.6: Maximum relative vorticity (s^{-1}) and vorticity equation terms ($s^{-1} m^{-1}$) of horizontal (Hadv) and vertical (Vadv) advection, convergence (Conv) and tilting/twisting (Tilt) as a function of time since fire flaming, for exp025m, exp075m, exp100m and exp200m experiments, in a box of 1.5 km x 1.5 km over the fire area (1.5 km to 3 km west-east, 3 km to 4.5 km south-north), at 50, 100, 200 and 600 m agl, respectively.



Appendix III

Figures

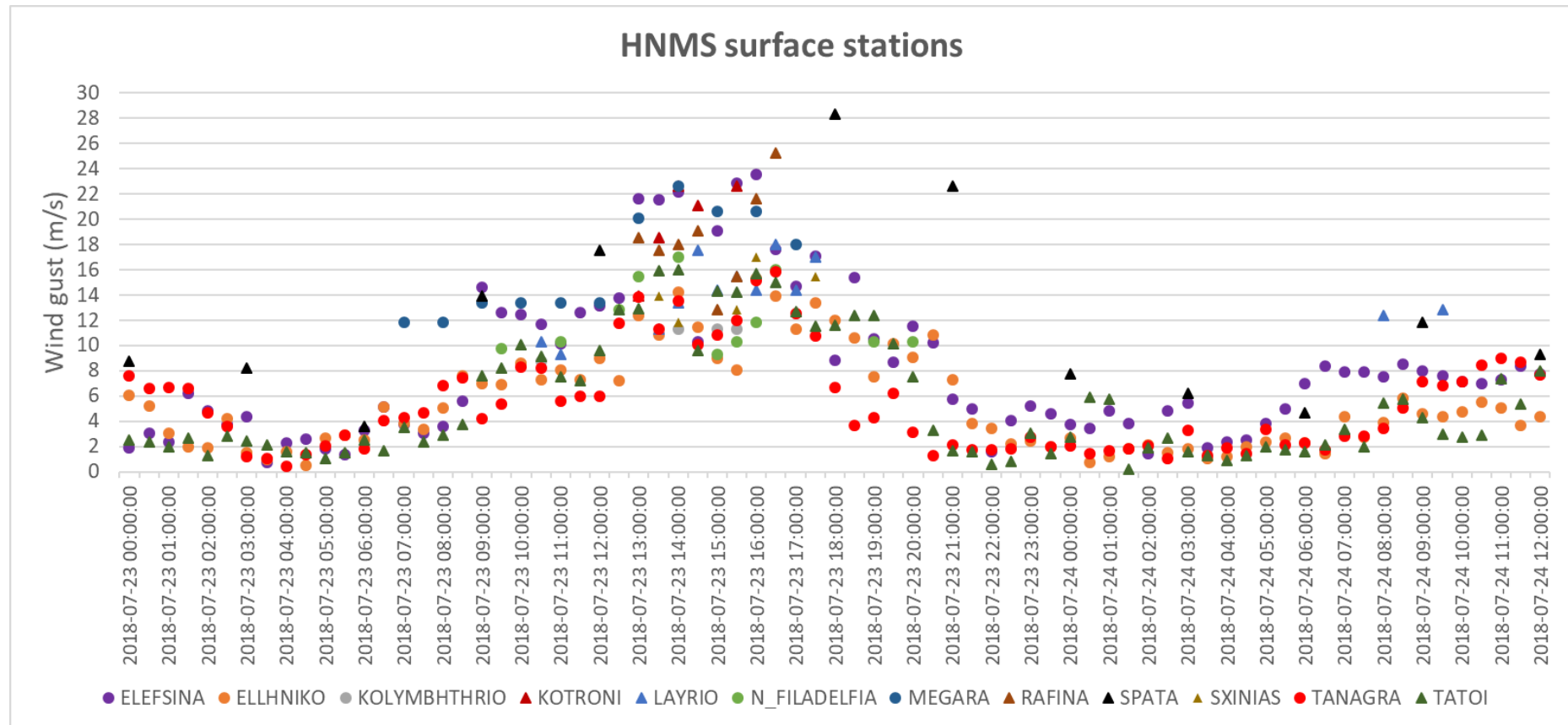


Fig. C.1: Time series of the recorded wind gusts ($m s^{-1}$) from all available HNMS stations, on 23rd of July 2018.

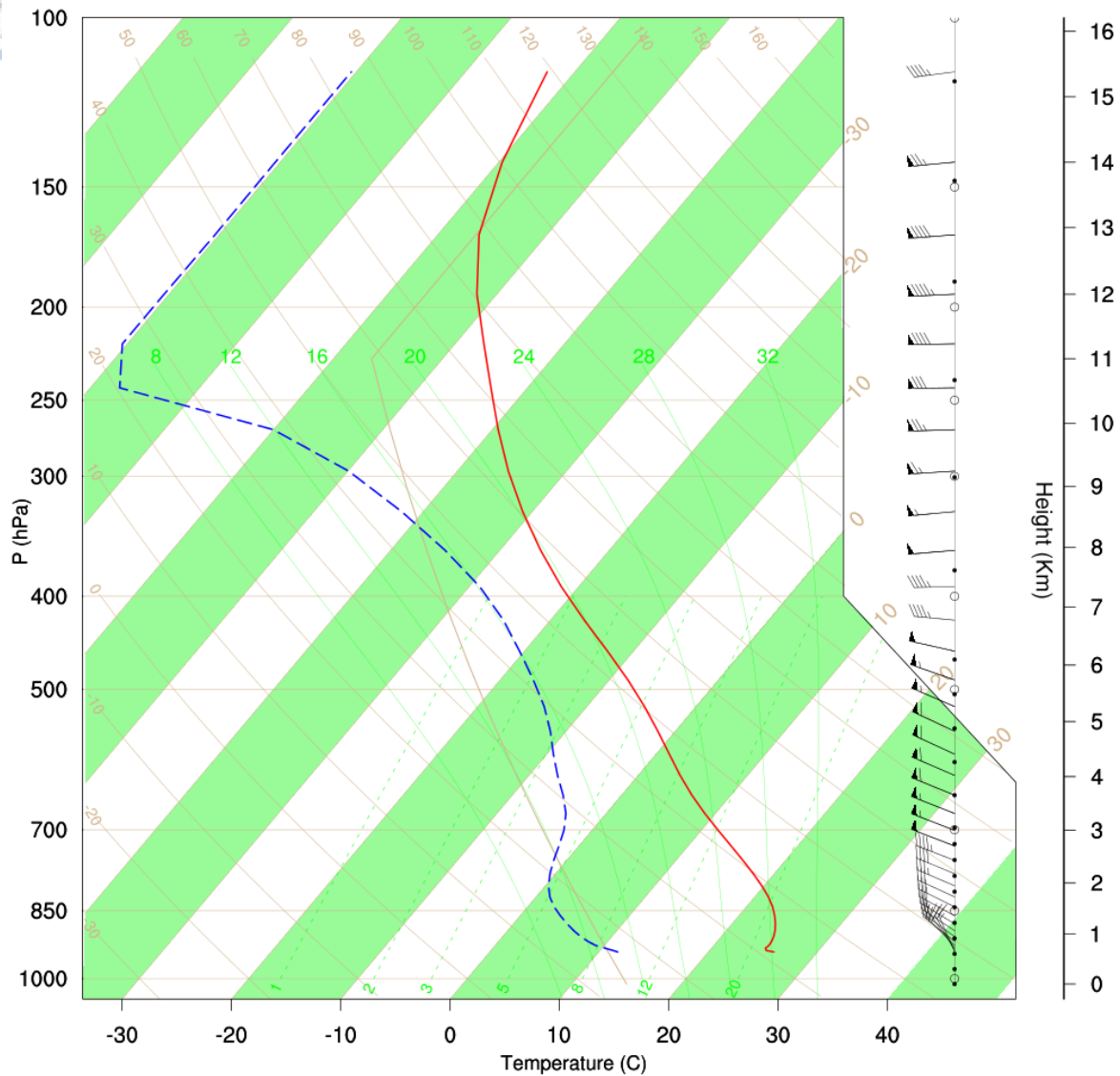


Fig. C.2: Sounding data extracted from the WRF-D03 initial conditions (interpolated ECMWF analyses) at a location (37.951oN, 23.148°E) downwind of Gerania Mts. at 06Z. Red solid and blue dashed lines represent air temperature and dew-point temperature profiles, respectively.

